Observational Insights into White Dwarf Planetary Systems

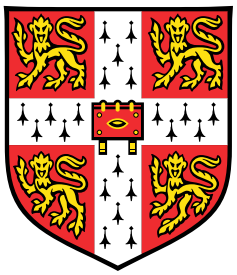

Laura Kathryn Rogers

Institute of Astronomy
University of Cambridge

This dissertation is submitted for the degree of
Doctor of Philosophy

Jesus College

August 2022

To my astronomically amazing and supportive parents, Sue and Paul.

Declaration

I hereby declare that except where specific reference is made to the work of others, the contents of this dissertation are original and have not been submitted in whole or in part for consideration for any other degree or qualification in this, or any other university. I state that except where specific reference is made in the text to the work of others, including any collaborators, the contents of this dissertation are the result of my own work. This dissertation contains fewer than 60,000 words including summary/abstract, tables, footnotes and appendices.

Chapter 2 has been adapted from the publication: *'Near-infrared variability in dusty white dwarfs: tracing the accretion of planetary material'* L. K. Rogers, et al., MNRAS, Volume 494, Issue 2, May 2020, Pages 2861–2874.

Chapter 4 has been adapted from work submitted to MNRAS: *'Tracing the composition of exoplanetary building blocks using seven polluted white dwarfs'* L. K. Rogers, et al. (2022, submitted).

Laura Kathryn Rogers
August 2022

Abstract

Observational Insights into White Dwarf Planetary Systems

Laura Kathryn Rogers

In recent decades the number of known planets has escalated from the eight solar system planets to over 5000 exoplanets; the focus has now shifted to their characterisation. Spectroscopic studies of white dwarfs 'polluted' by planetary material are a unique laboratory allowing measurements of their bulk composition. This thesis focuses on these polluted white dwarfs to observationally investigate how the material ultimately accretes onto the white dwarfs, and the inferences made about the composition of exoplanetary bodies.

These white dwarfs become polluted due to the scattering of exoplanetary bodies on star grazing orbits where they tidally disrupt, producing dusty debris detectable as excess infrared emission, and then subsequently accrete onto the white dwarf. The scattering and accretion are expected to be stochastic processes with variability predicted on human time-scales. Chapter 2 reports near-infrared (*JHK*) monitoring campaigns of the dust emission with the UKIRT/WFCAM and NTT/SOFI. Over timescales of hours, days, months, and years no statistically significant variation is found. Chapter 3 reports spectroscopic monitoring campaigns of the metal features in the white dwarfs using SALT/HRS and Magellan/MIKE. Across more than 10 years and thousands of sinking timescales, no unambiguous statistically significant variability in the amount of material in the photospheres of the white dwarfs is found. Both results agree that the processes driving the accretion do so at a constant rate.

Polluted white dwarfs with infrared emission tend to be the most heavily polluted systems. Chapter 4 presents the first composition studies from a novel programme which identifies new heavily polluted white dwarfs discovered from their infrared excess. The planetary material that polluted these seven white dwarfs are broadly consistent with rocky material, but show some compositional and geological diversity. Some of the white dwarfs appear to have accreted a fragment of a larger core-mantle differentiated body. Using oxygen budgeting, two white dwarfs are discovered to have accreted oxygen-rich material which may imply water-rich bodies. Also, evidence points towards one of the white dwarfs accreting material from two distinct planetary bodies, this challenges the commonly used assumption that there is one body in the white dwarf's atmosphere at once.

Acknowledgements

I would firstly like to thank my wonderful supervisors, Amy Bonsor and Simon Hodgkin, without which I would have never made it to the end of the PhD. Thank you for the endless support and for always making time to help and encourage me during my PhD (and for putting up with the endless silly questions). I will forever be grateful for Amy as my primary advisor; she has been such a supportive, encouraging, and knowledgeable supervisor relating to both research and life. I wish I could thank Amy a million times over, she has been such an amazing role model and mentor and I will always look up to and aspire to be like her.

I am incredibly grateful for funding from the Science and Technology Facilities Council which allowed me to pursue my dream of a PhD in astronomy. I would also like to acknowledge funding from the University of Cambridge and Jesus College, Cambridge.

I am so grateful to my 'unofficial' supervisor, Siyi Xu; Siyi has supported me throughout my PhD, her willingness to teach me and help me develop as a researcher has meant the world to me and I am so grateful for her time, knowledge and patience, especially considering the 11 hour time difference! I am so thankful to numerous members of the astronomical community who have helped me throughout my PhD, but would especially like to thank: Beth Klein, Ted von Hippel, and Patrick Dufour for their help and guidance.

I have loved learning about observing and have been very fortunate to gain lots of observational experience during my PhD. I am incredibly grateful to Mike Shara and Ted von Hippel for enabling me to obtain my very first data set using the HRS/SALT (reported in Chapter 3). Thank you so much for your generosity, knowledge, and advice as I have learnt infinite amounts from this project. I was also incredibly fortunate to go on an observing trip to Chile with Anais Gonneau as part of my first accepted PI proposal, not only did I learn lots from her, but we had such a wonderful time. I would also like to thank Claudia Aguilera Gómez for teaching me all she knows about observations and for letting me watch her remotely to observe.

I have thoroughly enjoyed my time as a PhD student at the IoA, and have especially enjoyed the friendly and collaborative feel of the department. Thank you to everyone both past and present for making the IoA such an amazing place to study for my PhD, even if some of it was during a global pandemic! I have really appreciated the wealth of knowledge

at the IoA and want to thank Mark Wyatt, Mike Irwin, and Matt Auger for always being willing to answer my questions. I would distinctly like to thank Paul Hewett and Debbie Peterson, I will be eternally grateful for their time, help and guidance. They both made it possible and easy for me to continue and finish my PhD under difficult circumstances. My PhD has been very unconventional, beginning full time and transitioning to part time after a period of absence due to a head injury. However, the positive side of doing a PhD over 6 years meant that I got to overlap with 10 cohorts of amazing and inspiring PhD and Masters students. It has been awesome sharing my time at the IoA with each and every one of them, and I am so thankful for their support, friendships, and laughs. I would especially like to thank all those who started their PhD at the same time as me, with special thanks to my fellow polluted white dwarf enthusiast John, I learnt so much from John including the best goalkeepers to pick for fantasy league. I would also like to thank the wonderful humans from the years below who welcomed me into their years with open arms. I would especially like to thank: Amy, Sophie, Anjali, Aoife, Chiara, Matthew, and Luis, your friendship and support has been incredible. I also want to shout out to my numerous amazing office mates, the white dwarf group, and the board games crews for always keeping me sane and happy.

I want to thank all my family and friends for their non-stop encouragement, care, and love throughout this journey. I have chosen to dedicate my thesis to my amazing parents, Paul and Sue, who have always shown me unconditional love and support. Thank you so much for always being there for me, for encouraging me when I didn't believe in myself, and looking after me when I needed it most. To my amazing siblings Sarah, Matthew and Sophie, thanks for always being there for me and I am so sorry for all the times you have had to listen to me go on about astronomy! To my niece, Ella, thank you for always making me smile, I love that you love the moon more than I do! To my friends outside of my PhD, thank you so much for keeping me sane over these years and for the never ending love, laughs, and support: Rosie, Kris, Thomas, Kitty, Georgia, and George, and to all my Jesus College and Cambridge friends, thank you for making this such a memorable experience.

Finally, I want to thank my incredible partner, Dave. Life has been a roller coaster with the PhD, head injury, and pandemic, but you have always been my calm constant that keeps me grounded. You make me a better person and your love and support throughout the PhD is something I am thankful for, far beyond words.

Table of contents

List of figures

List of tables

Chapter 1

Introduction

Astronomy has entered the era of large observational surveys, providing us with unprecedented information about the Universe, and our place within in. Exoplanets are now known to be ubiquitous with planets predicted to outnumber stars in the Milky Way (Cassan et al., 2012). Over the last few decades the field of exoplanetary science has rapidly developed with the focus shifting away from discovery and towards the characterisation of exoplanets and exoplanetary populations. Key questions driving the field are: what are the compositions of exoplanets? How similar are exoplanet compositions and system architectures to that of the solar system? Do other planetary systems have the conditions to develop extraterrestrial life? White dwarfs are unique laboratories that can contribute to studying these questions. Between 25–50% of white dwarfs have accreted planetary material from their remnant planetary systems (Zuckerman et al., 2003, 2010; Koester et al., 2014; Wilson et al., 2019). Spectroscopic observations of these white dwarfs reveal the bulk composition of the exoplanetary material accreted. This is the *only* observational method to directly infer exoplanetary interior composition. These *polluted* white dwarf systems and what they reveal about the composition of exoplanetary material is the focus of this thesis. This chapter will first introduce the knowledge gained from studying planetary composition and architecture of the solar system, then will discuss this in relation to exoplanets, and finally will combine these topics to introduce white dwarfs and their remnant planetary systems.

1.1 Solar System

Before the 1990s, the solar system was the only planetary system known. Therefore, research on planets concentrated on the solar system planets and small bodies consisting of the four terrestrial bodies: Mercury, Venus, Earth and Mars, the four gas giants: Jupiter, Saturn, Uranus and Neptune; and the small bodies: asteroid belt, Kuiper-belt, Oort cloud and their

various constituents. The solar system formed from a collapsing cloud of dust and gas around 4.567 billion years ago forming the proto-Sun with an orbiting disc of gas and dust (Connelly et al., 2012). The first solids condensed out of the protoplanetary nebula which constituted the building blocks for the planets. The process of planetesimal formation is an extensive field of scientific research, for further details refer to the review by Raymond & Morbidelli (2022). Although the solar system is the only planetary system where planetary material can be directly sampled, numerous open questions regarding the formation and evolution of the solar system remain.

1.1.1 Rocky bodies in the solar system

Small bodies

Meteorites are debris from outer space that survive the journey through the Earth's atmosphere to land on the surface. Laboratory measurements reveal their composition and structure and thus gives insight into solar system formation, composition, and evolution. The main classifications of meteorites are chondritic and achondritic. Chondritic meteorites are primitive asteroids that contain the earliest solids and consequently define the age of the solar system as 4.567 billion years (Connelly et al., 2012). They provide the abundances of the material that condensed to form the solar system constituents, which provides powerful information about the formation of planetary bodies. Achondritic meteorites have undergone geological and collisional processing (melting and core–mantle differentiation, which are discussed in more detail in the following section). These meteorites include those from the asteroid belt, Mars, and the Moon, and can consequently reveal the formation and internal structure of the terrestrial planets (Mittlefehldt et al., 1998; Weisberg et al., 2006).

Chondritic meteorites are composed of: chondrules, refractory inclusions (0.01—10 % volume), metallic Fe and Ni (<0.1—70% volume), and are surrounded by a fine-grain matrix (1—80% volume). Chondrules are millimeter sized particles that form by the melting of material in the solar nebula, which are subsequently deposited onto the mid-plane of the protoplanetary disc with other particles. Chondrules are mostly composed of olivine and pyroxene minerals which have crystallised rapidly between temperatures of $\sim$ 1800 and 1300 K (Scott, 2007). Refractory inclusions are crystalline silicates and oxides which form at high-temperatures ($>$ 1300 K) from processes such as melting, evaporation and condensation. The inclusions consist of calcium-aluminium rich inclusions (CAI's) and amoeboid olivine aggregates (AOA). Fe and Ni metallic grains can be present both within and outside of chondrules. Similar to chondrules and inclusions they also form at the highest temperatures.

The fine-grain matrix material contains volatile-rich minerals, which fills the space between the other constituents of the chondritic meteorite (Alexander et al., 2018).

The three major classes of chondrites are: carbonaceous, ordinary, and enstatite. These classes are sub-divided into 15 groups with variations that are categorised by chondrule sizes, the quantity and composition of the refractory inclusions, the amount of metallic iron and nickel, and the relative fraction of mineral matrix (Bizzarro et al., 2017). Carbonaceous chondrites contain a significant fraction of volatiles, including carbon, and are thought to originate furthest from the Sun, they account to 5% of known meteorites. The CI group of carbonaceous chondrites have a composition most similar to the solar photosphere, as seen in Figure 1.1, and chemically are the most primitive group of meteorites. Ordinary chondrites are most common, consisting predominantly of chondrules, with small components of refractory inclusions, Fe, Ni metals, and matrix. The rarest are enstatite which account to 2% of known meteorites, which contain a significant fraction of the mineral enstatite with Fe taking the form of metallic-Fe rather than oxides. Enstatites likely formed in reduced environments close to the proto-Sun.

Meteorites are thought to be the result of the fragmentation of asteroids that fall to Earth. Understanding how the classes of meteorites link to classes of asteroids has been subject to intensive study as their connection and properties can inform about the history and evolution of the solar system. Asteroids have experienced significant dynamical and collisional evolution which affects their composition, size, shape, rotation and location; making it difficult to model the evolution of the small bodies. Asteroids are defined based on their albedo and spectral features. C-class (carbonaceous) asteroids are thought to be the precursors to carbonaceous chondrite meteorites and are typically associated with the outer asteroid belt, they have low albedos and can contain up to 10% water by mass. Whereas, the S-type (stony) asteroids have much higher albedos, have spectral signatures of silicates and are dry with less than 0.1% water by mass, these asteroids are believed to be associated with the ordinary chondrite class of meteorites. (Michel et al., 2015; Alexander et al., 2018). The asteroid belt contains a mixture of both volatile-poor asteroids (S-type) in the inner regions and volatile-rich asteroids (C-type) in the outer regions. Originally it was hypothesised that this was due to the ice lines and formation conditions, but abundance and isotopic studies revealed these asteroids formed in different reservoirs (Warren, 2011; Budde et al., 2016; Kleine et al., 2020). Significant progress has been made modelling the solar system formation and evolution, but no proposed model is able to explain all observations in the solar system, including how the asteroid belt became a mix of two distinct reservoirs of small bodies (e.g. Raymond & Morbidelli, 2022).

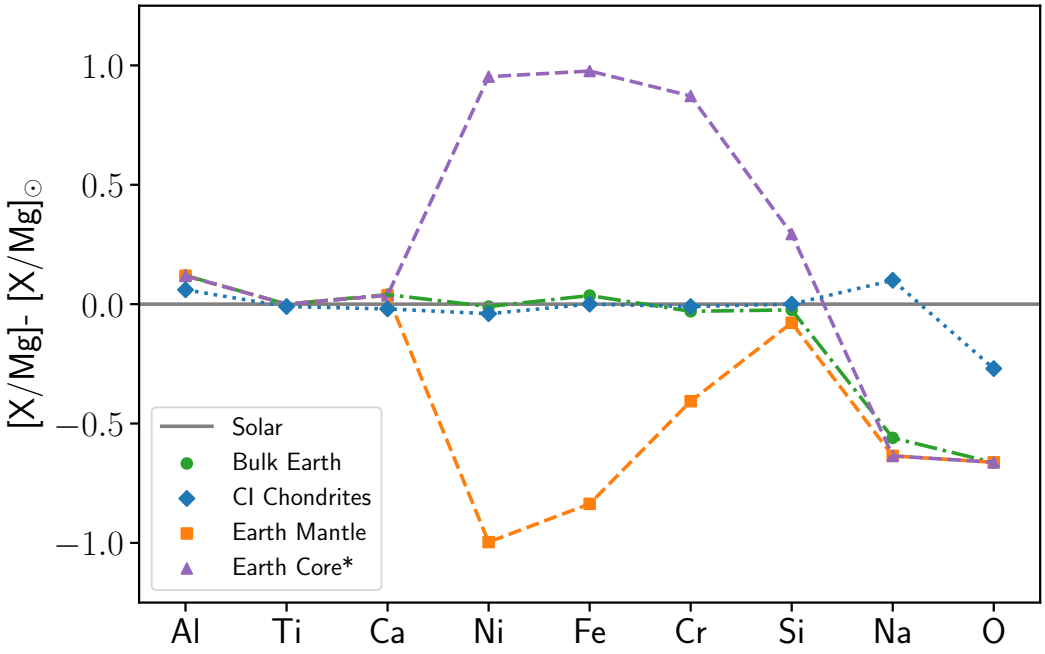

Fig. 1.1 Abundance ratio of element X to Mg, normalised to solar for compositions of: CI Chondrites, bulk Earth, Earth's mantle, and Earth's core. Data are from: McDonough (2003b); Grevesse et al. (2007). * The core composition is: 2/3 core and 1/3 mantle.

Core–mantle differentiation

The Earth has an iron rich core and is surrounded by an iron poor mantle. These layers are key to the Earth being habitable and maintaining habitable conditions over time. The molten Earth's core generates a magnetic field which is crucial for shielding the Earth from harmful solar winds. The mantle and crust result in tectonic activity which regulates the temperature and atmospheric conditions of the planet, for example, by regulating the quantities of carbon dioxide in the atmosphere via the carbon cycle, thus keeping the temperature stable.

Core–mantle differentiation is the process by which melting causes siderophilic ('iron loving') elements to separate and sink towards the centre of the body, and lithophilic ('rock loving') elements to go towards the surface of the body where they can combine readily with oxygen. In order to melt the material such that core–mantle separation can occur, a heat source is required. For larger bodies greater than ~ 1500 km, the release of gravitational potential energy during formation can result in large scale melting and differentiation into a core and mantle. However, in the solar system the decay of ^{26}Al is required to form cores in asteroids as they are not massive enough to generate heat via gravitational potential energy. Modelling indicates that for planetesimals greater than ~ 20 km in diameter, ^{26}Al heating could cause melting and core formation (Hevey & Sanders, 2006; Elkins-Tanton, 2012).

Terrestrial planets

The terrestrial planets in the inner solar system are all composed of silicate material and metals (e.g. iron). All four terrestrial planets are differentiated and have a core component and a mantle/crust component. Differentiation into core and mantle is expected to have occurred early in the formation of terrestrial bodies as the gravitational potential energy released upon accretion was significant enough to melt their interior. The mass fraction of the metallic core in Mercury, Venus, Earth, and Mars decreases as a function of distance from the Sun from approximately 3/4, to 1/3 (Venus and Earth), to 1/5, respectively (Sohl & Schubert, 2007).

The structure and composition of the Earth's interior has been subject to extensive studies. For example, measuring the velocities of seismic waves propagating through the Earth reveals the density profile and therefore layered structure of the Earth; and studying rock samples from the crust and upper mantle reveals the composition of the outer layers of the Earth. The best estimate of the bulk constituents of the Earth by mass is: 32% iron, 29.7% oxygen, 16.1% silicon, 15.4% magnesium, 1.82% nickel, 1.71% calcium, 1.59% aluminium, plus others in smaller amounts (McDonough, 2003b). The core of the Earth is enhanced in siderophilic elements, such as iron and nickel, and the mantle of the Earth is depleted in siderophilic

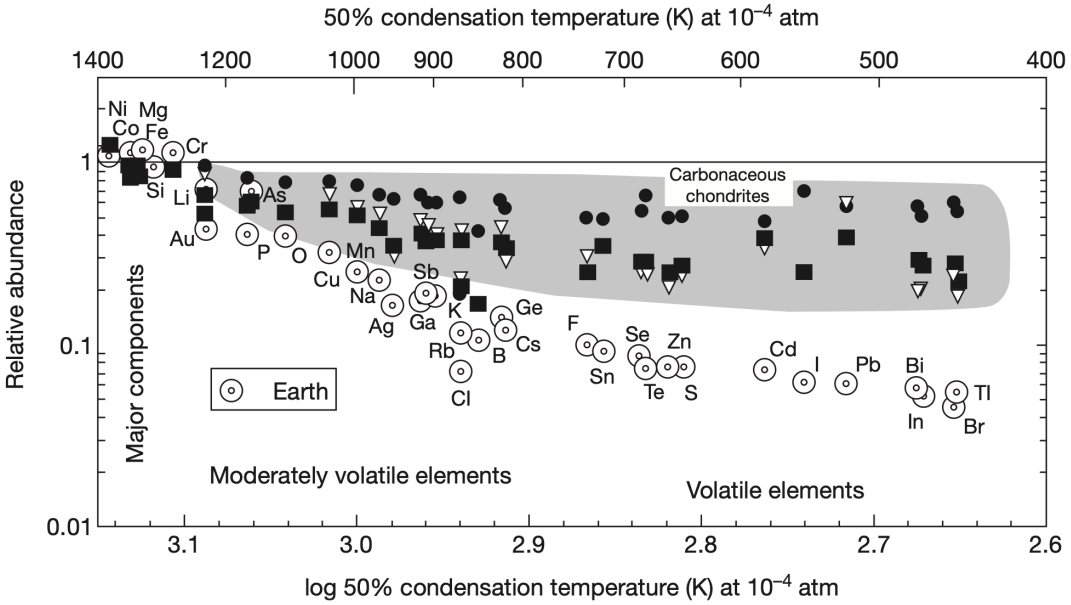

Fig. 1.2 The relative abundance of X/Mg for bulk Earth (open circles) and classes of carbonaceous chondrites (CM class is shown as filled circles, CV as filled squares, and CO as open triangles), normalised to CI chondrites, plotted against the log temperature at which 50% of the element would have condensed from a gas at 10^{-4} bar. The shaded regions defines the area covered by the three carbonaceous chondrites classes. The volatility depletion trend in bulk Earth and carbonaceous chondrites is clear. Figure from McDonough (2003a).

elements, as can be seen in Figure 1.1. The bulk composition of the Earth, disregarding volatiles, matches that of the most primitive meteorites, CI chondrites, as seen in Figure 1.1. These meteorites are assumed to be the building blocks of the Earth, although exactly which is debated.

The volatiles, especially water, significantly contributed to the Earth becoming a habitable planet. Figure 1.2 shows the volatility depletion trend in bulk Earth. The chemical composition of the Earth was largely inherited from the condensation and accretion of nearby material in the protoplanetary disc. The standard model of the disc which the solar system formed has the snow line at 2.7 au (Hayashi, 1981), the Earth formed within this line so appears to have formed dry. However, water is present on the Earth with a mass fraction of $\sim 0.1\%$, greater than would be expected based on its formation location (Van Dishoeck et al., 2014). It is actively debated as to whether the volatiles were already present on Earth or whether volatile-rich bodies were later accreted. If they were later accreted, it is thought that volatile delivery from icy planetesimals is crucial for the present day levels of water on Earth (Wänke, 1981; McDonough, 2003a; Ballhaus et al., 2013; Yoshizaki & McDonough, 2021). The ratio of deuterium, a stable isotope of hydrogen, to hydrogen ([D/H]) is a useful diagnostic of where in the solar system objects formed as the [D/H] ratio changes depending on the location in the protoplanetary disc the bodies originated from (Hallis, 2017). Therefore, the [D/H] ratio can be used to investigate what bodies contributed to seeding the Earth with water and where in the solar system they originated from. The [D/H] ratio of the outer asteroid belt and the Kuiper belt have similar values to the Earth's oceans and as they also have high fractions of water, it is hypothesised that these reservoirs significantly contributed to water delivery on Earth and the terrestrial planets (Van Dishoeck et al., 2014). Instabilities which cause mixing of the different reservoirs are pivotal for understanding of the solar system evolution and volatile delivery, for further discussions see (Raymond & Morbidelli, 2022).

1.2 Exoplanets

1.2.1 Discovery

It wasn't until the 1990s that the first exoplanets were discovered (e.g. Wolszczan & Frail, 1992). The confirmation of exoplanets gauged much interest and excitement worldwide as people began to wonder what these other worlds are like, could they potentially be habitable and host life, and ultimately whether we are alone in the universe.

The advancement of modern technology has expanded our knowledge immensely; to date, over 5,000 exoplanets have been discovered, Figure 1.3 shows the exoplanets discovered

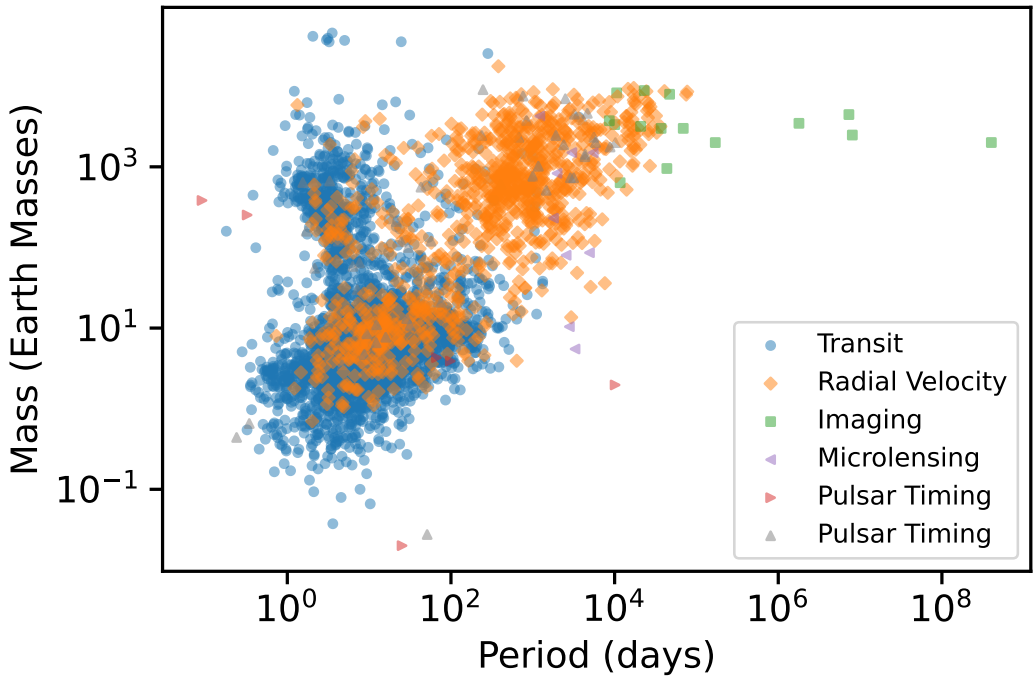

Fig. 1.3 Orbital period versus planet mass for exoplanets with both measured/estimated orbital period and mass. The colours highlight the different discovery methods. Figure using data from the NASA exoplanet archive[1].

thus far[1]. Exoplanets appear to be ubiquitous and outnumber stars in the Milky Way (Cassan et al., 2012). The first exoplanets discovered were around a millisecond pulsar, found using precise timing measurements of the pulses (Wolszczan & Frail, 1992). Following this, the first exoplanet discovered around a Sun-like star was 51 Pegasi b (Mayor & Queloz, 1995), a Jupiter mass planet discovered with the radial velocity technique. The radial velocity technique detects the presence of an orbiting companion from the Doppler shift in the stellar spectral lines. The star and planet orbit the common centre of mass; if the stellar mass is known, the minimum mass of the planet can be inferred (Fischer et al., 2015). Despite the successes of these two detection methods delivering the first exoplanet discoveries, more than three quarters of exoplanets were discovered with the transit technique.

The transit technique photometrically monitors a star; as a planet passes in front of the stellar disc a flux drop proportional to the relative sizes of the star and the planet is observed. This method provides information on the radius of the planet, assuming the radius of the star is known, and constrains the inclination of the orbit. The first exoplanet transit detection was around HD 209458, where radial velocity measurements had previously confirmed an orbiting planet (Charbonneau et al., 1999). Other techniques have been employed to detect exoplanets, such as, direct imaging, microlensing, and astrometry. The current detection statistics are low, but with technology developments, current (e.g. *Gaia*, Collaboration et al., 2016) and future space missions (e.g. *LIFE*, Quanz et al., 2021), as well as the upcoming ground based extremely large telescopes, many more planets are expected to be discovered with these methods.

Figure 1.3 shows the exoplanets discovered so far with the regions in parameter space that these techniques are most sensitive to clearly standing out. The success of the *Kepler* and *TESS* space missions significantly contributed to the discovery of transiting exoplanets (e.g. Borucki et al., 2010; Guerrero et al., 2021), which has allowed the field of exoplanet demographics to flourish (e.g. Batalha, 2014). The transit technique is sensitive to larger planets, on close in orbits as this increases the transit depth and the probability of the transit (as the star and planet must be aligned). The radial velocity technique is sensitive to more massive planets on shorter orbits, as these produce larger amplitude signals and multiple orbital periods can be measured. With current and future generations of higher-resolution and higher-stability instruments, radial velocity surveys can push to discover Earth mass planets around Sun like stars. However, stellar activity signals now dominate the noise so in order to discover planets that are increasingly lower in mass and on longer orbital periods, stellar variability needs to be better understood and quantified (e.g. Rajpaul et al., 2015; Vanderburg et al., 2016; Nava et al., 2019). Direct imaging is most sensitive to planets on

[1]Data from: https://exoplanets.nasa.gov/discovery/discoveries-dashboard/ on 26/07/2022

wide (> 5 au) orbits, the best targets tend to be those that are young and massive as these are self-luminous due to heat from formation. The photons from the planet are directly measured demonstrating the power of this technique as these planets can be studied both photometrically and spectroscopically. Exoplanets detected via microlensing events happen when a background object becomes aligned with an intermediate star with an orbiting planet. The star and planet act as a lens and cause brightening of the background source. This technique does not depend as strongly on planetary mass so has a wide discovery space which includes free-floating planets (Gaudi, 2012).

1.2.2 Characterisation

With the number of exoplanet discoveries increasing everyday, the research focus has shifted towards their characterisation. The field of characterisation is focused on the composition of their interior and atmosphere, and the potential of these worlds to be habitable.

To constrain a planet's bulk composition, measurements of its mass and radius are required. The first exoplanet characterised in this way was HD 209458, radial velocity measurements provided a minimum planetary mass (M sin i), and transit photometry provided the inclination (i), resulting in the determination of the true planetary mass. The combined mass estimate from the radial velocity technique with the radius estimate from the transit technique provides an estimate for the average density of the exoplanet, the average density was low and due to its size it was designated a gas giant (Charbonneau et al., 1999), therefore beginning the era of exoplanet characterisation.

Theoretical mass-radius relationships derived from interior models can be compared to derived mass and radii of exoplanets to infer the interior structure of the exoplanets. Various compositions and interior structures can be invoked in the models, for example, the models can be in the form of a single composition, e.g. 100% Fe, or 100% H/He; or multi-layered composition with combinations of: Fe core, $MgSiO_3$ mantle, H_2O layer; or more exotic compositions (e.g. Seager et al., 2007; Dorn et al., 2015). However, degeneracies arise as different compositions can produce similar mass-radius curves, thus introducing uncertainties in the determination of bulk compositions. In order to more accurately determine the bulk composition of these bodies, additional input information or alternate measurement techniques are required.

The study of exoplanet atmospheres reveals information about the outer layers of an exoplanet (e.g. Crossfield, 2015; Madhusudhan, 2019). Over the coming decades the study of exoplanetary atmospheres will be a key focus of the field. For transiting planets, the opacity of the atmosphere varies with wavelength due to its composition, and measuring the transit depth as a function of wavelength, the 'transmission spectrum', can reveal information

about its atmospheric composition. Transiting planets are also eclipsed by their host star, subtracting the spectrum of the star alone from the combined star and planet spectrum, reveals the thermal 'emission spectrum' of the planet. Current space missions such as *Hubble* and *JWST* have been revealing the spectrum of increasingly smaller planets. Directly imaged planets allow direct spectroscopy without contamination from the stellar spectrum to reveal their thermal emission spectra. With plans for future large telescopes e.g. *LUVOIR*, *LIFE* missions, this technique will enable characterisation of non-transiting planets, not possible via other methods and on longer period orbits.

With increasing amounts of data and computing power, the field of exoplanet characterisation is moving towards a combined approach, where models and results from sub-fields are combined to gain a global understanding of individual exoplanets, for example, interior and atmospheric coupling (e.g. Madhusudhan et al., 2020). The study of exoplanet atmospheres reveals the bulk properties of exoplanets (e.g. planetary mass, radius, atmospheric properties), these can be input into exoplanet interior models to constrain the internal structure and thermodynamic conditions. Continued efforts to combine observations and computational techniques from sub-fields will help to piece together what these other worlds are like.

1.3 White dwarfs

1.3.1 Formation

White dwarfs are the final product of stellar evolution for stars with an initial main sequence mass in the range 0.07 to 8 $M_\odot$. It is predicted that as the Milky Way ages more than 97% of the stars will eventually evolve to white dwarfs (Fontaine et al., 2001). Figure 1.4 shows how a solar mass star evolves from the zero age main sequence (ZAMS) to the white dwarf phase. On the main sequence, stars burn hydrogen to helium via the proton-proton chain, building up helium in their core. Stars spend $\sim 90\%$ of their lifetimes on the main sequence. Once hydrogen fusion in the core ceases, the central temperatures are not sufficient to ignite helium fusion, however, the hydrogen shell surrounding the core reaches the temperature and pressure required for proton-proton chain fusion, and hydrogen shell burning commences. The stellar envelope expands, cooling the star and increasing the luminosity, positioning the star on the sub giant branch (SGB). As the shell burns hydrogen to helium, helium is dumped onto the core, increasing its mass and eventually the helium core becomes degenerate. The stellar envelope continues expanding causing a rapid increase in luminosity and it travels up the red giant branch (RGB). Due to the larger temperature gradients, energy transport is via convection rather than radiation. This causes large convection zones which dredges

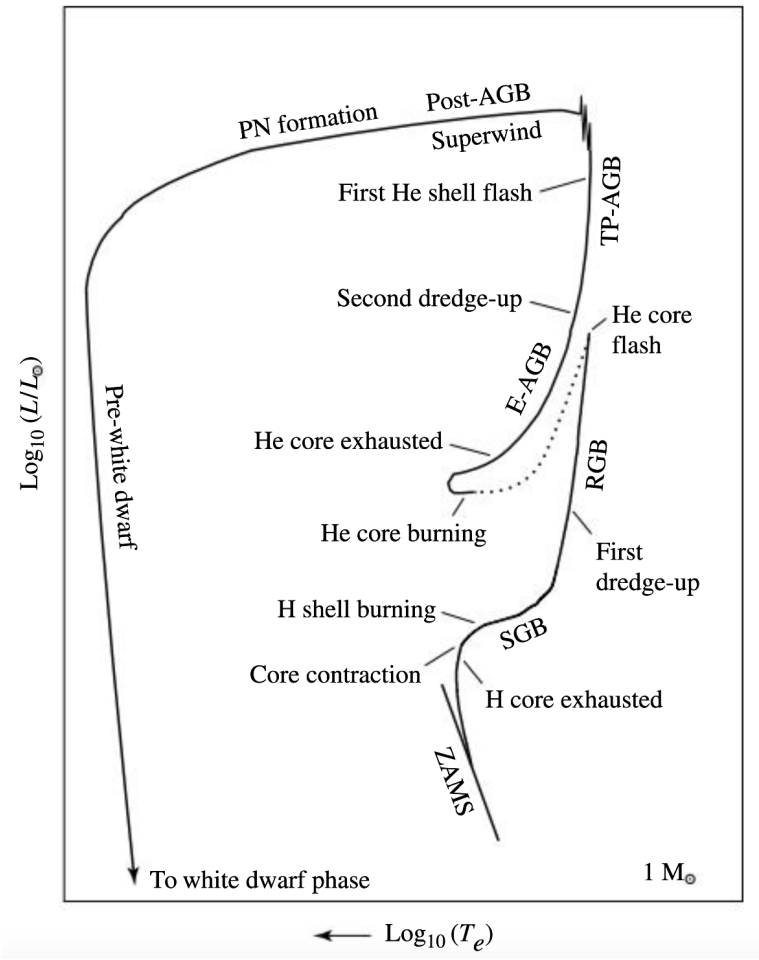

Fig. 1.4 A diagram highlighting the evolution of a solar mass star from the zero age main sequence (ZAMS) to the white dwarf phase. Figure from Carroll & Ostlie (2017).

up material that has been modified by nuclear processes - the first convective dredge up. Helium continues to be produced and dumped onto the core, and as the core is degenerate, the increased mass causes core contraction. Eventually the conditions in the core are sufficient for helium to fuse via the triple alpha process; this causes the helium flash. The core expands and is no longer degenerate, so helium core burning and hydrogen shell burning occurs as the star settles onto the horizontal branch (HB). The HB is the equivalent of the hydrogen burning main sequence for helium burning, except the lifetime is much shorter due to the higher luminosity. Once the star has exhausted helium in the core, the core contraction results in a degenerate core consisting of C and O. The temperature is not sufficient for C and O to burn in the core, but the core contraction generates sufficient energy that helium and hydrogen shell burning can occur. The outer layers of the star expands and luminosity increases moving it up the asymptotic giant branch (AGB) to transition to a red super-giant. Instabilities in the burning shells result in thermal runaways driving thermal pulses which cause the outer layers of the star to be ejected producing a planetary nebula. The remnant stellar core has insufficient gravity to fuse so becomes a carbon-oxygen white dwarf supported entirely by electron degeneracy pressure. The average mass of a white dwarf is $\sim 0.6\,M_{\odot}$ with radii similar to that of the Earth. They form extremely hot ($>$100,000 K) and radiate as they fade over long cooling times, $\tau_{\rm cool}$:

$$\tau_{\rm cool} \propto L^{-5/7}, \tag{1.1}$$

where L is their luminosity (Mestel, 1952; Van Horn, 1971). This demonstrates the connection between a white dwarfs age and its temperature, with the coolest systems being the oldest. Consequently, white dwarfs can be used to constrain the ages of stellar populations in the Milky Way (e.g. Fontaine et al., 2001). It is expected that white dwarfs will eventually cool and fade into a black dwarf (Adams & Laughlin, 1997).

1.3.2 White dwarf properties

White dwarfs are powerful laboratories to study numerous aspects of physics and astrophysics, including: degenerate states of matter, age history of stellar populations in the Milky Way, and the bulk composition of exoplanets. However, without knowledge of the stellar properties, this work is not possible. The following discussion focuses on the determination of the effective temperature and log(g). There are two main methods to observationally determine these parameters: the spectroscopic method and the photometric method.

The spectroscopic method fits white dwarf models to the H/He lines in their spectrum. The cores of white dwarfs are made of degenerate matter due to the high pressures ($\sim 10^6\,{\rm g\,cm^{-3}}$), this electron degeneracy pressure prevents the further collapse of the core. These degenerate

C-O cores are surrounded by a layer of non-degenerate gas, most often He, with a thin H layer on top. Therefore, the spectra of most white dwarfs exhibit only absorption lines from hydrogen and/or helium, and these absorption lines are pressure broadened by a variety of mechanisms. For example, the Stark Broadening Effect; due to the extreme temperatures, the envelopes of the white dwarfs are often ionised, these moving charges give rise to local electric fields. As a consequence of the extreme densities, the neutral emitters feel the presence of the electric field which results in the shifting of energy levels via the Stark Broadening Effect (Stark, 1913), one of the main causes of the broadening of the spectral lines in the temperature range of interest in this thesis ($> 15{,}000\,\mathrm{K}$). The profiles of the Balmer lines, and optical helium lines are very sensitive to temperature, therefore, comparing the observed H/He absorption profiles with those predicted from theoretical models, the white dwarf parameters can be determined, this is the *spectroscopic method* (e.g. Holberg et al., 1985; Bergeron et al., 1992, 2011).

The photometric method fits white dwarf models to broad band photometry. For this method, the white dwarf models are convolved with the band-passes of the photometric filters and are fitted to the broad band photometry. Combining the parallax to give the distance, theoretical mass-radius relations, and the synthetic photometry gives the best-fitting effective temperature and surface gravity, ($log(\mathrm{g}) = log(\mathrm{M}) - 2log(\mathrm{R}) + 4.437$ in solar units). Reddening becomes important for objects $> 100\,\mathrm{pc}$, and so it is crucial to de-redden the photometry before fitting for accurate parameter determination. Genest-Beaulieu & Bergeron (2019) highlights the importance of including the Sloan Digital Sky Survey (*SDSS*) 'u' band for accurate and consistent parameter determination as often the optical photometry lies on the Rayleigh Jeans slope, but the 'u' band samples the peak of the white dwarf's spectral energy distribution (SED), therefore, including 'u' band photometry allows for improved estimates of the effective temperature.

1.3.3 Spectral classification

White dwarfs tend to be classified based on their spectra. Spectral classifications begin with the letter 'D' which highlights that it is a degenerate object. The main spectral classifications of white dwarfs are: DA, DB, DC, DO, DQ, and DZ, Figure 1.5 shows an example spectrum from each sub-class. Most white dwarfs are DAs, where strong hydrogen absorption lines are present in their atmospheric spectra due to an outer hydrogen envelope on top of a helium layer. DBs, however, show strong helium absorption lines (McCook & Sion, 1999), it is hypothesised that they fused their outer hydrogen envelope during the post main sequence and are left with a pure helium envelope. The pressure broadening of the spectral lines (discussed above), makes the hydrogen and helium lines strong and observable. The strength of the DA

and DB spectral features change by significant amounts between stars due to the white dwarf parameters and differing histories, for example, due to accretion events, convective mixing or rotation (Fontaine & Michaud, 1979; Chayer et al., 1995a,b). DC white dwarfs contain no hydrogen or helium lines, this most often occurs when DA white dwarfs cool below 6,000 K, or when DB white dwarfs cool below 11,000 K. Therefore, below 6,000 K it is not possible to differentiate between hydrogen or helium dominated white dwarf atmospheres. DO white dwarfs contain absorption lines of ionised helium (He II), it is thought that around 45,000 K these DO white dwarfs transition to DB white dwarfs. DQ white dwarfs have spectra that show strong carbon absorption features. Cool DQs are thought to have deep convection zones which can result in carbon dredge up from the core to the atmosphere. Hot DQs are thought to arise due to binary mergers. DZs are white dwarfs which contain absorption lines from metals. They are cool DC white dwarfs which have accreted metals into their atmosphere. It is possible for a white dwarf to have multiple classifications and for those the letters are listed in order of which absorption features dominate, for example, DAZ and DBZ are DA and DB white dwarfs which also show strong metal absorption features.

The combination of strong gravitational and electric fields in the outer stellar layers causes elements to become separated by diffusion. This leaves only the lightest elements, hydrogen or helium, in the observable atmosphere. The separation of the elements is expected to occur quickly as diffusion time scales are much shorter than white dwarf cooling times ($\sim$ 1 Gyr for an effective temperature of 10,000 K). This picture is complicated by stellar winds, convection, accretion and radiative levitation (Vauclair et al., 1979; Koester & Chanmugam, 1990) which can disrupt the layers.

1.4 Polluted White Dwarfs

In recent years evidence for planetary systems around white dwarf stars has grown, from the discovery of planets orbiting white dwarfs (e.g. Vanderburg et al., 2020; Blackman et al., 2021), to approximately 25–50% of white dwarfs being observed with planetary material polluting their atmospheres (e.g. Zuckerman et al., 2003, 2010; Koester et al., 2014; Hollands et al., 2017). The latter are titled *polluted* white dwarfs. The rapid gravitational settling times in comparison to the white dwarf's cooling age implies that for metals to remain in the white dwarfs' atmosphere ongoing accretion from an external reservoir is required (Koester, 2009). Figure 1.6 shows a schematic of these polluted white dwarf systems including the settling of the metals.

vMa2 was the first single white dwarf discovered, but spectroscopic follow up revealed it had strong metal lines and was therefore designated as a 'F type' star (Van Maanen,

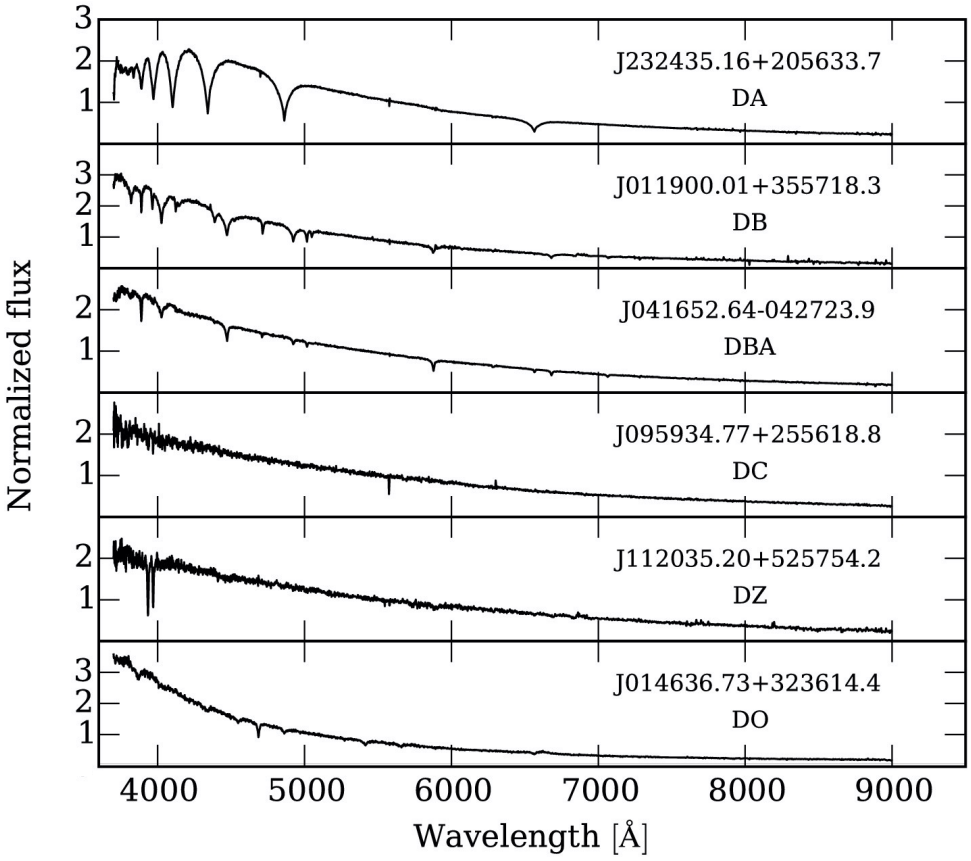

Fig. 1.5 Example spectra of white dwarf spectral types from LAMOST. Figure from Gentile Fusillo et al. (2015).

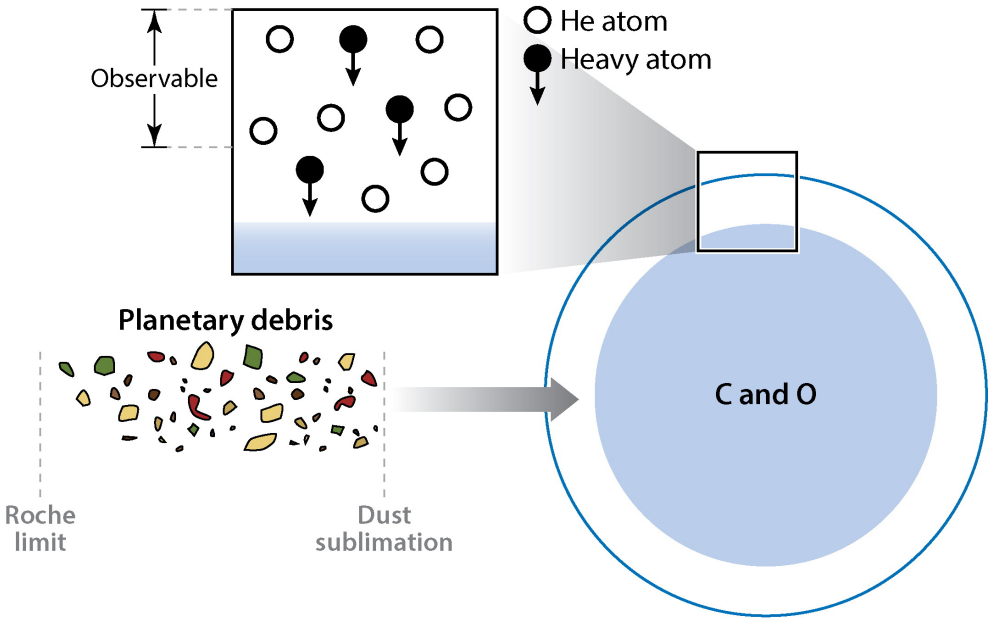

Fig. 1.6 A diagram to demonstrate the polluted white dwarf systems, taken from Jura & Young (2014). The composition of the pollution in the atmosphere will be discussed in Section 1.4.2 and the planetary debris will be discussed in Section 1.4.3.

1917). Almost a century later it was determined that this was a white dwarf which had been polluted with planetary material. Therefore, exoplanetary material has been observed for over a century. The first unambiguous detection of metal pollution that was attributed to a white dwarf was G74−7, this was hypothesised to be accretion from the interstellar medium (ISM) (Lacombe et al., 1983; Dupuis et al., 1993). This hypothesis involves a white dwarf transitioning a dense region of the ISM; dust and gas become gravitationally attracted to the star and therefore polluting its atmosphere. Much evidence invalidated this claim with the main argument being that the abundances of the accreted material did not correlate with the position and kinematics of the white dwarf in comparison to the ISM (Hansen & Liebert, 2003; Farihi et al., 2010a). It is now unambiguously known that these polluted white dwarfs are accreting material from their remnant planetary systems.

1.4.1 How do the white dwarfs become polluted?

The favoured theory regarding the pollution source is that it originates from planetesimals scattered on eccentric orbits towards the white dwarf where they tidally disrupt, migrate inwards, sublimate, and finally accrete onto the atmosphere of the white dwarf (as seen in Figure 1.6). These planetesimals have masses comparable to solar system asteroids (Debes

& Sigurdsson, 2002; Jura, 2003; Farihi et al., 2010a; Jura & Young, 2014; Veras et al., 2014). Additional support for the asteroid tidal disruption model is the discovery of disintegrating planetesimals transiting the polluted and dusty white dwarf WD 1145+017 (Vanderburg et al., 2015). The deepest transit of this star has a period of 4.5 hours and blocks 60% of the flux from the star in the optical (Rappaport et al., 2016; Gary et al., 2017). Following this discovery, transiting debris was found around ZTF J032833.52−121945.27 with periods of 9.9 and 11.2 hrs (Vanderbosch et al., 2021).

For the asteroid tidal disruption model, planetary bodies need to be scattered inwards from the surviving outer planetary system of the white dwarf. There are many dynamical mechanisms which can perturb planetesimals onto star-grazing orbits, the favoured theories cite planets as the source. Stellar mass loss can induce instabilities whereby a planet or planets perturb planetesimals onto star-grazing orbits (Debes & Sigurdsson, 2002; Bonsor et al., 2011; Veras et al., 2011; Debes et al., 2012a; Mustill et al., 2018). There is now evidence that planets can survive to the white dwarf phase (Gänsicke et al., 2019; Vanderburg et al., 2020), supporting these models. Alternative mechanisms to scatter planetesimals include: perturbations due to wide binary companions (Hamers & Portegies Zwart, 2016; Veras et al., 2016; Petrovich & Muñoz, 2017; Stephan et al., 2017; Smallwood et al., 2018), and the liberation of exo-moons (Payne et al., 2016; Trierweiler et al., 2022).

1.4.2 Composition of polluting bodies

When assessing the composition of pollutant bodies, it must be acknowledged that certain phenomena occurring inside white dwarfs can contribute to metals polluting their atmospheres. For white dwarfs with an effective temperature greater than $\sim$25,000 K, radiative levitation can lead to an observable amount of heavy elements in the atmosphere (Vauclair et al., 1979; Chayer et al., 1995a,b). Convection zones that extend deep into the white dwarf interior can also cause the dredge up of heavy elements such that they appear in the outer layers of the convective zone of white dwarfs (Pelletier et al., 1986). This causes difficulty in determining the origin of polluting heavy elements for these temperature ranges. However, for white dwarfs with effective temperatures between 10,000 K and 25,000 K, the pollutant must be external, and therefore, the bulk composition of the pollutant can be directly measured using spectroscopic techniques.

Spectroscopic studies of polluted white dwarfs combined with white dwarf atmospheric models allow the measurement of the bulk composition of extrasolar planetesimals making them unique laboratories. So far, 23 heavy elements have been discovered across all polluted white dwarfs (see references in Table 1. of Klein et al., 2021). The polluted white dwarf GD 362 has absorption features from 19 elements, the most elements detected for a given

white dwarf (e.g. Zuckerman et al., 2007; Xu et al., 2013; Melis & Dufour, 2016; Xu et al., 2017). For the majority of systems, the polluting materials' abundance resembles rocky material similar to asteroids and the terrestrial planets in the inner solar system as seen in Figure 1.7 (Jura & Young, 2014). The inferred accreted mass is consistent with the masses of solar system asteroids ($\sim 10^{20}$ g). The polluted white dwarf SDSS J073842.56+183509.06 has the most mass inferred in its photosphere, 7×10^{23} g, similar to the mass of the dwarf planet Ceres in the solar system (Dufour et al., 2012).

Accretion phase:

In order to reconstruct the abundances of the parent body that was accreted by the white dwarf, it is crucial to consider the differential sinking of elements and the affects this can have on the observed abundances. There are three accretion and diffusion scenarios that could occur. Build up stage - when accretion has just started so the observed abundances correspond closely to the actual abundances of the parent body,

$$\frac{nX(A)_{\text{par}}}{nX(B)_{\text{par}}} = \frac{nX(A)_{\text{WD}}}{nX(B)_{\text{WD}}}, \tag{1.2}$$

where $nX(A)_{\text{par}}$ and $nX(B)_{\text{par}}$ are the abundances for element A and B respectively of the parent body before being accreted by the white dwarf, and $nX(A)_{\text{WD}}$ and $nX(B)_{\text{WD}}$ are the derived number abundances for element A and B from the observations of the photosphere of the white dwarf (Koester, 2009; Harrison et al., 2018). Steady state – when accretion and diffusion processes have reached an equilibrium. For this phase the abundances derived for the accreted material need to be modified to consider gravitational settling for the elements in the white dwarf photosphere,

$$\frac{nX(A)_{\text{par}}}{nX(B)_{\text{par}}} = \frac{\tau_B}{\tau_A}\frac{X(A)_{\text{WD}}}{X(B)_{\text{WD}}}, \tag{1.3}$$

where τ_A and τ_B are the diffusion time-scales of element A and B respectively through the white dwarfs photosphere. Declining phase – after the parent body has been fully accreted by the white dwarf, the abundances decrease exponentially with the decay factors depending on the time since accretion ceased, t,

$$\frac{nX(A)_{\text{par}}}{nX(B)_{\text{par}}} = \frac{nX(A)_{\text{WD}}}{nX(B)_{\text{WD}}}\frac{e^{-t/\tau_B}}{e^{-t/\tau_A}}. \tag{1.4}$$

The sinking timescales of the heavy metals in the photospheres of white dwarfs varies depending both on the element sinking and the white dwarf properties. Warm DAZ white dwarfs have sinking timescales on the order of days–years, whereas DBZ white dwarfs have much longer sinking timescales on the order of 10^2 to 10^6 years. The sinking timescales are most often based on 1D models (e.g. Koester, 2009). However, recent works have been incorporating various mixing mechanisms (e.g. convective instability, thermohaline instability[2]) at the surfaces of white dwarfs in 3D atmosphere models, this has the effect of increasing the sinking timescale of metals in white dwarfs (e.g. Cunningham et al., 2019). As inferences about the pollutants relies on accurate knowledge of the sinking timescales, further work is required to confirm the sinking timescales.

Differentiation:

Fragments of core-mantle differentiated bodies have been observed in the atmospheres of polluted white dwarfs, where observations show enhancement or depletion in siderophilic elements (core-rich or mantle-rich respectively) (e.g. Zuckerman et al., 2011; Hollands et al., 2018; Harrison et al., 2018). Figure 1.7 shows that some white dwarfs are enhanced in elements commonly found in the mantle (Mg, Si) compared to core (Fe), e.g. SDSS J1043+08556 (S1043), and others are enhanced in core elements, e.g. PG 0843+516 (PG0843). If the white dwarfs are accreting the collisional fragments of parent bodies that formed an iron core, a large (as much as two thirds) fraction of white dwarfs may have accreted fragments of larger core-mantle differentiated bodies (Bonsor et al., 2020). This implies that the process of (iron) core formation in exo-asteroids is likely ubiquitous across exoplanetary systems.

Water:

Water is widely recognised as one of the key components required for life, and therefore, there is much astrophysical interest in its detection. Water-rich exoplanetary material which pollutes white dwarfs cannot be directly detected in the white dwarf photospheres as it dissociates into oxygen and hydrogen. However, by calculating how much oxygen would be expected to be in the form of metal oxides (MgO, SiO_2, Al_2O_3, CaO, and FeO), the oxygen remainder can be attributed to water (Klein et al., 2010). A handful of objects have accreted bodies rich in water-ice (Farihi et al., 2011, 2013; Raddi et al., 2015; Hoskin et al., 2020;

[2]The thermohaline instability arises due to unstable gradients in composition which become stabilised by a temperature gradient. Therefore, in polluted white dwarfs the thermohaline instability could lead to additional mixing as the significant mean molecular weight of the material that has accreted compared to the atmosphere of hydrogen below can lead to this instability arising.

Klein et al., 2021), Figure 1.7 shows WD 1425+540 (WD 1425), WD 1232+563 (WD 1232), SDSS 1242+5226 (S 1242), WD 0738 (WD J0738+1835), and GD 61 have excess oxygen and are inferred to be ice-rich objects. WD 1425+540 has accreted a fragment of a Kuiper-belt like icy body rich in both water and nitrogen ices (Xu et al., 2017). Trace hydrogen is detected in up to 75% of DB white dwarfs (Koester & Kepler, 2015). Gentile Fusillo et al. (2017) found a link between trace hydrogen and metal polluted white dwarfs, demonstrating another way to infer the accretion of water-rich planetesimals onto white dwarfs.

Carbon:

Carbon is a key species for the understanding of life. It can be in the form of graphite, organics or ices and is a volatile element, hence the amount of carbon in solid species in the solar system is depleted in comparison to the solar photosphere. There is only one report of carbon rich material, in Ton 345; however, the abundance is debated. Ground based spectroscopy revealed that it was carbon rich with a composition similar to Kuiper Belt objects with small amounts of ice due to the low oxygen abundance (Jura et al., 2015), whilst space based UV observations revealed a much lower abundance of carbon (Wilson et al., 2015). Therefore, there is no definitive evidence for any white dwarf accreting carbon-rich exoplanetary bodies, and all but one demonstrate a carbon depletion (Jura, 2006; Wilson et al., 2016). The body that does not show a carbon depletion is that polluting WD 1425+540, discovered by Xu et al. (2017), as mentioned in the previous section. This body was also the first exo-planetary debris to be detected with Nitrogen; this insinuates that this body formed in a Kuiper belt-like region. UV spectroscopy is most sensitive to detecting carbon, therefore with more UV spectra of polluted white dwarfs providing detections and stringent limits on the carbon abundance, further understanding about the form of carbon in exo-planetary worlds will be revealed.

1.4.3 Circumstellar Discs

Observations of dust discs:

Dust debris from tidally disrupted planetesimals has been discovered via excess infrared emission above that expected from the white dwarf around 1.5–4% of white dwarfs (e.g. Becklin et al., 2005; Kilic et al., 2006; Jura et al., 2007b; Rebassa-Mansergas et al., 2019; Wilson et al., 2019; Xu et al., 2020). G29-38, one of the brightest and most heavily polluted white dwarfs, was the first polluted white dwarf to be discovered with excess emission at infrared wavelengths, as seen in Figure 1.8. It was initially hypothesised that the excess was caused by a brown dwarf companion (Zuckerman & Becklin, 1987). However, pulsation

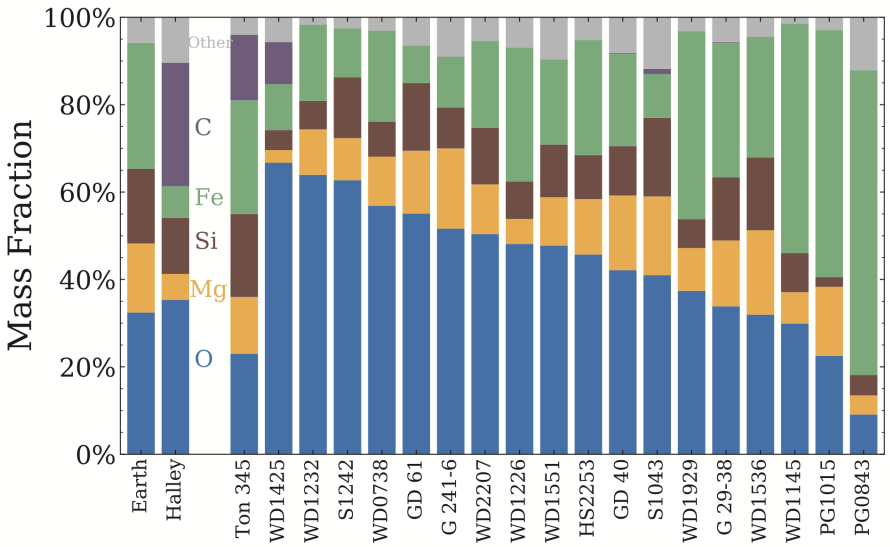

Fig. 1.7 Bar charts showing the pollutant mass fractions of: O, Mg, Si, Fe, C, for 19 polluted white dwarfs. The bulk compositions of the Earth and comet Halley are shown on the left for comparison. Figure from Xu & Bonsor (2021).

timing in the optical and infrared found echoing signals which were difficult to explain with the presence of a brown dwarf companion. Also, infrared spectra demonstrated an excess emission at 10 µm, triple the intensity expected from a brown dwarf (Graham et al., 1990). These arguments favour the infrared excess resulted from a dust disc close to the white dwarf.

The number of infrared excess detections remained at one for nearly two decades. Ground based observations discovered GD 362 as the second white dwarf with an infrared excess associated with a dust disc, with GD 40 closely following this (Becklin et al., 2005; Kilic et al., 2005, 2006). The launch of the Spitzer Space Telescope in 2003 exponentially increased the number of detected discs. To date, tens of white dwarfs have been found with an infrared excess associated with a dust disc, and all are found to also be polluted, implying that the circumstellar material is accreting onto the atmosphere (e.g. Jura et al., 2007b).

Infrared spectra of the dust can inform about the composition of the dust grains. Low signal-to-noise Spitzer spectra from the infrared spectrograph (IRS) of a number of polluted white dwarfs demonstrates strong 10 µm silicate emission features, originating from the orbiting dust disc (Jura et al., 2007a, 2009a). All spectra show the 10 µm feature, with the red wing extending to 12 µm. This feature is characteristic of micron-sized olivine glasses, associated with a tidally disrupted asteroid. G29-38 is the only dusty white dwarf bright enough to have a sufficiently high signal-to-noise infrared spectrum that an in depth mineralogy study could be conducted. Reach et al. (2009) reported a 1–35 µm spectrum,

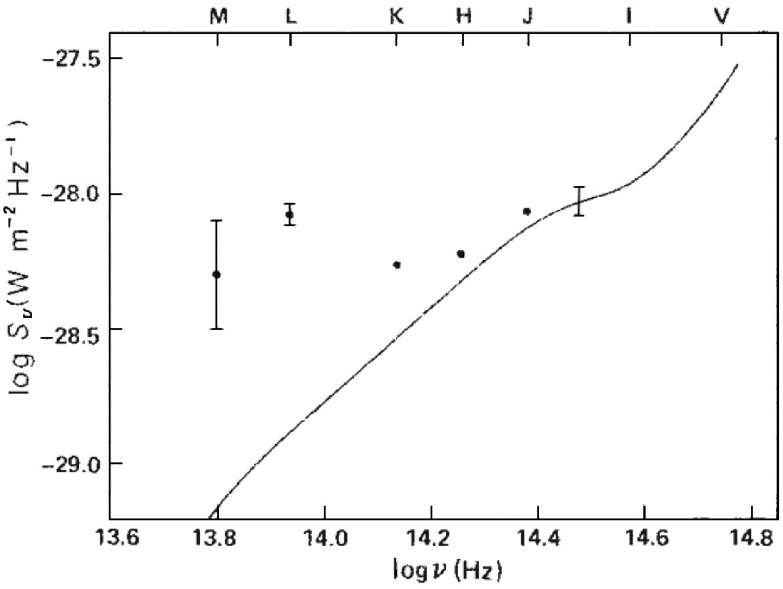

Fig. 1.8 The spectral energy distribution of G29-38. It shows the first infrared excess discovered around a polluted white dwarf (Zuckerman & Becklin, 1987). The data was taken using the NASA Infrared Telescope Facility. An excess at near to mid-infrared wavelengths is clear.

as shown in Figure 1.9, and determined the possible mineral compositions of the dust disc. Disc modelling found it likely that the disc is formed of amorphous carbon, amorphous and crystalline silicates, water ice and metal sulphides. Xu et al. (2014) compared the disc abundances with those in the white dwarf atmosphere and found that the overall agreement is consistent, except for a few elements. *JWST* will provide high quality mid-infrared (mid-IR) spectra that covers strong features from different minerals for discs fainter than G29-38. This will allow further investigation into the correlation between the atmospheric pollution and the disc material, and reveal both the chemical and mineral compositions of extrasolar planetesimals.

It has been suggested that there may be observable signatures of dust beyond the tidal radius, in the form of an asteroid belt or Kuiper belt analogue. This could supply the planetesimals that eventually accrete onto the white dwarfs. Xu et al. (2013) used the *Herschel* Space Observatory to search for a parent population of dusty bodies around GD 362, the data resulted in null detections and stringent upper limits were placed. Farihi et al. (2014) used the *Herschel* Space Observatory and the Atacama Large Millimetre/submillimetre Array (*ALMA*) to search for this parent population around the closest and brightest dusty white dwarf, G29-38. Both *Herschel* Space Observatory and *ALMA* data resulted in null detections,

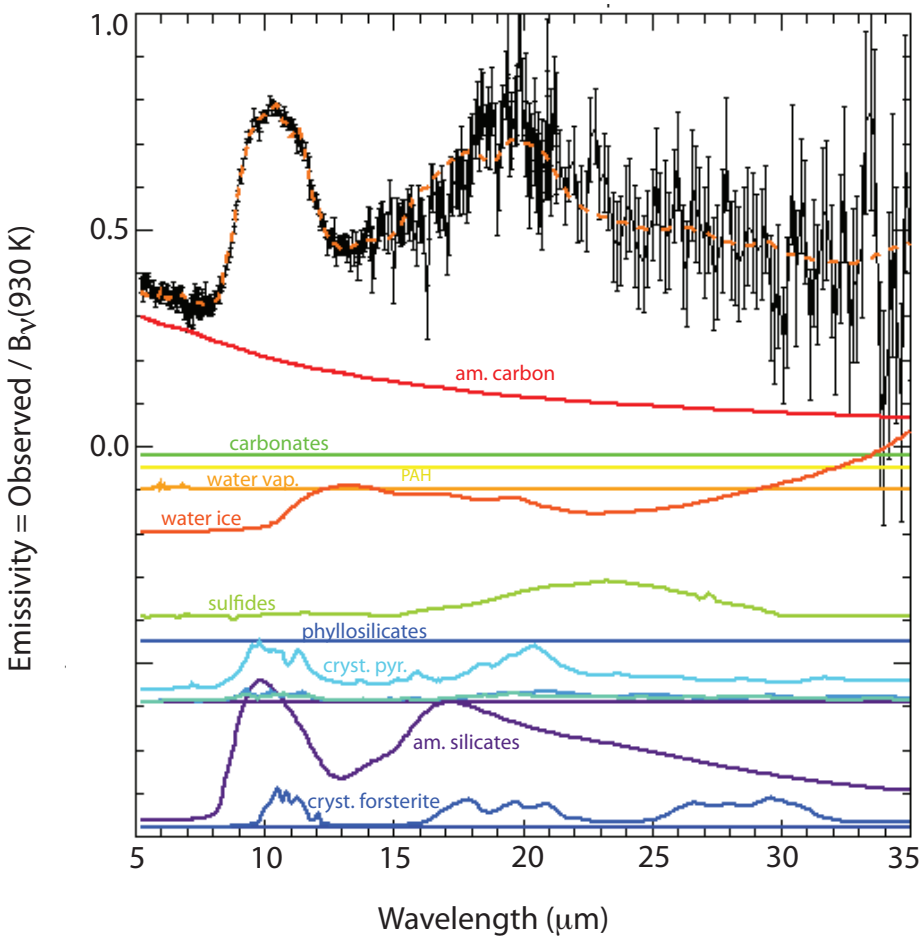

Fig. 1.9 Spitzer/IRS spectrum of the dust around G29-38. The observed spectrum was divided by a blackbody of temperature 930 K to give the black data points. The best fitting linear combination of 12 minerals is plotted as the red dashed line, to show the potential composition of the dust. The contribution of each mineral is shown by the coloured lines (Reach et al., 2009). The composition of this dusty material should match the composition of the material polluting the star. Water ice, amorphous silicates and forsterites all have distinguishable features in the mid-IR.

putting strong upper limits on the amount of cold dust in the systems. Further observations of dusty white dwarfs using the full capabilities of *ALMA* could be beneficial.

Contrary to this, there are detections of cold dust, however, they are discovered around hot white dwarfs $\sim$ 100,000 K. These hot systems are different to the cool metal rich white dwarfs. Su et al. (2007) discovered excess infrared emission from the central region of the Helix nebula. The central star is a hot white dwarf, WD 2226-210, with an effective temperature of $\sim$ 110,000 K. Spitzer detected excess emission at 8, 24 and 70 µm, which was hypothesised to be from a dust disc, with a blackbody temperature in the range 90–130 K. It is thought the dust originates from Kuiper belt-like objects, which have survived the violent evolution of the host star and collided to form a disc. This demonstrates it is possible for cold dust to survive and exist around white dwarf systems. Motivated by this work, Chu et al. (2011) used the Spitzer Multi-band Imaging Photometer to investigate a sample of 71 hot white dwarfs, or pre-white dwarfs to search for excess emission at 24 µm. Excess emission was discovered for a number of the sources so it can be hypothesised that dust at $\sim$ 100 K should be found around $\gtrsim$ 15 % of white dwarfs and pre-white dwarfs. However, these cool infrared excesses are widely debated as a number of these objects have been discovered to host companions.

Observations of gas discs:

21 of the white dwarfs with dust debris also show evidence of circumstellar gas in emission near the same radius as the dust (Gänsicke et al., 2006, 2007, 2008; Melis et al., 2010; Farihi et al., 2012a; Melis et al., 2012; Brinkworth et al., 2012; Debes et al., 2012b; Dennihy et al., 2020; Melis et al., 2020; Gentile Fusillo et al., 2020). These systems are identified by their double peaked emission features, usually strongest at the Ca II infrared triplet (8498 Å, 8542 Å, and 8662 Å). WD 1226+110 was the first of such detections, where Ca II emission lines in the optical and near infrared (NIR) were observed. The Ca II emission line profiles for WD 1226+110 are shown in Figure 1.10. The double peaked spectral lines are characteristic of Doppler broadening due to a Keplerian rotating gaseous disc. This has a rotational velocity law of $\Sigma_{\rm K} \alpha r^{-3/2}$ where the inner disc rotates faster than the outer disc. Gaia J0611−6931 has the most elements detected in emission, with observations of Ca, O, Si, Mg, Na and Fe (Dennihy et al., 2020; Melis et al., 2020). As there are a lack of hydrogen and helium spectral features in the gaseous discs, this implies the gas discs are metallic. The only gas disc found to consist of predominantly volatiles (H, O, S) is that around WD J091405.30+191412.25 as reported in Gänsicke et al. (2019), where the chemical composition matches that found deep in the atmospheric layers of icy giant planets.

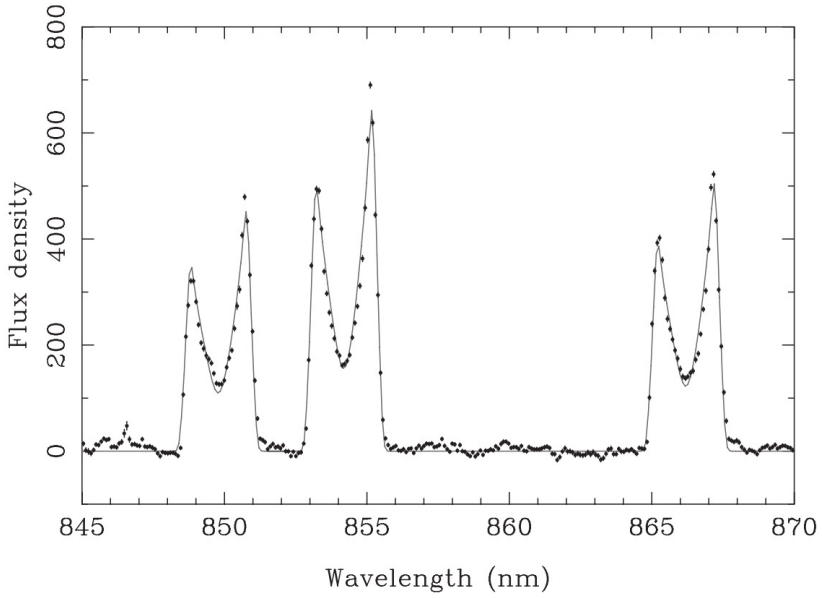

Fig. 1.10 The Ca II emission line profiles for WD 1226+110 from Gänsicke et al. (2006). The double peaked profiles are clear, arising due to Keplerian rotation. There are clear asymmetries in the red and blue Doppler shifted lines, indicating the disc is eccentric.

Disc Variability:

The scattering of planetary bodies that lead to pollution is expected to be a stochastic process, with the potential for variability on human time scales as seen in Figure 1.11 by the predicted order of magnitude changes in the accretion rate over timescales of less than a year (Wyatt et al., 2014). Such dust variability has previously been identified. The first infrared variability associated with the dust was for white dwarf WD J0959-0200. The fluxes in both Spitzer (Infrared Array Camera) channels, 3.6 µm and 4.5 µm, dropped by approximately 35 % within a year baseline. The NIR *K* band flux also dropped by 20 %, emphasising the dust is close to the star and dissipating on short time scales (Xu & Jura, 2014). Several scenarios could explain the large drop in flux for WD J0959-0200. One scenario involves planetesimals being scattered inward by a large outer planet and impacting a pre-existing disc. Scattering from a size distribution of small bodies can be approximated as continuous accretion, but infrequent scattering of larger bodies can affect the disc and accretion signatures, with the frequency of impact being be as often as once every 30 years or less (Jura, 2008; Wyatt et al., 2014). Mutual collisions between fragments can cause the inner disc to evaporate. If this hypothesis is supported, Xu & Jura (2014) suggested that WD J0959-0200 lost approximately 3 % of the disc mass within 300 days, implying that white dwarf accretion is intrinsically variable.

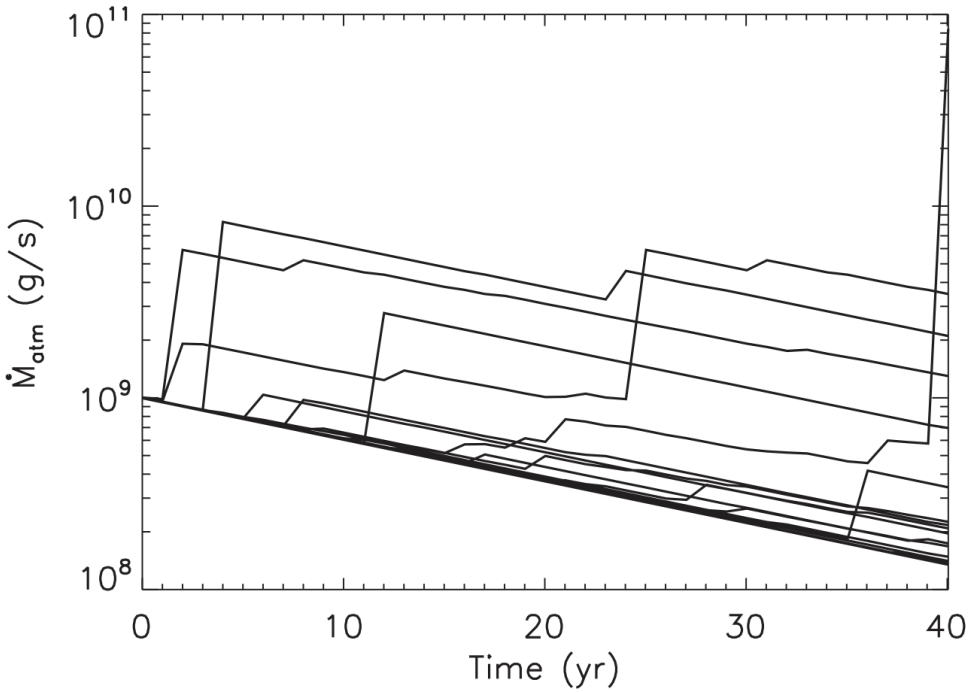

Fig. 1.11 Figure from Wyatt et al. (2014) showing model predictions for accretion rate over time for 20 stars modelled to be similar to G29-38. Changes in the accretion rate can be up to an order of magnitude over timescales of less than a year.

Investigations into whether the accretion rate of white dwarfs varies as a function of time have been conducted previously for one white dwarf, G29-38 (von Hippel & Thompson, 2007; Debes & López-Morales, 2008). Further observations of accretion rate over time will allow insight to be gained into whether this model is correct. Another scenario could explain the variability if the white dwarfs are observed with both circumstellar gas and dust. The dust and gas may interact and cause the inner disc to evaporate, resulting in non-steady state accretion. WD J0959-0200 has both gas and dust discs, emphasising this assumption is reasonable. However, variability has now been observed to be ubiquitous in the mid-infrared even for those systems without observable gas discs, with no preference for increases or decreases in dust flux as shown in Figure 1.12 (Swan et al., 2019a, 2020).

Variability in the circumstellar gas has also been observed for white dwarfs with circumstellar gaseous discs (Wilson et al., 2014, 2015; Manser et al., 2015, 2016b; Dennihy et al., 2018). Variability tends to be morphological variations in the line profile shape, or increases/decreases in the equivalent widths of the spectral features. The variability is mostly attributed to the precession of eccentric rings, collisions, or planetesimals orbiting within the debris discs (Manser et al., 2019).

Jura (2003) Flat and Opaque Disc Model:

In 2003 it was well known that metals polluted the atmospheres of some white dwarfs, however, the only known infrared excess was that of G29-38. Jura (2003) developed a model to explain both the atmospheric pollutants and the infrared excess for G29-38. Scattered planetesimals perturbed onto highly eccentric orbits can fall within the Roche radius of the white dwarf. This causes them to become tidally disrupted, and over time the system relaxes into a flat orbiting dust disc. It is assumed that the white dwarf illuminates the thin, flat, optically thick disc and the incident flux is re-radiated in the infrared. The thermal emission of the discs are of the order 10^3 K, demonstrating these discs lie close to their host star. The closest solar system analogue are the rings of Saturn; the physics of these rings can mostly be applied to white dwarfs (Brahic, 1977; Dones, 1991). The temperature of the white dwarf disc, $T_{\rm disc}$, as a function of distance from the star, R, which has a stellar radius of R_* and a temperature of T_*, is given by:

$$T_{\rm disc} \approx \left(\frac{2}{3\pi}\right)^{1/4} \left(\frac{R_*}{R}\right)^{3/4} T_*. \tag{1.5}$$

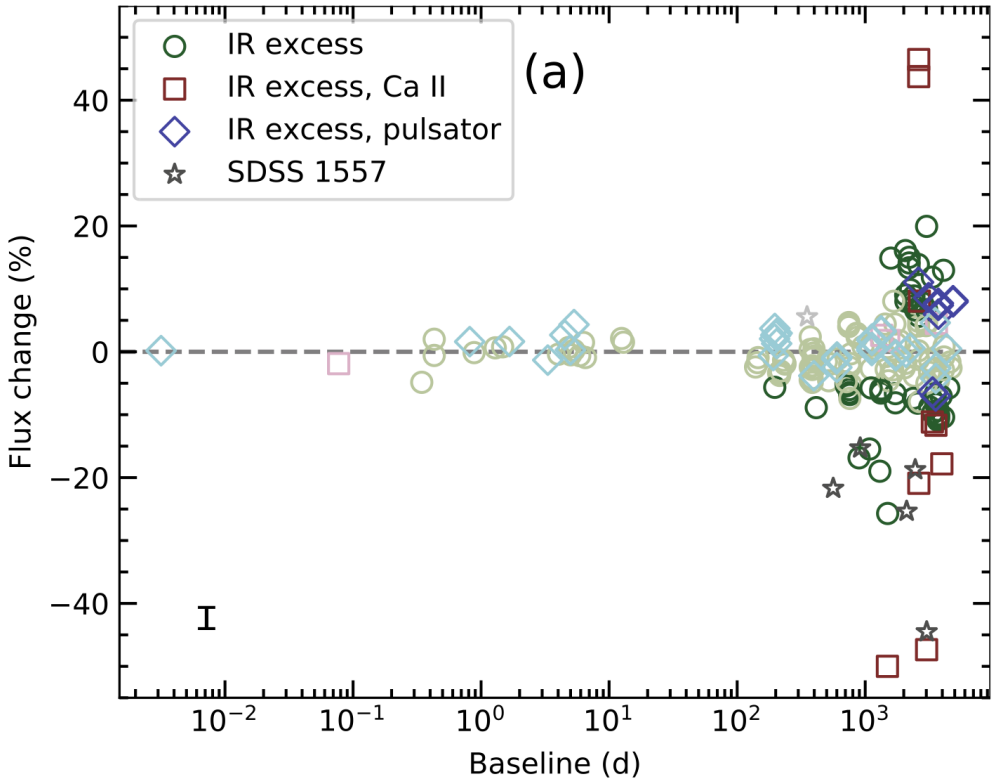

Fig. 1.12 Figure from Swan et al. (2020) showing the mid-infrared variability observed in a sample of $\sim$ 40 white dwarfs using the Spitzer space telescope. The largest flux changes seem to occur over longer baselines with the largest changes being those with circumstellar gaseous discs.

The flux from the disc, is predicted to be:

$$F_{\rm disc} = \frac{2\pi \cos i}{D_*^2} \int_{R_{\rm in}}^{R_{\rm out}} B_\nu \left(T_{\rm disc}\right) R \, dR, \tag{1.6}$$

where D_* is the distance to the white dwarf, i is the inclination angle of the disc, R_{in} and R_{out} are the inner and outer radii of the dust disc respectively and B_ν is the Planck function. In this model, the inner radius is defined by the sublimation radius of solids. The sublimation radius, $R_{\rm S}$, is given by:

$$R_{\rm S} = \frac{\sqrt{\varepsilon} R_*}{2} \left(\frac{T_*}{T_{\rm S}}\right)^2, \tag{1.7}$$

where ε is the ratio of the emissivity of the particle for the white dwarf radiation and for its own thermal radiation, and $\rm T_S$ is the sublimation temperature for the particles in the disc (Rafikov, 2011a). The dust ring is expected to form from the tidal disruption of an asteroid, therefore the outer radius is defined by the tidal radius of the white dwarf. This radius, $R_{\rm tide}$, is given by:

$$R_{\rm tide} = C_{\rm tide} \left(\frac{\rho_*}{\rho_a}\right)^{1/3} R_*, \tag{1.8}$$

where ρ_* is the density of the white dwarf, ρ_a is the density of the asteroid and $C_{\rm tide}$ is a constant, $\mathcal{O}(1)$, dependent on the composition, rotation and orbit of the asteroid (Davidsson, 1999).

The process of accretion from the disc onto the stellar atmosphere is complicated and refuted. After the asteroid is tidally disrupted, collisions result in the dissipation of energy, such that the dust settles onto a flat plane. Veras et al. (2015) established that the radiation from the white dwarf can circularise and compress the orbiting dust. The radiation from the white dwarf drives matter towards the sublimation radius via Poynting-Robertson (PR) drag (Robertson, 1937; Burns et al., 1979) shown in Figure 1.13. This delivers material to a reservoir of metallic gas close to the white dwarf. Viscous torques provide the means for metals to accrete onto the white dwarf surface (Rafikov, 2011a). Rafikov (2011b) demonstrated that PR drag is sufficient to achieve metal accretion rates of at least $10^8\,{\rm g\,s^{-1}}$. But this is not sufficient to explain the accretion rates of the highest accretors ($\sim 10^{11}\,{\rm g\,s^{-1}}$).

Paradigm Shift:

The model of the flat opaque disc as developed in Jura (2003) was revolutionary as it provided a framework to understand these enigmatic polluted white dwarf systems. However, there is increasing evidence for the requirement of an optically thin component, moving the field away from the flat opaque disc model. The 10 µm silicate emission features detected for

a number of white dwarfs with infrared excesses must result from an optically thin region (Jura et al., 2009a). In order to fit the strong 10 μm features and the shape of the infrared excesses, GD 362 (Jura et al., 2007a) and G29-38 (Reach et al., 2009) were fitted with models which invoked warped/flared discs. Large infrared variability is observed in a number of systems with both increases and decreases observed. In order to explain this collisional models are proposed where collisions cause infrared brightening as dust is produced, and then dimming occurs as the cascade grinds the material down such that it no longer emits at micron wavelengths (Farihi et al., 2018; Swan et al., 2020, 2021).

The tidal disruption model implies that observable dust discs should be more frequent than is detected. Bonsor et al. (2017) found that no more than 3.3% of white dwarfs can have a wide, flat, opaque dust disc and suggest four reasons to explain the lack of discs observed. These reasons are extracted from Figure 1.14 where the accretion rate is plotted against the white dwarf temperature. The green region (A) may represent white dwarfs which have already accreted their disc. This is possible if a white dwarf has a long sinking time scale such that pollutants exist in the atmosphere after the full dissipation of the disc. The blue region (B) may represent white dwarfs which are surrounded by undetectable optically thin dust. The brown region (C) may explain the lack of infrared excess for hot white dwarfs where the sublimation radius of solids lies outside of the tidal disruption radius. This means that gas is accreted onto the stellar photosphere without a disc forming (Steckloff et al., 2021). The red region (D) represents an area of phase space where there is enhanced accretion, although it is difficult to explain the lack of infrared detections here. Although further work is required to confirm these hypotheses, this work emphasises the need for a paradigm shift away from the optically thick, razor thin model.

As previously stated, 21 systems have been observed with both circumstellar dust and gas discs. These gas discs extend to a similar radii as the dust discs (e.g. Melis et al., 2012). This is surprising as gas is observed at radii larger than the sublimation radius for refractory elements. The vertical extent of the gas disc appears to be much greater than the flat, opaque dust disc. Different theories have been proposed to explain the production of the gas - sublimation of solids, and collisions. Metallic gas inwards of the sublimation radius feeds the stellar atmosphere via viscous torques. To conserve angular momentum a proportion of the gas produced at the sublimation radius viscously spreads outwards causing an overlap in the location of the dust and gas (Rafikov, 2011a; Metzger et al., 2012). This gas disc has a higher temperature than the dust disc enabling the gas disc to exist outside of the sublimation radius. This outwardly spreading gas causes drag on the dust particles and thus accelerates their accretion onto the white dwarf creating a runaway effect; this might explain the highest accretion rates observed in polluted white dwarfs (Rafikov, 2011a). To

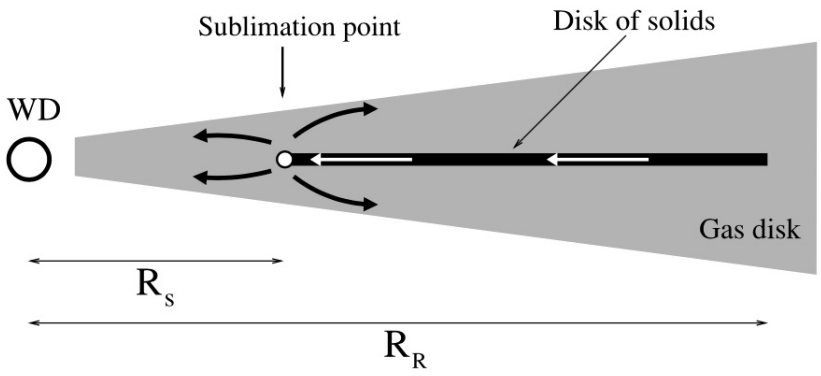

Fig. 1.13 A diagram from Rafikov (2011a) illustrating an interacting dust disc (black) and gaseous disc (grey). The radial extent of the dust disc is defined on the inner edge by the sublimation radius of solids and the outer edge by the tidal disruption radius of the white dwarf. The gas disc has the same radial extent as the dust, with a reservoir close to the white dwarf, feeding the atmosphere with metallic gas. The movement of high metallicity materials is demonstrated by the arrows.

investigate this, the accretion rates of white dwarfs with circumstellar gas needs to be studied in comparison to the population. A schematic of this theory is shown in Figure 1.13. An alternative explanation for the gas emission is collisional cascades of planetesimals within the Roche radius of the white dwarf, these collisions produce gaseous material (Kenyon & Bromley, 2017a,b). Observations of infrared variability in WD 0145+234 appear consistent with simple collisional cascade models (Swan et al., 2021). It is likely numerous routes of planetesimals arriving in the white dwarf atmosphere are active to explain the diversity in the architecture of the systems and accretion rates, a more thorough discussion appears in Brouwers et al. (2022).

Dust provides information regarding how planetary material arrives into the atmosphere of these polluted white dwarfs. No theoretical models can encompass all dust observations, including the shapes of the SEDs, the silicate emission features, and the dust variability. Dust variability studies are crucial as they can reveal information about the optical depth and geometry of the circumstellar dust. However, as of 2016 (when this thesis work begun), studies of dust variability only focused on individual systems rather than the population, so creating theoretical models that can explain the population was impossible. Therefore, it is crucial to determine how frequent variability is within the population and at what wavelengths this variability is dominant.

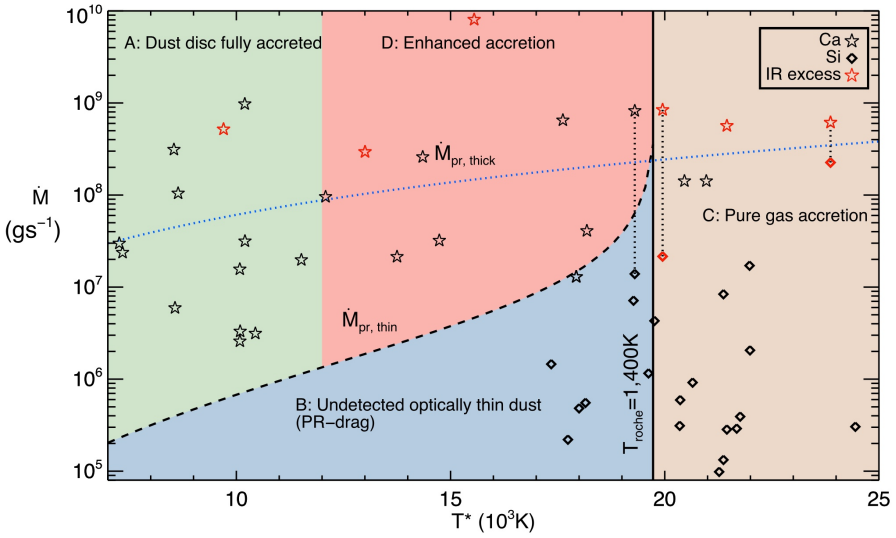

Fig. 1.14 This figure is taken from Bonsor et al. (2017). It demonstrates the accretion rate plotted against the temperature of the white dwarfs. The plot has been subdivided into four regions to explain the lack of observations of infrared excesses around polluted white dwarfs.

1.4.4 The Link with the Main Sequence

The asteroid destruction model relies on the survival of at least one large planet as well as planetesimals from the main sequence to the white dwarf phase. As nearly all stars are expected to end their lives as white dwarfs, looking at the planetary systems around main sequence stars can reveal what could survive. There are over 5,000 exoplanets confirmed to date, with a large range of radius, mass, semi-major axis and orbital period. Due to this diversity, it is likely that some exoplanets have the necessary location and properties to survive to the white dwarf phase.

The post main sequence evolution of a star is a violent process, however dynamicists have hypothesised that certain planets can survive. Mustill & Villaver (2012) argued that terrestrial planets need an initial semi-major axis of at least 2.8 AU and gas giants need an initial semi-major axis of 5 AU to avoid being engulfed by the expanding envelope of the giant star. During the asymptotic giant branch phase, the star loses a large fraction of its initial mass. This mass loss occurs over such long time scales that it is possible for objects to have stable expanding orbits (Debes & Sigurdsson, 2002). Therefore, if planets have a sufficiently large semi-major axis, they could survive to the white dwarf phase and perturb asteroids into highly eccentric orbits. The fate of this asteroid could be: a collision with another surviving body, to be ejected from the planetary system, to directly hit the white dwarf, or to fall within the tidal disruption radius of the white dwarf (Villaver & Livio, 2007;

Veras et al., 2011, 2013; McDonald & Veras, 2021). A fraction of main sequence planets have been observed with these large semi-major axis, so the idea that they could survive to the white dwarf phase is reasonable.

Bonsor & Wyatt (2010) found that debris belts with sufficiently massive planetesimals that lie beyond a few AU can survive to the white dwarf phase. However, the masses of the discs are reduced significantly; this is mainly due to the loss of small planetesimals. The small planetesimals are subsequently replenished via collisions once the system has settled into the white dwarf phase. It has been shown that 25–50% of white dwarfs are polluted (e.g. Zuckerman et al., 2003). Therefore, the study of these objects could provide information about main sequence exo-planetary systems, if we assume that this observed pollution is due to scattered planetesimals. This implies that at least 25–50% of low mass main sequence systems must have a massive planetesimal belt with enough debris to survive to the white dwarf phase and pollute the atmosphere of the white dwarf. Cold outer belts around main sequence stars have detection rates of 30% around A stars and about 20% for FGK stars (Marino, 2022). This is broadly consistent with the fraction of white dwarfs found to be polluted.

Sub-stellar bodies have been discovered around white dwarfs. Numerous brown dwarf companions to white dwarfs have been discovered (Longstaff et al., 2019; van Roestel et al., 2021), but a limited number of planets have been found. Most notably, the giant transiting planet candidate, WD 1856+534b (Vanderburg et al., 2020). Although it is expected that planets around white dwarfs should be commonplace in order for 25–50% of white dwarfs to be polluted, few other planet candidates have been observed (Xu et al., 2015a; Belardi et al., 2016). This is unsurprising as the probability of observing a transiting planet is low due to small radii of white dwarfs and surviving planets are predicted to be far from the star (Debes & Sigurdsson, 2002). *Gaia* will enable planets to be discovered around white dwarfs astrometrically. *Gaia* eDR3 resulted in a candidate super-Jupiter around WD 0141−675, if confirmed this would be the first polluted white dwarf with an exoplanet detected (Collaboration et al., 2022). With the release of *Gaia* DR5 it is expected that *Gaia* will astrometrically discover 6±1 planets between 1.6–3.91 au with masses between 0.03 – 13 M_J (Sanderson et al., 2022) allowing investigations into the evolution of planetary systems from the main sequence to white dwarf phase.

1.5 This Thesis in Context

Polluted white dwarfs are unique laboratories that can be used to directly sample the bulk composition of exoplanets; this is not possible via any other method. We are transitioning

into the era of big data. For white dwarfs, *Gaia* has aided the discovery of $>350{,}000$ white dwarfs (Gentile Fusillo et al., 2021), and with large spectroscopic surveys upcoming such as 4MOST, DESI, WEAVE, and SDSS-V, thousands of new polluted white dwarfs will be discovered. Each white dwarf tells its own unique story about the exoplanetary material surrounding it, therefore, it will be crucial to follow up with high resolution instruments across large wavelength ranges to ensure a thorough characterisation and understanding of this exoplanetary material. These individual studies have led to ground-breaking discoveries regarding the composition and geology of planetary material around other stars, such as the discovery of water-rich exoplanetary bodies (e.g. Farihi et al., 2011), which in turn has prompted further investigations into the possibility of life in exoplanetary systems.

For exoplanets, over the next decades a myriad of rocky planets will be discovered and characterised with current missions such as *TESS*, *CHEOPS*, and *JWST*; and future missions, such as: *PLATO*, *LUVOIR*, and *LIFE*. With this wealth of new data, collaboration will be crucial, information about exoplanetary material from polluted white dwarf systems can help to answer big questions about the solar system, exoplanetary systems, and galactic populations, and similarly these subjects can help inform inferences from white dwarf planetary systems. In order to fully understand and characterise exoplanetary rocky worlds, as well as determine whether they could be habitable, it is crucial to understand what they are made of. Current models of the interiors of exoplanets suffer from degeneracies; however, the population of the bulk composition of exoplanetary material, as inferred from polluted white dwarfs, can be used as inputs into planetary interior modelling to help to break these degeneracies. With the wealth of data coming it is crucial for sub-fields to collaborate such that a new era of Earth 2.0 discovery can begin. Our place in the solar system and galaxy appears to be key to life developing on Earth, but it is unknown whether the solar system is common, or how planet formation is affected by our place in the galaxy. Polluted white dwarfs can reveal the population of exoplanetary material which can be used to answer these questions. Combining the inferred exoplanetary composition with *Gaia* astrometric information reveals whether different galactic populations have different planet compositions and the affects this has on the resultant planetary systems.

This thesis focuses on white dwarf planetary systems, with an emphasis on using observations to inform models of the disruption and accretion processes, and using large ground based spectrographs to make inferences about exoplanetary composition of individual systems. Chapter 2 reports large ground-based near-infrared photometric monitoring campaigns of the circumstellar dust around ~ 40 white dwarfs. There is increasing evidence for a paradigm shift away from the model where a planetesimal tidally disrupts and forms an opaque flat disc (Jura, 2003). Dust variability sheds light on the dynamics of the planetary

bodies, the distribution of the dust, and the optical depth and properties of the dust. Chapter 3 reports an optical spectroscopic monitoring campaign of 5 DAZ white dwarfs over decade long timescales. Stochastic models of the accretion of planetesimals predicts variability in the accretion rate, and therefore the amount of material in the atmosphere. Warm DAZ white dwarfs have accretion rates on the order of days, therefore enabling the search for variability in the accretion rate using spectroscopic monitoring. Constraining accretion rates provides valuable information to inform models of accretion and disc lifetimes. Chapter 4 reports the abundances for the material accreting onto seven white dwarf stars and the composition and geological history of these exoplanetary bodies. These findings can be used to aid interior structure models of exoplanets, investigate whether the composition of solar system bodies are unique, and study volatiles and their delivery in exoplanetary systems. Finally, Chapter 5 presents the conclusions from this thesis and provides suggestions for future work to contribute to questions raised.

Chapter 2

Dust Variability

The favoured theory regarding the source of white dwarf pollution is that it originates from planetesimals scattered onto eccentric orbits towards the white dwarf where they tidally disrupt, producing dusty debris detectable as excess infrared emission, and subsequently accrete onto the atmosphere of the white dwarf. This inwards scattering of planetary bodies that leads to pollution is expected to be a stochastic process (Wyatt et al., 2014), with variability predicted on human time-scales. Variations could come in the form of gaseous emission, dusty emission, or total flux caused by transiting debris. Studying the circumstellar dust via time series photometry of the infrared emission can reveal how this planetary material arrives in their atmospheres.

The first white dwarf discovered to show dust emission variability was WD J0959−0200. The 3–5 μm flux dropped by 35% between observations separated by a year and appeared to be stable afterwards, and the near-infrared K band flux dropped by 18.5% between observations separated by 8 years (Xu & Jura, 2014). The large K band excess for this white dwarf implies that the dust is hot and close-in. These findings imply that the variability event was large and became stable quickly. Motivated by the large variability in WD J0959−0200, ground based near-infrared monitoring campaigns were conducted to search for variability in the dust for white dwarfs with infrared excesses. This chapter focuses on these monitoring campaigns and characterising how white dwarfs vary in the near-infrared in order to better understand how dusty material arrives in the atmospheres of the white dwarfs. Section 2.1 presents a near-infrared monitoring campaign of 34 white dwarfs with circumstellar dust emission using the UKIRT/WFCAM to search for variability on timescales of months – years. Section 2.2 presents a near-infrared monitoring campaign of 8 white dwarfs with dust emission using the NTT/SOFI to search for variability over timescales of hours – days.

2.1 The UKIRT/WFCAM near-infrared monitoring

A near-infrared monitoring campaign of 34 white dwarfs with infrared excesses was conducted with the aim to search for variability in the dust emission. Time series photometry of these white dwarfs from the United Kingdom Infrared Telescope (Wide Field Camera) in the *J*, *H* and *K* bands were obtained over baselines of up to three years. No statistically significant variation is found in the dust emission in all three near-infrared bands. Specifically, variability at $\sim 1.3\%$ can be ruled out for the 13 white dwarfs brighter than 16th mag in *K* band, and at $\sim 10\%$ for the 32 white dwarfs brighter than 18th mag over time-scales of three years. Although to date two white dwarfs, SDSS J095904.69−020047.6 (Xu & Jura, 2014) and WD 1226+110 (Xu et al., 2018b), have shown *K* band variability, in the sample no evidence of new *K* band variability at these levels is seen. One interpretation is that the tidal disruption events which lead to large variabilities are rare, occur on short time-scales, and after a few years the white dwarfs return to being stable in the near-infrared.

2.1.1 UKIRT Observations

An infrared monitoring campaign was completed using the Wide Field Camera (WFCAM) on the UKIRT on Maunakea, Hawaii (PI: Xu). WFCAM operates in the near-infrared between 0.83 and 2.37 µm ; this includes the *J*, *H* and *K* filters (Hewett et al., 2006). WFCAM has four detectors composed of 2048 by 2048 18 micron pixels, with a pixel scale of $0.4''$.

The sample consists of 34 white dwarfs with infrared excesses. Table 2.1 shows the sample, giving the white dwarf parameters and the nature of the infrared excess. In the sample, 30 white dwarfs have dust emission confirmed with *Spitzer* observations, the 4 remaining objects are identified by *WISE* and are labelled as dust candidates. *JHK* broadband photometry was obtained for the 34 targets with the UKIRT. 48 hours of UKIRT WFCAM time between semesters 2014B and 2017A were used to study long-term variability in the near-infrared. The dates of the observations for the 34 white dwarfs are shown in Table 6.1.

Each white dwarf was observed up to 6 times across the 3 year campaign. The UKIRT observations probed short time-scales (minutes) between individual frames taken on a given night, and long time-scales (years) between observation dates. Further discussions about time-scales are given in Section 2.1.3. The observations were designed such that a signal-to-noise ratio (SNR) of 30 was obtained for the *J* and *H* bands, and 40 for the *K* band. To achieve the required SNR, the brightest white dwarfs in the sample required 25 s of exposure time for the *J* and *H* band, and 75 s for the *K* band. For the faintest white dwarfs, this required 150 s for the *J* band, 450 s for the *H* band, and 1250 s for the *K* band. As the infrared sky is bright, each frame consisted of a dithered stack of five 5 s or 10 s exposures. Table 6.2

Table 2.1 The UKIRT sample of dusty polluted white dwarfs and their properties. H/He column highlights the dominant element in the atmosphere.

WD Name	Other Name	H/He	T_{eff} ⋆	log(g)⋆	Nature of Excess †
WD 0010+280	PG 0010+281	H	23700	7.73[1]	Dust[α]
WD 0106−328	HE 0106−3253	H	16200	8.03[1]	Dust[β]
WD 0146+187	GD 16	He	11500	8.00[2]	Dust[γ]
WD 0300−013	GD 40	He	13600	8.02[3]	Dust[δ]
WD 0307+077	HS 0307+0746	H	10100	7.99[1]	Dust[β]
WD 0408−041	GD 56	H	14200	7.96[1]	Dust[δ]
WD 0435+410	GD 61	He	15700	8.04[3]	Dust[ε]
WD J0738+1835*	SDSS J073842.57+183509.6	He	14000	8.40[4]	Dust[ζ]
WD J0959−0200*	SDSS J095904.69−020047.6	H	13300	8.06[5]	Dust[η]
WD 1015+161	PG 1015+161	H	19200	8.03[1]	Dust[δ]
WD 1018+410	PG 1018+411	H	21700	8.05[1]	Dust[θ]
WD 1041+092	Gaia DR2 3869060540584643328	H	17600	8.12[1]	Dust[ζ]
WD 1116+026	GD 133	H	12600	8.04[6]	Dust[δ]
WD 1145+017	HE 1145+0145	He	15900	8.00[7]	Dust[ι]
WD 1145+288	Gaia DR2 4019789359821201536	H	12400	7.96[1]	Cand[κ]
WD 1150−153	EC 11507−1519	H	11400	7.98[1]	Dust[λ]
WD J1221+1245*	SDSS J122150.81+124513.3	H	12300	8.20[5]	Dust[η]
WD 1225−079	PG 1225−079	He	10800	8.00[8]	Dust[β]
WD 1226+110	Gaia DR2 3904415787947492096	H	20900	8.11[1]	Dust[μ]
WD 1232+563	Gaia DR2 1571584539980588544	He	11800	8.30[3]	Cand[κ]
WD 1349−230	HE 1349−2305	He	18200	8.13[9]	Dust[ν]
WD 1456+298	G166-58	H	7390	8.00[1]	Dust[ξ]
WD 1504+329	Gaia DR2 1288812212565231232	H	7180	8.06[10]	Cand[κ]
WD 1536+520	Gaia DR2 1595298501827000960	H	16700	7.70[6]	Cand[κ]
WD 1551+175	Gaia DR2 1196531988354226560	He	15600	7.96[11]	Dust[π]
WD 1554+094	KUV 15519+1730	H	21800	7.63[12]	BD+Dust[ρ]
WD J1617+1620*	SDSS J161717.04+162022.4	H	13200	8.04[1]	Dust[ζ]
WD 1729+371	GD 362	H	10300	8.13[6]	Dust[ξ]
WD 1929+011	Gaia DR2 4287654959563143168	H	25400	8.17[1]	Dust[θ]
WD 2132+096	HS 2132+0941	H	13100	7.96[13]	Dust[π]
WD 2207+121	Gaia DR2 2727904257071365760	He	14800	7.97[3]	Dust[σ]
WD 2221−165	HE 2221−1630	H	9900	8.12[1]	Dust[β]
WD 2326+049	G29-38	H	11200	8.00[1]	Dust[τ]
WD 2328+107	PG 2328+108	H	17900	7.74[1]	Dust[θ]

Notes:

⋆ **Temperature and log(g):** Temperature and log(g) come from photometric fits, where possible, otherwise a new fit considering the *Gaia* distances was performed (see Section 2.1.3). (1) This work, (2) Koester et al. (2005), (3) Coutu et al. (2019), (4) Dufour et al. (2012), (5) Farihi et al. (2012a), (6) Dufour et al. (2017), (7) Vanderburg et al. (2015), (8) Klein et al. (2011), (9) Voss et al. (2007), (10) Barber et al. (2014), (11) Bergeron et al. (2011), (12) Farihi et al. (2017), (13) Gentile Fusillo et al. (2018).

† **Nature of infrared excess references:** 'dust' refers to white dwarfs with confirmed dust detection with *Spitzer* observations and the reference is that of the *Spitzer* observations, otherwise it is labelled 'cand' (candidate), and the reference is the paper that first refers to dust emission. WD 1554+094 has a brown dwarf companion and dust. (α) Xu et al. (2015b), (β) Farihi et al. (2010b), (γ) Farihi et al. (2009), (δ) Jura et al. (2007b), (ε) Farihi et al. (2011), (ζ) Brinkworth et al. (2012), (η) Farihi et al. (2012a), (θ) Rocchetto et al. (2015), (ι) Xu et al. (2018a), (κ) Debes et al. (2011), (λ) Jura et al. (2009a), (μ) Brinkworth et al. (2009), (ν) Girven et al. (2012), (ξ) Farihi et al. (2008), (π) Bergfors et al. (2014), (ρ) Farihi et al. (2017), (σ) Xu & Jura (2012), (τ) Reach et al. (2005).

(Appendix 1: Chapter 6) shows the exposure time for each of the five individual exposures making up the dithered stack. All data obtained with WFCAM were pipeline-processed by the Cambridge Astronomical Survey Unit using standard infrared photometry data reduction steps (CASU, Irwin et al., 2004; Dye et al., 2006).

Further processing using the LIGHTCURVES software[1] was executed to improve the precision of the photometry (Irwin et al., 2007). List driven photometry was performed using a master frame to force the centroid positions for the objects. Here, the master frame is the stacked image of all frames; this increases the SNR of the master frame and reduces errors associated with inaccurately placed centroids. Each frame used in the construction of the lightcurves was re-aligned to the same set of astrometric calibrators (from 2MASS) as the master frame, which gives significantly improved precision in aperture location when compared to centroiding for faint sources (see Irwin et al., 2007). For a particular object, all frames had an aperture between 3–5 pixels (1.2–2″), depending on which aperture gave the lowest root mean square (RMS) value. Using a large number of non-variable stars, the zero-point shift for each frame was calculated to reduce atmospheric effects, and a 2D polynomial was fitted to the magnitude residuals to minimise the error associated with the position on the detector. LIGHTCURVES outputs a robustly calibrated lightcurve for each filter and for each object in the catalogue list. For variability searches this is essential as it allows us to probe changes down to the percent level.

2.1.2 Variability Analysis

Analysis Method

This work aimed to obtain high precision *JHK* photometry of a sample of dusty white dwarfs and to search for and constrain the level of variability in the photometry over the length of the survey. Throughout the analysis the Vega magnitude system was adopted. In order to robustly study the statistics of the photometry, the same analysis method was applied to all white dwarf observations regardless of the magnitude of the white dwarf and the number of measurements in the *J*, *H* and *K* bands. Gaussians were fitted to the distribution of photometrically corrected magnitudes from the LIGHTCURVES software using all dithered stacked frames, as demonstrated in Fig. 2.1. The total number of dithered stacked frames for each filter is shown in Table 6.2 (Appendix 1: Chapter 6), this ranges from 3 to 125, with the median number of frames for the *J*, *H* and *K* bands being 9, 12 and 20 respectively. A Markov Chain Monte Carlo (MCMC) approach was implemented to model the magnitude distribution of each star with a Gaussian profile, yielding posterior distributions for the

[1] https://github.com/mdwarfgeek/lightcurves

mean and standard deviation thereof. In the analysis, the median values from the posteriors are adopted. Uniform priors were used for the magnitude between 0 and 20, and standard deviation between 0 and 2. Larger upper values for the assumed prior range are used to test the sensitivity on the parameters. The results remained consistent independent of the size of the prior. A python package, PYMC[2] (Patil et al., 2010), was used for MCMC parameter estimation. Five walkers were used, each resulting in 100,000 posterior samples, with the first 40% of the chain being discarded in the burn-in phase. The Gelman-Rubin statistic (Gelman et al., 1992) was implemented to check for chain convergence. For the two parameters (magnitude and standard deviation), all white dwarfs had values $1.000 < \mathrm{GR} < 1.037$ for the J band, $0.999 < \mathrm{GR} < 1.002$ for the H band, and $1.000 < \mathrm{GR} < 1.005$ for the K band, demonstrating good convergence. The median value of the posterior distribution of the standard deviation was used for the variability measurement. The errors are quoted using the 16th and 84th percentiles of the posterior distribution. This median variability measurement is a robust and reliable way of measuring variability.

To ensure that any variability detected was real, stellar objects in the field of view were analysed using the same approach for comparison. For all field stars the median value of the standard deviation of the Gaussian as a function of magnitude was used to represent the sensitivity of the survey as a function of magnitude. Using the median ensures no variable field stars are contaminating the function. The white dwarfs were then compared to the median MCMC standard deviation of the non-variable field stars at the same magnitude as the white dwarf. If the standard deviation of the white dwarf was significantly higher than that of the field stars, then they were identified as variable. The field objects selected for the comparison were those classified by LIGHTCURVES as stellar and those observed in the same detector as the white dwarf. The number of field stars used in the comparison for each white dwarf ranged from 110 for white dwarfs in sparse fields of view up to 6700 for white dwarfs in densely populated regions. The median number of field stellar objects used in the comparison for each white dwarf was 210.

Variability Results

Table 2.2 shows the results of the MCMC runs, and lists the median magnitude and median standard deviation on this magnitude for all white dwarfs in the survey. Fig. 2.2 plots these median magnitudes and standard deviations for the white dwarfs and field stars in the J, H and K bands. Most white dwarfs have standard deviations which are consistent with that of the field stellar objects. This implies that most of the white dwarfs have J, H and K fluxes

[2]https://www.pymc.io

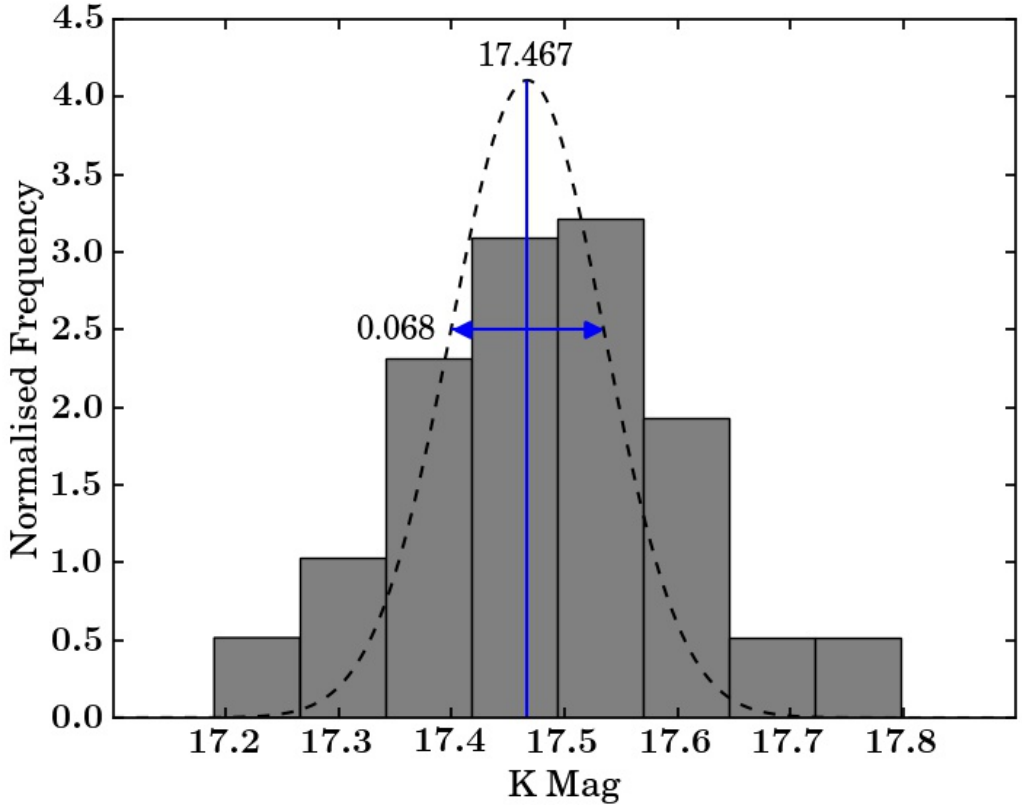

Fig. 2.1 A normalised histogram showing the distribution of photometrically corrected magnitudes from the LIGHTCURVES software using all dithered stacked frames for WD 1145+017. Each dithered stacked frame contains 5×10 second exposures. This white dwarf has 102 measurements in the K band over 782 days. The Gaussian curve shows the median best-fitting Gaussian, with a median magnitude of 17.467, and a median standard deviation of 0.068 mags.

which are no more variable than the field stars, which are taken to be a proxy of the sensitivity of the survey as a function of magnitude.

A typical SED for a white dwarf that is representative of the sample peaks in the optical, whereas the dust emission peaks in the infrared. Of the near-infrared bands, the *K* band is more sensitive to the dust emission. Consistent fluxes in the *K* band imply there was little change in the *K* band dust emission for the white dwarfs. A few objects stand out from the plots, these objects are discussed further in the following section. Objects from the literature that previously showed variability are also discussed.

Discussion of Individual Sources

WD 1145+017:

Vanderburg et al. (2015) discovered that WD 1145+017 is transited by multiple disintegrating planetesimals. The transit periods were approximately 4.5 hours and lasted various lengths from minutes to hours, with varying transit depths; the deepest blocks 60% of the flux from the star in the optical. The transits were not always present, and the transit activity level was variable (Gary et al., 2017).

The pink inverted triangle in Figs. 2.2a, 2.2b, and 2.2c show WD 1145+017 was variable at 4.1 σ in the *J* band, 2.1 σ in the *H* band, and was not significantly variable in the *K* band. From the UKIRT lightcurves of this white dwarf, shown in Fig. 2.3, it appears that the *J* band and possibly *H* band magnitudes were fainter on 09/05/2017. The *J*, *H* and *K* band observations were taken consecutively, the length of the observations were 3.5, 7.5 and 17 minutes respectively. Therefore, as the median dip duration is 9 minutes (Gary et al., 2017), it is possible that the transit occurred during the *J* band observations, with an overlap into the *H* band observations. Alternatively, as the variability was strongest in the *J* band and weakest in the *K* band it is consistent with the transit depth measurements found in Xu et al. (2018a), and could also explain the differences in the observed variability. Near contemporaneous optical observations indeed show transits in the lightcurve (B. Gary, private communications[3] Rappaport et al., 2017). The decrease in the *J* and *H* band flux is very likely to be caused by transits, rather than dust variability.

[3] http://www.brucegary.net/zombie6/

Table 2.2 The resulting median magnitude and standard deviation found from the Gaussian fits to the photometry from the UKIRT observations in the *J*, *H* and *K* bands. The errors are quoted as the 16th and 84th percentiles from the posterior distributions.

WD Name	J Mag	J Std	H Mag	H Std	K Mag	K Std
WD 0010+280	$16.304^{+0.014}_{-0.014}$	$0.016^{+0.019}_{-0.011}$	$16.375^{+0.011}_{-0.011}$	$0.014^{+0.016}_{-0.010}$	$16.345^{+0.019}_{-0.018}$	$0.043^{+0.023}_{-0.019}$
WD 0106−328	$15.616^{+0.009}_{-0.009}$	$0.008^{+0.011}_{-0.006}$	$15.831^{+0.020}_{-0.020}$	$0.041^{+0.026}_{-0.017}$	$15.836^{+0.035}_{-0.034}$	$0.038^{+0.049}_{-0.027}$
WD 0146+187	$15.679^{+0.007}_{-0.007}$	$0.006^{+0.008}_{-0.004}$	$15.650^{+0.010}_{-0.010}$	$0.013^{+0.014}_{-0.009}$	$15.472^{+0.029}_{-0.029}$	$0.060^{+0.039}_{-0.025}$
WD 0300−013	$15.888^{+0.006}_{-0.006}$	$0.006^{+0.007}_{-0.004}$	$15.873^{+0.013}_{-0.013}$	$0.017^{+0.017}_{-0.012}$	$15.861^{+0.014}_{-0.014}$	$0.022^{+0.020}_{-0.015}$
WD 0307+077	$16.274^{+0.013}_{-0.013}$	$0.012^{+0.016}_{-0.008}$	$16.159^{+0.012}_{-0.011}$	$0.016^{+0.017}_{-0.011}$	$16.217^{+0.018}_{-0.018}$	$0.046^{+0.020}_{-0.015}$
WD 0408−041	$16.005^{+0.006}_{-0.006}$	$0.007^{+0.008}_{-0.005}$	$15.909^{+0.012}_{-0.012}$	$0.010^{+0.012}_{-0.007}$	$14.968^{+0.011}_{-0.011}$	$0.012^{+0.014}_{-0.008}$
WD 0435+410	$15.305^{+0.017}_{-0.018}$	$0.022^{+0.055}_{-0.015}$	$15.318^{+0.043}_{-0.037}$	$0.055^{+0.138}_{-0.035}$	$15.271^{+0.011}_{-0.011}$	$0.010^{+0.012}_{-0.007}$
WD J0738+1835	$18.080^{+0.015}_{-0.016}$	$0.026^{+0.022}_{-0.017}$	$17.857^{+0.012}_{-0.012}$	$0.028^{+0.019}_{-0.018}$	$17.329^{+0.011}_{-0.011}$	$0.065^{+0.012}_{-0.012}$
WD J0959−0200	$18.388^{+0.027}_{-0.025}$	$0.044^{+0.037}_{-0.029}$	$18.221^{+0.022}_{-0.021}$	$0.090^{+0.024}_{-0.021}$	$17.809^{+0.015}_{-0.015}$	$0.085^{+0.019}_{-0.019}$
WD 1015+161	$16.044^{+0.013}_{-0.012}$	$0.016^{+0.020}_{-0.011}$	$16.114^{+0.016}_{-0.015}$	$0.019^{+0.023}_{-0.013}$	$16.016^{+0.018}_{-0.018}$	$0.018^{+0.022}_{-0.012}$
WD 1018+410	$16.954^{+0.024}_{-0.022}$	$0.029^{+0.039}_{-0.021}$	$16.964^{+0.025}_{-0.024}$	$0.045^{+0.037}_{-0.024}$	$16.835^{+0.019}_{-0.019}$	$0.026^{+0.026}_{-0.018}$
WD 1041+092	$17.701^{+0.014}_{-0.014}$	$0.014^{+0.016}_{-0.010}$	$17.690^{+0.015}_{-0.015}$	$0.020^{+0.021}_{-0.014}$	$17.761^{+0.018}_{-0.018}$	$0.037^{+0.028}_{-0.024}$
WD 1116+026	$14.852^{+0.008}_{-0.008}$	$0.008^{+0.013}_{-0.006}$	$14.825^{+0.013}_{-0.013}$	$0.013^{+0.023}_{-0.009}$	$14.795^{+0.006}_{-0.007}$	$0.005^{+0.006}_{-0.004}$
WD 1145+017	$17.671^{+0.031}_{-0.031}$	$0.118^{+0.030}_{-0.024}$	$17.680^{+0.015}_{-0.015}$	$0.075^{+0.016}_{-0.014}$	$17.467^{+0.012}_{-0.012}$	$0.068^{+0.015}_{-0.015}$
WD 1145+288	$17.671^{+0.016}_{-0.016}$	$0.015^{+0.017}_{-0.011}$	$17.664^{+0.015}_{-0.015}$	$0.040^{+0.020}_{-0.022}$	$17.281^{+0.012}_{-0.012}$	$0.056^{+0.016}_{-0.017}$
WD 1150−153	$16.236^{+0.007}_{-0.007}$	$0.008^{+0.009}_{-0.006}$	$16.189^{+0.010}_{-0.010}$	$0.011^{+0.012}_{-0.008}$	$15.847^{+0.011}_{-0.011}$	$0.014^{+0.014}_{-0.010}$
WD J1221+1245	$18.413^{+0.029}_{-0.029}$	$0.039^{+0.037}_{-0.027}$	$18.264^{+0.026}_{-0.024}$	$0.103^{+0.029}_{-0.027}$	$17.841^{+0.013}_{-0.013}$	$0.039^{+0.026}_{-0.025}$
WD 1225−079	$14.963^{+0.009}_{-0.008}$	$0.010^{+0.014}_{-0.007}$	$14.960^{+0.015}_{-0.015}$	$0.013^{+0.023}_{-0.010}$	$14.957^{+0.007}_{-0.007}$	$0.012^{+0.010}_{-0.008}$
WD 1226+110	$16.965^{+0.012}_{-0.012}$	$0.011^{+0.013}_{-0.008}$	$16.944^{+0.011}_{-0.011}$	$0.012^{+0.013}_{-0.008}$	$16.623^{+0.015}_{-0.015}$	$0.029^{+0.022}_{-0.019}$
WD J1234+5606	$18.279^{+0.023}_{-0.023}$	$0.035^{+0.032}_{-0.023}$	$18.240^{+0.023}_{-0.022}$	$0.056^{+0.032}_{-0.033}$	$17.797^{+0.021}_{-0.020}$	$0.122^{+0.022}_{-0.020}$
WD 1349−230	$17.018^{+0.011}_{-0.011}$	$0.016^{+0.015}_{-0.011}$	$17.056^{+0.013}_{-0.013}$	$0.022^{+0.019}_{-0.015}$	$16.982^{+0.018}_{-0.017}$	$0.031^{+0.027}_{-0.021}$
WD 1456+298	$14.995^{+0.013}_{-0.012}$	$0.020^{+0.025}_{-0.012}$	$15.062^{+0.012}_{-0.012}$	$0.012^{+0.021}_{-0.009}$	$14.830^{+0.009}_{-0.009}$	$0.014^{+0.013}_{-0.010}$
WD 1504+329	$18.234^{+0.038}_{-0.036}$	$0.061^{+0.055}_{-0.041}$	$18.056^{+0.018}_{-0.017}$	$0.052^{+0.026}_{-0.028}$	$18.029^{+0.022}_{-0.021}$	$0.142^{+0.023}_{-0.022}$
WD 1536+520	$17.749^{+0.011}_{-0.011}$	$0.011^{+0.012}_{-0.008}$	$17.546^{+0.011}_{-0.011}$	$0.019^{+0.016}_{-0.013}$	$16.830^{+0.009}_{-0.008}$	$0.042^{+0.010}_{-0.010}$
WD 1551+175	$17.642^{+0.015}_{-0.015}$	$0.028^{+0.021}_{-0.017}$	$17.736^{+0.014}_{-0.013}$	$0.031^{+0.019}_{-0.019}$	$17.708^{+0.018}_{-0.017}$	$0.086^{+0.021}_{-0.021}$
WD 1554+094	$19.019^{+0.033}_{-0.033}$	$0.039^{+0.042}_{-0.027}$	$18.973^{+0.045}_{-0.042}$	$0.193^{+0.047}_{-0.042}$	$18.662^{+0.035}_{-0.034}$	$0.194^{+0.037}_{-0.036}$
WD J1617+1620	$17.337^{+0.011}_{-0.011}$	$0.018^{+0.016}_{-0.012}$	$17.202^{+0.013}_{-0.013}$	$0.049^{+0.015}_{-0.013}$	$16.865^{+0.012}_{-0.012}$	$0.026^{+0.020}_{-0.017}$
WD 1729+371	$16.130^{+0.005}_{-0.005}$	$0.008^{+0.007}_{-0.005}$	$16.068^{+0.007}_{-0.007}$	$0.012^{+0.011}_{-0.008}$	$15.853^{+0.006}_{-0.006}$	$0.008^{+0.008}_{-0.005}$
WD 1929+011	$14.820^{+0.006}_{-0.006}$	$0.006^{+0.008}_{-0.004}$	$14.843^{+0.007}_{-0.007}$	$0.011^{+0.009}_{-0.007}$	$14.656^{+0.007}_{-0.007}$	$0.007^{+0.008}_{-0.005}$
WD 2132+096	$16.238^{+0.005}_{-0.005}$	$0.006^{+0.006}_{-0.004}$	$16.283^{+0.009}_{-0.009}$	$0.015^{+0.013}_{-0.010}$	$16.282^{+0.008}_{-0.008}$	$0.017^{+0.012}_{-0.011}$
WD 2207+121	$17.600^{+0.011}_{-0.011}$	$0.030^{+0.014}_{-0.013}$	$17.452^{+0.011}_{-0.010}$	$0.037^{+0.013}_{-0.014}$	$17.245^{+0.012}_{-0.011}$	$0.062^{+0.013}_{-0.013}$
WD 2221−165	$15.978^{+0.009}_{-0.010}$	$0.011^{+0.012}_{-0.008}$	$15.902^{+0.009}_{-0.009}$	$0.010^{+0.011}_{-0.007}$	$15.858^{+0.020}_{-0.021}$	$0.033^{+0.029}_{-0.022}$
WD 2326+049	$13.143^{+0.080}_{-0.078}$	$0.113^{+0.229}_{-0.058}$	$13.038^{+0.053}_{-0.049}$	$0.071^{+0.178}_{-0.037}$	$12.652^{+0.006}_{-0.006}$	$0.011^{+0.009}_{-0.007}$
WD 2328+107	$15.999^{+0.004}_{-0.004}$	$0.007^{+0.006}_{-0.005}$	$16.004^{+0.006}_{-0.006}$	$0.006^{+0.007}_{-0.004}$	$16.071^{+0.011}_{-0.011}$	$0.024^{+0.015}_{-0.015}$

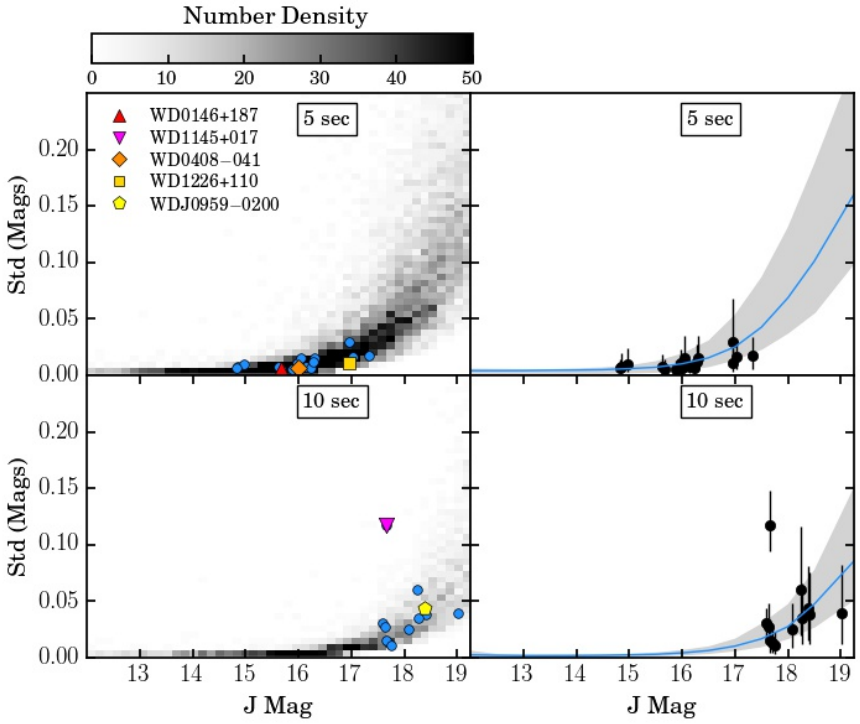

(a) *J* Band Observations

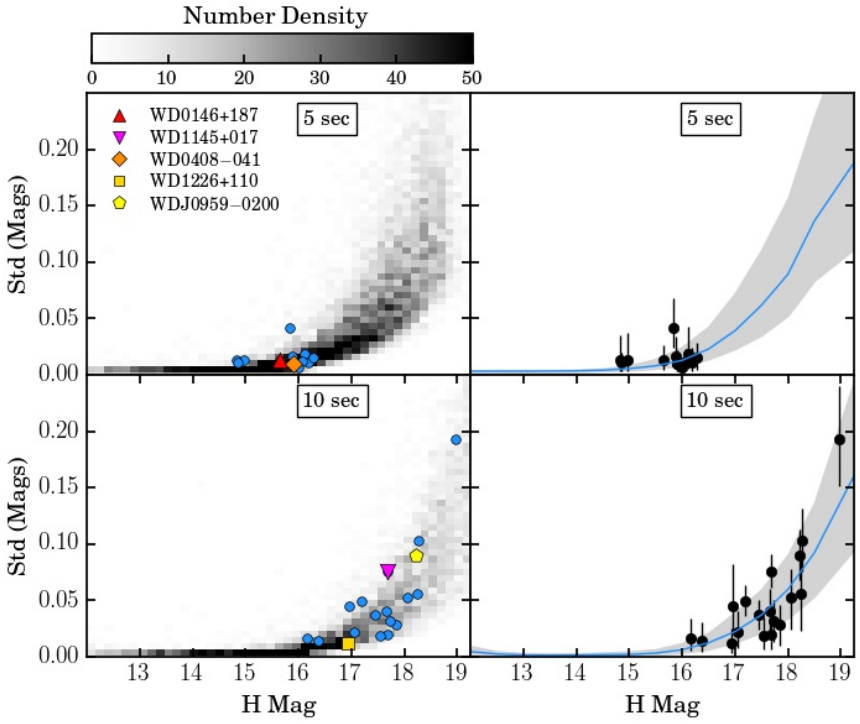

(b) *H* Band Observations

Fig. 2.2

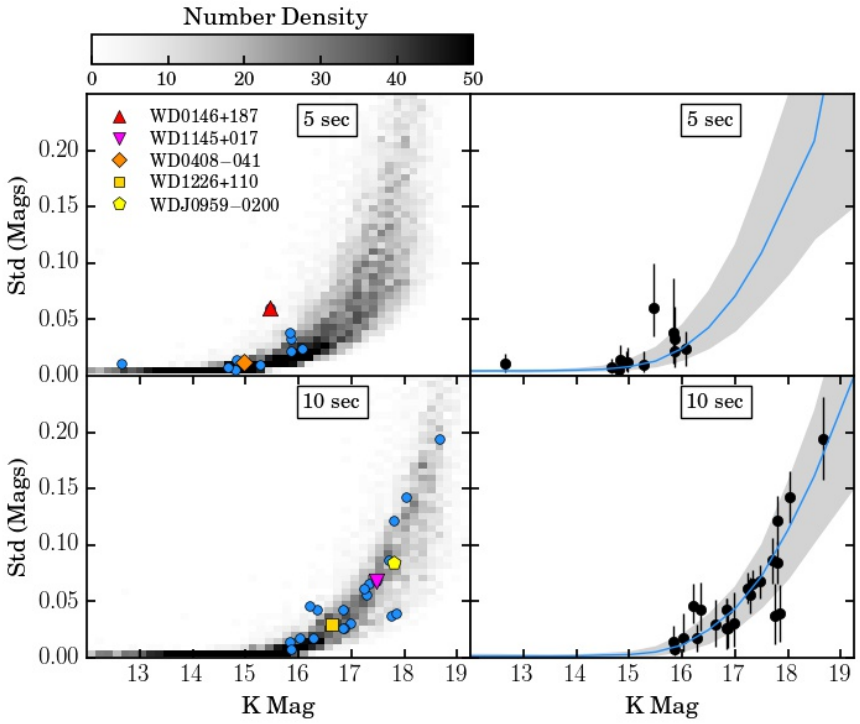

(c) *K* Band Observations

Fig. 2.2 The median observed magnitudes in the (a) *J*, (b) *H* and (c) *K* bands plotted against the median standard deviation of this magnitude for all white dwarfs and field stars. The two different observing modes, with 5 and 10 second frame times, are analysed separately. The density plots on the left hand side show the parameters for all field stellar objects in the field of view, there are of the order 10^4 field stars in each plot. The blue points show the white dwarfs, with the objects discussed in Section 2.1.2 labelled. The right hand plots show the median magnitude and standard deviation with 16th and 84th percentile confidence levels for field stars, in bins of width 0.5 mag. This forms a distribution about that median which should not comprise contaminant variable stars. The white dwarfs are over-plotted in black with the same values as in the left hand plots, but also including the 16th and 84th percentiles. This plot can be used to distinguish white dwarfs which are variable from those that follow the field star distribution.

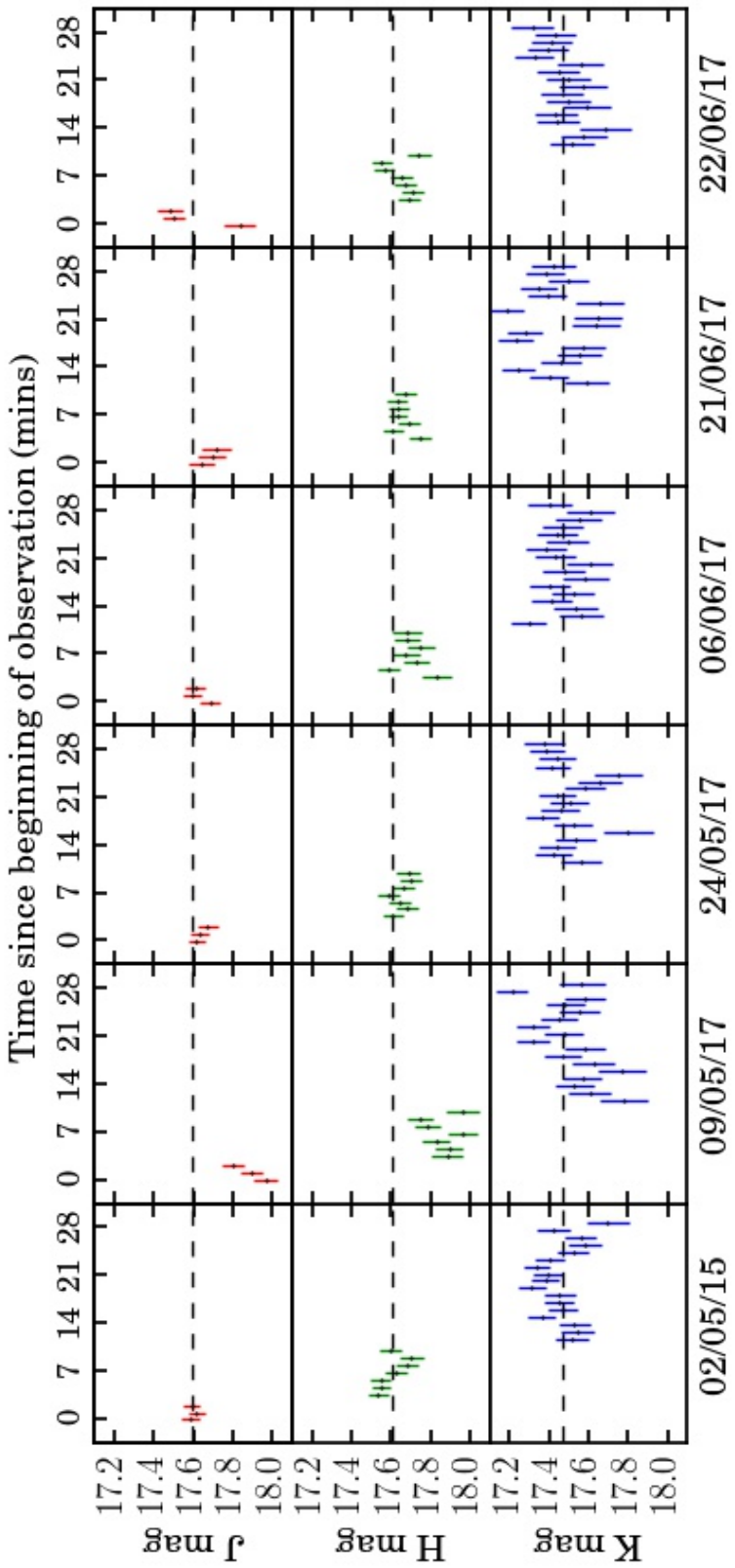

Fig. 2.3 A lightcurve in the *J*, *H* and *K* bands for WD 1145+017. At each observation date a number of observations were taken in the *J*, *H* and *K* bands, totalling 28 minutes. The dotted lines show the mean magnitude for each band calculated from the first observation date, 02/05/15. This highlights how there was an apparent dip on 09/05/17 in the flux in the *J* and *H* bands attributed to dust transit features.

WD 0146+187:

The object with the most significant deviation in the *K* band was WD 0146+187. In Fig. 2.2c the red triangle, which represents this object, shows a $2\,\sigma$ variability in the *K* band. There was a flux brightening of 0.14 mag from the 1st to the 2nd stacked frames on 03/10/14. There were no significant variations between the subsequent frames. Further investigations revealed there was nothing anomalous in the pixel map, and objects in the field of view within $100''$ do not show the same brightening trend. This could be a real change, but as there is only one data point, and the variation is not statistically significant, it is difficult to make any substantial conclusions. Swan et al. (2020) did not find variation in the *Spitzer* 3.6 µm band for this white dwarf but observed variability at the 7 percent level in the 4.5 µm band. Therefore, as no variability is seen at the 3.6 µm band it is likely that the *K* band variability is not real.

WD J0959−0200:

WD J0959−0200 was previously observed to display a 35% flux drop in 2010 in both *Spitzer* 3.6 and 4.5 µm Infrared Array Camera (IRAC) channels. The *K* band flux also dropped by 18.5% between 2005 and 2014 (Xu & Jura, 2014). This variability measurement uses the peak-to-peak method, where the maximum flux change between two frames is quoted. After the Xu & Jura (2014) UKIRT data taken on the 27/03/14, the *K* band data were consistent between multiple observations spanning 1153 days (Nov 2014, Feb 2015, Mar 2016, May 2016, May 2017). The *K* band flux was stable within $7.5\,^{+1.6}_{-1.6}$ % ($\sigma = 0.085\,^{+0.019}_{-0.019}$) over these observations, seen in Fig. 2.2c as the yellow pentagon.

WD 1226+110:

The peak-to-peak drop in flux of WD 1226+110 was 20% in the *Spitzer* 3.6 and 4.5 µm bands, and 13% in the *K* band, when comparing the 2007 UKIRT Infrared Deep Sky Survey *K* band flux with the 2015 UKIRT observation in this work (Xu et al., 2018b). Since 2015, this UKIRT survey has shown no significant changes in flux for WD 1226+110 with multiple observations separated by 738 days (May 2015, Feb 2016, May 2016, May 2017). The *K* band flux was stable within $2.7\,^{+1.9}_{-1.7}$ % ($\sigma = 0.029\,^{+0.022}_{-0.019}$) for these observations, seen in Fig. 2.2c as the gold square.

WD 0408−041:

Previously observed dust emission variations for WD 0408−041 (GD56) were seen at 3–5 µm showing brightening and dimming with peak-to-peak changes of 20% over 11.2 yrs (Farihi et al., 2018). This was attributed to dust production and consequentially depletion. In

Table 2.3 The level of variability that can be detected at each magnitude in the *K* band, calculated from the field stars. The objects which were observed with 5 and 10 second frames were analysed separately. The median percentage variability is quoted for the field stars in bins with a width of one mag, along with the 16th and 84th percentiles.

Magnitude	5 s variability (%)	10 s variability (%)
11.0-12.0	$0.41^{+0.08}_{-0.02}$	$0.20^{+0.27}_{-0.08}$
12.0-13.0	$0.41^{+0.07}_{-0.02}$	$0.15^{+0.14}_{-0.04}$
13.0-14.0	$0.43^{+0.10}_{-0.04}$	$0.14^{+0.12}_{-0.04}$
14.0-15.0	$0.57^{+0.29}_{-0.11}$	$0.20^{+0.18}_{-0.07}$
15.0-16.0	$1.27^{+1.31}_{-0.51}$	$0.52^{+0.58}_{-0.27}$
16.0-17.0	$3.91^{+3.47}_{-1.75}$	$2.32^{+1.65}_{-1.17}$
17.0-18.0	$9.43^{+6.23}_{-3.89}$	$6.34^{+3.33}_{-2.52}$
18.0-19.0	$16.14^{+7.67}_{-6.48}$	$13.16^{+5.38}_{-4.62}$

this work, the fluxes were found to be consistent between multiple observations separated by 851 days (Oct 2014, Oct 2016, Jan 2017). The *K* band dust emission appears to be stable within $1.1\,^{+1.2}_{-0.8}$ % ($\sigma = 0.012\,^{+0.014}_{-0.008}$) for these observations, seen in Fig. 2.2c as the orange diamond. WD 0408−041 will be discussed again in Section 2.1.3 in reference to the *Spitzer* variability.

Expected Variability

From the UKIRT survey the level at which variability could be detected and ruled out is determined. Table 2.3 shows the level of variability that can be detected at each *K* band magnitude. For each non-variable star in the fields of views of the white dwarfs, the median standard deviation of the magnitude measurements from the MCMC model is output. The level of variability is the median value of the non-variable stars' standard deviations, found in magnitude bins with a width of one mag. This median standard deviation was then converted to a percentage in flux space. This rules out *K* band flux variability at $1.3^{+1.3}_{-0.5}$ % for objects brighter than 16th mag in the *K* band, and at $9.4^{+6.2}_{-3.4}$ % for objects brighter than 18th mag.

Fig. 2.4 shows a cumulative distribution of the level of variability ruled out for all white dwarfs. In other words, the percentage of white dwarfs where the *K* band flux was seen to vary by no more than the plotted value. This was calculated as the median standard deviation converted to a percentage in flux space. This was also calculated for the 16th and 84th percentile errors, which is shown as the shaded region in the figure. The *K* band flux of each

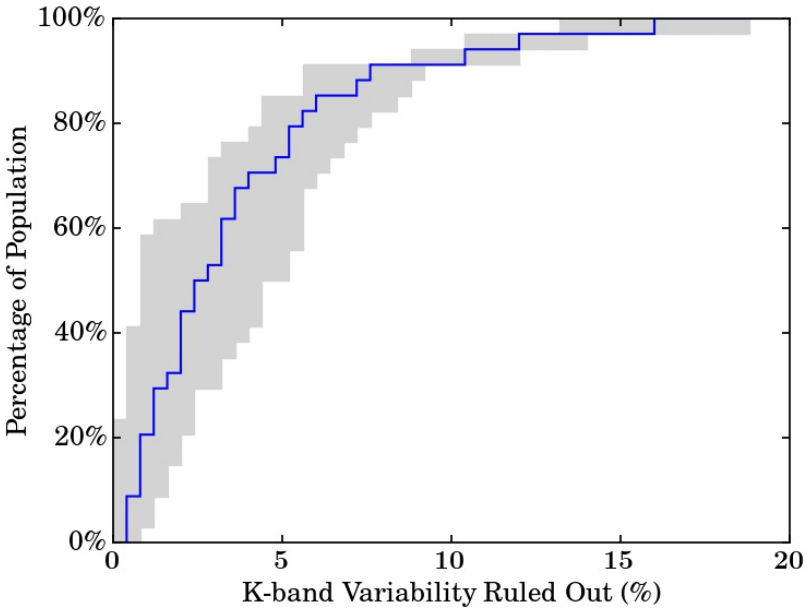

Fig. 2.4 A cumulative distribution showing the level of K band variability that can be ruled out for the white dwarfs. The blue line shows the median cumulative distribution, with the contours as the cumulative distribution on the upper and lower limits (16th and 84th percentiles). For 90% of the sample, the K band flux varied by less than 10%.

white dwarf cannot have varied more than its equivalent standard deviation. Therefore, the K band flux has varied at less than $16.4 \pm 2.8\%$ for the entire sample, and less than $2.88^{+2.5}_{-1.9}\%$ for the median case. For greater than 90% of the sample variability is ruled out at the 10% level, and for the 10 most constrained cases, variability is ruled out at the percent level, $1.57^{+1.1}_{-1.0}\%$.

Fig. 2.5a shows the percentage variability ruled out for each white dwarf plotted against the maximum time-scale over which that white dwarf was monitored in this survey. For example, for the white dwarf monitored over the longest period, WD 1929+011, variability is ruled out at the $0.7^{+0.7}_{-0.5}$ % level over a time-scale of 1013 days.

There are a handful of objects in the literature with previous detections of a change in their dusty emission, as discussed in Section 2.1.2. For WD J0959−0200, Xu & Jura (2014) found a drop in K band flux from 57 μJy to 46 μJy which is equivalent to a peak-to-peak drop of 18.5%, and Xu et al. (2018b) found a K band peak-to-peak drop of 13% for WD 1226+110. It is noted that there is difficulty in comparing the peak-to-peak variability quoted for these objects with the median variability quoted in this work. With two measurements it is not possible to constrain the distribution of fluxes that an object could be demonstrating, so the quoted variability is peak-to-peak. As there are more K band measurements, a median

variability is used for all white dwarfs, which is compared to the distribution of the field objects to constrain the level of variability. Typically, peak-to-peak variability is larger than the medium variability adopted here. The peak-to-peak variability was also calculated for the sample using the maximum difference between the mean flux at each observation date, and the conclusions are consistent. In this sample equivalent peak-to-peak and median variability are ruled out for all white dwarfs across the time-scales observed. The observations of both WD J0959−0200 and WD 1226+110 suggest that the campaign is capable of detecting the same level of variability as observed previously, and yet no such variability is detected during the survey time span for all white dwarfs.

2.1.3 Discussion

K Band Excess

For all objects in the sample, a white dwarf atmospheric model was fitted to find the expected contribution from the white dwarf photosphere to the *K* band flux. The white dwarf model atmospheres were kindly provided by P. Dufour using models from the Montreal white dwarf group (Bergeron et al., 2011; Coutu et al., 2019). The temperature, and log(g) used for the models are shown in Table 2.1; where possible, these parameters were taken from a previous photometric fit. For a number of white dwarfs where no photometric fit was available, a new fit was performed including data from the *Gaia* Data Release 2 (Prusti et al., 2016; Brown et al., 2018). The white dwarf radii (R) were determined from the photometric fit and the distances (D) were from the *Gaia* parallax (except for WD J0959−0200 which was from Farihi et al. (2012a)). The SED fits are shown in Appendix 1: 6.2; the photometric fit works well in most cases. Sometimes, additional adjustments were needed in R/D to improve the fits to the Sloan Digital Sky Survey (SDSS) and Pan-STARRS photometry. Those systems often had a large uncertainty in the parallax.

The white dwarf models were convolved with the bandpass of the UKIRT WFCAM *K* band filter (Hewett et al., 2006) to find the expected flux contribution from the white dwarf photosphere. From this, the excess flux associated with the dust was determined.

White dwarfs are usually photometrically stable and are often used as flux standards. A few white dwarfs in the sample are variable pulsators, however the optical variability is small, typically $< 1\%$. Assuming the white dwarf photosphere displays no flux variations, the *K* band variability limit can be converted to the dust variability limit,

$$\sigma_{\rm dust} = \sigma_{\rm K} \frac{F_{\rm K}}{F_{\rm K} - F_{\rm WD}}, \tag{2.1}$$

where $\sigma_{\rm dust}$ is the variability constraint for the dust, $\sigma_{\rm K}$ is the variability constraint for the K band (dust and photosphere), $F_{\rm K}$ is the UKIRT K band flux measurement, and $F_{\rm WD}$ is the convolved model flux in the K band for the white dwarf photosphere. This puts a constraint on how much the dust could have changed without being detected in this survey assuming the star remains constant.

The maximum variability not detected in the K band is used and converted to a maximum variability not detected in the dusty emission using equation 2.1. Fig. 2.5b is a similar plot to Fig. 2.5a, but instead showing the level of variability ruled out for the dust emission after the white dwarf photosphere is subtracted. A K band excess is seen for 23/34 of the white dwarfs, as seen in the SEDs in Appendix 1: 6.2. The 11 white dwarfs without a significant K band excess are: WD 0106−328, WD 0300−013, WD 0307+077, WD 1041+092, WD 1225−079, WD 1456+298, WD 2132+096, WD 2221−165, WD 2328+107, WD 1504+329, and WD 1551+175. For the 23 objects with significant K band excesses, limits are constructed on how much dust variation could be hidden from detection. For 11 white dwarfs ($\sim 50\%$ of the sample with significant K band excesses) dust changes were constrained to be less than 10%, demonstrating the dust emission was stable over the course of the monitoring period. For the 11 systems where the K band excess was negligible, the dust variability constraint would have been 100%. For these objects it was only possible to be sensitive to an increase in dust emission, not a decrease. Therefore, the dust could have completely disappeared, and it could not be distinguished from the dust displaying no variability. For those with no significant K band excess, it is imperative to go to the mid-infrared for dust variability searches.

Expected Variability at 4.5 µm

Using the variability constraint derived from the UKIRT survey, the expected variability at 4.5 µm can be predicted by assuming the dust emission has a constant colour temperature (i.e., the change is due to the amount of dust, not the location). So the shape of the dusty emission is assumed to remain constant, such that the percentage change of the dusty emission at K wavelengths can be equalled to the percentage change at 4.5 µm . Paralleling the K band analysis and equation 2.1, the expected variability at *Spitzer* 4.5 µm wavelengths is calculated,

$$\sigma_{[4.5]} = \sigma_{\rm dust} \frac{F_{[4.5]} - F_{\rm WD}}{F_{[4.5]}}, \tag{2.2}$$

where $\sigma_{[4.5]}$ is the predicted variability constraint for the 4.5 µm *Spitzer* waveband, $\sigma_{\rm dust}$ is calculated from the K band using equation 2.1, $F_{[4.5]}$ is the 4.5 µm *Spitzer* flux, and $F_{\rm WD}$ is the convolved model flux in the 4.5 µm band for the white dwarf photosphere.

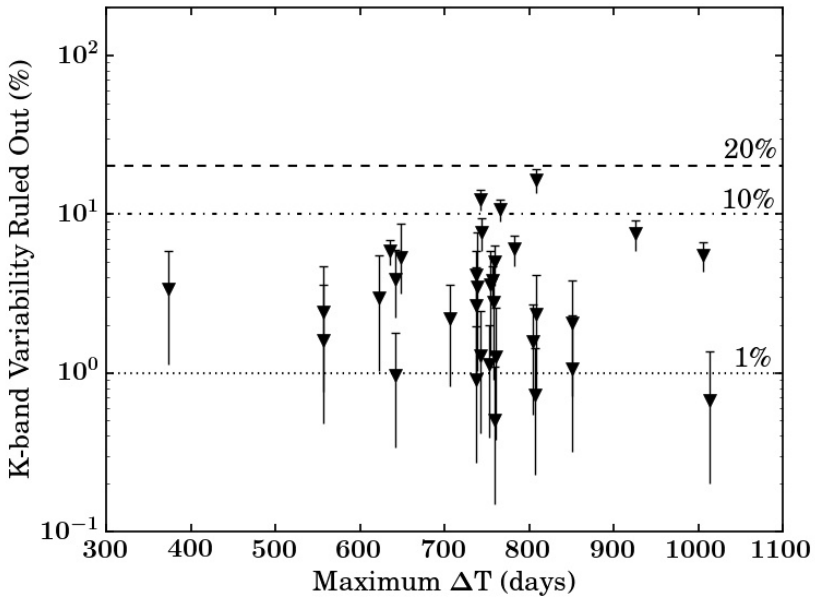

(a) *K* band variability

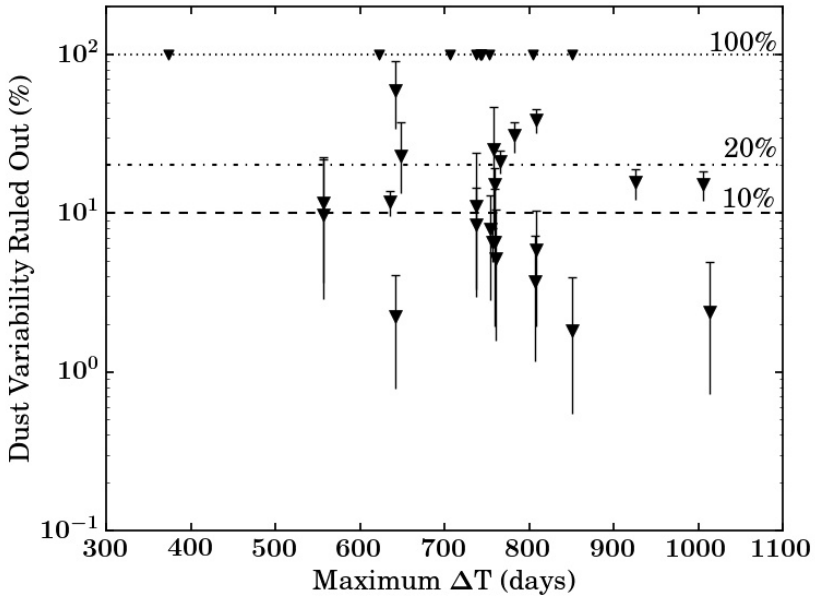

(b) Dust variability

Fig. 2.5 (a) The maximum *K* band median variability of each white dwarf that would not have been detected over the time-scale of the survey. (b) The maximum dust variability of each white dwarf that would not have been detected over the time-scale of the survey. The variability constraint of the dust component to the *K* band flux was calculated using equation 2.1.

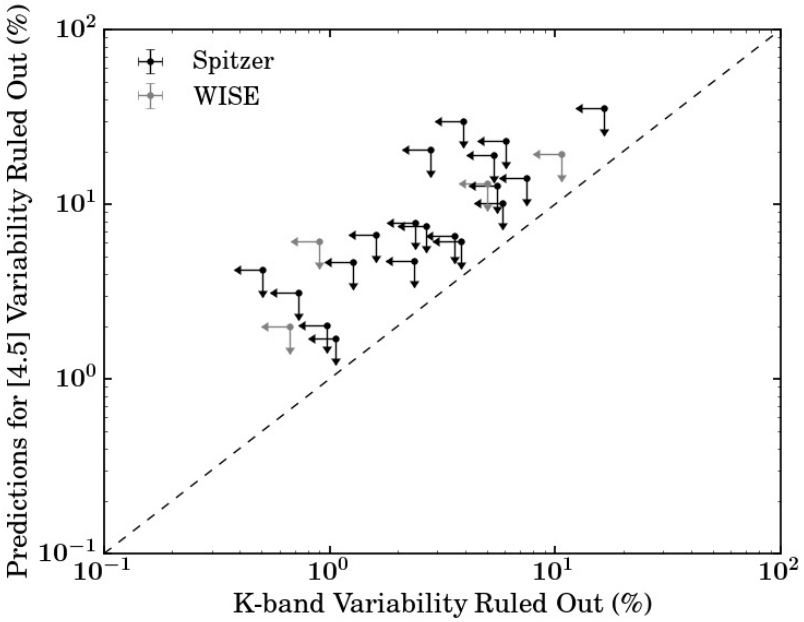

Fig. 2.6 Predictions for the maximum median variability at 4.5 µm that would have escaped detection based on the maximum median *K* band variability not detected with this UKIRT survey. The arrows represent that each axis is a constraint on the level of variability. Most objects had *Spitzer* 4.5 µm data, but for four objects *WISE* data was used as no *Spitzer* data was available. Swan et al. (2019b, 2020) assessed the level of *Spitzer* and *WISE* mid infrared variability at levels above these limits, future analyses that combine the results from these studies are crucial for understanding these dusty white dwarfs.

Fig. 2.6 shows the *K* band variability constraint, converted into a *Spitzer* 4.5 µm band variability constraint using equation 2.2. The *Spitzer* data was taken from the references listed in Table 2.1. If there was no *Spitzer* 4.5 µm data available then *WISE* 4.6 µm data was used instead. The dust excess at 4.5 µm is larger than that at the *K* band, therefore, the variability constraint in flux units will be larger for 4.5 µm, as seen in the figure. Those white dwarfs with negligible *K* band excess are excluded from this study. For those 23 white dwarfs with significant *K* band excess, at *Spitzer* wavelengths it is predicted that variability can be ruled out above 10% for ∼60% of the sample, above 20% for ∼ 85% of the sample, and above 36% for all the sample.

A particular application using the UKIRT survey can be applied to the WD 0408−041 system. Farihi et al. (2018) found the dust emission of WD 0408−041 to increase and decrease with a peak-to-peak variability of 20% over ∼ 11 years. As can be seen from Appendix 1: 6.2, the SED of WD 0408−041 demonstrates a large *K* band excess. Therefore, any variability observed at mid-infrared wavelengths should be mimicked at a lower level in the *K* band, unless there is a colour change associated with the flux change. Fig. 2.7 shows

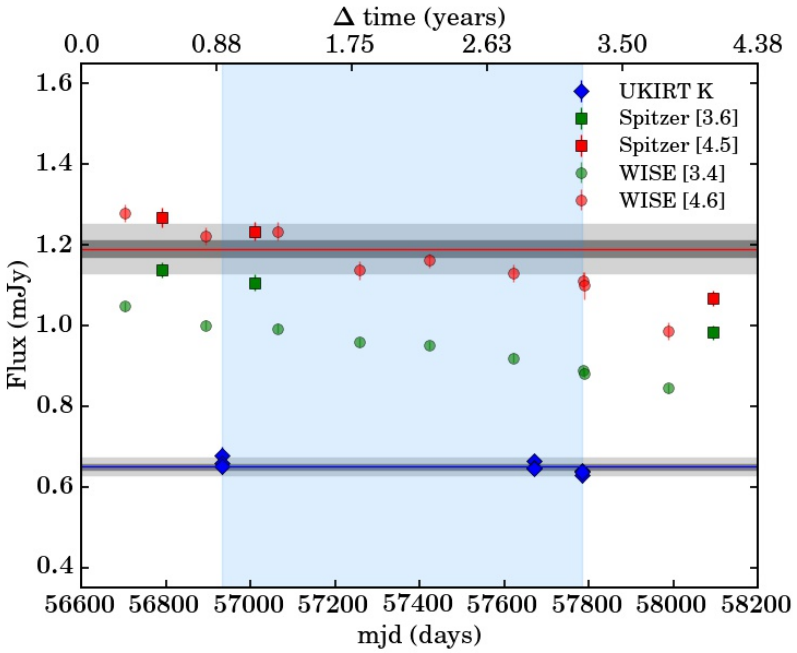

Fig. 2.7 A lightcurve of WD 0408−041 showing the UKIRT *K* band data, and the *Spitzer*/*WISE* data at which Farihi et al. (2018) observed a drop in the mid-infrared flux. The grey regions represent the 1 and 3 σ median variability constraint for the *K* band, and then scaled up to *Spitzer* wavelengths using equations 2.1 and 2.2 (assuming no colour change). The blue region shows the period of time with UKIRT observations. Figure adapted from Farihi et al. (2018).

the lightcurve for WD 0408−041 over approximately four years showing *Spitzer*, *WISE* and UKIRT *K* band data. The drop in mid-infrared flux is evident. There are not UKIRT *K* band observations which cover the full mid-infrared time-scale, as shown by the blue shaded region. Using equations 2.1 and 2.2, the *K* band variability ruled out using the UKIRT survey is scaled up to mid-infrared wavelengths. The change in the *Spitzer* 4.5 µm flux is consistent with the variability constraint derived from the *K* band data, implying that the variability could be consistent with the same colour temperature of the dust emission during the three year UKIRT survey. However, looking across the four year baseline, even at 3 σ, the *Spitzer* flux values lie outside of the shaded region, i.e. prior to 56880 MJD and after 58100 MJD. The most significant drop in *Spitzer* flux was around 58100 days. There are not simultaneous *K* band observations, with the closest *K* band measurement being over a year previous to this. There is previous evidence that large scale flux changes can occur on time-scales of less than a year (Xu & Jura, 2014). A further *K* band measurement is needed in order to understand whether the *K* band flux also dropped around MJD58100, or if there is a colour change associated with this variability.

Variability Time-scales

Fig. 2.8 shows the characteristic sampling for all the white dwarfs in the sample. This survey was sensitive to short time-scales on the order of minutes to hours and long time-scales on the order of years. Previous examples of gas variability show changes on both these time-scales (e.g. Manser et al., 2019), and previous example of dust variability show changes on year long time-scales (e.g. Xu & Jura, 2014).

A toy model is considered where the K band flux of every white dwarf varies as a step function by Δ%, every t days. The probability of detecting this variability in this UKIRT survey is calculated. Each white dwarf has a minimum detectable variability which is $3\,\sigma$ above the median variability of the field stars at the same magnitude as the white dwarf, where σ is the standard deviation on this median variability. If Δ was smaller than the minimum detectable variability for that white dwarf, the probability of detection was 0. For every combination of Δ and t, the lightcurve was randomly sampled 1000 times for each white dwarf using the UKIRT sampling times to calculate the probability that if it were varying in this manner, it would have been detected in this survey. By averaging over all 34 white dwarfs at each Δ and t, the overall probability of detection was deduced, as shown in Fig. 2.9. The colour scheme represents the probability that the UKIRT survey would have detected that combination of Δ and t if all white dwarfs varied in this way. The highest probability time-scales show that the survey was sensitive to variability over days, and years. Models where all white dwarfs vary on time-scales of $\sim$ 1–2 years with large amplitudes are ruled out. However, it isn't possible to rule out models where white dwarfs vary on time-scales much longer than this, or with smaller amplitudes (< 10%). This may explain why some objects from the literature which have been previously found to vary are consistent with little or no variability in this survey. For example, using seven years of *WISE* data, Swan et al. (2019a) found variability in a number of dusty white dwarfs. Using this model it can be seen that for these longer time-scales, there is less than a 30% chance of detecting variability.

Implications

The leading explanation for white dwarf pollution cites asteroids as the source which are scattered inwards stochastically. How frequently these asteroids are scattered inwards remains an open question, with debate in the literature between whether pollution is caused by a single large body, or many small bodies (e.g. Jura, 2008; Jura et al., 2009b; Wyatt et al., 2014).

Wyatt et al. (2014) presented a model whereby white dwarf pollution is explained by a continuous stream of many small asteroids, with the stochastic scattering of the largest

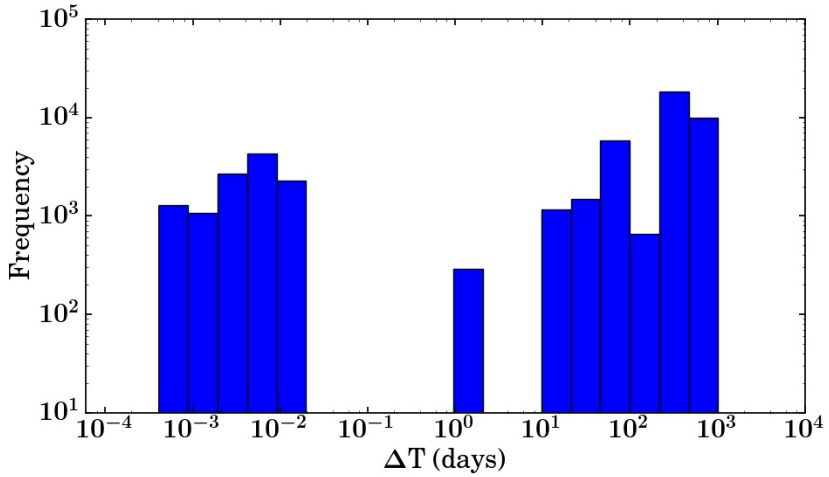

Fig. 2.8 A histogram showing the characteristic survey sampling to search for variability. The plot shows the distribution of all time-scales between frames of a given white dwarf, for all white dwarfs. This demonstrates that for all white dwarfs the survey was sensitive to minute/hour time-scales and year time-scales.

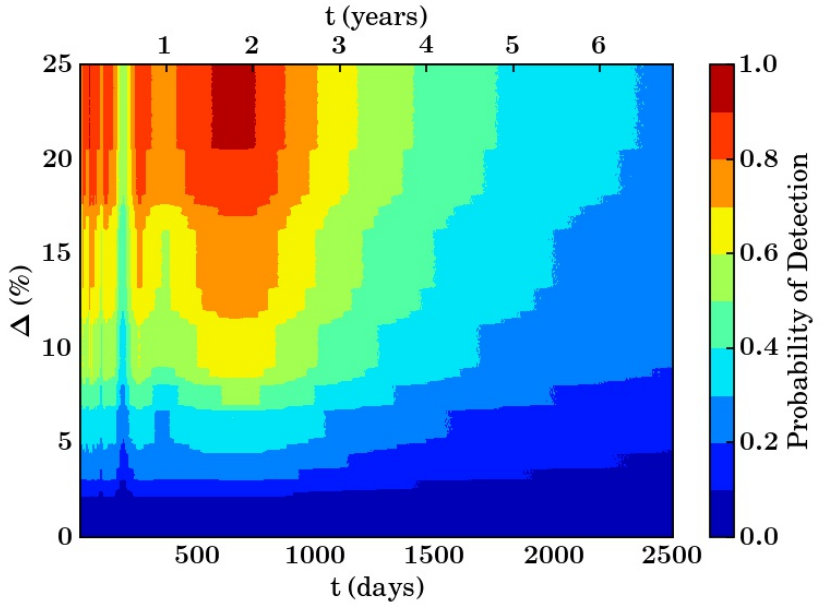

Fig. 2.9 A toy model in which every white dwarf in the sample is considered to have a K band flux that varies by $\Delta\%$ every t days. The density plot indicates the probability of detecting that combination of Δ and t for white dwarfs in the UKIRT survey. The smallest grid scale is 1 day and 0.1%.

bodies dominating the accretion rates. In this model, the lifetime of the dusty material is a free parameter, with a best-fitting value of 20 years. The survey would be unlikely to detect variations on such long time-scales. However, if the disc lifetime was instead an order of magnitude smaller (~ 2 years), large amplitude variations in the infrared flux on these time-scales would be expected. In this survey, large variability is ruled out over these time-scales. Therefore, the results of this survey provide further evidence in support of long (> 3 year) lifetimes for the dusty material around white dwarfs. It also demonstrates that disruption events large enough to be detectable in the infrared do not regularly occur on short time-scales such as years. This is crucial, as for many highly polluted DA white dwarfs, material can sink out of the atmospheres on time-scales of days to years. This work provides observational evidence that dusty material has a lifetime of at least 2–3 years. Therefore, it is highlighted that further monitoring in the infrared is needed to discover the frequency of scattering events.

2.1.4 Conclusions from the UKIRT survey

Infrared studies are crucial for understanding the accretion processes associated with polluted white dwarfs. This work reports a near-infrared *J*, *H*, and *K* band monitoring campaign with the UKIRT, completed over three years which studied 34 polluted white dwarfs with infrared excesses. High precision *J*, *H*, and *K* band photometry was reported for the white dwarfs in the sample, for many of these objects high precision photometry is not previously reported. The main results are summarised as follows.

1. The *K* band flux was stable within the error of the survey for all observations of the white dwarfs, where the observation sampling rates were on the order of minutes and years. Of the near-infrared bands, the *K* band is the most sensitive to the dust. It was possible to rule out median *K* band variability greater than $16.4^{+2.8}_{-2.8}\%$ for the faintest white dwarf in the sample and greater than than $2.88^{+2.5}_{-1.9}\%$ for half of the sample. For $> 90\%$ of the sample variability at the 10% level was ruled out, and for the 10 most constrained white dwarfs, *K* band variability was ruled out at the percent level, $< 1.57^{+1.1}_{-1.0}\%$.

2. WD J0959−0200 and WD 1226+110 have previously exhibited variability in their dusty emission as seen at the *K* band (18.5% for WD J0959−0200 and 13% for WD 1226+110) and *Spitzer* 3.6 and 4.5 µm bands. These objects did not display any significant variability in the study. For most of the sample (except the faintest object, WD 1554+094) similar *K* band variability to these white dwarfs was ruled out. This highlights that these large *K* band variability events are rare.

3. Assuming there is no colour change associated with the dust emission, the variability at 4.5 µm was predicted based on the K band variability. The white dwarfs should not vary at 4.5 µm above 10% for $\sim$60% of the sample, above 20% for $\sim$85% of the sample, and above 36% for all the sample.

4. It was demonstrated that any white dwarf with large amplitude ($>$20%) near-infrared variability on short ($<$3 year) time-scales should have been found with this survey. This implies that major tidal disruption events that lead to white dwarf pollution occur less frequently than every three years, and are consequently rare. Infrared variability around white dwarfs with infrared excesses does exist as revealed by other observations. The constraints provided from the K band survey imply that such events, if they occur, do so on short time-scales, and quickly become stable within a few years.

5. Ground based near-infrared searches for white dwarf dust variability are fruitful, and as demonstrated in this survey can search for variability down to the percent level for the brightest sources. This survey was not sensitive to long time-scale ($>$3 year) variability and, therefore, it is crucial to highlight the need for long-term monitoring of white dwarfs with infrared excesses. Also, with recent advances finding variability in the gas discs over periods of hours (Manser et al., 2019), it is also crucial to search for variability over hours–days timescales in the dust to fully understand these highly enigmatic and dynamic systems.

2.2 NIR dust variability with SOFI/NTT

Variability in the near infrared was ruled out over timescales of months–years using the UKIRT/WFCAM. However, there are previous examples of white dwarfs with remnant planetary systems demonstrating variability on shorter timescales such as hours. Manser et al. (2019) discovered rapid variability in the gaseous disc of WD 1226+110. A 123.4 minute stable period was observed in the spectral shape of the gaseous emission features and was attributed to a planetesimal orbiting within the disc on a short period. Furthermore, time series lightcurves of a number of white dwarfs reveal they are being transited by material and have periods as short as a few hours (e.g. Vanderburg et al., 2015). The material orbiting the white dwarfs on timescales of hours are on close-in orbits, and studying this material can shed light on exactly how this material ultimately disrupts, migrates towards the white dwarf, and accretes. No studies have searched for variability in the dust emission at short timescales of hours – days, this is the focus of the following section.

2.2.1 NTT Observations and data reduction

A near-infrared monitoring campaign was conducted using the SOFI near-infrared imaging instrument on the New Technology Telescope in La Silla, Chile between April 17th 2019 – April 24th 2019 (PI: Rogers). Table 2.4 lists the white dwarfs observed. The targets consist of eight white dwarfs that: have atmospheric pollution, have infrared emission associated with a dust disc, are brighter than 17th magnitude in the K band, and were observable from the southern hemisphere during the observing run.

The observing run had two main goals: to search for dust emission changes through K_S band observations over timescales of hours–days for a sample of white dwarfs with dust discs, and to obtain a continuous K_S band lightcurve of WD 1226+110 over a number of hours. For the first goal, the observing strategy was to obtain sets of J, H and K_S band photometry separated by hours, and then days, but due to extreme weather conditions it was difficult to plan cadences. G166-58 is missing the set of observations separated by hours, but is still included in the analysis. The aim was to achieve a SNR of 30 for each frame for the J and H band, and 40 for the K_S band, mirroring the UKIRT/WFCAM observing strategy. Dithering enables the removal of instrument signatures, such as bad pixels, and allows the removal of the sky background, therefore, a five point dither pattern was used with each pattern producing one frame. For the second goal, the aim was to obtain a continuous K_S band lightcurve of WD 1226+110 whilst it was above an altitude of 30 degrees in the sky. In total 340 frames of 10 second K_S band exposures were taken which spanned across $\sim$ 6 hours. Exposure times of 10 seconds per frame were used to avoid detector saturation. Sets of five frames were stacked together to produce a single K_S band frame providing one stacked frame every $\sim$ 6 minutes.

Standard infrared imaging data reduction techniques were used to process the images using ESO SOFI pipeline (v1.5.10), including dark subtraction, flat fielding and sky subtraction. WCS information was updated using the WCSFIT package as part of CASUTOOLS to obtain more accurate positional information using 2MASS catalogue sources. Photometric calibration was performed using 2MASS sources in the field of view. LIGHTCURVES was used to obtain improved precision of the photometry as described in Section 2.1.1 for the UKIRT/WFCAM data.

2.2.2 Variability Analysis

JHK$_S$ photometry for seven white dwarfs

This work aimed to obtain high precision JHK_S photometry of seven dusty white dwarfs to investigate whether variability is observed over timescales of hours–days. Of the near-

Table 2.4 Observations of the white dwarfs listing the number of sets of *JHK* photometry obtained and the baseline for these observations.

WD Name	Other Name	N sets	Min Baseline	Max Baseline
WD 0959−57	WG 14	8	0.3 hrs	7 days
EC 05365−4749	-	3	0.4 hrs	7 days
WD 1929+011	-	4	2 hrs	3 days
WD 2115−560	-	3	2 hrs	2 days
WD 2221−165	HE 2221−165	3	1.1 hrs	2 days
WD J1617+1620	SDSS J161717.04+162022.4	3	2 hrs	2 days
G166-58	-	2	2 days†	2 days†
WD 1226+110	SDSS J122859.93+104032.9	340*	6 mins	6 hours

Notes:

* WD 1226+110 has 340 K_S band frames taken over 6 hours.

† G166-58 has only 2 sets of JHK observations so minimum and maximum baseline is the same.

infrared bands, the K_S band is the most sensitive to the dust, as discussed previously, therefore it will be investigated whether there is variability in the K_S band that is not present in the J or H bands. Throughout the analysis the Vega magnitude system was adopted.

LIGHTCURVES was used to perform differential photometry and fit 2D polynomials to the magnitude residuals to minimise the error associated with the position on the detector, allowing improved precision lightcurves for the white dwarfs. It is crucial to have enough comparison stars in the field of view for LIGHTCURVES. Table 2.5 lists the number of comparison stars used in LIGHTCURVES, the number varies from 15–1155. G166-58 has the smallest number of comparison stars, further investigations varying the parameters used in LIGHTCURVES revealed no significant changes to the final results.

Figure 2.10 shows the output K_S band magnitude over time from LIGHTCURVES for the seven white dwarfs. As can be seen, no statistically significant variability is observed in these lightcurves. This rules out variability in the K_S band dust emission over timescales of hours and days for these white dwarfs.

The median K_S band magnitude is measured for each white dwarf and compared with historic K_S band data from 2MASS, K_S band data Dennihy et al. (2016), and the UKIRT K band magnitudes in Section 2.1 for those where there is overlap (see Table 2.5). The only white dwarf displaying discrepant K band measurements are for WD 1929+011. The 2MASS K_S band is ~ 0.2 mags brighter than the measurement here. Other K band measurements from the literature, 14.62 ± 0.05 (Melis et al., 2011) and 14.66 ± 0.01 (Rogers et al., 2020) are consistent with the K_S band measurement from SOFI, when correcting for the differences in the magnitudes from the K_S and K filters (Carpenter, 2001). Melis et al. (2011) discusses the discrepancy between 2MASS and their K band measurement and find that it is likely

Table 2.5 Table listing dates of observations for the white dwarfs in the sample, and number of exposures. N comp is the number of comparison stellar objects in the frame.

WD Name	2MASS J	2MASS H	2MASS K_S	N comp	K_{obs}
WD 0959−57	15.18±0.07	15.03±0.09	15.16±0.18	1155	15.17±0.10
EC 05365−4749	16.10±0.01 †	15.92±0.18	16.11±0.04 †	53	16.05±0.08
WD 1929+011	14.66±0.05	14.54±0.09	14.45±0.10	513	14.63±0.06
WD 2115−560	14.11±0.0	13.99±0.06	14.02±0.06	31	14.02±0.03
WD 2221−165	15.80±0.06	15.79±0.14	15.86±0.03 *	30	15.74±0.10
WD J1617+1620	17.34±0.02 *	17.20±0.05 *	16.87±0.03 *	58	16.77±0.11
G166-58	14.97±0.05	14.61±0.08	14.74±0.13	15	14.72±0.03

Notes:

* Magnitude from the UKIRT survey in Section 2.1. Note: UKIRT is *K* band whereas SOFI is K_S, so the magnitudes are not directly comparable.

† EC 05365−4749 *J* and K_S band magnitudes from Dennihy et al. (2016).

WD 1929+011 suffers from contamination from background sources in 2MASS, which due to the large pixel sizes for 2MASS can cause discrepant photometry. Therefore, no statistically significant variability is observed for these white dwarfs which reinforces the conclusions from the UKIRT survey.

WD 1226+110

LIGHTCURVES was used to output K_S band aperture photometry lightcurves for WD 1226+110 and four comparison stars. The field of view of WD 1226+110 is sparse, therefore, insufficient numbers of comparison stars were in the field of view for LIGHTCURVES to perform differential photometry or to fit 2D polynomials to the magnitude residuals to minimise the error associated with the position on the detector. Instead four stars were selected from the LIGHTCURVES output for manual differential photometry, these were selected as they were: less than one magnitude brighter than WD 1226+110, more than 100 pixels from the edge of the detector, and classified as non-variable stars. The K_S band lightcurves for the four comparison stars are shown in Figure 2.11. The offset required to correct the lightcurve of WD 1226+110 for photometric variation induced by external factors (e.g. atmospheric/cloud variations) was constructed by calculating the weighted mean Δ K of the four stars for each frame, weighted by the measurement error for each magnitude in the lightcurve. For each object, LIGHTCURVES flags frames where the aperture contained bad or saturated pixels, so the associated measurements from these frames were excluded from the calculation and are not plotted in Figure 2.11. The magnitude 'offset' lightcurve is plotted in black along the top of Figure 2.11, and this is subtracted from the K_S band lightcurve for WD 1226+110 to

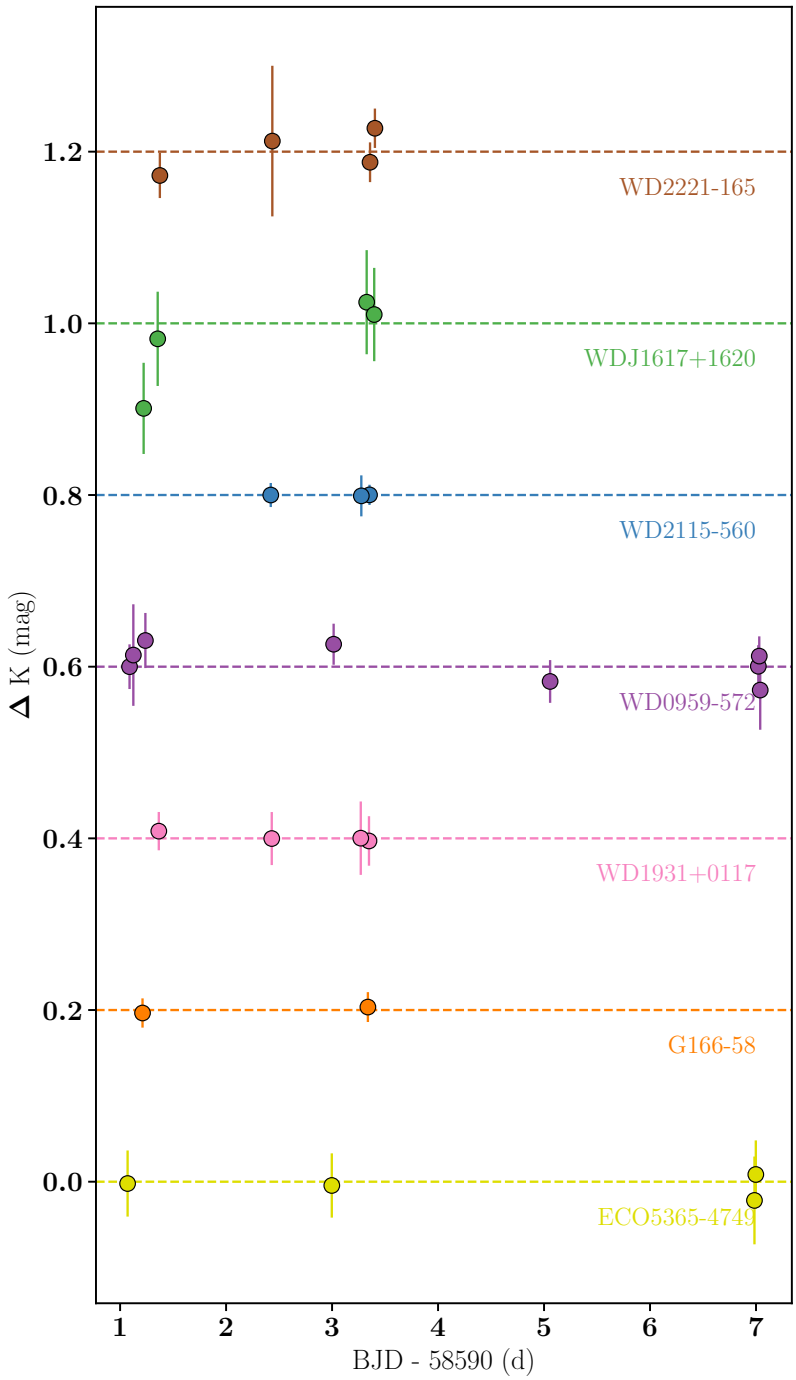

Fig. 2.10 K_S band measurements for the seven white dwarfs in the sample, all offset by 0.2 mags. Observations were taken separated by hours and days. ΔK is the output K_S band magnitude subtracted from the median magnitude of the lightcurve, such that > 0 is brighter than the median magnitude and < 0 is fainter.

obtain the corrected lightcurve shown in Figure 2.12 with measurement errors output from the aperture photometry of LIGHTCURVES added in quadrature with the errors from the offset lightcurve.

By eye, the lightcurve of WD 1226+110 reveals no significant variations. However, it should be noted that the errors are large due to poor weather conditions, with SNR per frame $<$10. The median offset in Δ K, as shown in Figure 2.11, is 0.31 mags, and the maximum offset is 1.5 mags. In order to search for hidden periodicities, a Lomb-Scargle periodogram was constructed using ASTROPY[4] tools, Figure 2.13 (Lomb, 1976; Scargle, 1982; VanderPlas, 2018). Lomb-Scargle periodograms are a powerful tool that can detect periodic signals when observations are unevenly spaced in time. Frames that were flagged by LIGHTCURVES are excluded from this study. Periods between 7 minutes and 300 minutes were sampled, the periodogram reveals two peaks at: 0.011 days and 0.039 days. In order to assess whether these periods are significant, false alarm probabilities are calculated. This finds the probability that a peak would be measured at this height or above if it is assumed that the data only consists of Gaussian noise with no periodic signals. The peaks at periods of 0.011 days and 0.039 days have false alarm probabilities of 0.62 and 0.60 respectively. Therefore, the false alarm probability is high and so the peaks are unlikely to be real. In order to decrease the false alarm probability, further and more precise time series data needs to be taken.

Manser et al. (2019) observed a 123.4 minute period in the gaseous component to the disc surrounding WD 1226+110, this period is not observed in the dust emission. The vertical dashed line in Figure 2.13 shows the 123.4 minute period found in the gaseous component, no peaks in the periodogram are observed around this period.

2.2.3 Discussion

As with the UKIRT survey over timescales of years, white dwarfs displaying large amplitude near-infrared variability appear to also be rare over shorter timescales of hours–days. From the UKIRT survey it was hypothesised that large events leading to K_S band variability are rare and could be occurring on shorter timescales and quickly become stable, therefore, predicting variability over shorter periods. However, this is not observed in this work. Comparing historic near-infrared magnitudes confirmed no variability in the near-infrared over timescales of years. This is especially important for the three white dwarfs that did not overlap with the UKIRT survey (WD 0959$-$57, EC 05365$-$4749, WD 2115$-$560), where the historic magnitudes were all consistent within 1 σ to the SOFI/NTT magnitudes. These conclusions are limited as the sample is small, with limited sets of *JHK* data. With more white dwarfs

[4]https://www.astropy.org

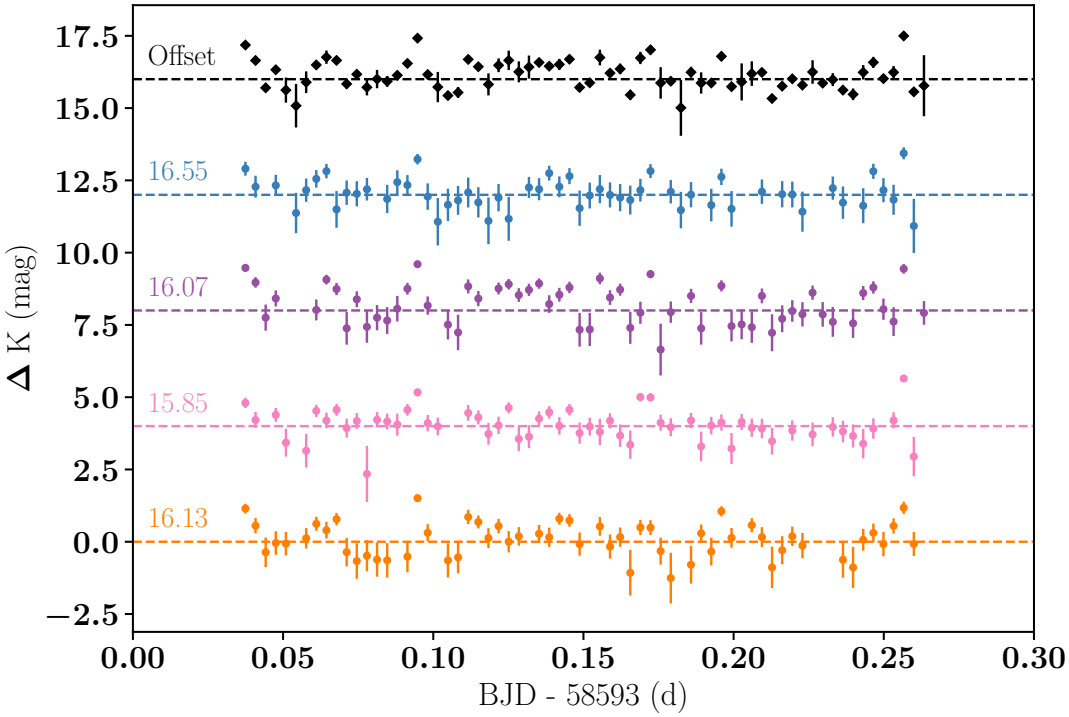

Fig. 2.11 The lightcurves of the four stars in the field of view of WD 1226+110 that were used to perform differential photometry, each offset from one another. Δ K is the output K_S band magnitude subtracted from the median magnitude of the lightcurve, such that > 0 is brighter than the median magnitude and < 0 is fainter. The median K_S band magnitude of each comparison star is labelled. The lightcurve labelled 'offset' is the calculated offset from the four stars that was applied to the WD 1226+110 lightcurve to perform differential photometry.

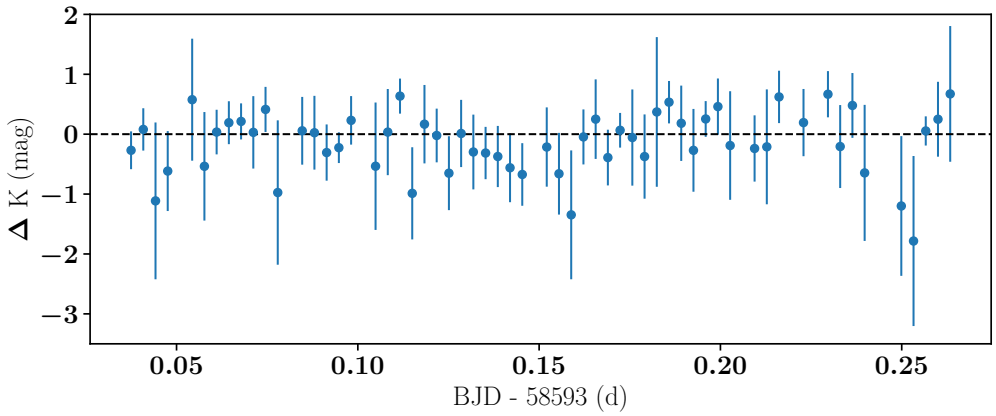

Fig. 2.12 K band lightcurve spanning $\sim$ 6 hours for WD 1226+110. Δ K is the output K_S band magnitude subtracted from the median magnitude of the lightcurve, such that > 0 means WD 1226+110 is brighter than the median magnitude and < 0 means it is fainter. The errors are large due to non-photometric conditions.

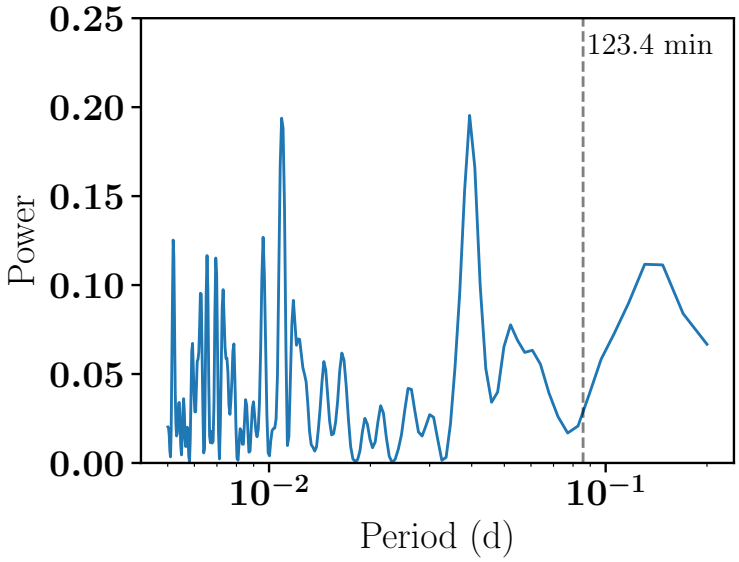

Fig. 2.13 Lomb-Scargle periodogram for WD 1226+110 using the lightcurve in Figure 2.12. The vertical dashed line shows the 123.4 minute period observed by Manser et al. (2019) in the gaseous component of the disc for WD 1226+110. The periodogram reveals two peaks at 0.011 days and 0.039 days but have false alarm probabilities of 0.62 and 0.60 respectively and are unlikely to be real.

with infrared excesses being discovered and confirmed (e.g. Lai et al., 2021), those which are brighter and have a more significant K_S band excess could be targeted to truly rule out near-infrared variability.

WD 1226+110

Variability in both the circumstellar dust and gas has been previously observed for the white dwarf WD 1226+110. Xu et al. (2018b) observed significant changes in the infrared dust flux for WD 1226+110 with a 20% ($3\,\sigma$) flux drop in Spitzer mid-infrared bands, and a 13% ($2.7\,\sigma$) drop in K band was observed between 2007 and 2015. Subsequent K band observations demonstrated that it remained at the same level for the following years, as seen in Section 2.1.2. Manser et al. (2016a) reported evolution of the calcium infrared triplet gas emission features over periods of 24–30 years, and interpreted it as the precession of the disc. Additional variability in the gaseous emission features was observed with a 123.4 minute period reported with a likely explanation of a planetesimal orbiting within the disc (Manser et al., 2019).

Although variability has been previously observed in both the circumstellar dust and gas emission, no K band variability is reported in this work. The work by Manser et al. (2019) proposed that the planetesimal could interact with the dust which causes the gaseous disc component and varying intensity pattern within the disc. If the planetesimal is first interacting with the dust, it may be expected that this 123.4 minute signal is mimicked in the dust emission. No 123.4 minute signal is observed in the K_S band lightcurve. Therefore, there doesn't appear to be a correlation between the dust and gas. This could imply: that the dust is not involved in causing the variable gaseous disc component, that the dust and gas are not co-orbital, or that dust variability associated with this interaction is undetectable.

These conclusions are limited by the observations. These observations were conducted over 6 hours which is roughly three times the length of the 123.4 minute period. Additional K band time series data which covers more periods would help to determine whether there truly is no 123.4 minute period. Also, observations taken under photometric conditions are preferable to help to reduce the measurement errors and result in detections of smaller amplitude variations. Furthermore, a wider field of view would enable more calibration stars to be included such that LIGHTCURVES could be utilised to produce high precision differential lightcurves for WD 1226+110.

2.2.4 Conclusions from the NTT/SOFI survey

This work reports a near-infrared monitoring campaign to search for dust variability over timescales of hours–days. Seven white dwarfs had multiple sets of J, H, and K_S band photometry measured over the space of hours and followed up again over timescales of days. A $\sim$6 hour continuous K_S band lightcurve was obtained for WD 1226+110 to study timescales of minutes/hours in detail and search for a dust variability signal equivalent to the 123.4 minute signal in the gaseous component of the disc. The main results are summarised as follows.

1. The K_S band flux, which of the near-infrared bands is most sensitive to the dust, was stable within the error of the survey for all observations of the eight white dwarfs, where the observation sampling rates were on the order of hours and days. Comparing with historic K band magnitudes, no statistically significant changes were observed.

2. The constraints from the UKIRT survey implied that if these large tidal disruption events that cause near-infrared variability occur, they do so on short time-scales, and quickly become stable within a few years. This limited sample does not support short term variability. WD J0959−0200 (Xu & Jura, 2014) and WD 1226+110 (Xu et al., 2018b) remain the only white dwarfs to show significant K band variability from previous studies emphasising the rarity of K band variability. It is also interesting to note that both these system display detectable circumstellar gaseous discs hinting at a link between K band variability and the most extreme collisions.

3. No significant variability is detected in the 6 hour continuous K_S band lightcurve of WD 1226+110. The dust does not appear to be varying over these short timescales despite a 123.4 minute period variation in the gaseous component to the disc. This may imply there is no link between the dust and the gas variability.

4. Swan et al. (2019a) and Swan et al. (2020) show that mid-infrared variability appears to be more common than in the near-infrared. In depth modelling is required to understand these systems and the links between the near and mid infrared. This can be difficult due to degeneracies between the distance of the dust from the white dwarf, the dust size, the dust composition and albedo. It is crucial to model the near and mid infrared dust emission and variability to understand the temperatures, sizes and compositions of the grains, and how this material ultimately ends up in the white dwarf photosphere. With developing technologies such as GRAVITY+, it may become possible to obtain images of the spatially resolved dust for some of the brightest infrared excess white dwarfs.

This would help to calculate the radial extent of the dust, breaking the degeneracy between dust size and dust distance from the white dwarf.

Chapter 3

Metal line variability

The events that lead to planetary material ultimately accreting onto white dwarfs are violent and variable. The dynamic and stochastic nature of these systems consequently predicts the accretion rate to also vary. For warm DAZ white dwarfs (12,000 K – 25,000 K), sinking timescales of pollutant metals are of the order days – months. Therefore, any temporal variations in the accretion rate or amount of material in the photosphere of the white dwarf, should be detectable with spectroscopic monitoring over timescales longer than the sinking timescales. von Hippel & Thompson (2007) reported an increase of $\sim 70\%$ in the equivalent width of the Ca II K line in G29-38 over 3 years. However, a follow up study by Debes & López-Morales (2008) found no evidence for changes in the equivalent width of the Ca II K line, nor a number of other spectral lines, and hypothesised that the variations found previously were due to differing spectral resolutions. Papers reporting time series of circumstellar dust or gas observations of individual objects investigate whether the photospheric lines appear to change as a by product (Wilson et al., 2014; Farihi et al., 2018), with no further detections of variability. There have been no studies investigating a sample of DAZ white dwarfs systematically to search for variability and constrain the level of variability in the accretion rate.

This Chapter reports a spectroscopic monitoring campaign of five DAZ white dwarfs using two medium resolution spectrographs. Each white dwarf was observed over a total baseline of $>$10 years with between 12–30 data sets obtained, covering timescales of days, months and years. This samples between 50–2000 sinking timescales, depending on the white dwarf properties, so if the accretion rate were to change this should be discovered. However, no unambiguous changes in accretion rate are discovered. Section 3.1 reports the target selection, spectroscopic observations of the selected targets, and the data reductions and processing. Section 3.2 discusses the methods used to determine the equivalent width over

time. Finally Sections 3.4 and 3.5 discuss and conclude the results from the spectroscopic monitoring survey.

3.1 Observations and Data Reduction

3.1.1 Target Selection

When searching for variability in the metal lines, target selection is crucial. For this reason, five white dwarfs that satisfy particular physical conditions were selected, as shown in Table 3.1. Firstly, the targets must be warm DAZ white dwarfs. DAZ white dwarfs have sinking timescales on the order of days–years, so if changes in the amount of material in the white dwarfs' photosphere occurs, it should be detectable over the baseline of the observations (see Table 3.2), whereas DBZ white dwarfs have much longer sinking timescales on the order of 10^2 to 10^6 years. The targets must have temperatures which aren't too cold $< 10{,}000$ K such that the sinking timescales of the different elements are of the order of days–months rather than tens of years (Koester, 2009), and not too hot such that radiative levitation becomes a dominant mechanism to bring heavy elements to the photosphere ($> 20-25{,}000$ K) (Chayer et al., 1995a,b; Barstow et al., 2014). One of the hottest target, WD 1929+011, was found to have a negligible radiative levitation contribution of material in comparison to accreted material (Koester et al., 2014). Finally, the white dwarfs must show evidence for atmospheric pollution at a strong level with detections of at least Ca and Mg, with abundances of [Ca/H] > -7.0 and [Mg/H] > -6.0, as shown in Table 3.2. Four of the five white dwarfs display an infrared excess associated with circumstellar dust, however, this wasn't a requirement for the programme. G29-38 was included in this programme, as studied by both von Hippel & Thompson (2007) and Debes & López-Morales (2008). The latter paper highlighted the importance of observing using similar resolution instruments, therefore, this work will re-visit the results from these studies using two medium resolution spectrographs.

3.1.2 Spectroscopic observations

Debes & López-Morales (2008) highlighted the importance of *systematic* observations to search for variability in the metal features. Their R$\sim$40,000 spectra gave a median equivalent width value of 260 mA, however, when re-binning this R$\sim$40,000 spectra down to resolutions of R$\sim$500 they found significant deviations in the derived equivalent width with values between 140 mA and 350 mA, significantly discrepant from the R$\sim$40,000 equivalent width of 260 mA. Therefore, it is crucial to study white dwarf metal variability using the same

Table 3.1 The sample of polluted white dwarfs stating their effective temperature and log(g) derived from a spectroscopic fit in previous works. The dust column highlights whether they are confirmed to have an infrared excess from circumstellar dust.

WD Name	Other Name	Gaia eDR3 Number	T_{eff}	log(g)	Dust?
WD 0106−328	HE 0106−3253	5026963661794939520	17350 $^{\alpha}$	8.12 $^{\alpha}$	Yes[1]
WD 0408−041	GD 56	3251748915515143296	15300 $^{\beta}$	8.09 $^{\beta}$	Yes[2]
WD 1457−086	...	6332172027974304512	22200 $^{\beta}$	7.99 $^{\beta}$	- *
WD 1929+011	GALEX J193156.8+011745	4287654959563143168	21200 $^{\gamma}$	7.91 $^{\gamma}$	Yes[3]
WD 2326+049	G29-38	2660358032257156736	11800 $^{\delta}$	8.40 $^{\delta}$	Yes[4]

Temperature/log(g) References: (α) Xu et al. (2019), (β) Gianninas et al. (2011), (γ) Gänsicke et al. (2012), (δ) Xu et al. (2014).
Dust References: (1) Farihi et al. (2010b), (2) Jura et al. (2007b), (3) Rocchetto et al. (2015), (4) Zuckerman & Becklin (1987).
* Dust emission candidate but photometry likely contaminated (Dennihy et al., 2017).

Table 3.2 The pollution levels and sinking timescales for the sample of white dwarfs. Sinking timescales interpolated from Koester et al. (2020).

WD Name	[Ca/H]	[Mg/H]	τ_{Ca} (d)	τ_{Mg} (d)	log(q)
WD 0106−328	−5.93±0.11 [1]	−5.57±0.20 [1]	1.13	1.83	−16.71
WD 0408−041	−6.86±0.20 [1]	−5.55±0.20 [1]	2.75	4.58	−16.19
WD 1457−086	−6.23±0.20 [1]	−5.47±0.20 [1]	5.50	9.59	−15.78
WD 1929+011*	−5.83±0.10 [2]	−4.10±0.10 [2]	4.39	7.48	−16.00
WD 2326+049	−6.58±0.12 [3]	−5.77±0.13 [3]	80.45	86.01	−14.00

References: (1) Xu et al. (2019), (2) Melis et al. (2011), (3) Xu et al. (2014).
*The white dwarf parameters used in this work are from Gänsicke et al. (2012), so abundances will not be directly comparable.

or similar spectrographs to reduce systematics. This work focuses on spectra taken from two similar mid-resolution echelle spectrographs. Tables 3.3–3.7 report the observations highlighting the instrument, date of observation, exposure time, and signal-to-noise ratio (SNR). The SNR was calculated per pixel from the continuum normalised spectra, the median signal around the line of interest was divided by the median absolute deviation (multiplied by 1.48 to give the standard deviation).

HRS/SALT

Spectroscopic observations of the white dwarfs were taken with the High Resolution Spectrograph (HRS) mounted on The Southern African Large Telescope (SALT) at the Sutherland Observatory in South Africa. Observations spanned across 7 semesters from Semester 2017/1 to 2020/2 covering 3.5 years. The HRS (Barnes et al., 2008) is a dual-beam (370–550 nm & 550–890 nm) fiber fed, echelle spectrograph. The LR mode was used to yield a resolution of $\sim$14,000. This was a queue based programme with both high priority time, where up to 3 sets of spectra were taken consecutively for each white dwarf to obtain high SNR data, and low priority time, where one spectrum was obtained as a filler between other programmes or during poor weather. Therefore, for each observing night, the exposure times and SNR varied. The data were reduced by the MIDAS pipeline which produced flat fielded, wavelength calibrated and merged spectra (Kniazev et al., 2016; Kniazev et al., 2017). There is little overlap between the orders so no spectral lines fall into multiple orders. For the observations where multiple consecutive spectra were obtained, they were normalised individually and stacked weighted by their inverse variance.

MIKE/Magellan

Spectra were taken between 2007–2011 on the MIKE spectrograph at the Magellan Clay Telescope at the Las Campanas Observatory in Chile (Bernstein et al., 2003) (PI: Debes). The MIKE spectrograph is a double echelle spectrograph with two arms covering wavelengths of 3350–5000 Å (blue) and 4900–9500 Å (red). The data were obtained under varying atmospheric conditions but almost always using the 0.7" x 5" slit. This gave a spectral resolution of $\sim$ 35,000 for the red arm and 46,000 for the blue arm. The spectra were binned at 2 x 2 and had a slow readout speed. The data were reduced using the CarPy suite of MIKE reduction tools to produce calibrate spectra.

Table 3.3 WD 0106−328 observation details. SNR determined from the continuum around the Mg II line at 4481.125 Å as defined in Section 3.1.2.

Instrument	Date	Exp Time (s)	SNR
MIKE	2007-10-25	1800	42.3
MIKE	2007-10-26	2400	12.8
MIKE	2008-08-20	1800	49.9
MIKE	2008-08-21	1800	53.0
MIKE	2008-08-22	1800	45.8
MIKE	2009-10-15	3600	39.7
SALT	2019-06-08	1800	9.5
SALT	2019-09-06	1800	21.5
SALT	2020-07-29	1450	22.0
SALT	2020-08-07	2900	12.6
SALT	2020-09-17	2900	22.9
SALT	2020-10-24	2900	36.4

Table 3.4 WD 0408−041 observation details. SNR determined from the continuum around the Mg II line at 4481.125 Å as defined in Section 3.1.2.

Instrument	Date	Exp Time (s)	SNR
MIKE	2007-10-25	3600	51.6
MIKE	2007-10-26	3600	35.9
MIKE	2008-08-21	4800	61.0
MIKE	2008-08-22	3600	57.2
MIKE	2008-08-23	3600	59.5
MIKE	2009-10-14	4800	67.2
SALT	2018-11-28	1800	8.5
SALT	2019-08-04	1800	14.2
SALT	2019-11-17	2900	23.5
SALT	2019-11-23	2900	17.3
SALT	2019-11-24	2900	24.2
SALT	2019-12-16	2900	23.2
SALT	2020-01-15	2900	10.7
SALT	2020-09-17	2900	17.9
SALT	2020-11-20	2900	17.4
SALT	2020-12-14	2900	9.1

Table 3.5 WD 1457−086 observation details. SNR determined from the continuum around the Mg II line at 4481.125 Å as defined in Section 3.1.2.

Instrument	Date	Exp Time (s)	SNR
MIKE	2008-03-21	3600	70.1
MIKE	2008-03-22	3600	69.9
MIKE	2009-05-18	3600	61.8
MIKE	2010-06-17	3600	46.9
MIKE	2010-07-07	3600	13.5
MIKE	2010-08-03	3580	48.1
SALT	2018-06-05	2850	17.4
SALT	2020-05-31	3140	15.0
SALT	2020-06-15	3140	21.1
SALT	2021-04-02	3140	11.3
SALT	2021-04-10	3140	19.2
SALT	2021-04-14	1800	13.6

Table 3.6 WD 1929+011 observation details. SNR determined from the continuum around the Mg II line at 4481.125 Å as defined in Section 3.1.2.

Instrument	Date	Exp Time (s)	SNR
MIKE	2010-06-16	2687	21.2
MIKE	2010-06-17	1200	50.9
MIKE	2010-07-08	900	63.2
MIKE	2010-08-02	1800	77.4
MIKE	2010-08-03	1200	49.5
MIKE	2011-06-09	2400	64.9
SALT	2017-07-06	2700	18.4
SALT	2017-07-11	2700	17.8
SALT	2017-07-22	2700	39.4
SALT	2017-07-30	2700	25.7
SALT	2017-08-02	1800	41.9
SALT	2017-08-09	2700	43.4
SALT	2017-08-13	2700	19.9
SALT	2017-08-23	2700	44.8
SALT	2017-09-26	1800	39.3
SALT	2018-06-05	900	17.2
SALT	2018-06-11	900	18.0
SALT	2019-08-20	2900	34.3
SALT	2020-05-15	2400	44.1
SALT	2020-05-24	2400	38.2
SALT	2020-05-31	2400	36.4
SALT	2020-06-20	1200	31.3
SALT	2020-07-19	1200	26.8
SALT	2020-07-24	1200	30.6
SALT	2020-07-27	2400	28.2
SALT	2020-07-30	1200	32.0
SALT	2020-08-24	2400	57.5
SALT	2021-04-12	2400	28.9
SALT	2021-04-14	2400	26.6
SALT	2021-04-20	2400	21.7

Table 3.7 G29-38 observation details. SNR determined from the continuum around the Mg II line at 4481.125 Å as defined in Section 3.1.2.

Instrument	Date	Exp Time (s)	SNR
MIKE	2007-10-25	600	71.9
MIKE	2007-10-26	600	59.2
MIKE	2007-10-27	600	49.5
MIKE	2008-08-20	900	110.8
MIKE	2008-08-21	1800	98.8
MIKE	2008-08-22	900	100.1
MIKE	2008-08-23	1200	96.7
MIKE	2009-05-18	1500	77.3
MIKE	2009-05-20	1600	65.3
MIKE	2009-10-14	2389	4.4
MIKE	2009-10-15	2400	91.2
MIKE	2010-06-16	1225	35.1
MIKE	2010-06-17	400	50.9
MIKE	2010-08-02	1200	101.0
MIKE	2011-06-09	3600	129.4
SALT	2017-07-05	1800	55.8
SALT	2017-07-29	1800	49.5
SALT	2017-08-02	1800	77.8
SALT	2017-08-05	1800	69.5
SALT	2017-09-02	1800	62.6
SALT	2017-09-10	1800	81.9
SALT	2017-09-17	1800	45.2
SALT	2017-09-23	1800	46.2
SALT	2019-11-15	2400	56.5
SALT	2019-11-23	2400	60.0
SALT	2019-11-24	2400	72.6
SALT	2019-11-25	2400	49.4
SALT	2020-06-24	2400	47.5
SALT	2020-08-21	2400	87.1
SALT	2020-08-23	1200	34.9
SALT	2020-09-07	2400	67.6
SALT	2020-11-02	2400	83.9
SALT	2020-11-13	2400	84.6

3.2 Variability Analysis

Equivalent widths are most often used to quantify the strengths of spectral lines, this is a measure of the area of the spectral line relative to the continuum level. Therefore, accurate and precise continuum normalisation is critical. The continuum around the spectral line of interest was fitted using an iterative sigma clipping process where a low order polynomial (order 2–4) was fitted to the continuum around each line. Experiments with higher order polynomials tended to over-fit the continuum and include the wings of the lines, therefore, subsequent equivalent width measurements were systematically lower. To test the sensitivity of the equivalent width to the normalisation, the equivalent width was calculated whilst varying the parameters for the continuum normalisation. The order of the polynomial was varied between 2–4 and the wavelength range between 5–20 Å either side of the line of interest. From these experiments, the maximum variation in equivalent width was found to be 6%.

Voigt profiles are a convolution of the Gaussian and Lorentzian profiles and show the combined effect of both the Doppler broadening and pressure broadening of spectral lines in white dwarfs. Consequently, Voigt profiles are a good model to fit the shapes of spectral lines (Armstrong, 1967). A Markov Chain Monte Carlo (MCMC) approach was implemented to explore the range of Voigt profiles which fit the fluxes and associated errors for each spectral line; this better quantifies the uncertainties. A five parameter Voigt profile was used, allowing the continuum level to also be a free parameter. The Voigt profile doesn't have a defined equation but is related to the real part of the Faddeeva function, $w(z)$, with $z = \frac{x+iy}{\sigma\sqrt{2}}$:

$$V = \frac{\mathrm{Re}[w(z)]}{\sigma\sqrt{2\pi}} \tag{3.1}$$

$$V = O + A\frac{\mathrm{Re}[w(x - x_0 + 1j\gamma)]}{\sigma\sqrt{2\pi}} \tag{3.2}$$

where σ is the standard deviation of the Gaussian profile, γ is the half-width at half-maximum of the Lorentzian profile, x_0 is the wavelength value marking the center of the line, A is the amplitude, and O is the flux offset. The python package SCIPY[1] was implemented to find the optimal Voigt profile parameters for a particular spectral line in a data set, these parameters were used as an input for the MCMC. The EMCEE[2] python package was used to implement the MCMC sampling. 10 walkers were used to sample the posterior distributions of the parameters with 22,000 iterations each; 2,000 iterations were run and discarded for

[1]https://scipy.org
[2]https://emcee.readthedocs.io/en/stable

the burn-in phase. The chains were thinned by approximately the auto-correlation time, the number of iterations required for the walkers to 'forget' their initial position, to ensure the parameters in the chain were independent. For each set of Voigt model parameters in the chain (O, A, x_0, σ, γ), the equivalent width was evaluated. The Voigt profile was integrated with bounds of ± 3 times the full-width at half-maximum of the Voigt model, and divided by the continuum to give the equivalent width for that set of parameters. From this chain, the median value of the equivalent width is calculated and the errors are quoted using the 16th and 84th percentiles. These errors were combined in quadrature with the 6% continuum normalisation error.

The MIKE/Magellan spectra have significant overlap between consecutive orders and often the spectral lines fall on multiple orders. For the spectral lines where this occurred, the data were normalised individually and then were stacked weighted by their inverse variance. However, the sensitivity of the detector can drop off steeply towards the edges of the orders. For WD 1929+011, the Mg II 4481.125 Å line overlapped between two orders, one line was in the centre of its order and the other on the edge of the consecutive order. The equivalent widths were calculated separately to ensure that the line close to the order edge did not bias the results. The discrepancies between the equivalent widths derived from the two orders were up to 30%. Therefore, spectral lines which were within ~ 5 Å from the order edge or fell on the steepest parts of the sensitivity curve were not used for the final equivalent width measurements.

When comparing data obtained from different spectrographs, variations in the spectral resolution can significantly bias the results (Debes & López-Morales, 2008). Before the equivalent width was determined, the MIKE/Magellan spectra were linearly interpolated to match the wavelengths of the HRS/SALT data to reduce this bias.

3.3 Results

This work reports spectroscopic monitoring campaigns of five DAZ white dwarfs to determine whether the mass of material in their photosphere changes over time. 6–15 data sets were obtained between 2007 and 2011 using MIKE/Magellan, and 6–24 data sets were taken with HRS/SALT between 2017 and 2021. For the warm DAZ white dwarfs the Mg II doublet at 4481.125 Å is most often the strongest metal line; Figures 3.1–3.5 show the evolution of the Mg II spectral line across the data sets for each white dwarf. G29-38 is the coolest white dwarf in the sample, and its strongest metal line is instead the Ca II K line at 3933.663 Å, Figure 3.6 shows this line for all observations taken in the MIKE data-set. It should be noted that the HRS/SALT is not sensitive around the 3933.663 Å line.

This section reports the results from the MCMC analysis to robustly determine the equivalent width of the spectral lines over time. For the strongest line/s, an equivalent width can be obtained from each data set, therefore probing timescales from days–years. For the weaker lines, all spectra obtained with one spectrograph were stacked together to obtain one high SNR spectrum. This resulted in one measure of equivalent width for the MIKE/Magellan data set and one measure for HRS/SALT, probing an equivalent width change over timescales of ~ 10 years. Results for each white dwarf are reported separately.

3.3.1 WD 1929+011

WD 1929+011 is a heavily polluted white dwarf with strong lines from numerous elements (Mg, Ca, Si, Fe, O) in the optical range. From Figure 3.4, the shape and depth of the Mg II doublet appears consistent between the spectra. The lack of variation in the Mg II line is quantified in the top panel of Figure 3.7. The equivalent width measurements are all consistent within 1 σ. A horizontal line model was fitted to the data points to investigate if the equivalent widths are consistent with no variability using the chi squared statistic (χ^2), and the reduced chi squared statistic ($\widetilde{\chi^2} = \chi^2/N(dof)$, where $N(dof)$ is the number of degrees of freedom). A $\widetilde{\chi^2}$ of 1 implies that a horizontal line model is a good fit to the data, $\widetilde{\chi^2} < 1$ implies the model is over-fitting the data, $\widetilde{\chi^2} > 1$ implies the model is under-fitting the data, and $\widetilde{\chi^2} \gg 1$ implies the model is a poor fit to explain the data. The best fitting equivalent width for the Mg II doublet was 464.0 mÅ with a $\widetilde{\chi^2}$ fit of 0.42. Therefore, the model describing a constant equivalent width over time can explain the data, although appears to be over-fitting the data. The over-fitting is likely a consequence of inflated errors from the normalisation; due to the strength of this absorption line, the true normalisation error is likely $< 6\%$. This analysis was also done for the strongest lines of Ca and Si for WD 1929+011. Figure 3.7 shows that for the Ca and Si lines, the equivalent widths over time are also consistent with a constant equivalent width model. Consequently, the mass and abundance of the material present in the photosphere of WD 1929+011 is constant over time.

The MIKE/Magellan spectra and HRS/SALT spectra were stacked separately to produce two higher SNR spectra separated by ~ 10 years. The MCMC equivalent width analysis was run on the stacked spectra. Table 3.8 compares the output equivalent width values from the Mg II doublet and Table 3.8 reports values from other lines that are well resolved in the stacked spectra. These data are reported graphically in Figure 3.8. Nearly all the lines have statistically the same equivalent widths, with the exception of a few weak Fe lines.

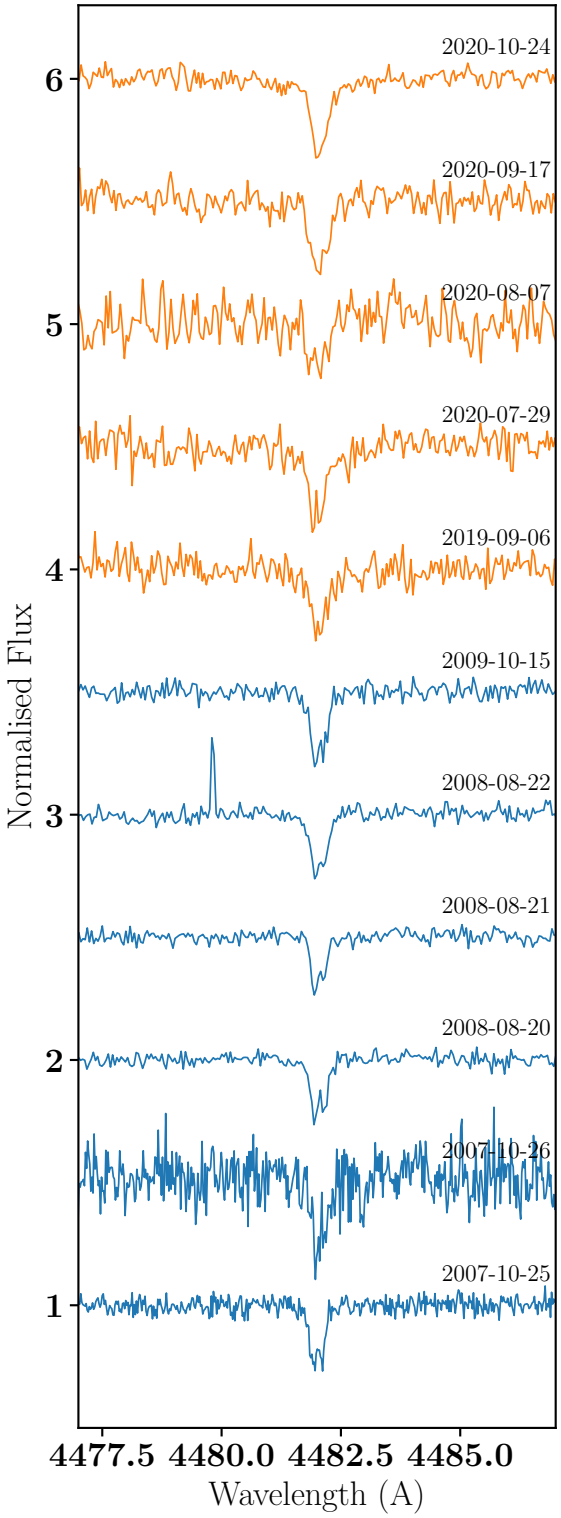

Fig. 3.1 The Mg II 4481.125 Å spectral line from the MIKE/Magellan (blue) and HRS/SALT (orange) spectra spanning more than a decade for WD 0106−328. The spectra have been continuum normalised and are offset by 0.5. Spectra with SNR < 10 are not plotted.

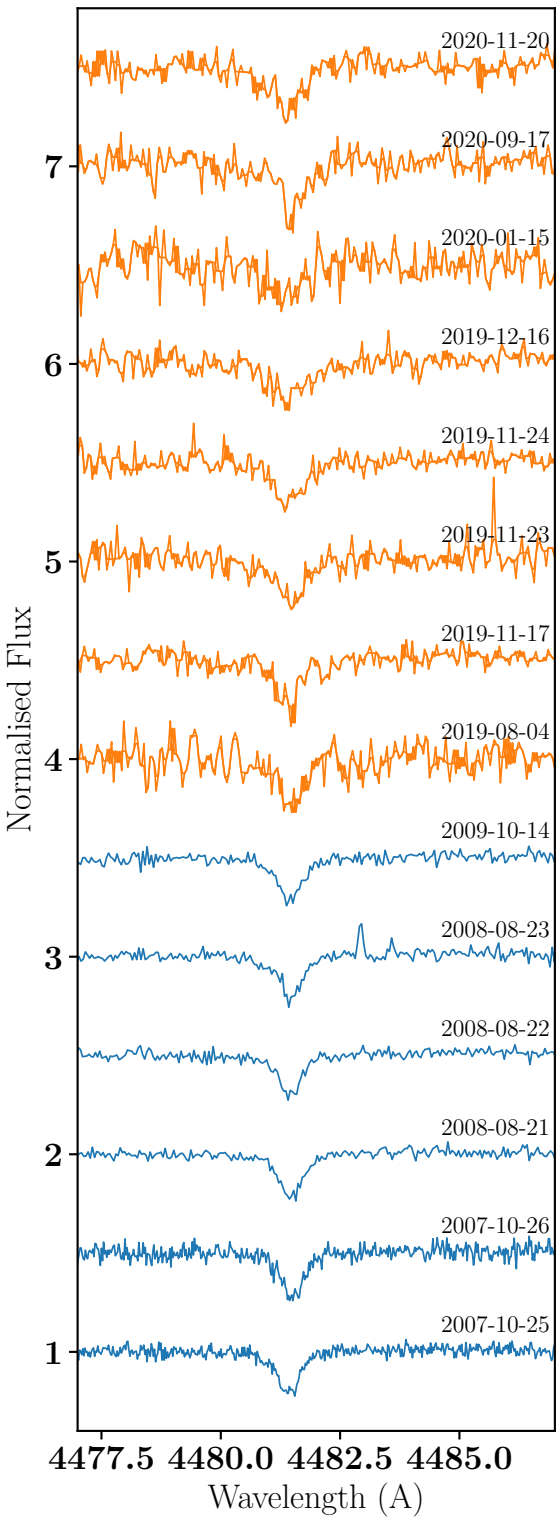

Fig. 3.2 The Mg II 4481.125 Å spectral line from the MIKE/Magellan (blue) and HRS/SALT (orange) spectra spanning more than a decade for WD 0408−041. The spectra have been continuum normalised and are offset by 0.5. Spectra with SNR < 10 are not plotted.

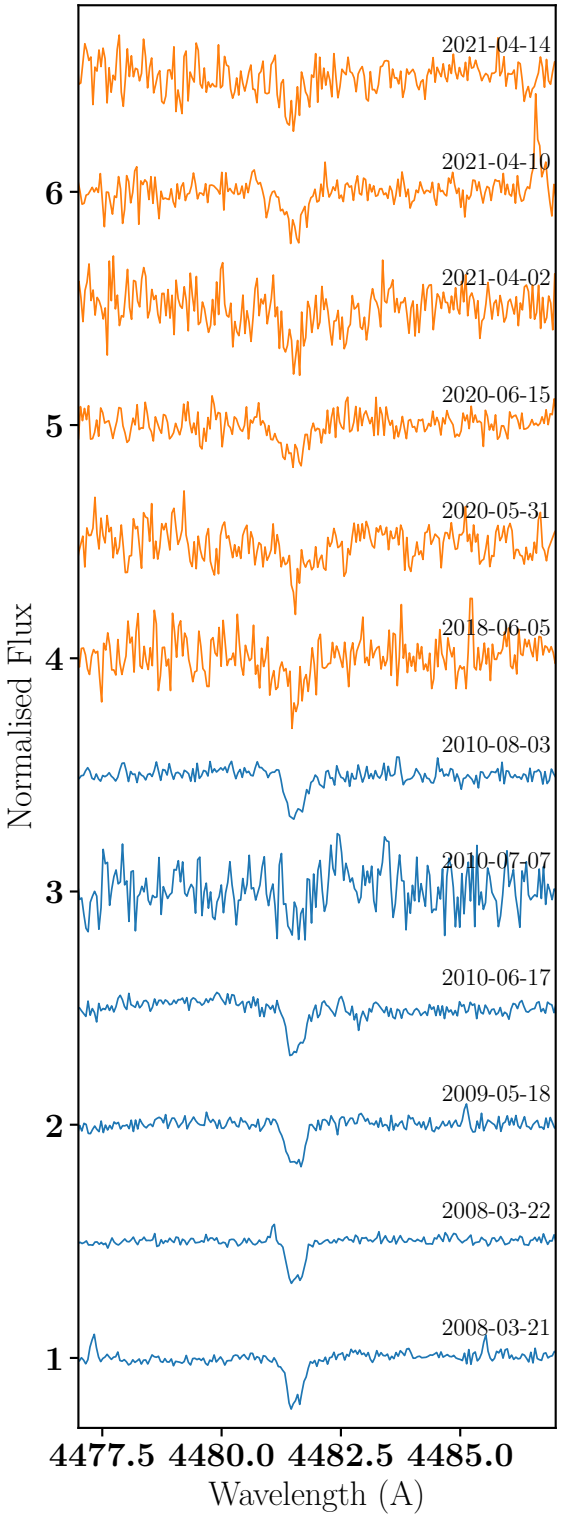

Fig. 3.3 The Mg II 4481.125 Å spectral line from the MIKE/Magellan (blue) and HRS/SALT (orange) spectra spanning more than a decade for WD 1457−086. The spectra have been continuum normalised and are offset by 0.5.

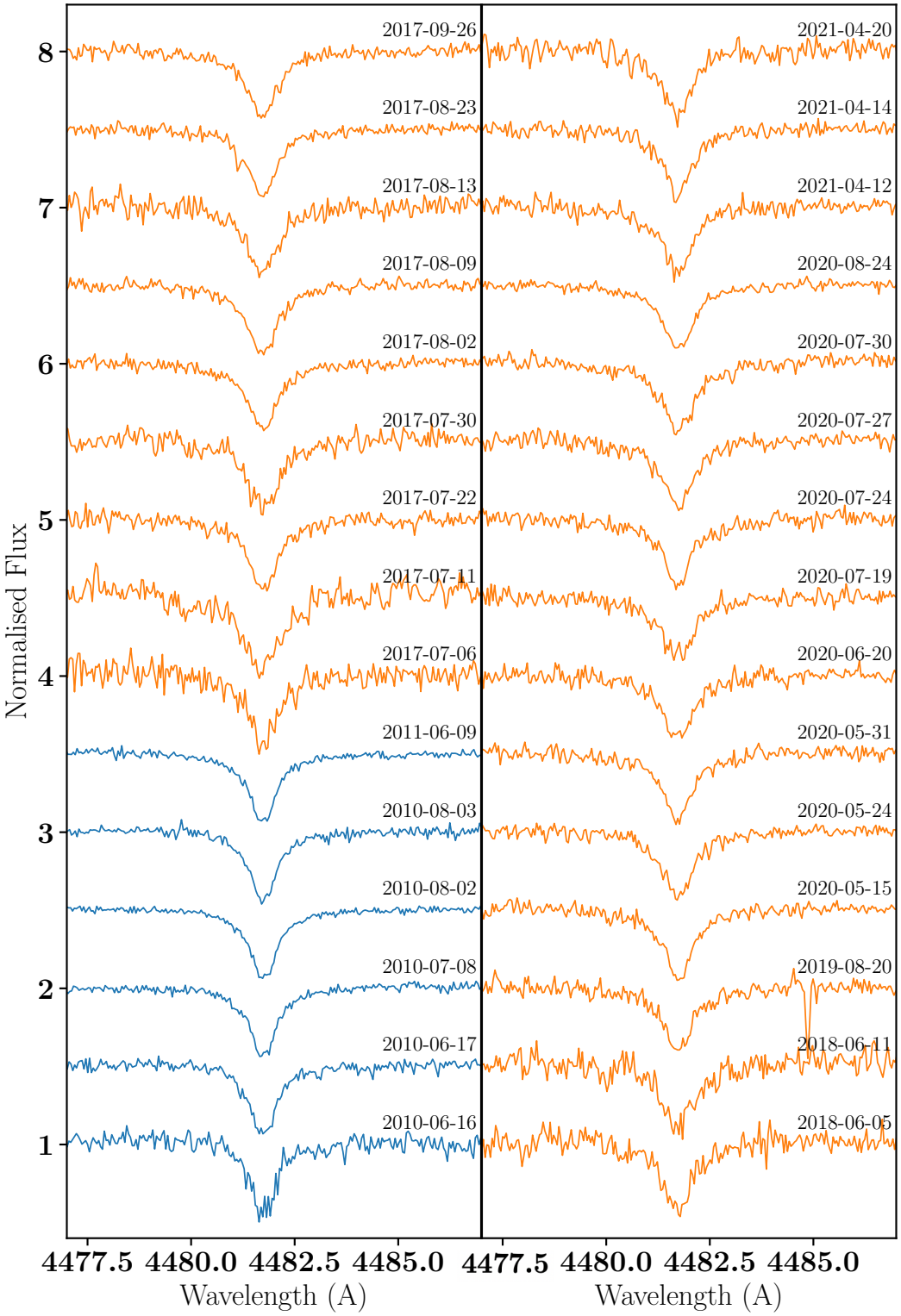

Fig. 3.4 The Mg II 4481.125 Å spectral line from the MIKE/Magellan (blue) and HRS/SALT (orange) spectra spanning more than a decade for WD 1929+011. The spectra have been continuum normalised and are offset by 0.5.

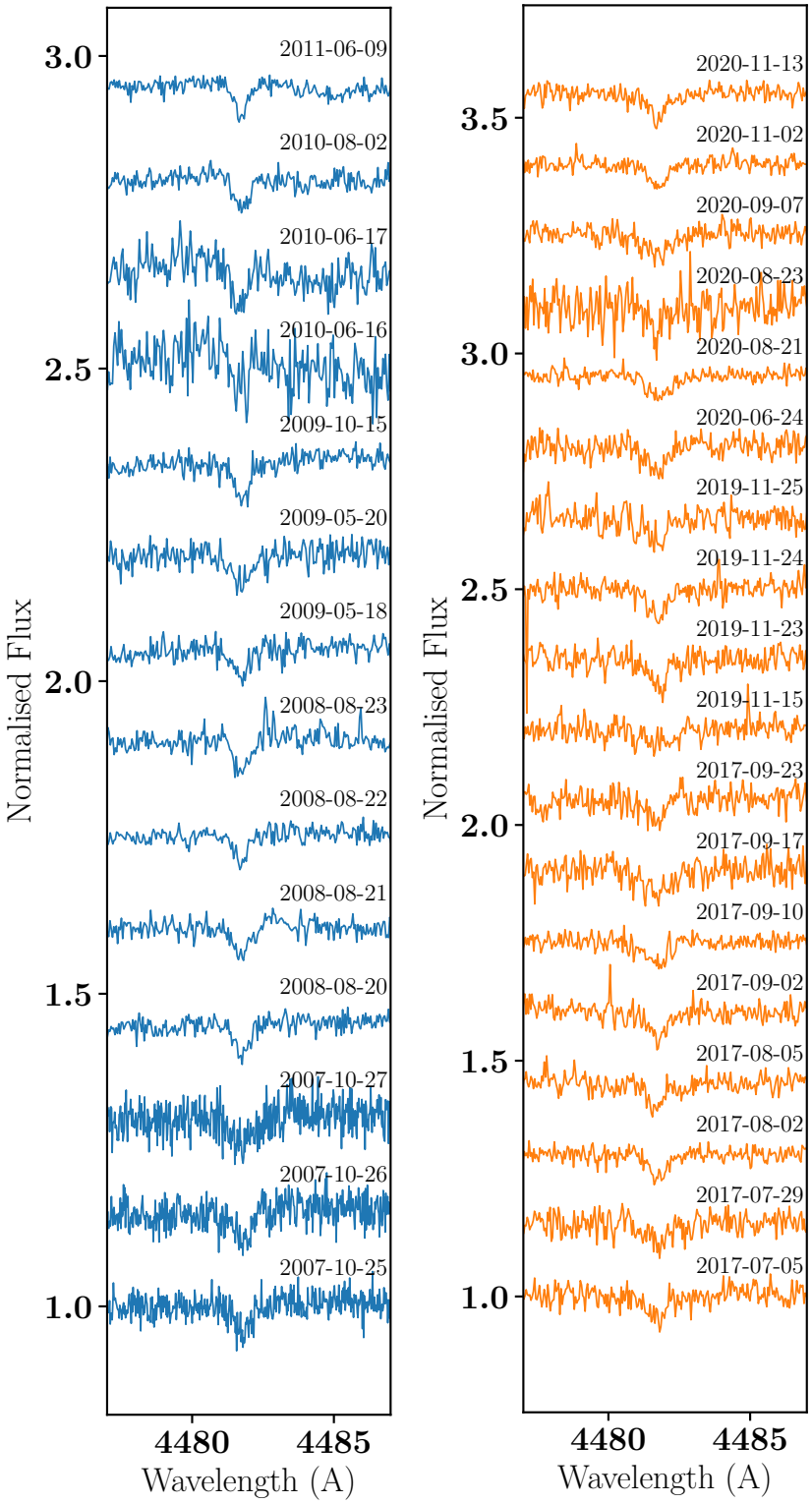

Fig. 3.5 The Mg II 4481.125 Å spectral line from the MIKE/Magellan (blue) and HRS/SALT (orange) spectra spanning more than a decade for G29-38. The spectra have been continuum normalised and are offset by 0.15. Spectra with SNR < 10 are not plotted.

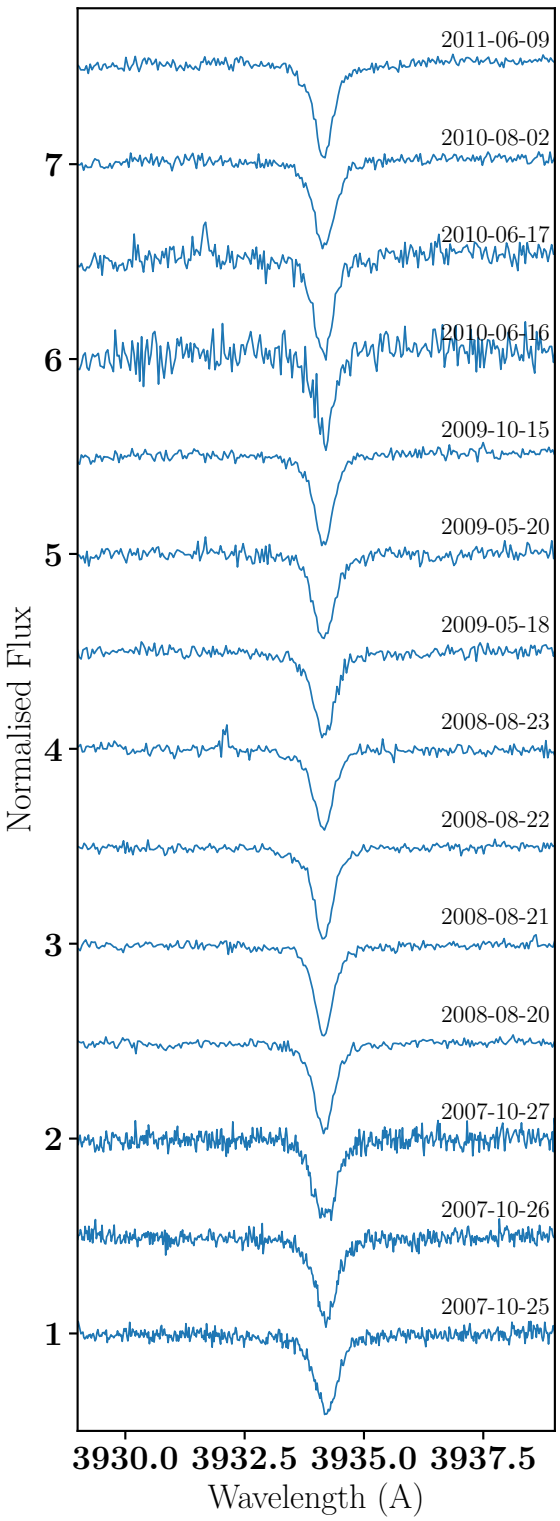

Fig. 3.6 The Ca II 3933 Å spectral line from the MIKE/Magellan (blue) for G29-38. The spectra have been continuum normalised and are offset by 0.5. Spectra with SNR < 10 are not plotted.

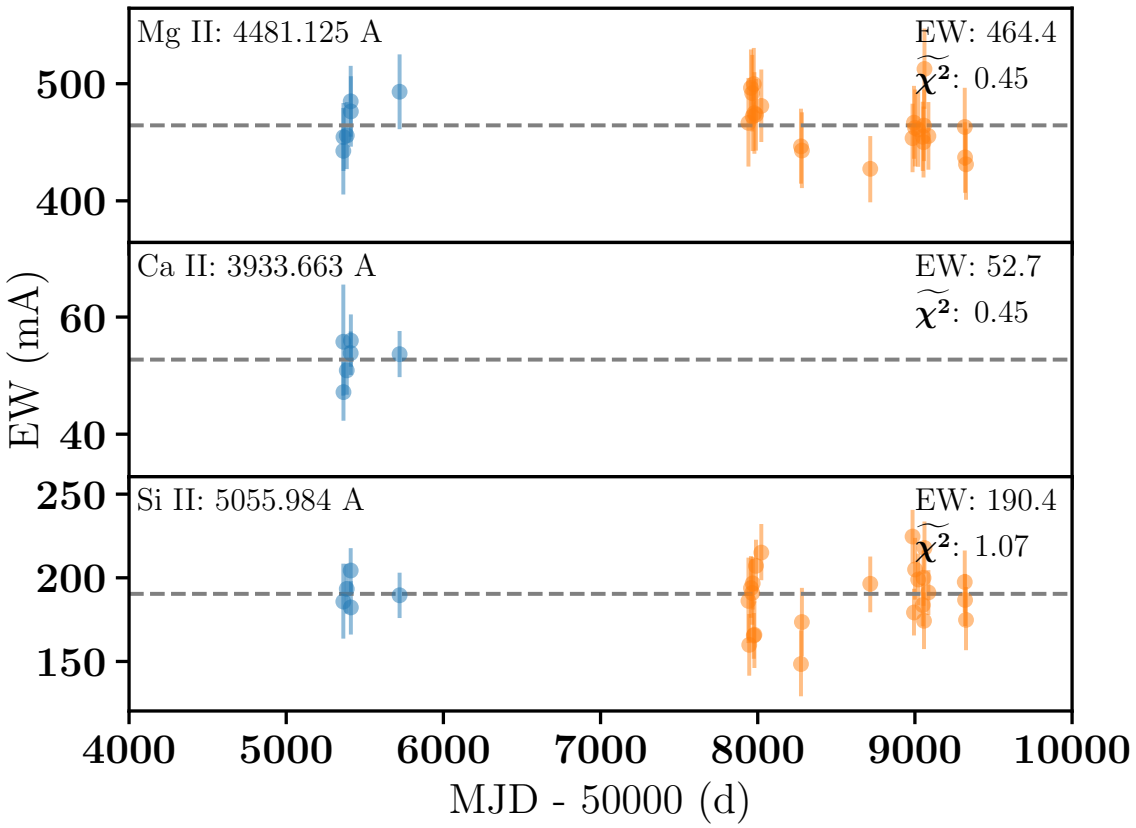

Fig. 3.7 The Mg II (top), Ca II (middle), and Si II (bottom) equivalent width (EW) measurements over time for WD 1929+011. Measurements from MIKE/Magellan are reported as blue data points between 5000–6000 days, and measurements from HRS/SALT are reported as orange data points after 7000 days.

Table 3.8 The median equivalent width (mÅ) and error for the HRS/SALT (S) data and the MIKE/Magellan (M) data obtained from the stacked spectra for the Mg II doublet at 4481.125 Å.

	WD 0106 (mÅ)	WD 0408 (mÅ)	WD 1457 (mÅ)	WD 1929 (mÅ)	G29-38 (mÅ)
MIKE/Magellan	99.7±6.4	142±8.8	81.0±5.0	455±28	43.3±3.0
HRS/SALT	134±9.1	155±12	86.5±8.8	464±29	39.2±2.0

Table 3.9 The median equivalent width and error for the stacked HRS/SALT (S) data and the MIKE/Magellan (M) data for weaker lines for WD 0106−328, WD 1929+011, and G29-38.

Element	λ_{air}	WD 0106 EW (mÅ)		WD 1929 EW (mÅ)		G29-38 EW (mÅ)	
	Å	M	S	M	S	M	S
Ca I	4226.727	-	-	-	-	18.2±1.3	22.3±2.3
Fe II	4923.927	-	-	16.1±1.35	10.9±1.07		
Fe II	5018.440	16.5±2.6	16.8±3.8	24.6±2	20.7±1.6	-	-
Fe II	5169.033	18±2.2	13±12	30.8±2.1	25.1±1.9	-	-
Si II	5041.024	-	-	111±6.9	106±7	-	-
Si II	5055.984	-	-	198±12	186±12	-	-
Si II	5957.560	-	-	45.2±3.1	44.6±3.5	-	-
Si II	5978.930	-	-	55.5±4.1	43.2±3.0	-	-
Si II	6347.100	-	-	152±9.3	145±9.3	-	-
Si II	6371.360	-	-	106±6.5	108±6.7	-	-
Mg I	5172.683	-	-	-	-	19.3±1.3	18.3±1.4
Mg I	5183.602	-	-	-	-	36.1±2.3	35.2±2.2
Mg II	7877.054	-	-	56.5±4.1	73±5.3	-	-
Mg II	7896.366	-	-	99.8±7.6	129±9.6	-	-
O I	7771.944	-	-	41.2±3.8	41.1±3.4	-	-

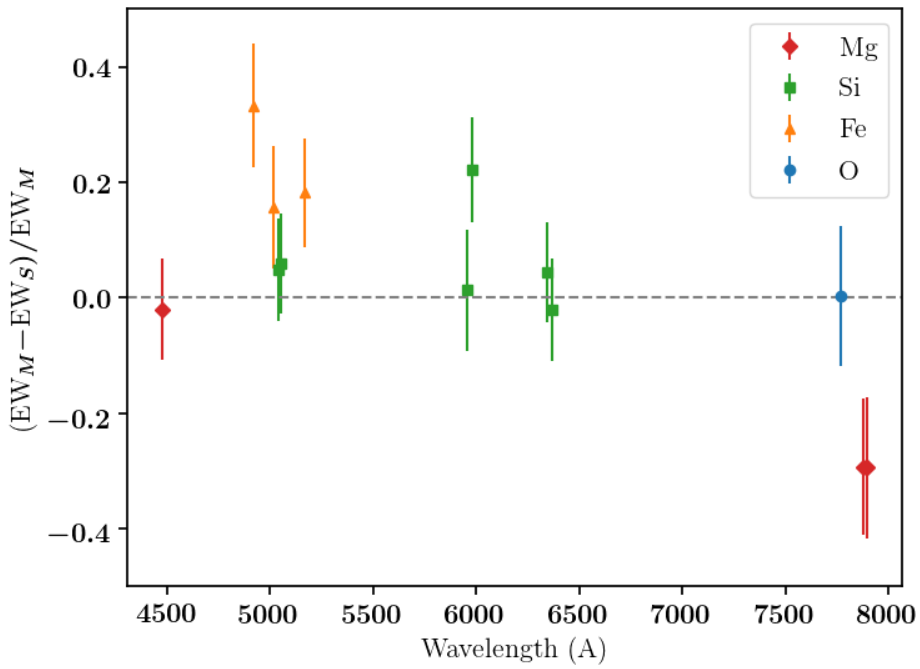

Fig. 3.8 Comparison of the equivalent width (EW) measurements from the MCMC analysis on the MIKE/Magellan (M) and HRS/SALT (S) stacked spectra for WD 1929+011. Markers represent different lines of Mg, Si, Fe and O with their transition wavelength along the x axis.

3.3.2 G29-38

G29-38 is a cooler DAZ white dwarf, with sinking timescales of $\sim$ 80 days (Table 3.2). G29-38 is a ZZ Ceti pulsator and therefore experiences periodic changes in brightness of between 1–3%. These pulsations can result in equivalent widths that are discrepant from the mean equivalent width. Longer integration times ($\gg$ 20 minutes - approximately the maximum pulsation period, Kleinman et al., 1998) average out the effects of the pulsations on the equivalent widths (von Hippel & Thompson, 2007). Therefore, for spectra taken on consecutive days, these are stacked and processed together to obtain a longer total exposure to gain more accurate measure of equivalent width.

For G29-38, the strongest line is the Ca II K line, the evolution of this line from the MIKE/Magellan data is shown in Figure 3.6. No obvious change in the shape or depth of the line is evident. Figure 3.5 shows the evolution of the Mg II doublet over time for both the MIKE/Magellan and HRS/SALT spectra. This line is much weaker than the Ca II K line; it should be noted that each spectrum is offset by 0.15 compared with 0.5 for the Ca II K line, so the high SNR of the spectra (up to $\sim$ 130 for 2011-06-09) means this line can be resolved above the noise in each individual spectrum, although some detections are marginal.

Figure 3.9 shows the equivalent width over time for the 4481.125 Å Mg II doublet, the Ca II K line (3933.663 Å), and the 5183.602 Å Mg I line. The HRS/SALT is not sensitive bluewards of $\sim$ 4000 Å, and therefore only the data from MIKE/Magellan are reported for the Ca II K line. $\widetilde{\chi^2} < 1$, so the constant equivalent width model fits the data here, and again due to the strength of the line, it is likely that the true normalisation error is $< 6\%$, accounting for the apparent over-fitting of the model to the data. For the Mg II and Mg I lines, the $\widetilde{\chi^2}$ is 1.90 and 1.52 respectively. To assess whether these values of $\widetilde{\chi^2}$ imply that the data can not be fit by a constant equivalent width model (the null hypothesis) the critical value of χ^2 ($\chi^2_{\rm crit}$) is used. Given a probability level, if $\widetilde{\chi}^2_{\rm measured} > \widetilde{\chi}^2_{\rm crit}$ then the null hypothesis can be rejected. For a probability of 99.9% ($> 3\sigma$) the $\widetilde{\chi}^2_{\rm crit}$ is 2.19, as the $\widetilde{\chi}^2_{\rm measured}$ values lie below the critical value, there is no evidence to reject the null hypothesis of constant equivalent width over time.

The MCMC equivalent width analysis was run on the stacked MIKE/Magellan spectra and HRS/SALT spectra. Table 3.8 reports the values from the Mg II doublet and Table 3.9 reports values from other lines that are well resolved in the stacked spectra. The derived equivalent width for the Mg II doublet, the Ca I line at 4226.727 Å , the Mg I line at 5172.683 Å , and the Mg I line 5183.602 Å are consistent within 1σ between the MIKE/Magellan and HRS/SALT stacked spectra. Therefore, based on these data, there has been no change in the mass or abundances of the material in the photosphere of G29-38.

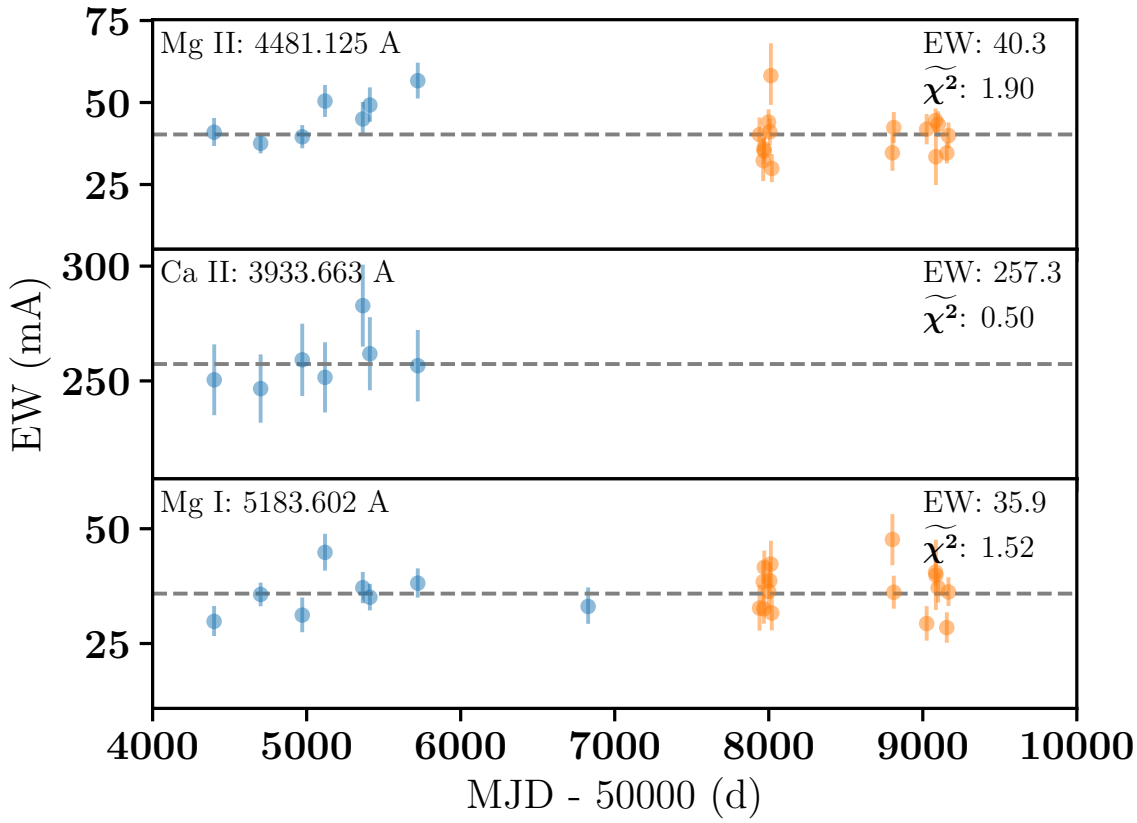

Fig. 3.9 The Mg II doublet (top), Ca II K line (middle), and Mg I line, 5183.602 Å (bottom) changes of equivalent width (EW) over time for G29-38. Measurements from MIKE/Magellan are reported as blue data points between 5000–7000 days, and measurements from HRS/SALT are reported as orange data points after 7000 days.

3.3.3 WD 0106−328

The evolution of the Mg II doublet over time for WD 0106−328 is shown in Figure 3.1. The metal lines are particularly narrow in this white dwarf, and therefore the two Mg lines in the doublet are resolved in the MIKE/Magellan data, and partially resolved in the HRS/SALT data.

The top panel in Figure 3.11 shows the equivalent width of the Mg II doublet over time. There appears to be a significant offset between the equivalent widths measured from the MIKE/Magellan data and those measured from the HRS/SALT data. Indeed the $\widetilde{\chi}^2_{\rm measured}$ value is high at 6.83. The $\widetilde{\chi}^2_{\rm crit}$ value is 3.10, and as the measured value lies above the critical value so the null hypothesis, that there is no equivalent width variability, can be ruled out with 99.9% confidence based on the equivalent width measurements of the Mg II doublet.

This result is also seen when the MCMC equivalent width analysis was run on the stacked MIKE/Magellan spectrum and the stacked HRS/SALT spectrum. A significant ($>3\sigma$) increase in equivalent width of the Mg II doublet is seen between the MIKE/Magellan the HRS/SALT stacked spectra. This is also shown in Figure 3.10.

As mentioned previously, the metal lines for this white dwarf are particularly narrow so obtaining an equivalent width for all spectra for other metal lines is not possible. However, the MIKE/Magellan and HRS/SALT stacked spectra revealed weak lines that can be compared between the two epochs. As reported in Table 3.9, the 5018.440 Å and 5169.033 Å Fe II lines are consistent within 1σ between the MIKE/Magellan and HRS/SALT data. From these weaker Fe lines there is no strong evidence that the equivalent widths have changed over time. In order to distinguish whether accretion rate variability occurred, further high SNR spectra are required.

3.3.4 WD 0408−041

The evolution of the Mg II doublet over time for WD 0408−041 is seen in Figure 3.2. The MIKE/Magellan data has a higher SNR than the HRS/SALT making it difficult to compare the lines by eye.

The middle panel in Figure 3.11 shows the equivalent width of the Mg II doublet over time for WD 0408−041. The variance of the equivalent widths is larger for the HRS/SALT data, likely due to the lower SNR. The $\widetilde{\chi}^2_{\rm measured}$ value is 1.99 and the $\widetilde{\chi}^2_{\rm crit}$ value is 2.74, and as the measured value lies below the critical value, the null hypothesis of no change in equivalent width can not be ruled out.

The MCMC equivalent width analysis was run on the stacked MIKE/Magellan spectrum and the stacked HRS/SALT spectrum. The results are reported in Table 3.8. The derived

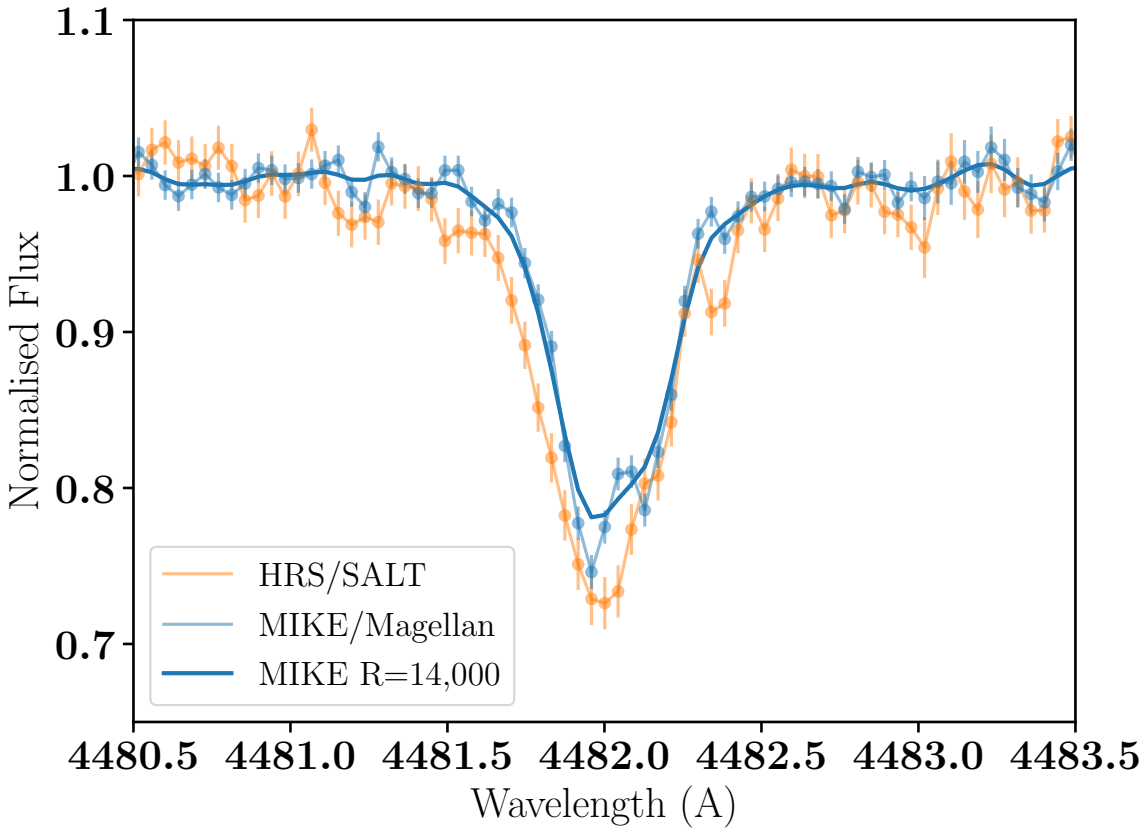

Fig. 3.10 The stacked MIKE/Magellan and SALT/HRS data for the Mg II doublet for WD 0106−328. The darker blue line is the MIKE/Magellan spectra interpolated and convolved to the resolution of HRS/SALT.

equivalent width for the Mg II line from the stacked spectra are consistent within 1σ. Therefore, based on these data, there has been no change in the mass of material in the photosphere of WD 0408−041.

3.3.5 WD 1457−086

Figure 3.3 shows the evolution of the Mg II doublet over time for WD 1457−086. Similar to WD 0408−041, the MIKE/Magellan data has a higher SNR than the HRS/SALT again making it difficult to compare the lines by eye.

The bottom panel of Figure 3.11 shows the output of the MCMC analysis with the equivalent width of the Mg II doublet over time for WD 1457−086. The $\widetilde{\chi}^2_{\rm measured}$ value is 1.49, and for a confidence level of 99.9%, the $\widetilde{\chi}^2_{\rm crit}$ value is 2.96. The measured value lies below the critical value and so the null hypothesis of no equivalent width change can not be ruled out. The equivalent width derived from the stacked data as reported in Table 3.8 show that the Mg II doublet is consistent within 1σ. Therefore, based on these data, there has been no change in the mass of material in the photosphere of WD 1457−086.

3.4 Discussion

The aim of this work was to investigate whether the mass of the pollutants in the photosphere of five warm DAZ white dwarfs changed over time. With such dynamic circumstellar environments, variability in the accretion rates and therefore amount of material in the photosphere, is predicted. For four of the five white dwarfs, no statistically significant variability was observed. For one of the white dwarfs, WD 0106−328, these data were inconclusive.

3.4.1 Discussion of methods

Using optimisation and MCMC methods allows a full exploration of the posterior distribution of the parameters. However, for weaker lines and low SNR data, the MCMC struggled to converge. This meant that low SNR data-sets ($<$10) were omitted from the analysis. Also, for WD 1929+011 one of the sets of data demonstrated extra absorption $\sim$1.5 Å bluewards of the Mg II doublet, see Figure 3.4 date 2017-07-11. This skewed the Voigt profile such that the wings were broad, giving a large equivalent width value. If this is additional Mg absorption, the absorption was at a different radial velocity so is not photospheric. This data set was therefore omitted from the analysis.

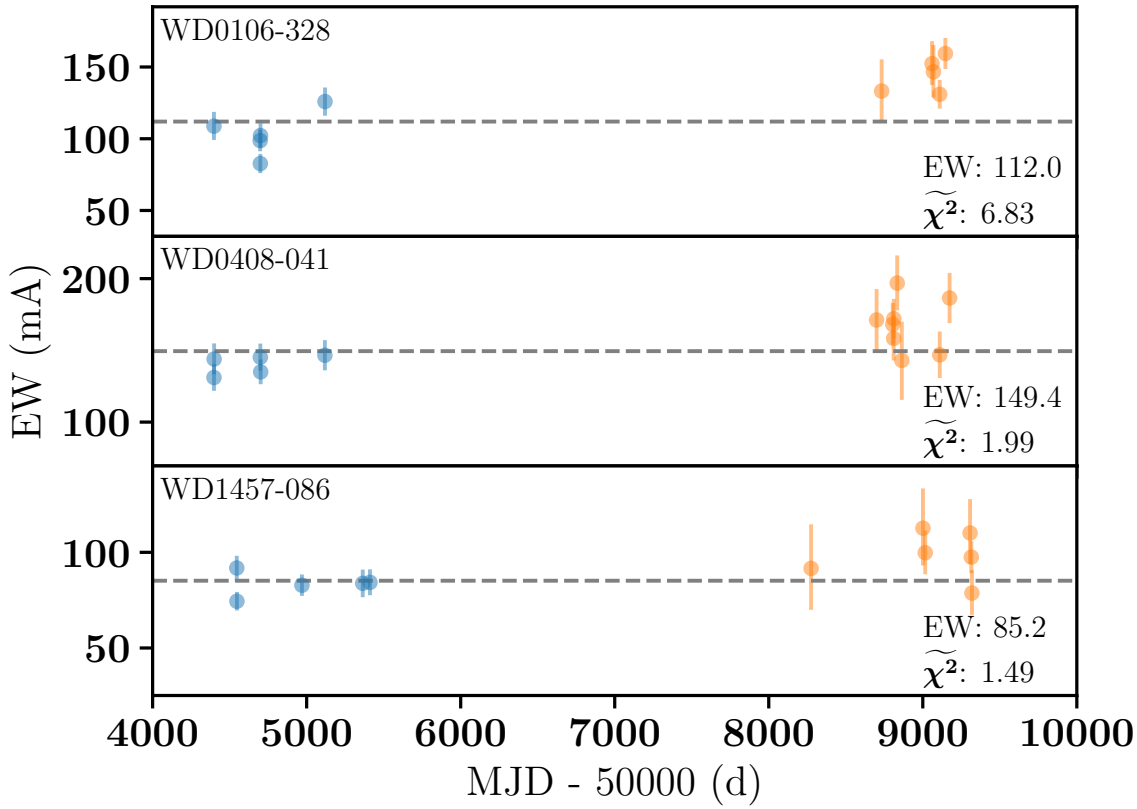

Fig. 3.11 The equivalent width of the Mg II doublet over time for WD 0106−328, WD 0408−041, and WD 1457−086.

The first three sets of data for G29-38 from MIKE/Magellan (2007-10-25, 2007-10-26 and 2007-10-27) are the same as those reported in Debes & López-Morales (2008), allowing a direct comparison between methods to determine equivalent widths. The equivalent widths derived here for these data sets are consistent within 1 σ to those reported in Debes & López-Morales (2008). Slight discrepancies between measurements could be due to differing handling of the continuum normalisation or the equivalent width measurement. Debes & López-Morales (2008) normalised the regions around the spectral lines using high-order polynomials between third and twelfth order. Whereas, this work fitted lower order polynomials using a sigma clipping method, and then allowed the continuum to be a free parameter in the Voigt model. Also, Debes & López-Morales (2008) integrated the line profile from the data, whereas this work modelled the lines with Voigt profile. The fact that the results agree within 1 σ where identical data sets are used is reassuring for this analysis.

This work is only sensitive to equivalent width variations of the order of 10% or larger. Therefore, variability in the equivalent widths at the level of a few percent will be hidden.

3.4.2 G29-38

Searches for equivalent width changes for G29-38 have been studied previously by von Hippel & Thompson (2007) and Debes & López-Morales (2008). von Hippel & Thompson (2007) found evidence for large scale variability with the Ca II K line changing from 165 mÅ to 280 mÅ . Whereas, Debes & López-Morales (2008) found the equivalent widths to be consistent with a median of 264 mÅ and proposed that the variability found previously was likely due to comparing low resolution data (R$\sim$500) with higher resolution data. In this work the best fitting equivalent width across the MIKE/Magellan observations was 257 mÅ for the Ca II K line, with no statistically significant variations found. Therefore, this work corroborates the findings of Debes & López-Morales (2008).

3.4.3 WD 0106−328

For WD 0106−328, there appears to be a significant increase in the equivalent width of the Mg II doublet. The MIKE/Magellan spectrum was interpolated and convolved to the same resolution as HRS/SALT (R$\sim$14,000) to check whether the differing resolutions were impacting the results. As shown in Figure 3.10 there remains a significant difference in line profiles between the HRS/SALT and MIKE/Magellan stacked spectra. However, the Fe II 5018.440 Å line reported in Table 3.9 is not consistent with the same increase in variability. Also, as WD 0106−328 has particularly narrow metal lines, for HRS/SALT the resolution of the spectrograph is close to the line width. This could therefore be affecting the line profiles

Table 3.10 The inferred accretion rates assuming a bulk Earth composition for the best fitting [Mg/H] abundance for the 2020-08-24 data set (−4.25, in italics), and for abundance +0.2, +0.4, −0.2, and −0.4 dex from the measure [Mg/H] value. $M_{\mathrm{acc,\,10\,yrs}}$ reports the mass of material that would accrete over a 10 year baseline. Assuming the abundance in the photosphere changed from [Mg/H] = −4.25, $\Delta M_{\mathrm{acc,\,10\,yrs}}$ reports the change in mass between the new [Mg/H] value and [Mg/H] = −4.25 that would accrue over 10 years, reported as a fraction of the mass of Ceres, a dwarf planet in the asteroid belt, and the fraction of the mass of Comet Halley.

[Mg/H]	$\dot{M}$ (g/s)	$M_{\mathrm{acc,\,10\,yrs}}$ (g)	$\Delta M_{\mathrm{acc,\,10\,yrs}}$	
			M_{Ceres}	$M_{\mathrm{C.Halley}}$
−4.65	6.0×10^{8}	1.9×10^{17}	-3.2×10^{-8}	−1.3
−4.45	9.6×10^{8}	3.0×10^{17}	-1.9×10^{-8}	−0.8
−4.25	*1.5*$\times10^{9}$	*4.8*$\times10^{17}$	*0.0*	*0.0*
−4.05	2.4×10^{9}	7.6×10^{17}	$+3.0\times10^{-8}$	+1.3
−3.85	3.8×10^{9}	1.2×10^{18}	$+7.9\times10^{-8}$	+3.3

and equivalent width measurements with the HRS/SALT. Therefore, this variability analysis is inconclusive, and follow up spectra using MIKE/Magellan would be required to confirm the variability.

3.4.4 Accretion rates

The equivalent width limit can be converted to a limit on the metal abundance of the pollutant, and therefore accretion rate. This was calculated for the strongest line across the five DAZ white dwarfs, the Mg II doublet for WD 1929+011. Figure 3.12(a) shows the best fitting model to the highest SNR spectrum from HRS/SALT for WD 1929+011 (2020-08-24). The best fitting Mg abundance is [Mg/H] = −4.25. Models are plotted every 0.2 dex spreading to +/- 1.0 dex in [Mg/H]. The equivalent widths for these models were added to Figure 3.12(b); this work would have been sensitive to an increase or decrease of 0.2 dex in the abundance of material accreted by the white dwarf. The inferred mass accretion rates are calculated in Table 3.10, assuming magnesium makes up 15.8% of the total mass, as in Bulk Earth. Xu et al. (2019) demonstrated that this was the most reliable and consistent way of measuring and comparing accretion rates. If the accretion rate changed between the sets of MIKE/Magellan and HRS/SALT observations, over a $\sim$ 10 year baseline, this work would be sensitive to changes of mass accretion down to Comet Halley sized objects. Therefore, the mass accretion rate was stable and consequently, there is no evidence for new scattered bodies being accreted by WD 1929+011.

Polluted white dwarf systems are dynamic, with variability observed in the circumstellar material from as short as hours (e.g. Vanderburg et al., 2015) to as long as decades (e.g.

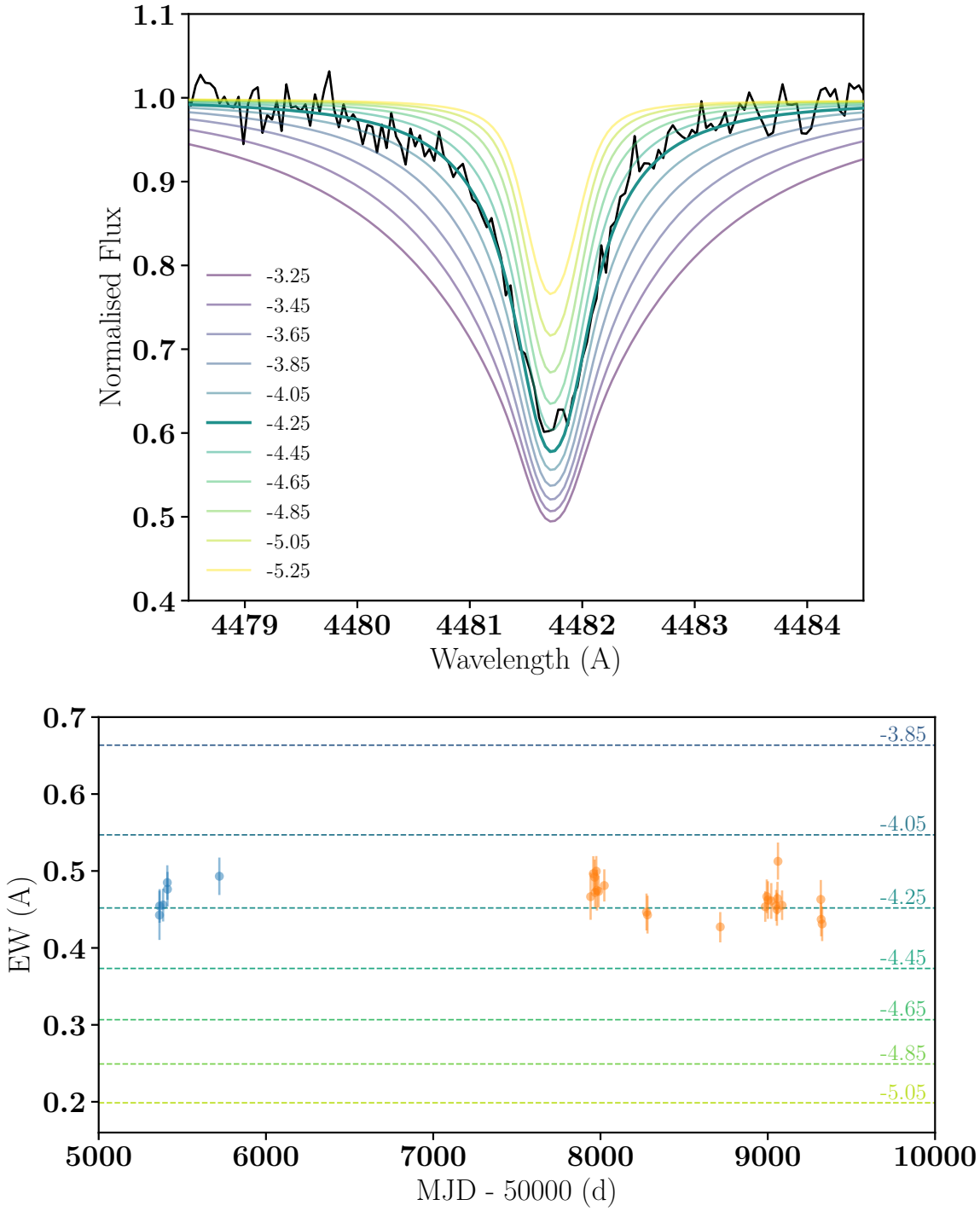

Fig. 3.12 (a) The best fitting model to the 2020-08-24 HRS/SALT spectrum of the Mg-II doublet WD 1929+011. The best fitting Mg abundance is [Mg/H] = −4.25. Models are plotted every 0.2 dex spreading to +/- 1 dex in [Mg/H]. Models kindly provided by P. Dufour (Dufour et al., 2012). (b) The equivalent width of the Mg II doublet over time for WD 1929+011. The equivalent width for each model in (a) is plotted, showing the expected equivalent width values for each [Mg/H] abundance.

Farihi et al., 2018). The dynamic and stochastic nature of these systems predicts for periods of increased accretion onto these white dwarfs. If the accretion is dominated by smaller asteroids scattered often, then the subsequent accretion rates can increase by up to an order of magnitude (Wyatt et al., 2014; Trierweiler et al., 2022), (Trierweiler, private communications). The lack of variability found in this study implies that scattering events that lead to variable accretion occur on timescales longer than decades.

3.4.5 White dwarf models

Theory predicts that the accretion rates are on the order of days for DAZ white dwarfs, but these are based on 1D models. Understanding mixing mechanisms (e.g. convection, diffusion, thermohaline instability) at the surfaces of white dwarfs is crucial to ensure accurate sinking timescales. Cunningham et al. (2019) performed 3D models that included convective instabilities. The onset of convective instabilities occurs at 18,000–18,250 K, white dwarfs cooler than this may therefore be unstable to convection which consequently may increase the diffusion timescales by 1.5–3 orders of magnitude (Cunningham et al., 2019). WD 0106−328, WD 0408−041, and G29-38 lie in this temperature regime and may therefore have longer sinking timescales than those reported in Table 3.2. Figure 3.13 compares the results from Cunningham et al. (2019) for sinking timescales of Ca, Mg, and Fe as a function of white dwarf effective temperature. For WD 0106−328 the sinking timescale increases to 4.0 days for Ca and 6.4 days for Mg (factor 3.5 increase), for WD 0408−041 it increases to 33.3 and 37.6 days for Ca and Mg respectively (factor 8 increase), and G29-38 increases to 658.3 and 549.2 days for Ca and Mg respectively (factor 8 increase). Therefore, especially for G29-38, these observations cover a limited number of sinking timescales, and further follow up spectra would be required to definitively rule out variability. It has been hypothesised that warm DAZ white dwarfs ($>$ 10,500 K) do not spread the metals homogeneously across the surface, therefore predicting surface abundance variations of the metals (Cunningham et al., 2021). The rotation periods of white dwarfs are longer than the spectroscopic exposure times in this work, and therefore, this work should have been sensitive to surface feature changes, providing the abundance variations would be significant enough. Therefore, this may imply that the accretion is spherically homogeneous. Thermohaline instabilities are predicted to affect the amount of material in the photosphere and have been used to explain the orders of magnitude lower accretion rates of DA's than DB's (Bauer & Bildsten, 2019), this can consequently affect the diffusion times. The longer diffusion times predicted from vertical mixing theory would align with the results of no detectable variability, however, the horizontal spreading is at odds with this. Continued efforts in modelling mixing in these

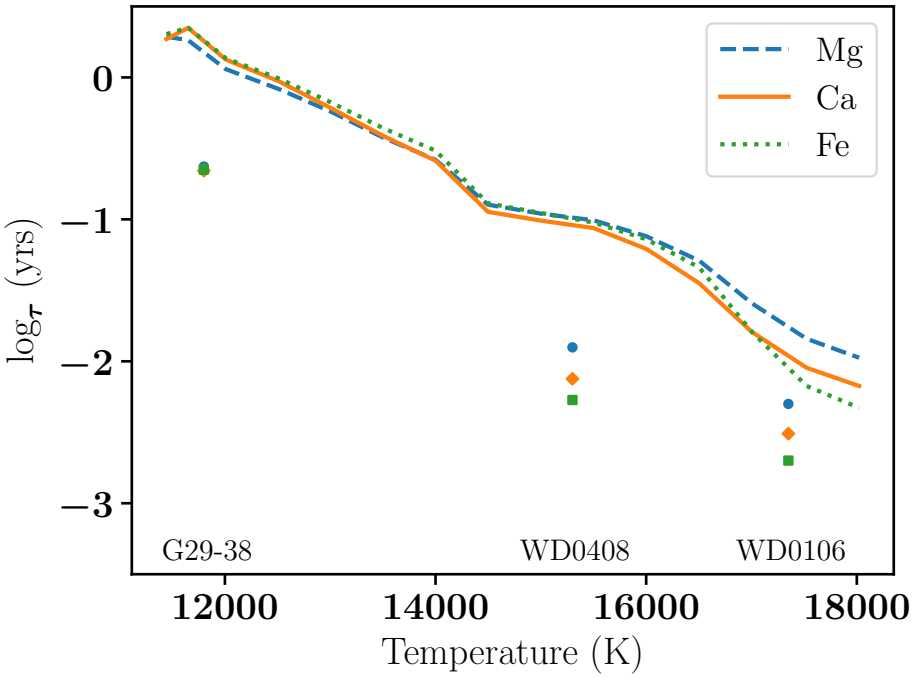

Fig. 3.13 The updated sinking timescales using 3D models including convection. The 1D sinking timescales reported in Table 3.2 are plotted for the three white dwarfs in the temperature regime of interest. Figure adapted from Cunningham et al. (2019) Figure 22.

systems will enable further understanding as to whether variability in the metal abundances in the photospheres are expected.

3.4.6 The link with circumstellar variability

Four of the white dwarfs have confirmed infrared excesses due to circumstellar dust (Table 3.1). All five white dwarfs have Spitzer epoch photometry (Swan et al., 2020), with at least two observations separated by 2000 days. Four of the white dwarfs have near-infrared *K* band data from Rogers et al. (2020) with at least two measurements spanning a baseline of up to three years. The variability analysis of these data is reported in Table 3.11 and shown graphically in Figure 3.14. There is overlap between the optical spectroscopic monitoring campaigns of the metal features and the infrared data.

WD 0106−328, WD 0408−041 and G29-38 show significant mid-infrared variability, whereas WD 1929+011 and WD 1457−086 do not. For WD 1457−086 this is unsurprising as it is suspected that this white dwarf does not have detectable circumstellar dust. WD 1929+011 appears to have no variability either in the circumstellar dust nor the accretion rate. No recent collisional or tidal disruption event has occurred and so the processes driving

Table 3.11 Infrared variability from previous studies. The *K* band data is from Rogers et al. (2020) where the variability measure is an upper limit that corresponds to the measurement limit of the observations. The Spitzer data are from Swan et al. (2020) showing the percentage change and significance of the data.

WD Name	K	Sp Ch1	Sp Ch2
WD 0106−328	<3.9%	9.0% (6σ)	10% (6σ)
WD 0408−041	<1.1%	16% (9σ)	26% (13σ)
WD 1457−086	-	2.0% (1σ)	0.8% (0.5σ)
WD 1929+011	<0.64	1.0% (0.7σ)	2.0% (2σ)
G29-38	<1.0%	12% (7σ)	9.0% (4σ)

the accretion of the circumstellar material are stable. G29-38 is a pulsator and consequently there can be pulsation induced infrared variability. Xu et al. (2018b) predicts the effects of pulsations on the infrared fluxes for different wavebands, these maximum infrared variations are plotted in Figure 3.14 as filled in regions. Therefore, the infrared variability cannot be unambiguously associated with the dust for G29-38. For WD 0106−328, this work studying variability in the equivalent width is inconclusive. However, the mid-infrared flux is significantly decreasing across the $\sim$ 10 year baseline between the MIKE/Magellan and HRS/SALT observations. If the increase in equivalent width over time for the Mg II line is confirmed, this may provide evidence for the inner disc quickly evaporating and accreting such that there is anti-correlation between the infrared flux, and the accretion rate, as predicted in Xu & Jura (2014). WD 0408−041 shows significant variability in the mid-infrared flux, with increases and decreases in the dust flux between $\sim$4000–8500 days (MJD−50,000) (Farihi et al., 2018). There is no evidence for a change in the equivalent width of the spectral lines from this work, and therefore no evidence for change in accretion rate onto this white dwarf. This implies that either physical processes are acting to stabilise the accretion rate, such as an inner viscous gas disc, or that there is a significant time delay between the delivery time of solids and a change in the accretion onto the white dwarf. If it is the latter then continual follow up spectroscopic monitoring of WD 0408−041 is crucial.

3.5 Conclusions

A spectroscopic monitoring campaign of five DAZ white dwarfs using two medium resolution spectrographs has been conducted. Each white dwarf was observed over a total baseline of $>$10 years with between 12–30 data sets obtained, covering timescales of days, months, and years. This samples between 50–2000 sinking timescales depending on the properties of the white dwarfs, or 6–1500 sinking timescales if considering updated sinking timescales from

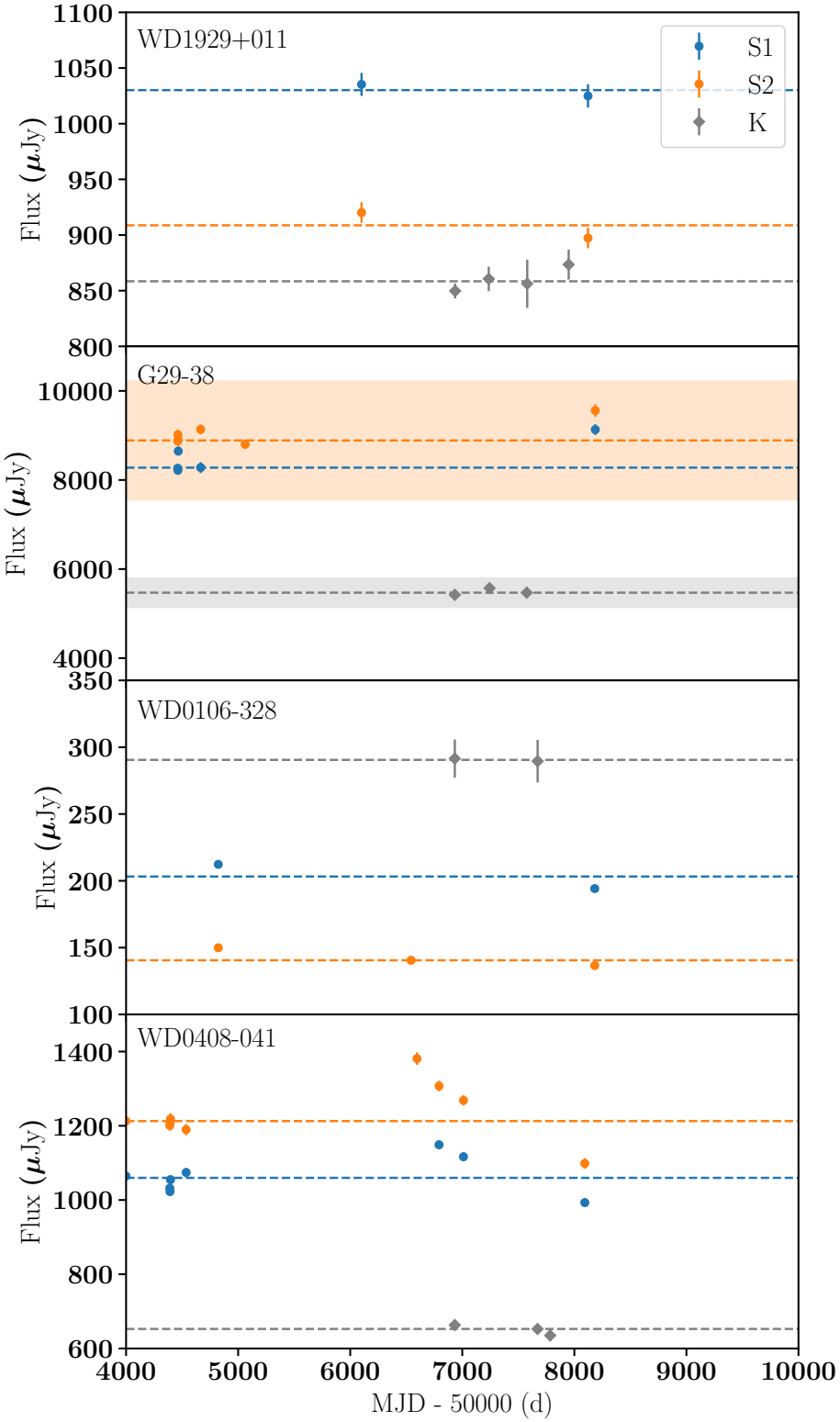

Fig. 3.14 The infrared fluxes of the white dwarfs with confirmed dust emission over time. S1 and S2 are the Spitzer channels 1 and 2 with data from Swan et al. (2020) (private communications). The *K* band data are from Rogers et al. (2020), as reported in Chapter 2. The horizontal dashed lines are the median values for each photometric band.

Cunningham et al. (2019). Therefore, if there was a change in accretion rate or abundance of the metals in the photosphere, it should have been detected above a particular level.

The equivalent widths of the spectral features were calculated across the sample. For four of the five white dwarfs in this sample, no statistically significant variation in the equivalent widths were observed. For one of the white dwarfs, WD 0106−328, these data were inconclusive. This was inconclusive as only one metal line could be resolved in each spectrum, and as the lines are particularly narrow in this white dwarf, of the order of the resolution of the HRS/SALT, comparisons between the data from the two spectrographs is difficult. Follow-up observations with MIKE/Magellan will help to confirm this variability.

No unambiguous variability in the equivalent widths of the spectral lines has been found. This may imply that the underlying source of the accretion is surprisingly steady. This has implications for models of the inner regions of the circumstellar environments as it may imply the need of a viscous gas accretion disc to regulate the accretion rate. Pollution is expected to be as a result of the scattering of small bodies, this work predicts that these scattering events must be less frequent than every 10 years. On the contrary, lack of variability could imply that the sinking timescales in the white dwarfs are orders of magnitude longer than the current models predict. These models are only just beginning to explore sinking timescales using 3D atmosphere models and mixing mechanisms, therefore, unknown mixing mechanisms may therefore increase the sinking timescales.

It should be noted that this work cannot rule out variability completely, as variability below that which can be detected with this programme is likely. This work shows that studying the metal lines with similar spectrographs allows for reduced systematic uncertainties such that smaller equivalent width changes can be probed. Therefore, further spectroscopic monitoring should be done with similar medium resolution spectrographs.

Chapter 4

Tracing the composition of exoplanetary building blocks

Observations of planetary material *polluting* the atmospheres of white dwarfs provide a unique means to probe the bulk composition of exoplanetary material. Less than one percent of polluted white dwarfs host both observable circumstellar dust and gas discs; it is unknown whether these systems represent an early phase in the disruption and accretion of planetary bodies, or if they are accreting larger planetary bodies. This work presents medium- and high-resolution optical spectroscopy of seven such white dwarfs to reveal the chemical composition and history of the accreted exoplanetary material. The white dwarfs are accreting planetary bodies with a wide range of volatile contents; two show evidence of accreting oxygen-rich material, potentially from water-rich bodies, whilst others are accreting dry, rocky material similar to asteroids in the solar system. The accretion of highly refractory material, similar to CAIs, would explain both the high Ca/Mg in the planetary material accreted by Gaia J0347+1624 and the high blackbody temperature of its circumstellar dust. Based on the limited spectral lines, there is an indication that up to three of the white dwarfs could be accreting fragments of a core-mantle differentiated body; core-mantle differentiation and disruptive collisions appear commonplace in exoplanetary systems. White dwarfs with circumstellar gas are good targets for studying photospheric abundances as they yield many detectable elements, and there is no substantial evidence for significant differences in the accreted abundance ratios for those polluted white dwarfs with or without circumstellar gas.

This work reports observations of seven white dwarfs with circumstellar dust and gas, where the abundances of the planetesimals that have polluted their atmospheres has been determined, and the population of these extreme systems is compared to the general population of polluted white dwarfs. This chapter is structured as follows. Section 4.1 describes the optical spectra of these seven systems taken with VLT/X-shooter, KECK/HIRES and

Table 4.1 Stellar parameters derived from the spectroscopic (spec) and photometric (phot) fitting methods. Distances (D) are inferred from *Gaia* parallaxes.

WD Name	SpT	Spec T_{eff}	Spec log(g)	Phot T_{eff}	Phot log(g)	D (pc)
Gaia J0006+2858	DAZ	23921 (335)	8.04 (0.04)	22837	7.86	152
Gaia J0347+1624	DAZ	21815 (305)*	8.10 (0.04)*	18854	7.84	141
Gaia J0510+2315	DAZ	21700 (304)*	8.20 (0.04)*	18723	8.05	65
Gaia J0611−6931	DAZ	17749 (248)	8.14 (0.04)	-	-	143
Gaia J0644−0352	DBZA	18350 (422)	8.18 (0.05)	16999	7.98	112
WD 1622+587	DBZA	18850 (434)*	7.80 (0.05)*	20204	7.92	183
Gaia J2100+2122	DAZ	25565 (358)	8.10 (0.04)	21997	7.92	88

Notes:

No available SDSS or Pan-STARRS photometry for Gaia J0611−6931, so no photometric solution was derived.

* Spectroscopic parameters from Melis et al. (2020).

Magellan/MIKE. Section 4.2 describes how the composition of the polluting body is inferred from the optical spectra, with the results reported in Section 4.3. Section 4.4 investigates whether the pollutants of these white dwarfs with detectable gaseous discs represent a special sub-class of objects. Section 4.5 discusses the chemical and geological composition of the pollutant exoplanetary material, and the conclusions are presented in Section 4.6.

4.1 Observations and Data Reduction

4.1.1 Targets

This work targets seven newly identified polluted white dwarfs discovered in Dennihy et al. (2020) and Melis et al. (2020) as listed in Table 4.1. These systems all show evidence of atmospheric pollution, infrared excess from circumstellar dust emission, and observable circumstellar gaseous discs. With >1000 polluted white dwarfs known, but only 21 systems with both detectable circumstellar dust and gas (Gänsicke et al., 2006, 2007, 2008; Melis et al., 2010; Farihi et al., 2012a; Melis et al., 2012; Brinkworth et al., 2012; Debes et al., 2012b; Dennihy et al., 2020; Melis et al., 2020; Gentile Fusillo et al., 2020), this represents a unique sub-sample of polluted white dwarfs.

Table 4.2 Observations of the seven white dwarfs listing dates of observations, exposure times in seconds, and SNR as defined in Section 4.1.2. The SNR for X-shooter UVB, HIRESb and MIKE-blue were calculated from the continuum around the Ca II K line (3933.7Å). The SNR for X-shooter VIS, HIRESr and MIKE-red were calculated from the continuum around 6600Å.

WD Name	X-shooter	Exp UVB	Exp VIS	SNR UVB	SNR VIS	HIRESb	Exp	SNR	HIRESr	Exp	SNR
Gaia J0006+2858	15-08-2019	3400	3458	31	36	07-07-2019	3300	57	16-07-2019	5400	40
Gaia J0347+1624	-	-	-	-	-	05-12-2019	5000	23	-	-	-
Gaia J0510+2315	-	-	-	-	-	05-12-2019	2400	33	09-12-2019	4800	71
Gaia J0611−6931†	15-10-2019	3400	3458	31	38	27-08-2021†	3100	12	27-08-2021†	3100	17
Gaia J0644−0352	15-09-2019	3400	3458	99	48	13-09-2020	1740	58*	09-12-2019	2700	35
	-	-	-	-	-	08-10-2020	3000	58*	-	-	-
WD 1622+587	-	-	-	-	-	10-07-2019	5400	33	16-07-2019	3300	31
Gaia J2100+2122	13-07-2019	3400	3458	134	127	10-07-2019	3600	115*	16-07-2019	3300	73
	-	-	-	-	-	07-07-2019	2700	115*	-	-	-

Notes:

* SNR is reported based on the stacked spectra.

† Gaia J0611−6931 MIKE blue and red data listed under HIRESb and HIRESr respectively.

Table 4.3 Number abundances (log n(Z)/n(H(e)) of the pollutant material using the photometric and spectroscopic white dwarf parameters separately. For the derivation of the upper limits and the analysis of the abundances the spectroscopic solutions are used. Photometric abundances for Gaia J0510+2315 are less reliable and are quoted in brackets.

[X/H(e)]	Spec/Phot	Gaia J0006	Gaia J0347	Gaia J0510	Gaia J0611	Gaia J0644	WD 1622	Gaia J2100
H	-	-	-	-	-	-5.16	$-4.80^{\dagger}$	-
O	Spec	$< -3.92^{*}$	-	-4.23 ± 0.10	-3.67 ± 0.10	-5.19 ± 0.14	$< -5.40^{*}$	$< -4.10^{*}$
"	Phot			(-4.42 ± 0.10)	-	-5.61 ± 0.12		
Na	Spec	< -5.11	-	< -5.44	-	< -5.65	< -6.00	< -5.18
Mg	Spec	-4.95 ± 0.10	-5.78 ± 0.10	-5.23 ± 0.10	-4.59 ± 0.10	-5.75 ± 0.15	-6.25 ± 0.32	-5.08 ± 0.10
"	Phot	-5.03 ± 0.10	-6.05 ± 0.10	(-5.45 ± 0.10)	-	-6.33 ± 0.10	-5.88 ± 0.28	-5.35 ± 0.10
Al	Spec	< -5.56	< -5.18	< -5.75	< -4.48	-6.76 ± 0.10	< -6.40	< -6.28
"	Phot					-7.05 ± 0.10		
Si	Spec	-4.95 ± 0.13	< -5.30	-5.15 ± 0.18	-4.69 ± 0.10	-5.98 ± 0.10	-6.35 ± 0.19	-5.13 ± 0.12
"	Phot	-5.04 ± 0.12		(-5.13 ± 0.20)	-	-6.30 ± 0.19	-6.05 ± 0.17	-5.38 ± 0.13
Ca	Spec	-6.17 ± 0.10	-5.69 ± 0.10	-6.31 ± 0.10	-6.05 ± 0.19	-6.74 ± 0.18	-7.68 ± 0.37	-6.23 ± 0.13
"	Phot	-6.32 ± 0.10	-6.01 ± 0.40	(-7.10 ± 0.10)	-	-7.44 ± 0.18	-7.21 ± 0.38	-6.65 ± 0.10
Ti	Spec	< -6.30	< -6.43	< -5.86	< -5.64	-8.37 ± 0.12	< -8.00	< -6.69
"	Phot					-9.14 ± 0.10		
Cr	Spec	< -5.71	< -5.47	< -4.53	< -3.50	-7.81 ± 0.13	< -6.93	< -5.78
"	Phot					-8.58 ± 0.12		
Fe	Spec	$< -4.66^{*}$	$< -4.38^{*}$	$< -4.10^{*}$	-4.24 ± 0.10	-6.46 ± 0.16	$< -6.53^{*}$	-4.96 ± 0.10
"	Phot				-	-7.09 ± 0.18		-5.50 ± 0.10
Ni	Spec	< -4.99	< -4.67	< -3.77	< -3.00	< -7.21	< -6.03	< -5.11

Notes:

*Denotes gaseous emission present when deriving the upper limit.

†H for WD 1622+587 from Melis et al. (2020)

4.1.2 X-shooter

Four of the white dwarfs were observed with the echelle spectrograph X-shooter (Vernet et al., 2011) on Unit Telescope 2 (UT3, Melipal) of the Very Large Telescope (VLT) at Paranal Observatory, Chile (PI: Xu). X-shooter allows simultaneous observations in the 3 arms: UVB (300–559.5 nm), VIS (559.5–1024 nm) and NIR (1024–2480 nm). The white dwarfs are too faint to have strong signals in the NIR arm, so the NIR data was excluded from this study. The observations were taken between July–October 2019 during runs 0103.C-0431(B) and 0104.C-0107(A). For all observations, stare mode was used, with a 1.0 and 0.9 arcsec slit width for the UVB and VIS arms respectively, this gives an optimal resolution ($\lambda/\Delta\lambda$) of 5400 and 8900. Two exposures were taken lasting 1700 and 1729 s each for the UVB and the VIS band respectively. The data reduction was performed using esoreflex (v 2.11.3) with the X-shooter pipeline version 2.9.1 (Freudling et al., 2013). The standard reduction procedures were followed including minor alterations to optimise the signal to noise ratio (SNR) of the output spectrum, and reduce the number of cosmic ray contaminants. The details of the X-shooter observations are listed in Table 4.2. The SNR was calculated per pixel from the spectra, the median signal around the line of interest was divided by the median absolute deviation (multiplied by 1.48 to give the standard deviation). The SNR at the continuum around the Ca II K ($\sim$ 3993 Å) line was 30–134 for the UVB arm and the SNR at the continuum around 6600Å was 35–127 for the VIS arms depending on the flux of the white dwarf and observing conditions.

4.1.3 HIRES

Six of the white dwarfs were observed with the High Resolution Echelle Spectrometer (HIRES) on the Keck I Telescope, Hawaii (Vogt et al., 1994) (PI: Xu, PI: Klein). This has 2 modes, HIRESb and HIRESr, with a wavelength coverage of approximately 3200–5750 Å and 4700–9000 Å respectively. The C5 decker was used, which has a slit width of 1.148 arcsec and a spectral resolution of 37,000. The observations were taken between July 2019 and October 2020.

Data reduction including bias subtraction, flat fielding, wavelength calibration, and spectral extraction were performed using MAKEE (as in Xu et al., 2016). The final spectra were continuum normalised using low order polynomials and combined using IRAF functions (as in Klein et al., 2010). The details of the HIRES observations are listed in Table 4.2. The SNR was calculated in the same way as for X-shooter (Section 4.1.2) for one observation was 32–89 around the continuum at the Ca K line for HIRESb and 31–73 around the continuum at 6600 Å for HIRESr.

4.1.4 MIKE

Gaia J0611−6931 was observed with the Magellan Inamori Kyocera Echelle (MIKE) spectrograph (Bernstein et al. 2003) on the 6.5 m Magellan Clay Telescope at Las Campanas Observatory on 27 August 2021 with one exposure of 1800 s followed by a second of 1300 s (PI: Weinberger). Observations were taken at airmass 1.5 with the atmospheric dispersion corrector installed, but possibly not correcting the spectrum optimally, which would result in a lower SNR than expected in the blue. The SNR of the continuum was approximately 15 near the Ca infrared triplet, calculated in the same way as reported in Section 4.1.2. The seeing was 0.8 arcsec, and the employed $1''$ slit produces spectral resolution of R $\approx$ 28,000 on the blue side (3500–5060 Å) and 22,000 on the red side (5000–9400 Å). ThAr lamps taken before and after the exposures were used for wavelength calibration. Data reduction with the standard Carnegie Python MIKE pipeline included extraction, flat-fielding, and wavelength calibration using methods described in Kelson et al. (2000); Kelson (2003).

4.2 Modelling Methods

The white dwarf model atmospheres were kindly provided by P. Dufour using models from the Montreal white dwarf group to derive stellar parameters, and measure the abundance of the polluting material (Dufour et al., 2012).

4.2.1 White Dwarf Parameters

Two methods were used to derive the stellar parameters for each white dwarf. The first fitted white dwarf models to broad band photometry (the photometric method), and the second fitted white dwarf models to the pressure broadened hydrogen and helium spectral lines (the spectroscopic method). The derived values for the spectroscopic and photometric methods are reported in Table 4.1. These methods are discussed in more detail below.

For the photometric method, white dwarf models were fitted to SDSS and Pan-STARRS broad band photometry to extract the best-fitting effective temperature and log(g). Parallaxes from Gaia were required to obtain log(g) and the mass of the white dwarf. SDSS to AB corrections were included as outlined in Eisenstein et al. (2006). Reddening becomes important for objects $>$ 100 pc, and five of the white dwarfs fall into this distance range. For these white dwarfs the observational data were de-reddened using the method as described in Genest-Beaulieu & Bergeron (2019) before fitting. When available, a combination of SDSS and Pan-STARRS *ugrizy* were used to constrain the white dwarf parameters[1]. As discussed

[1]Photometry listed on: https://montrealwhitedwarfdatabase.org

in Genest-Beaulieu & Bergeron (2019), this provides the most accurate and consistent results. Otherwise, either the SDSS *ugriz*, or Pan-STARRS *grizy* were used. In the future Gaia DR3 BP/RP spectrophometry can be used to improve the photometric fitting methods.

The spectroscopic method fits white dwarf atmospheric models to the hydrogen and helium absorption lines to extract the best-fitting effective temperature and log(g). For the four white dwarfs with X-shooter data, updated stellar parameters were found and for the three objects without X-shooter data, the parameters derived in Melis et al. (2020) were used. The model fits to the Balmer lines for the three DA white dwarfs (Gaia J0006+2858, Gaia J0611−6931, and Gaia J2100+2122) are shown in Fig. 4.1. For the DBAZ white dwarf, GaiaJ0644−0352, models were fitted to the Helium lines, trace H is also present, and this abundance was also determined in this fit. Metals and hydrogen in cool DBZ stars may affect the pressure/temperature structure and therefore affect the derived white dwarf parameters (Dufour et al., 2012; Coutu et al., 2019). For GaiaJ0644−0352 it was tested whether including metals in the models affected the derived parameters; as this white dwarf is hot ($T_{eff} \sim$ 20,000K), the inclusion of metals had a negligible affect on the derived white dwarf parameters. The best-fitting white dwarf model is shown in Fig. 4.2.

The uncertainties in the spectroscopically derived effective temperature and log(g) for DA white dwarfs are from Genest-Beaulieu & Bergeron (2019), 1.4% in T_{eff} and 0.042 dex in log(g). For the two DBA white dwarfs, the uncertainties derived in (Bergeron et al., 2011) are used, 2.3% in T_{eff} and 0.052 dex in log(g).

To assess the reliability of the stellar parameters, SEDs of the white dwarfs were used to compare the X-shooter spectrum (where available) and the photometry from SDSS and/or Pan-STARRS, with the white dwarf models derived from the photometric method and spectroscopic method (Appendix 2: Fig. 7.1). Additionally, *GALEX* photometry is used to assess the reliability of the white dwarf models. UV wavelengths are sensitive to reddening so the *GALEX* photometry points may lie below the photometric models, few physical explanations exist that could cause the *GALEX* photometric points to lie above the photometric model, so to explain this, a higher temperature white dwarf model would be required. Gaia J0510+2315 and Gaia J2100+2122 have *GALEX* fluxes which lie significantly above the expected flux from the photometric models. It is likely that a hotter model, more consistent with the spectroscopic models, is required for these systems. Neither white dwarf has SDSS 'u' band photometry, reinforcing the idea that in order to obtain accurate photometric parameters, SDSS 'u' is required (Bergeron et al., 2019).

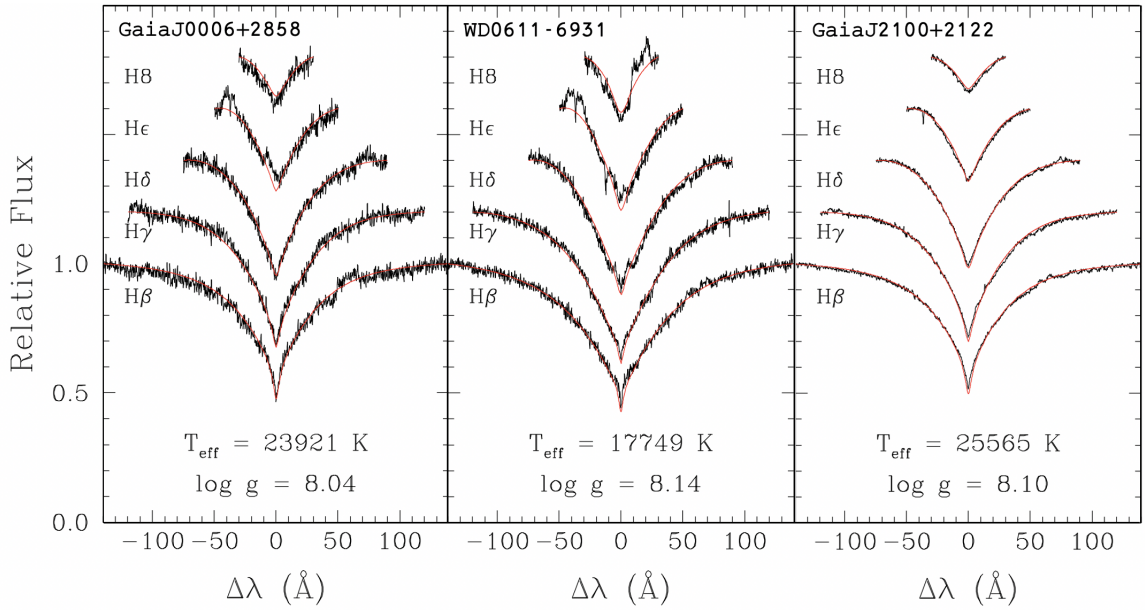

Fig. 4.1 Model fits (red lines) to the Hydrogen Balmer line profiles from the X-shooter spectra for Gaia J0006+2858, Gaia J0611−6931, and Gaia J2100+2122. The best-fitting model parameters are labelled on each panel. Doubled peaked emission lines from the circumstellar gas discs can be seen in the wings of the hydrogen lines.

4.2.2 Line Identification

A multitude of metal lines were identified in the spectra of each white dwarf. Using the IRAF task SPLOT (Tody, 1986) the equivalent width, line centre, and radial velocity of each spectral line was measured. For the equivalent width, a Voigt function was fitted to the profile of the line five times whilst changing the region used for the continuum fitting. From this the average equivalent width and standard deviation for each line was found, this was compared to a direct flux summation to ensure accuracy. The uncertainty on the equivalent width was calculated by combining in quadrature the standard deviation of the equivalent width measurements and the SPLOT fitting error. Appendix 2: Tables 7.1 – 7.7 list the spectral lines identified, the derived equivalent widths, line centres, and radial velocities.

4.2.3 Abundance of planetary material

The abundance of the planetary material that has polluted each white dwarf was measured using white dwarf models kindly provided by P. Dufour following Dufour et al. (2012). The spectra were divided into regions of 5–15 Å around each metal absorption line. The white dwarf effective temperature and log(g) was inputted, and the best-fitting abundance

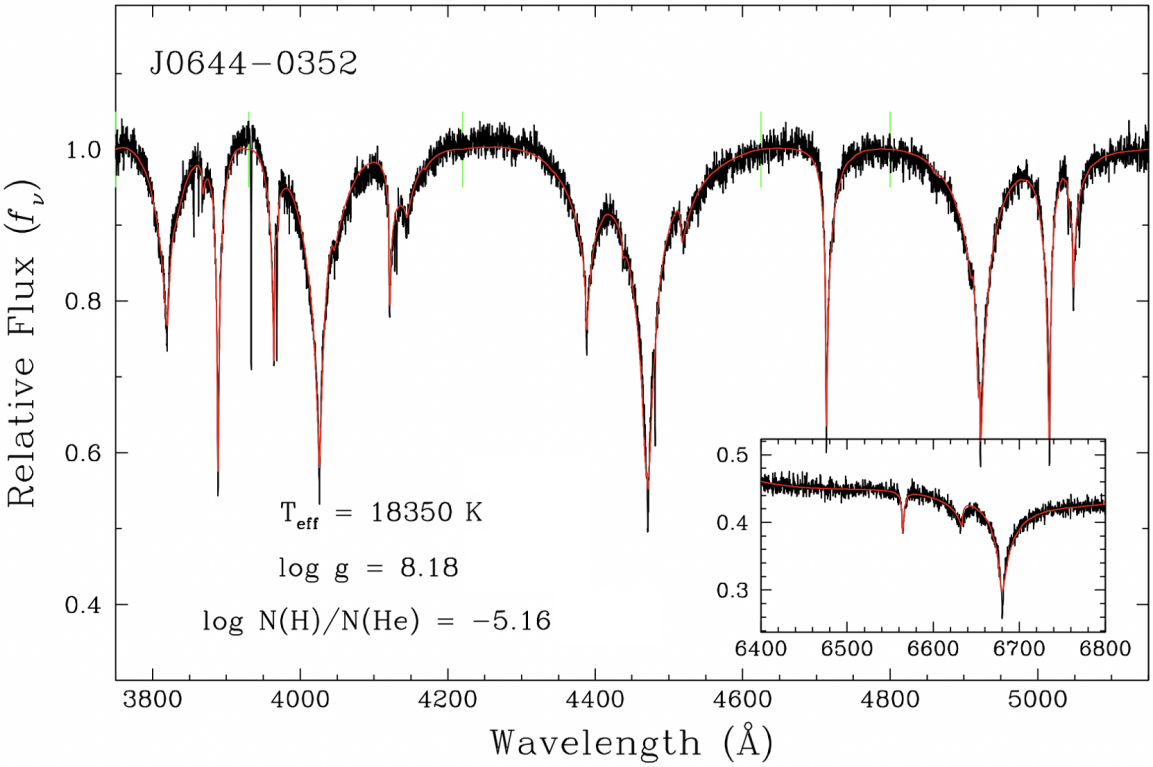

Fig. 4.2 Model fits (red lines) to the X-shooter Helium lines for Gaia J0644−0352. The best-fitting white dwarf parameters and hydrogen abundance are labelled. The green lines show the points used to re-normalise the spectrum to the models.

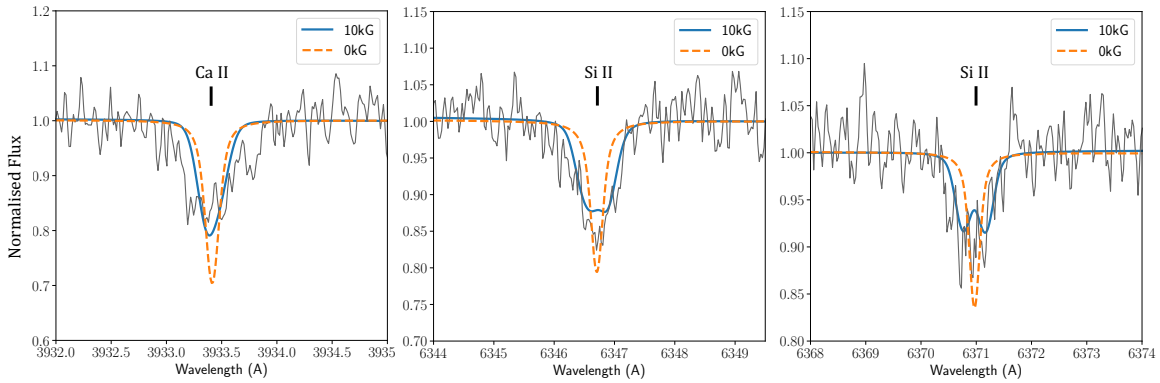

Fig. 4.3 Model fits to the HIRES data using the average abundances for WD 1622+587. Dashed orange line shows the model for a magnetic field of 0kG, and the blue solid line shows the model for a magnetic field of 10kG.

for that spectral line was found. The abundances of the lines were found using the effective temperature and log(g) from the photometric and spectroscopic methods separately. When more than one line of a particular element are present in the 5–15 Å region, the lines are fitted together. For each spectral line in both the X-shooter and HIRES data, the best-fitting abundance was derived, these are reported in Appendix 2: Tables 7.1 – 7.7.

A magnetic DB white dwarf

The widths of the absorption lines for WD 1622+587 are significantly wider than expected from pressure broadening for this DBZ white dwarf. A possible explanation is the presence of a weak magnetic field. The formulation presented in Dufour et al. (2015) is used (see also Hardy et al., 2017) but kept the surface magnetic field constant for simplicity (i.e. no geometry). Fig. 4.3 shows that a constant 10 kG field may account for the extra broadening of the Ca and Si lines.

Absorption features in the presence of emission features

Some absorption lines also have gaseous emission features present at the same wavelength which makes it difficult to disentangle the contribution from the photospheric absorption from the circumstellar emission. In Appendix 2: Tables 7.1 – 7.7. those lines which have photospheric absorption at the same wavelength as the gaseous emission features are noted. High order polynomials are fitted to the spectra to normalise out the broader gaseous emission features. In Klein et al. (2010) it is noted that through tests which varied the order of the normalisation polynomial, the effect of continuum normalisation on narrow absorption lines

in the presence of bumpy features was $< 1\%$. However, in this sample, the spectra contain both broad and sharp gaseous emission features which are less trivial to normalise out in order to obtain accurate equivalent widths of the photospheric features. To test how the sharp gaseous emission features affect the derived equivalent widths, tests were performed on the 3933 Å Ca II line in Gaia J0006+2858 and 7771 Å O I line in Gaia J0510+2315. The equivalent widths were measured using SPLOT, as explained in Section 4.2.2, using both the un-normalised and normalised HIRES spectra. The average equivalent width deviation was found to be 12%. For those spectral lines with gaseous emission features, this additional error of 12% was added in quadrature with the SPLOT fitting error. The equivalent width errors quoted in Appendix 2: Tables 7.1 – 7.7 include the additional error for those photospheric lines which lie in the presence of gaseous emission features. Gaia J0006+2858 has abundances determined from two calcium lines, 3179 Å and 3933 Å, where the latter has a weak gaseous emission feature at the same wavelength. The calcium abundance derived from 3933 Å and that derived from 3179 Å are consistent within the errors of 0.1 dex, providing confidence that the derived abundances in the presence of gaseous emission features are accurate.

Spectroscopic versus photometric white dwarfs parameters used to derive abundances

The spectroscopic and the photometric methods for determining white dwarf parameters result in different sets of absolute abundances derived for the pollutant planetary material. All derived white dwarf temperatures are hotter (except the magnetic white dwarf WD 1622+587) for the spectroscopic method, than for the photometric method. Derived heavy element abundance correlates with temperature, so the abundances of heavy elements when compared to the abundance of the principal element (H or He) as derived from the spectroscopic white dwarf parameters are larger. When considering the abundance ratios of heavy elements rather than absolute abundances, the discrepancy between the spectroscopic and photometric parameters disappears within the 1 σ error, and the choice of white dwarf parameters little affects the abundance pattern and interpretation.

Upper limits

Some important elements are not detected, and so an equivalent width upper limit that would have resulted in a 3σ spectral line detection was calculated. Either a detection or upper limit was determined for these elements for each white dwarf: O, Na, Mg, Al, Si, Ca, Ti, Cr, Fe and Ni. Around the strongest optical line for a particular element, a spectral line was artificially inserted at decreasing values of equivalent width, corresponding to decreasing abundance.

From this, the significance of the absorption feature was calculated, and repeated 10,000 times. The equivalent width upper limit was taken to be the point at which 99.7% of the lines were detected at 3σ for a certain equivalent width. The equivalent width upper limits are reported in Appendix 2: Table 7.8. The Montreal white dwarf models were used to convert from equivalent width to abundance assuming the spectroscopically derived temperature and log(g); the abundance upper limits are reported in Table 4.3. As mentioned previously, the hotter the temperature of the white dwarf used in the models, the larger the abundance is for the same spectral line and equivalent width. Therefore, the abundance upper limits consider the abundance error associated with temperature, and are applicable to both the spectroscopic and photometric abundances, with the exception of WD 1622+587.

Final Abundances of the accreted material

The final abundances are reported in Table 4.3. The abundances are reported as an average of X-shooter and HIRES abundances (or X-shooter and MIKE abundances for Gaia J0611−6931), weighted by the number of absorption lines for each element. If only one line of a particular element is present, the measurement uncertainty is propagated for the abundances and the error was set to 0.1 dex. If an element has a number of detected spectral lines then the uncertainty is dominated by the range of abundances derived for each element, and the standard deviation of the abundances is taken as the abundance error. Appendix 2: Figs. 7.2–7.7 show the average model abundance fit to the strongest spectral line for each element in each white dwarf, for WD 1622+587 the abundance fits are shown in Fig. 4.3. The average abundance is plotted which is derived from multiple spectral lines, so sometimes the fit to individual lines can be discrepant.

4.2.4 Interpreting the observed abundances

Bayesian Models

In order to interpret the final abundances of the accreted material, the PYLLUTEDWD software package was kindly run by A. Buchan on the abundances (Buchan et al., 2022)[2]. This was used to find the most likely explanation for the observed compositions, taking into account the differential sinking of elements in the white dwarf photosphere and the abundances of the accreted planetary material. Fundamentally, the model focuses on the volatile content and geological history of the planetary bodies accreted by the white dwarfs (Harrison et al., 2018, 2021; Buchan et al., 2022). The model assumes that only a single planetary body is

[2]https://github.com/andrewmbuchan4/PyllutedWD_Public

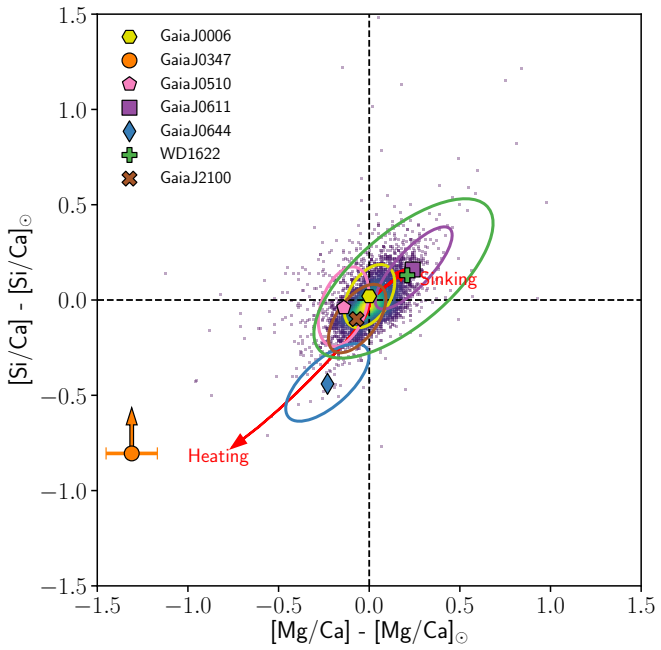

(a)

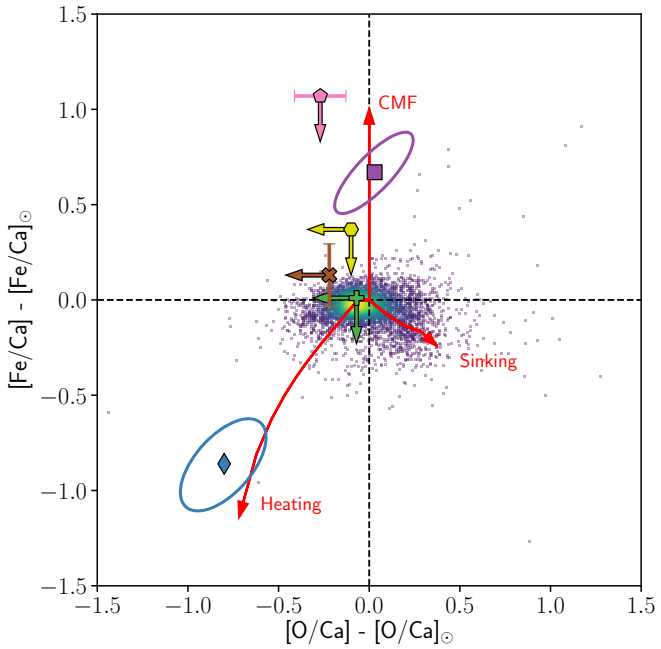

(b)

Fig. 4.4 (a) [Mg/Ca] vs [Si/Ca] abundance ratios of the pollutant, normalised to solar, derived from the spectroscopically determined white dwarf parameters. The ellipses show a 1 σ error ellipse on the abundance ratio. The Hypatia catalogue (Hinkel et al., 2014) of nearby main sequence stars is plotted as scatter points with a density histogram in the densest regions (around solar values - dashed lines at 0, 0). The red arrows show how sinking in the white dwarf atmosphere and heating affects the abundance ratios. Limits are shown with arrows. (b) [O/Ca] vs [Fe/Ca] abundance ratios normalised to solar, for reference the value of [O/Ca] normalised to solar for Bulk Earth is -0.7. An additional red arrow describes how the [Fe/Ca] ratio changes as the core-mass-fraction (CMF) of the planetary body is increased.

currently present in the white dwarf atmosphere. This is clearly a wide-reaching assumption, but as discussed in Turner & Wyatt (2020); Harrison et al. (2018), it is likely that the mass currently in the atmosphere is dominated by the most massive, single body accreted. The composition of this planetary body has potentially been altered due to differential sinking rates of elements in the atmosphere of the white dwarf. Additionally, three main processes are considered that dominate changes to the planetary body's composition. First, the composition of the initial material available for planet formation may differ from the solar system. Second, the planetary bodies may lose volatiles due to the high temperatures experienced during formation. Third, if there is sufficient heating that large-scale melting occurs, the segregation of the iron melt leads to the formation of a core and a mantle; additionally the influence of the internal pressure and oxygen fugacity are considered. Subsequent collisions or other processing that leads to fragmentation, can change the amount of core or mantle material that is accreted by the white dwarf.

The model uses a Bayesian framework to compare the likelihood of a basic primitive model explaining the abundances of the white dwarf pollutant, with a range of more complex models. The basic free parameters are listed below, with the additional more complex parameters listed as optional:

- 'Initial Composition': the body accreted by the white dwarf could have formed in planetary systems with a range of initial compositions, later altered by volatile depletion of metal-silicate segregation. The compositions of nearby stars is a good proxy for this range of initial compositions, utilising the catalogue of Brewer & Fischer (2016). In most cases, the white dwarf is equally likely to have accreted material that started with a wide range of initial compositions.

- 'Pollution fraction': the mass fraction of the white dwarf convection zone that is made up of observable metals M_Z/M_{CVZ}.

- 'Time since accretion onto the white dwarf' and 'accretion event time-scale': the model finds the most likely time since accretion started and length of time for which accretion lasted based on the abundances and relative settling of the detected elements. The diffusion time-scales used in the models are obtained from Koester (2009)[3]. It should be noted that there are model dependent differences in settling time-scales which contributes an additional uncertainty, see Figure A2 in Swan et al. (2019b) for further details. Based on this, the model finds whether it is more likely to be in build-up, steady-state or declining phase, these phases were discussed in detail in Chapter 1 Section 1.4.2. As all the objects in this sample have circumstellar gas and

[3]http://www1.astrophysik.uni-kiel.de/~koester/astrophysics/astrophysics.html

dust reservoirs, accretion is likely ongoing and dominated by one singular body. This is almost certainly occurring for the hot DA white dwarfs, with settling timescales on the order of days.

- '*Temperature*' (optional complex model): the depletion of volatiles is linked to the temperature (pressure) conditions at a certain location in the protoplanetary disc. This assumes that patterns of volatile depletion occur due to the incomplete condensation of hot gas in the inner regions of a protoplanetary disc. In reality it is not known when in the history of the planetesimal the heating occurred; collisions, impacts, or heating on the red giant branch may also alter the abundances, albeit in the same way as modelled here. Therefore, the '*Temperature*' parameter informs of any kind of volatile loss.

- '*Feeding Zone Size*' (optional complex model): the abundances of some planetary material are best explained by a mixture of material that experienced different temperatures. This would occur in reality when planetary bodies accrete material from a range of radial locations, or their feeding zone.

- '*Fragment Core Fraction*' (optional complex model): the white dwarf may have accreted material that is dominated by the core or the mantle of a larger planetary body. This is quoted by both number fraction and mass fraction.

- '*Differentiation pressure*' and '*oxygen fugacity*' (optional complex model): these parameters determine the composition of the core (mantle) based on the conditions that were present during core-mantle differentiation, notably the pressure and the availability of oxygen and its degree of oxidisation, parameterised by oxygen fugacity. The composition of the core or mantle most notably the Cr, Si, Ni content, is constrained based on a model for elemental partitioning during core formation, this model allows the core composition to differ from Earth's core and has 2 free parameters: core mantle boundary pressure ('*differentiation pressure*') and '*oxygen fugacity*' at the time of core formation (note this is different to oxygen fugacity of the final planetary body, as considered in Doyle et al. (2019)). The pressure and oxygen fugacity of the Earth as reported in Buchan et al. (2022) are roughly 45 GPa and -1.3. An asteroidal body, with significant lower pressure than Earth, would have a core with significantly higher Ni/Fe than Earth's core.

These Bayesian models were initially written and developed by John Harrison; the priors of the Bayesian models for the above parameters are defined in Table 1 of Harrison et al. (2021). Buchan et al. (2022) developed these Bayesian models to include differentiation pressure and oxygen fugacity during formation of the parent body. A uniform prior distribution

between 0 and 60 GPa was used for differentiation pressure, and -3 and -1 for the oxygen fugacity, see Doyle et al. (2019) for the formal definition of oxygen fugacity. All priors for the model parameters use a uniform distribution between two values to ensure that the priors are uninformative and not biasing the results towards a specific outcome.

The Bayesian framework compares the basic primitive model with no additional complex free parameters included (null hypothesis, M_0), with more complex models which incorporate additional free parameters, (alternative hypothesis, M_1). It is assessed whether the introduction of additional free parameters results in an improved Bayesian evidence using the Bayes factor. This compares the likelihood of the data given the alternative hypothesis, M_1, to the likelihood of the data given the null hypothesis, M_0. A Bayes factor of > 1 implies evidence for the alternate hypothesis, and a Bayes factor of > 100 implies extreme evidence for an alternate hypothesis. Additionally, this is converted to a frequentist statistic (N σ) to also show the significance of the model. The abundances and output of the Bayesian models are discussed in the results section below.

Oxygen Budget

In order to determine whether the pollutant is water rich, has any iron in metallic form, or is dry, rocky material, oxygen budgeting is done following the method used by Klein et al. (2010). O is assigned to: MgO, SiO_2, Al_2O_3, CaO, and FeO, if there is excess oxygen, this was probably in the form of water in the parent body. The abundances are corrected for sinking assuming the accretion is occurring in the steady state. If there is not a measured abundance for one or more of the major rock forming elements (Mg, Si, Al, Ca and Fe) then the abundance of that element predicted from the Bayesian model is used in the calculation. The oxidisation state of Fe is unknown and Fe could be in a number of forms (or a combination) including: FeO, Fe_2O_3 or metallic Fe. Therefore, the oxygen budgeting method is used to determine if there is excess oxygen rather than to explore the exact water content of a body. As well as the O assignment described above, the most conservative case possible is also considered, which is entirely ferric Fe (i.e. forming Fe_2O_3). This calculation does not consider carbon ices, including CO_2 ices, as in equilibrium these would only form at significantly lower temperatures than water ice.

4.3 Results from individual systems

Interpretation of the observed abundances for the planetary material that were accreted by each white dwarf is discussed here, whilst interpretation of the entire population is presented in Section 4.4. In what follows, the abundances obtained based on the spectroscopically

derived stellar parameters are used (see the discussion for additional details). However, as noted in Section 4.2.3, when considering abundance ratios rather than absolute abundances, the two sets of measurements agree within a $1\,\sigma$ error. When discussing abundances, abundances by number are used unless stated otherwise. The derived abundances are reported in Table 4.3, plots showing the average abundance fits to the spectra can be found in Appendix 2: 7.4 and Fig. 4.3 for WD 1622+587. The photospheric abundances for each target inform our understanding of the history and state of the planetary material accreted. These interpretations are presented first, followed by more detailed insights derived from the Bayesian models discussed in Section 4.2.4. The best-fitting parameters from the Bayesian models are reported in Appendix 2: 7.5 in Table 7.9.

4.3.1 Gaia J0006+2858

The exoplanetary body that polluted Gaia J0006+2858 has Si/Mg and Ca/Mg abundances that are close to solar and within the abundance range of nearby stars, as shown in Fig. 4.4a. The system is most likely in steady-state given the short settling time-scale of a few days. The derived oxygen upper limit provides no information about the volatile content of the accreted object.

These conclusions are supported by the Bayesian models which find that the abundances are most likely explained by the accretion of a primitive body in steady state.

4.3.2 Gaia J0347+1624

The abundance of the exoplanetary body that polluted Gaia J0347+1624 demonstrates super-solar values of Ca/Mg (Fig. 4.4a). One explanation is that a portion of the polluting body contained material depleted in moderate volatiles, including Mg-rich minerals, with respect to highly refractory calcium-rich minerals. This may be the result of experiencing hot temperatures, as seen in Fig. 4.4a the abundance follows the 'heating' arrow. As this white dwarf is a hot DAZ with short sinking time-scales, it is most likely to be accreting in steady-state phase.

The model with the highest Bayesian evidence invokes the accretion of a planetary body with a highly refractory composition (depleted in moderate volatiles) with Bayes factor of 2.1×10^{13} ($8.1\,\sigma$), as reported in Appendix 2: Table 7.9.

4.3.3 Gaia J0510+2315

The oxygen abundance of the body that polluted Gaia J0510+2315 is high when compared to more refractory species, such as: Mg, Si, and Ca, as shown in Fig. 4.4b. Based on the available optical spectra, Fe is not detected in the atmosphere of this white dwarf and the upper limit provides no further insights into the oxygen budget. The oxygen abundance is consistent with the accretion of a volatile rich body and has a similar abundance ratio to solar, rather than depleted in volatiles which the case for the rocky material typically accreted by white dwarfs. If the iron abundance was also found to be solar, consistent with the non-detection, the oxygen abundance is too high to account for all the metals, and thus there would be excess oxygen that may imply that Gaia J0510+2315 accreted a water-rich body. The abundances are most likely accreting in steady-state, as it is unlikely to catch the system in build-up phase given the settling time-scales of days.

The Bayesian model finds that the most likely explanation for the observed abundances is the accretion of a volatile rich body accreting in steady state. In order to consider the oxygen budget, iron is considered likely to be no more abundant than seen in nearby stars. Using the Bayesian models inference for iron the contribution of oxygen to the metal oxides can be estimated, as described in Section 4.2.4. If iron were significantly higher than the abundances seen in nearby stars, it is likely that this iron would take the form of Fe (metal) in a planetary core, rather than FeO, however, Ni or Cr abundances would be needed to confirm this interpretation. The remaining fraction of oxygen once the metals (including the Fe *prediction*) have been oxidised is 0.74 (0.48 water mass fraction) if Fe is in the form of FeO; this oxygen can bond with hydrogen as water. In order for the Fe abundance to balance the oxygen budgeting, the Fe abundance would have to be 1.1 dex higher than the range of stellar abundance from Brewer & Fischer (2016). Future UV spectra will confirm whether this system is indeed accreting a volatile rich body as the UV is sensitive to numerous of absorption lines from volatile species (e.g. O, C, N) enabling robust abundance determinations and limits to be obtained for the pollutant. Gaia J0510+2315 is a DA, so hydrogen from an accreted body cannot be spectroscopically distinguished from the hydrogen envelope of the white dwarf. The oxygen circumstellar gaseous emission features are particularly strong implying there could also be volatile-rich circumstellar material. Full radiative transfer calculations such as those in Gänsicke et al. (2019); Steele et al. (2021) are required to investigate whether the circumstellar gas is as rich in volatiles as the photosphere appears to be; this is beyond the scope of this chapter.

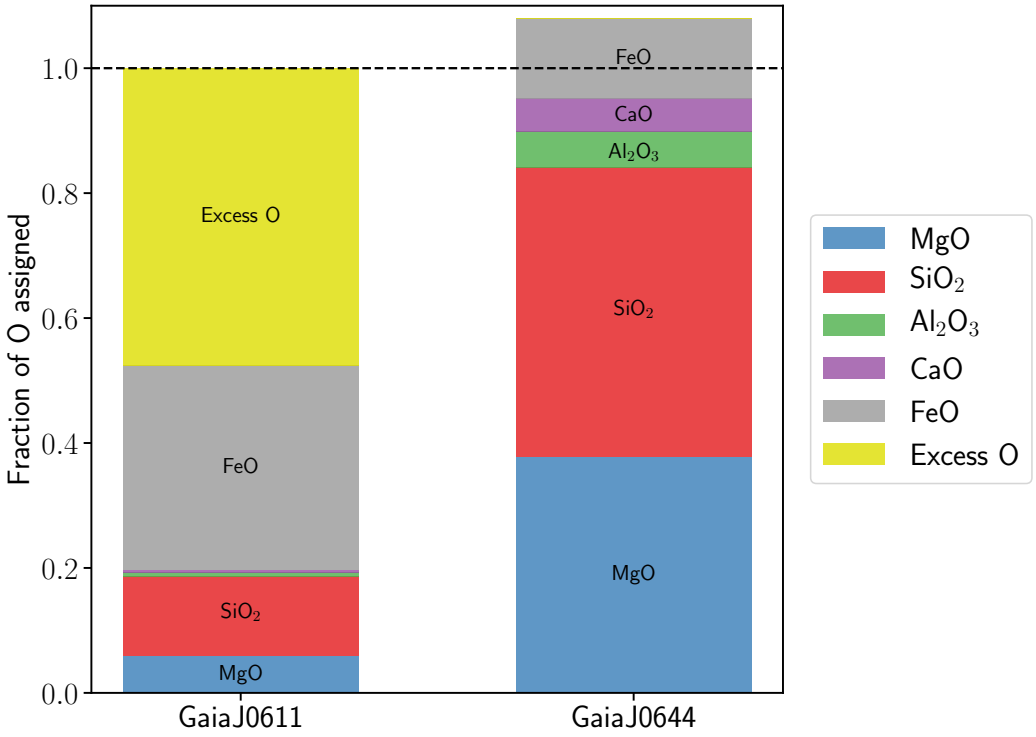

Fig. 4.5 The likely division of the observed oxygen abundance between metal oxides (MgO, SiO_2, Al_2O_3, CaO, and FeO) and water-ice (yellow), for Gaia J0611−6931 and Gaia 0644−0352. The approach is described in Section 4.2.4, using abundances adjusted for sinking in steady-state. For Gaia J0611−6931 the fraction of excess oxygen is 0.48, this excess oxygen is likely carried in water-ice. For Gaia 0644−0352, the oxygen can all be accounted for in metal oxides, and the pollutant was most likely dry and rocky.

4.3.4 Gaia J0611−6931

Gaia J0611−6931 has accreted a planetary body with approximately solar abundances of Ca/Mg, Si/Mg, and O/Mg. Solar (or close to) abundances of oxygen are seen in Kuiper belt objects from the cold outer regions of the solar system. The planetary body also has a super-solar abundance of Fe/Mg, as shown in Fig. 4.6. This iron abundance lies 5.8σ above that of solar. The high iron abundance is typical of planetary cores, indicating that the accreted object appears to be dominated by its iron core. The body accreted by Gaia J0611−6931 is both rich in iron and oxygen, as seen in Fig. 4.4b.

Oxygen budgeting was done on this system using the bulk composition of the parent body. The most likely accretion state is steady-state so the abundances are adjusted to consider the effects of differential sinking of elements. Assuming steady-state accretion, the measured oxygen abundance (Table 4.3) is sufficiently large that extra oxygen is indicated, over and above that which can be accounted for in metal oxides, see Fig. 4.5. The excess oxygen was calculated using two Fe oxidisation states: FeO and the more conservative Fe_2O_3. The oxidisation state of Fe (FeO or Fe_2O_3) leads to small uncertainty in the potential water fraction. Both oxidisation strategies show a significant oxygen excess: 0.48 for FeO and 0.31 for Fe_2O_3 which is equivalent to accreting a body with 0.22 and 0.14% water by mass respectively. Additionally some Fe could be metallic and so the oxygen excess is a lower limit.

The most likely Bayesian model is that of a volatile rich and core-mantle differentiated body; this is preferred over a primitive model with Bayes factor 4.3×10^4 (5.0σ). From Appendix 2: Table 7.9, a fragment number core fraction of $0.26^{+0.06}_{-0.05}$ is inferred, which equates to a core mass fraction of $0.52^{+0.07}_{-0.07}$, the equivalent core mass fraction for Earth is only 0.325. Gaia J0611−6931 has accreted material that is dominated by core-rich material, likely a core-rich portion of a larger parent body. The model determined that the body accreted by Gaia J0611−6931 was oxygen-rich, and inferred a correspondingly oxygen-rich mantle composition (87% by number). Assuming a single body was accreted by the white dwarf, the oxygen level is too high to be explained with standard oxidation of the rock forming elements, suggesting an additional oxygen reservoir, for example, a hydrosphere.

4.3.5 Gaia J0644−0352

Gaia J0644−0352 has solar abundances of Al, Ti, Ca, Cr, and Si, when compared to Mg, but has sub-solar O and Fe, as shown in Fig. 4.7. The oxygen abundance is depleted by $> 3\,\sigma$ indicating the accretion of dry and rocky material, oxygen budgetting calculations were performed which found that sufficient metals are present such that the oxygen likely arrived

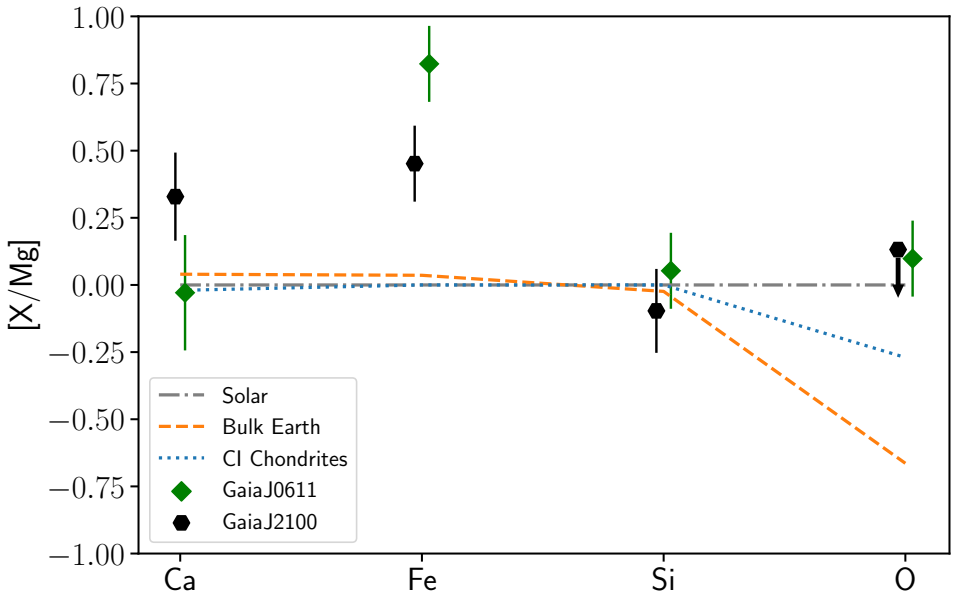

Fig. 4.6 The number ratio of elemental abundances in the parent body relative to Mg, normalised to solar (grey dash dot line). Abundances for the white dwarfs, Gaia J0611−6931 and Gaia J2100+2122, are shown as green diamond and black hexagon data points respectively, with 1σ errors, derived using the spectroscopic temperature and log(g). Abundances have been adjusted for sinking assuming steady state. The Fe/Mg for Gaia J0611−6931 lies 5.8 σ above solar, and for Gaia J2100+2122 the Fe/Mg value lies 3.2 σ above solar; both systems are enhanced in Fe compared to Mg.

in the form of metal oxides within the errors, as shown by Fig. 4.5. The low Fe abundance could be due to the accretion of a mantle-rich fragment which would naturally explain a depletion in iron.

The most likely explanation for the observed abundances (highest Bayesian evidence) is the accretion of volatile depleted material. The pollutant went through significant heating ($\sim 1381^{+182}_{-80}$ K) to fit the volatile depletion in this accreted body, as shown as the blue 'max Z' model in Fig. 4.7. The low Fe abundance observed for Gaia J0644−0352 is consistent with the accretion of mantle-rich material. A model in which Gaia J0644−0352 accreted mantle-rich material is a good fit to the data points, as shown by the grey median model with differentiation included in Fig. 4.7. A mantle-rich model does not have a higher Bayesian evidence than a model where the white dwarf accretes volatile depleted material (Bayes factor with 'max Z' model as null hypothesis and mantle-rich model as alternate hypothesis gives 0.4). Although the model including core-mantle differentiation is a better fit to the data points, the Bayesian model does not favour such a solution due to the additional model parameters. As there are measurements of nine abundances, the model renders it likely that the abundance of one of the elements could be discrepant from its true abundance by $2\,\sigma$, where σ is the measurement uncertainty, as required for the 'max Z' volatile-depleted model to explain the low Fe. The true Fe abundance could be significantly higher than that observed due to statistical uncertainties and observational errors. This is a limitation of the Bayesian model.

4.3.6 WD 1622+587

The Ca/Mg and Si/Mg abundances of the exoplanetary body that polluted WD 1622+587 are primitive and reflect bulk Earth, or compositions seen in nearby stars. The oxygen upper limit suggests the accreted body was rocky material, rather than volatile-rich.

4.3.7 Gaia J2100+2122

The Si/Mg abundance in the exoplanetary body that polluted Gaia J2100+2122 is primitive and reflects bulk Earth, or compositions seen in nearby stars. However, there is an enhancement of Ca and Fe in comparison to solar, as shown in Fig. 4.6. The Fe/Mg lies $3.2\,\sigma$ above that of solar, when assuming steady state accretion. This could be explained by the accretion of a core-rich fragment. There is insufficient information from the oxygen upper limit to constrain the volatile content for the body that was accreted by this white dwarf.

The Bayesian model that invokes core-mantle differentiation is preferred over a primitive model with a Bayes factor of 4.6×10^2 ($3.9\,\sigma$). The fragment core number fraction is

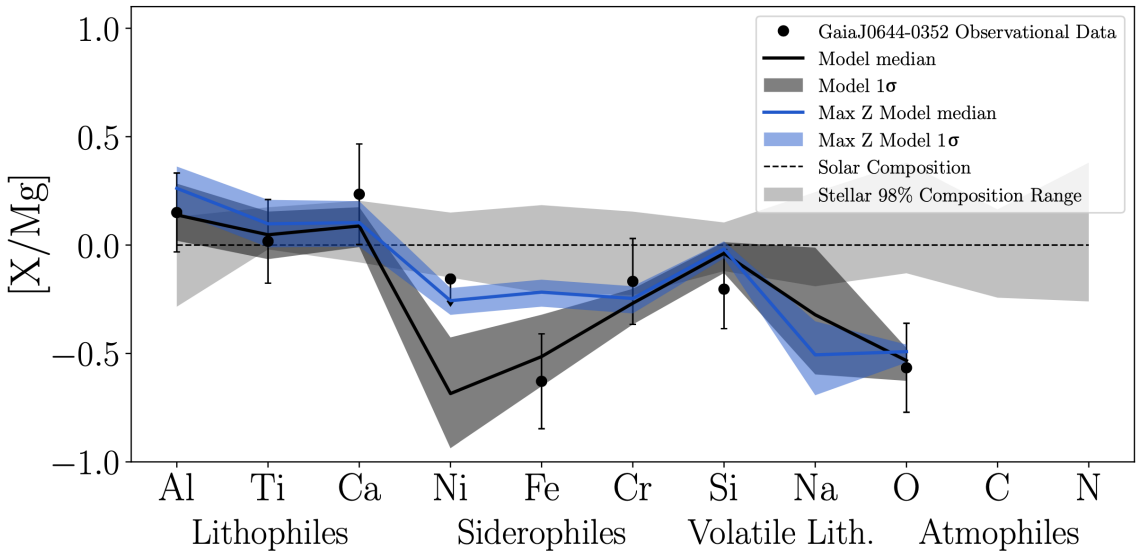

Fig. 4.7 The number ratio of elemental abundances in the pollutant material relative to Mg, normalised to solar (dashed line). Observed abundances for the white dwarf, Gaia J0644−0352, are shown as black points, with 1σ errors, derived using the spectroscopic temperature and log(g). Sinking effects are included in the model. The blue line represents the Bayesian model with the maximum likelihood (max Z). The black line represents the maximum likelihood median model with differentiation included and a 1σ error as the shaded dark grey region. The body that was accreted by Gaia J0644−0352 may be mantle rich, but there is insufficient statistical evidence to include an additional parameter in the model fit. The shaded light grey region indicates the range of abundances seen in nearby stars using the catalogue from Brewer & Fischer (2016).

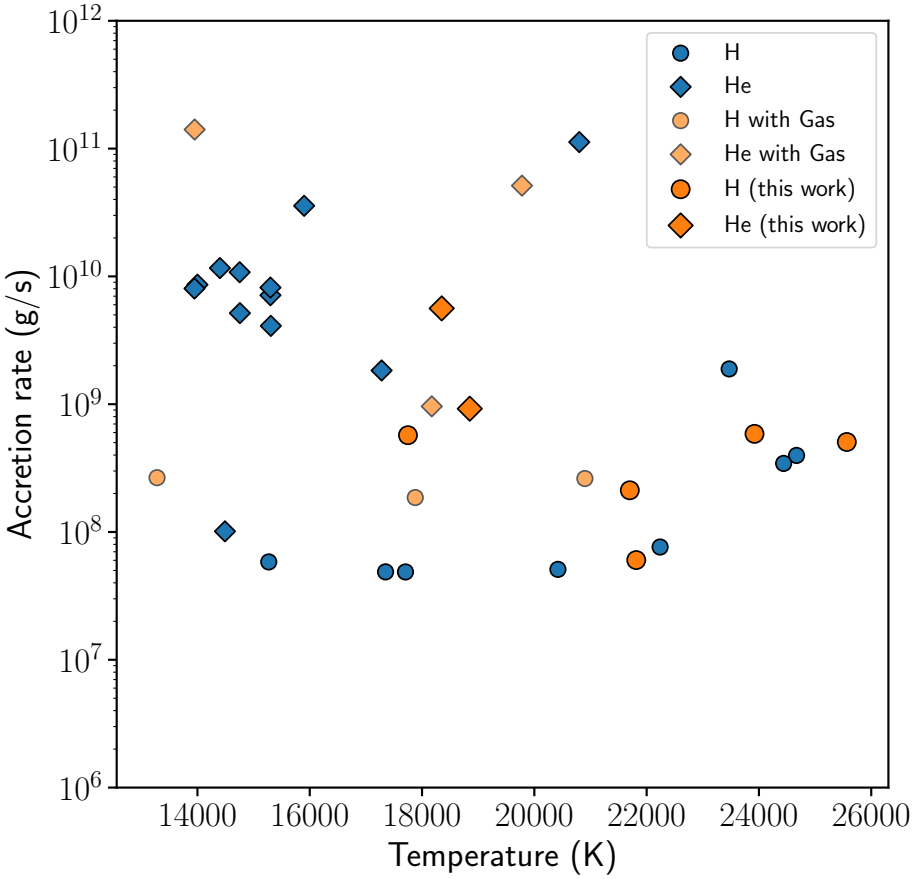

Fig. 4.8 The accretion rates of polluted white dwarfs with and without detectable gaseous discs in emission as a function of their effective temperatures. The data for the accretion rates of polluted white dwarfs without circumstellar gaseous discs are from Figure 3 in Xu et al. (2019), see reference for details. The accretion rates for gaseous disc systems are from Table 4.4 including the seven reported in this work.

$0.30^{+0.11}_{-0.08}$, and the equivalent core mass fraction is $0.52^{+0.12}_{-0.11}$, this is higher than bulk Earth which has a core mass fraction of 0.325.

4.4 Comparing pollution in white dwarfs with and without detectable circumstellar gas

The white dwarfs in this sample represent 7 of just 21 polluted white dwarf systems with detectable circumstellar gas and dust. The presence of circumstellar gas is not fully understood. One possibility is that it represents an early stage in the accretion process, which is followed by dust-rich accretion and then no detectable circumstellar material. Alternatively, detectable

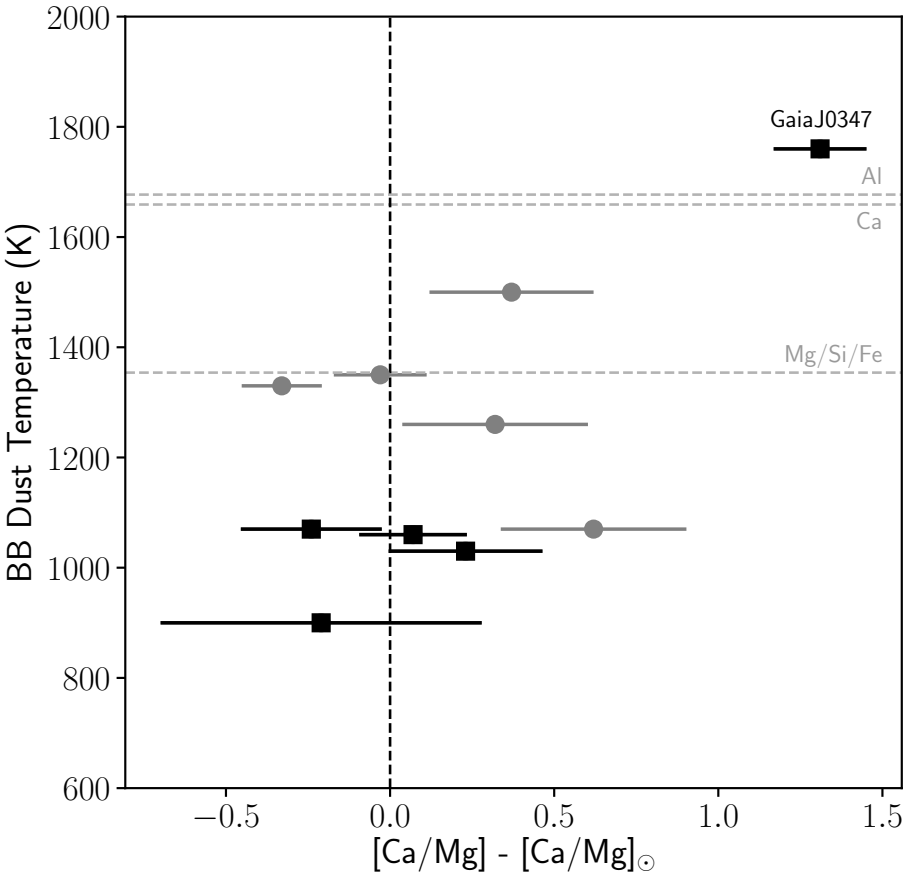

Fig. 4.9 Single blackbody dust temperature for the dust emission from the literature versus the [Ca/Mg] ratio, normalised to solar, of the pollutant body. Those in this work are black squares, and those from the literature are grey. Horizontal dashed grey lines show apparent condensation temperatures for Al, Ca, Mg, Si and Fe (Lodders, 2003). The material polluting Gaia J0347+1624 is depleted in moderate volatiles and has a composition most like Ca-Al–rich inclusions, it is hypothesised that the material underwent incomplete condensation during formation explaining the extreme [Ca/Mg]. Therefore the dust surrounding Gaia J0347+1624 can survive to higher temperatures, and so the dust emission has a hotter overall inferred blackbody temperature.

quantities of circumstellar gas may only be produced in the disruption of the largest planetary bodies, or those with the most violent collisions.

Previous work has found that detectable circumstellar gas is a rare phenomena in polluted white dwarfs (Manser et al., 2020). Xu et al. (2019) compared pollution levels for those white dwarfs with and without detectable circumstellar *dust*, compiling their work with data from the literature (Koester et al., 2011, 2014; Koester & Kepler, 2015; Hollands et al., 2018). No strong difference in total mass accretion rate or abundance of polluting material was found between those white dwarfs with detectable circumstellar dust and those without, although it should be noted that the authors consider there to be bias in the sample. Here the work of Xu et al. (2019) is expanded to compare the pollution between white dwarfs with and without detectable circumstellar *gaseous* discs, where without refers to all polluted white dwarfs without any evidence of circumstellar gas in emission.

4.4.1 Accretion rates

Previous studies investigating the link between the presence of a detectable gaseous disc and accretion rate based on a handful of systems found no correlation between accretion rate and the presence of circumstellar gas (Manser et al., 2016b, 2020). However, gas drag may cause enhanced accretion rates above what may be expected from PR drag alone. Combining white dwarfs with detectable circumstellar gas discs from the literature (which have reported abundances of at least Ca, and Mg in their photosphere) with the seven in this work, the sample size is doubled. The following discussion revisits whether white dwarfs with a circumstellar gas disc accrete planetary material at higher levels, compared to the population.

In order to compare the mass accretion rates between white dwarfs with and without detectable circumstellar gas discs, a systematic approach must be taken. The mass accretion rates were calculated from the magnesium abundance, assuming magnesium makes up 15.8% of the total mass, as in Bulk Earth. Xu et al. (2019) demonstrated this as the most reliable and consistent way to measure and compare accretion rates for a sample of polluted white dwarfs. The coolest white dwarf discovered with a circumstellar gaseous disc is WD 0145+234, with a temperature of 12,720 K (Melis et al., 2020), thus, when comparing to the population, the lower temperature cut off was set at $T > 12{,}720$ K. There is no correlation between temperature (white dwarf cooling age) and accretion rate above 10,000 K (Xu et al., 2019; Wyatt et al., 2014).

The accretion rates as a function of white dwarf temperature are plotted in Fig. 4.8, which compares those with detectable circumstellar gas discs to the population. The white dwarfs with gas discs tend to be hotter white dwarfs, which could be an observational bias, and can have accretion rates that match the upper end of the population. Given the statistics of

small numbers, at this time such a comparison is limited by this. The figure also highlights how the accretion rates of He dominated white dwarfs are higher than those in H dominated atmospheres (Farihi et al., 2012b; Xu et al., 2019). This may be due to the orders of magnitude longer settling time-scales for He dominated white dwarfs and therefore the rates represent an average historical accretion rate. Direct impacts onto the white dwarf (Brown et al., 2017; McDonald & Veras, 2021), or the disruption of massive asteroids $\sim$500 km which can collisionally evolve to produce enhanced accretion on short time-scales (Wyatt et al., 2014; Brouwers et al., 2022) can contribute to larger measured average accretion rates for DBZ white dwarfs. Alternatively, thermohaline mixing could explain the differences between DA and DB accretion rates. DBZ white dwarfs experience less thermohaline mixing than DAZ white dwarfs (Bauer & Bildsten, 2019). When including thermohaline mixing into the white dwarf models, larger accretion rates are required in order to account for this instability (Bauer & Bildsten, 2018). As it disproportionally affects DA white dwarfs, the accretion rates would need to be orders of magnitude larger for the DA white dwarfs to account for the thermohaline mixing.

Table 4.4 Total accretion rates based on Mg abundances for white dwarfs with an observable gaseous disc with emission features. This is calculated using $\dot{M} = (100/15.8) \times M_{\rm WD} \times 10^{q} \times 10^{[\rm Mg/H(e)]} \times A_{\rm Mg/H(e)}/\tau_{\rm Mg}$, where $q = log_{10}(M_{\rm CVZ}/M_{\rm WD})$, $A_{\rm Mg/H(e)}$ is the atomic mass of Mg divided by the atomic mass of H or He, depending on the dominant atmospheric (atm) constituent, and $\tau_{\rm Mg}$ is the sinking time of Mg.

WD Name	Atm	$T_{\rm eff}$ (K)	log(g)	$M_{\rm WD}$ ($M_\odot$)	log(q)	log($\tau_{\rm Mg}$) (yrs)	log(Mg/H(e))	$\dot{M}$ (g/s)	Reference
Gaia J0006+2858	H	23920	8.04	0.66	−15.5	−1.43	−4.95	5.86×10^{8}	This work
Gaia J0347+1624	H	21820	8.10	0.69	−16.2	−1.93	−5.78	6.03×10^{7}	This work
Gaia J0510+2315	H	21700	8.20	0.75	−16.5	−2.21	−5.23	2.12×10^{8}	This work
Gaia J0611−6931	H	17750	8.14	0.70	−16.7	−2.32	−4.67	5.72×10^{8}	This work
Gaia J0644−0352	He	18350	8.18	0.70	−6.4	5.29	−5.75	5.62×10^{9}	This work
WD 1622+587	He	18850	7.80	0.49	−6.0	5.81	−6.25	9.22×10^{8}	This work
Gaia J2100+2122	H	25570	8.10	0.69	−15.5	−1.47	−5.08	5.06×10^{8}	This work
SDSS J0738+1835	He	13950	8.4	0.84	−6.0	5.45	−4.68	1.41×10^{11}	Dufour et al. (2012)
SDSS J0845+2257	He	19780	8.18	0.71	−6.7	5.08	−4.70	5.13×10^{10}	Wilson et al. (2015)
SDSS J0959−0200	H	13280	8.06	0.64	−15.8	−1.59	−5.20	2.66×10^{8}	Farihi et al. (2012a)
SDSS J1043+0855	H	17880	8.12	0.69	−16.7	−2.29	−5.15	1.86×10^{8}	Manser et al. (2016b)
SDSS J1228+1040	H	20900	8.15	0.71	−16.5	−2.15	−5.10	2.62×10^{8}	Gänsicke et al. (2012)
HE 1349−2305	He	18170	8.13	0.67	−6.3	5.40	−6.50	9.62×10^{8}	Melis et al. (2012)

4.4.2 Metal abundances

The photospheric abundances of white dwarfs with circumstellar gas provide crucial information regarding the planetary bodies accreted. In this section, it is investigated whether there are differences in the composition of the planetary bodies accreted by white dwarfs with and without detectable circumstellar gas which might shed light on their respective histories.

The presence of circumstellar gas may reflect an early stage in the accretion history, or alternatively, the accretion of larger planetary bodies. Volatiles sublimate in the cooler regions, further from the star, whilst refractories sublimate close to the star. One could postulate that preferential production of volatile-rich gas occurs early in the lifetime of a circumstellar disc. This would be reflected in a volatile-rich photospheric composition. The abundances of volatile material polluting white dwarfs with and without circumstellar gas are shown in Fig. 4.10b. Given the small number statistics, there is no preference for the accretion of volatile rich material for those systems with gaseous discs when compared to those without gaseous discs.

The lithophilic abundances (Si, Ca, Mg) are compared between those white dwarfs which show detectable levels of circumstellar gas, and those without, as shown in Fig. 4.10a. Only white dwarfs with detections of Ca, Mg and Si are plotted, with the addition of Gaia J0347+1624 from this work which only has measurements of Ca and Mg. The abundance distribution cannot be explained by invoking a solar or local stellar abundance. The range of Ca, Mg, Si abundances seen in the atmospheres of white dwarfs with and without gas detections show similar trends, influenced only by their relative sinking and another process that enhances Ca relative to Mg. This might be due to the depletion of Mg-rich minerals in favour of highly refractory-rich minerals, containing Ca, Al, Ti, that would occur if a portion of the body experienced temperatures higher than $\sim$1250 K during formation or in the red giant phase. However, these conclusions, and those discussed above, are limited by small number statistics and therefore, require further detections of white dwarfs with circumstellar gaseous discs to be conclusive. Over the coming years surveys such as 4MOST and WEAVE will discover numerous new polluted white dwarfs with circumstellar gaseous discs, allowing these conclusions to be revisited in future studies.

4.5 Discussion

This chapter presents the abundances of the planetary material that was accreted by seven white dwarfs with circumstellar gas and dust, along with interpretation of the observed compositions in terms of the history of the accreted planetary body. The results reveal planetary bodies that have accreted material with a large range of volatile contents, from pure

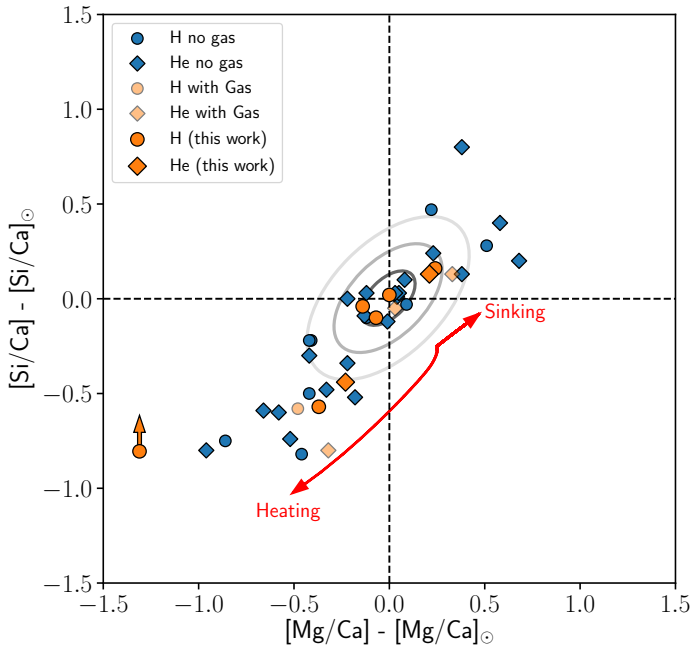

(a)

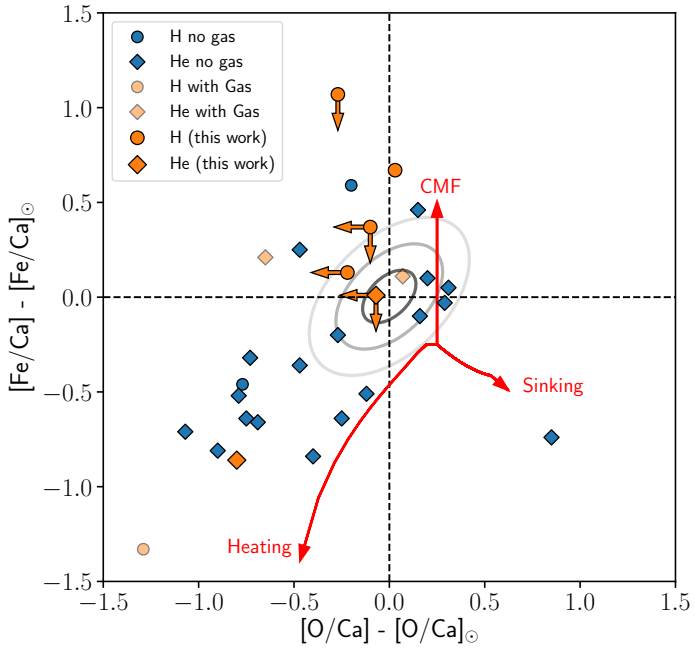

(b)

Fig. 4.10 (a) Comparison of the [Si/Ca] against [Mg/Ca] composition of the material that has polluted white dwarfs which have a detectable circumstellar gaseous disc compared to those without. (b) Comparison of the [Fe/Ca] against [O/Ca] composition. The grey ellipses show a 1 σ, 2 σ and 3 σ error ellipse based on solar abundances with Ca, Mg and Si errors of 0.1 dex. If a white dwarf accreted material of solar abundance with typical errors of 0.1 dex, the contours show the distribution of expected abundances. The arrows show how the abundances are affected by: sinking in the white dwarfs atmosphere, heating of the pollutant and increasing the core mass fraction (CMF).

rock, to rock and water-ice mixtures that are similar to Kuiper belt objects in the solar system. Evidence is presented for the geological process of core formation, and the accretion of highly refractory grains onto Gaia J0347+1624. In the following discussions, the robustness and implications of these conclusions are discussed.

The absolute abundances in the white dwarf photosphere are most affected by uncertainties in the derived stellar parameters, discussed in Section 4.5.1, as well as the quality of the spectroscopic data and the white dwarf models used to analyse and obtain the abundances. Crucially, interpretation of the observed compositions, which is based on elemental ratios, are less affected by uncertainties in the stellar parameters. However, limitations are introduced by uncertainties in relative sinking of various elements, uncertainties in the modelling of the atmospheres of white dwarfs, as well as by missing information regarding key species that evaded detection.

4.5.1 Effects of uncertainties on elemental abundances

In order to determine elemental abundances from the data, a number of systematics must be considered. Sometimes only one (or few) absorption line(s) of a particular element are present in the spectrum (see Appendix 2: Tables 7.1 – 7.7 for details). This is especially important for the five DAZ white dwarfs where there are few metal absorption lines and they can be weak. Both Gaia J0611−6931 (Section 4.3.4) and Gaia J2100+2122 (Section 4.3.7) have enhanced Fe/Mg abundances, however, each has just one Fe absorption line in the spectra, adding additional uncertainties to the conclusions. The abundances are also limited by the white dwarf models, for example, 3D mixing effects such as convection may affect the derived abundances (Cunningham et al., 2019). It should also be noted that UV-optical discrepancies in derived abundances have been observed (e.g. Gänsicke et al., 2012; Xu et al., 2019).

This work corroborates previous studies which identified the differences in deriving white dwarf parameters from spectral analysis compared to those derived from broad band photometry. Spectroscopic temperatures can exceed photometric temperatures by 5–10% above 14,000 K (Genest-Beaulieu & Bergeron, 2019). All white dwarfs in this study fall into this temperature range, and indeed this is reflected in the derived stellar parameters. The most accurate white dwarf parameters derived from broad band photometry are those that include the SDSS ‘u’ band with additional optical photometry, e.g. Pan-STARRS (Bergeron et al., 2019). Only three of the target white dwarfs have SDSS photometry, and as noted in Section 4.2.1, the photometrically derived parameters for Gaia J0510+2315 and Gaia J2100+2122 are less reliable due to comparison with *GALEX* photometry. Therefore, there are significant systematic uncertainties associated with the stellar parameters. It is likely that a hybrid

approach similar to Izquierdo et al. (2021) may result in improved parameters, however, this still requires SDSS 'u' band data and so is not performed in this study.

The metal abundance uncertainties quoted in Table 4.3 are measurement errors and do not include systematic errors arising from uncertain white dwarf parameters. Instead the abundances based on the two sets of stellar parameters are considered. The difference in temperature and log(g) between the two sets of stellar parameters are between 1000–3000 K and 0.1–0.25 dex respectively. In order to obtain reliable and accurate *absolute* abundances of the accreted planetary material it is crucial to obtain accurate stellar parameters. However, the relative elemental ratios, which are used to interpret the observed compositions, are consistent within 1 σ between the abundances derived from the spectroscopic stellar parameters compared with the photometric stellar parameters. The ratios are less sensitive to the derived stellar parameters. The Bayesian models were run for all the white dwarfs based on both sets of parameters. For all the white dwarfs, the best-fitting models are the same between the two sets of parameters. Therefore, until the uncertainties on the absolute abundances can be reduced, the differences between the photometric and spectroscopic temperatures and log(g) will not affect the results of the abundance analysis. If absolute abundances are important, (as when deriving accretion rates), the measurement errors as well as systematic errors associated with uncertain stellar parameters should be included and propagated.

4.5.2 Volatiles in exoplanetary systems

This work shows that there is a wide range in volatile content of the planetary material accreted by the white dwarfs in the sample. Gaia J0510+2315 and Gaia J0611−6931 show approximately solar levels of oxygen, this is significantly in excess to the oxygen abundance of bulk Earth. Without an iron detection for Gaia J0510+2315 it is not possible to assess the true volatile content of the planetary body that was accreted; future UV observations should detect iron, allowing improved oxygen budgeting calculations. Oxygen budgeting for Gaia J0611−6931 demonstrated a significant oxygen excess above that which could form metal oxides as discussed in Section 4.3.4. The accreted body is best explained by a mixture of rocks and water-ice. This adds to the handful of polluted white dwarf systems discovered that have accreted water rich bodies (Farihi et al., 2011, 2013; Raddi et al., 2015; Xu et al., 2017; Hoskin et al., 2020; Klein et al., 2021). On the other hand, Gaia J0347+1624 and Gaia J0644−0352 (discussed in Sections 4.3.2 and 4.3.5) appear to be accreting bodies that are dry and rocky, much like asteroids or terrestrial planets in the solar system.

A number of uncertainties affect the conclusions drawn here. To determine the oxygen excess, the oxygen was assigned to Fe, Ca, Al, Si and Mg; but not all the rock forming elements

are detected. Al has a low abundance, and therefore the absence of Al for Gaia J0611−6931 is unlikely to influence the oxygen budget. It should be noted that the quantity of the oxygen excesses and therefore water fraction of the body is uncertain. This is largely due to the fact that the form of iron is unknown. Fe could be in the form of FeO, Fe_2O_3, or metallic Fe. The latter is especially important for Gaia J0611−6931 given that the most likely composition of this body was core rich, so it is probable that a significant fraction of the Fe would be in the form of metallic Fe. Therefore, the fraction of excess oxygen that could have been in the form of water may be as high as 0.8 if all Fe were in the form of metallic Fe. This is equivalent to accreting a body with 37% water by mass. The conclusion regarding Gaia J0611−6931 accreting a volatile rich planetary body appears robust.

Gaia J0611−6931 accreting a volatile rich body demonstrates that volatiles can survive stellar evolution to the white dwarf phase. The fact that the sample of white dwarfs is accreting material with a wide range of volatile content implies that they are accreting material from a wide range of radial locations. Terrestrial planets are thought to form within the ice lines of volatile elements, and therefore form primarily dry. However, the Earth contains more volatiles than would be expected based on a formation distance of 1 au. Although various mechanisms that could deliver water early have been proposed, studies of the composition of the forming core and mantle over time demonstrated that the Earth was initially reduced and accreted volatiles later (Wood et al., 2008; Rubie et al., 2011). Volatiles delivered later by planetesimals originating past the snow lines and destabilised by Jupiter and Saturn are one potential pathway for water delivery to Earth (Morbidelli et al., 2000, 2012; Raymond & Izidoro, 2017). Discovery of water-rich planetesimals in other planetary systems is important as it informs us that volatile rich bodies can survive formation and subsequent evolution, and can deliver volatiles to planetary systems as late as in the white dwarf phase. Additional discoveries of water rich planetary bodies across the Milky Way can be linked to questions regarding extra-terrestrial life.

4.5.3 Evidence for the accretion of multiple bodies?

The simplest possible assumption to make is that the planetary material currently in the atmosphere of the white dwarf represents a single body, which is the assumption used throughout this work. However, if white dwarfs are polluted by many small asteroids (Jura, 2008), it is possible that currently, or historically, any given white dwarf may contain material from multiple planetary bodies. Also, models often assume that the bodies accreted are from the same planetesimal reservoir around the white dwarf.

Gaia J0611−6931 is accreting material that is both enhanced in Fe and O, as discussed in Section 4.3.4. This white dwarf may be accreting material from two bodies: one that is

enhanced in Fe and is a fragment of a core rich body, and the other enhanced in O and is a fragment of a water-rich body. When a planetary body undergoes large-scale melting to produce an iron-rich core, in general, temperatures are sufficiently high that volatiles, such as water, are lost (Lichtenberg et al., 2019). Unless the body was particularly large such that volatiles are retained in an atmosphere, or it accreted a substantial population of icy pebbles long after cooling, it is more difficult for a single planetary body to be both core-mantle differentiated and icy.

Gaia J0644−0352 is accreting dry, volatile depleted material, however, trace hydrogen is detected and there could be multiple origins. Hydrogen can be accreted from the ISM, be primordial and remain after stellar evolution or it could be interpreted as the accretion of water-rich material (Gentile Fusillo et al., 2017), which could have occurred at any point in its history as the hydrogen would stay on the surface of the white dwarf. If this hydrogen is truly from the accretion of a volatile-rich body in its past and isn't due to ISM accretion or is primordial, then the current abundance is conflicting. As Gaia J0644−0352 is currently accreting volatile depleted material inferred from the heavy elements, but in the past may have accreted volatile rich material, this implies that it is accreting material from a wide range of radial locations. It is highly unlikely that the current pollutant material for Gaia J0644−0352 contains significant water as oxygen budgeting reveals the heavy elements balance the oxygen and all oxygen can be in the form of metal oxides (see Fig. 4.5). This is a robust conclusion as all major rock-forming elements are detected, with between three and 11 spectral lines being used to determine the average abundance for each element. If this white dwarf did accrete a water-rich planetesimal, it did so when it was much younger, with the hydrogen remaining on the surface.

Evidence for the accretion of multiple bodies would be exciting support for the widely supported theory of the accretion of many small asteroids leading to white dwarf pollution (Turner & Wyatt, 2020). The diverse compositions in these bodies indicate that in a single system, planetary bodies can arrive onto the star from a wide range of radial locations in the planetary system. This has implications for scattering models used to explain how bodies get perturbed onto star grazing orbits, as there must be mechanisms which can stochastically scatter bodies from a wide range of orbits.

4.5.4 Are high Ca/Mg ratios explained by the accretion of a high proportion of refractory material?

Gaia J0347+1624 is accreting material with one of the highest Ca/Mg ratios observed, higher than even GD 362 (Jura & Xu, 2012). The accretion of material with high Ca/Mg could

be explained by the depletion of moderately volatile species, including Si, Mg and Fe-rich minerals, occurring at temperatures greater than 1250 K. Neither sinking nor geological processing can explain the high Ca/Mg abundance. In order to explain the observed abundances, it is hypothesised that a portion of the accreted body experienced temperatures higher than 1550 ± 20 K during formation in the inner region of the disc, much like CAIs in the solar system, or during the red giant phase of stellar evolution.

The temperature of the circumstellar dust around Gaia J0347+1624 when modelled by a single blackbody is 1760 K (Dennihy et al., 2020), the hottest dust surrounding any white dwarf with detectable circumstellar gas and dust. Fig. 4.9 shows how the Ca/Mg abundance ratio of the accreted planetary material relates to the blackbody dust temperature for white dwarfs in this study and from the literature (Dennihy et al., 2020; Rocchetto et al., 2015); there is a weak correlation between dust temperature and Ca/Mg ratio. The material accreting onto Gaia J0347+1624 is depleted in Mg-rich moderate volatiles, explaining the extreme Ca/Mg abundance, and so Gaia J0347+1624 is accreting refractory rich dust. This refractory rich dust can survive to hotter temperatures around the white dwarf explaining why the dust temperature is so extreme.

For Gaia J0347+1624, the conclusion is based on the abundance determination of two elements, where only one or two lines per element are present in the spectrum. Also, no optical spectrum is available red-ward of 6000 Å so no assessment can be made regarding more volatile species such as oxygen or sodium. It is vital to obtain follow up data to investigate the volatiles for this intriguing system.

4.5.5 Evidence for the formation of iron cores in exoplanetary systems

The high (low) Fe abundances relative to lithophile species (Ca, Mg, Si) are best explained by the accretion of a fragment that is dominated by core (mantle) material, potentially produced in a destructive collision of a larger body. Within the sample there is evidence for the accretion of core rich (Gaia J0611−6931 and Gaia J2100+2122) and possibly mantle rich (Gaia J0644−0352) exoplanetary fragments.

For Gaia J2100+2122 and Gaia J0611−6931, these conclusions are based on the enhanced iron in comparison to solar abundance. However, it is important to note that only one iron line was detected for each white dwarf, the 5169 Å line in Gaia J0611−6931 and the 3227 Å line in Gaia J2100+2122 (see Section 4.5.1). Both detections lie above solar to a significance of $> 3\,\sigma$, however, the true iron abundance may be different from that derived here. In terms of composition analysis, it is difficult to explain enhanced iron in any way other than invoking the accretion of a core-rich exoplanetary body. The maximum uncertainty for a DA white dwarf that has multiple detected lines of a particular element is 0.19 (see Table

4.3). The results are tested by including an uncertainty of 0.19 on the Fe abundance in the Bayesian models; the Fe is still significantly enhanced and differentiation is required, albeit to less significance. Upper limits for other elements are included (e.g. Cr and Ni), these are in agreement with the conclusions regarding the accretion of a core-rich fragment. For Gaia J0644−0352, on the other hand, whilst the accretion of a mantle-rich fragment is a good model for the data, as discussed in Section 4.3.5, there is insufficient evidence to rule out alternate explanations. A Ni or Cr detection might support the mantle-rich nature of the material (Harrison et al., 2018; Buchan et al., 2022).

The evidence for the accretion of up to three core-mantle differentiated fragments presented in this work indicates that core-mantle differentiation in exoplanetary systems is commonplace, as are the large destructive collisions required in these planetary systems to produce the observed fragments. Planetesimal belts are collisional systems, as witnessed by debris disc observations (e.g. Wyatt, 2021). This implies that during the post main sequence phase either massive planetesimal belts must be present, or there are high levels of collisional excitation, or both.

In the solar system, large-scale melting in asteroids is fueled by the decay of short-lived radioactive nuclides including ^{26}Al, as they are not massive enough to generate heat via gravitational potential energy (Urey, 1955; Elkins-Tanton et al., 2011). If the total mass of an accreted body is of asteroid-size, then differentiation requires the presence of a sufficient complement of short-lived radioactive nuclides such as ^{26}Al. The budget of short-lived radioactive nuclides across exoplanetary systems is unclear, with estimates ranging from suggestions that the solar system level abundances of ^{26}Al are very rare, accounting for $\sim 1\%$ of systems (Gounelle, 2015), to suggestions that solar system levels of ^{26}Al are common (Young, 2016). If the bodies accreted by white dwarfs are truly asteroid size, as indicated by the typical accretion rates observed, this would provide evidence that planetary systems enriched in short-lived radioactive nuclides are common. If the planetesimals that act as planet building blocks undergo large-scale melting and form iron cores it can inform planet formation models and in particular their volatile content, as differentiation has implications for how rocky exoplanets form.

4.5.6 Magnetic field of WD 1622+587

The first magnetic white dwarf was discovered in 1970 (Kemp et al., 1970), and since then several hundred magnetic white dwarfs have been discovered from observations of Zeeman splitting of absorption lines or by spectropolarimetry (see references in Kepler et al., 2021)). However, there are few examples of magnetic white dwarfs with atmospheric pollution and circumstellar dust and gas, and especially the absence of magnetic fields around hotter

polluted white dwarfs (>10,000 K) (Kawka & Vennes, 2014; Kawka et al., 2019; Ferrario et al., 2015; Hollands et al., 2015). WD 1622+587 is a hot DBZA white dwarf which possibly has a weak magnetic field of ∼10 kG. Schreiber et al. (2021) explains the high rate of weak magnetic fields in old metal polluted white dwarfs by beginning crystallisation of the cores. The hottest magnetic polluted white dwarf in their sample, WD 2105−820 (T∼11000 K) was explained as being massive enough that the crystallisation begins at hotter temperatures. However, at ∼18850 K and with a mass of ∼0.5 $M_{\odot}$, this explanation would not be valid for WD 1622+587. The magnetic field hypothesised here is weak, so a higher resolution spectrograph would be required to fully resolve the Zeeman splitting components of the lines and confirm the magnetic field. It should be noted that previous surveys have not had the sensitivity or resolution to probe magnetic fields down to 10 kG for polluted white dwarfs, and so it is likely that further hot polluted white dwarfs with magnetic fields are yet to be discovered.

Hogg et al. (2021) suggests that magnetic white dwarfs should circularise circumstellar dust faster due to magnetic drag forces. The disc lifetime is also decreased, for optically thick discs this occurs $>$ ∼10 kG and for optically thin discs this occurs $>$ 100 kG, a more thorough understanding of the structure and lifetime of the circumstellar disc of WD 1622+587 could help to disentangle whether the discs are predominantly optically thick or thin. Hogg et al. (2021) modelled a 10,000 K white dwarf and found that the dominant drag force on the dust changes between PR drag and magnetic drag at around 10 kG. WD 1622+587 is much hotter than 10,000 K, and as diametric drag dominance scales with inverse temperature squared, it will dominate out to a smaller radii. This would be within the sublimation radii of the white dwarf, and so it isn't expected that magnetic drag will dominate at the tidal disruption radius. Assuming the dust is optically thick, order of magnitude calculations reveal that PR drag accretion rates are broadly consistent with the accretion rate derived for WD 1622+587 in this work (Rafikov, 2011b), so given the current data, this system doesn't show evidence for enhanced accretion above that from PR drag. WD 1622+587 with a hypothesised magnetic field of $\sim$ 10 kG is an interesting case for further study on the nature of white dwarf debris discs, and the relation between magnetic drag and accretion rates.

4.6 Conclusions

This work presents X-shooter/VLT, HIRES/KECK and MIKE/Magellan optical spectroscopy of seven polluted white dwarfs that host both detectable circumstellar gas and dust emission. Calcium, and at least one other element is detected in the photosphere of each white dwarf, with the most elements detected in the atmosphere of Gaia J0644−0352 (O, Mg, Al, Si, Ca,

Ti, Cr, Fe). The observations inform processes that determine the composition of exoplanetary material, including volatile loss and core formation. The key findings are as follows:

- White dwarfs accrete planetary bodies with a range of volatile contents from dry, rocky bodies to water-rich bodies. Across the seven white dwarfs observed here, the accreted planetary material has experienced a range of temperatures, as indicated by different levels of volatile depletion observed. Planetary bodies can be perturbed onto white dwarfs from a wide range of locations across exoplanetary systems, with no particular preference for close-in orbits.
- White dwarfs with circumstellar gas are good targets for studying photospheric abundances. Not only do they accrete at high levels, yielding many detectable elements, but the distribution of accreted abundances is consistent with systems without detectable gas.
- Generally, Ca, Mg and Si abundances in the accreted material can be explained by relative sinking rates, but the accretion of highly refractory (Ca, Al-rich) material provides a plausible explanation to explain the high Ca/Mg of some white dwarfs.
- Gaia J0611−6931 has a high oxygen abundance in comparison to bulk Earth. Oxygen budgeting revealed it has likely accreted a water-rich body, potentially originating from the outer regions of the surviving planetary system.
- The material accreted by Gaia J0611−6931 appears to be both water-rich, and core-rich. Gaia J0644−0352 shows evidence for currently accreting a dry, rocky, body but, in the past, having accreted at least one water-rich body. Both these indicate that multiple bodies, from different radial locations, have been accreted by these white dwarfs.
- To explain its broad spectral lines, WD 1622+587 must have a magnetic field of at least 10 kG. This is the first 'hot' polluted white dwarf with a detected magnetic field and circumstellar gas and dust.

Chapter 5

Conclusions and Future Work

5.1 Conclusions

As we transition to an era where exoplanets are the norm rather than the exception, characterising and understand exoplanets is crucial. This thesis focused on white dwarfs polluted with planetary material as they are powerful laboratories to study the bulk composition of exoplanets, the architecture and evolution of planetary systems, and ultimately reveal the eventual fate of the solar system.

Dust provides crucial information regarding how planetary material arrives into the atmosphere of the white dwarfs. A growing number of observations reveal a shifting paradigm away from the flat, opaque disc (Jura, 2003), where PR drag causes the material to migrate inwards, sublimate, and accrete onto the white dwarf. Dust variability can reveal information about the optical depth and geometry of the circumstellar dust. Therefore, it is crucial to determine how frequently variability is within the population and at what wavelengths this variability is dominant. The first dust variability was reported in Xu & Jura (2014) where a 35 percent mid-infrared, and 18.5 percent near-infrared flux drop was observed. Motivated by this, a large near-infrared *JHK* monitoring campaign was conducted using the WFCAM/UKIRT sampling ~ 80 percent of the known white dwarfs with dust emission at the time across a time span of 3 years (as reported in Chapter 2). Surprisingly, no statistically significant variation is found in the dust emission in all three near-infrared bands. Specifically, variability at $\sim 1.3\%$ was ruled out for the 13 white dwarfs brighter than 16th mag in *K* band, and at $\sim 10\%$ for the 32 white dwarfs brighter than 18th mag over time-scales of three years. As the dust emission is stronger at 3–4 μm, some systems do not have strong *K* band emission; for those with significant *K* band excesses, any white dwarf with a similar large amplitude ($> 18.5\%$) near-infrared variability from Xu & Jura (2014) on short (< 3 year) time-scales should have been found with the survey. Additionally, a small

near-infrared monitoring campaign using the SOFI/NTT ruled out *K* band variability over timescales of hours–days for a sample of eight white dwarfs with dust emission, therefore, dust variability that leads to *K* band variability is consequently rare.

Contradictory to the near-infrared monitoring campaigns finding no variability, Swan et al. (2019a, 2020) found that most white dwarfs with infrared excesses show significant variability in the mid-infrared. If the emission of the dust in the near and mid infrared is dominated by the distance from the star rather than grain size, then the *K* band represents the closest in ($<$0.001 AU), hottest dust and the mid-infrared represents the further out, cooler dust. The cooler dust is experiencing dynamic and large variability events, but once the dust reaches the inner hot disc there is no variability. One hypothesis is that the outer disc is dominated by optically thin dust, where destructive collisions and/or tidal disruption events are occurring, therefore, explaining the extreme mid-infrared variability. As the dust collisionally grinds down and migrates via PR drag to the inner disc, physical processes are acting to stabilise the dust resulting in no *K* band variability. The inner disc may therefore be an optically thick, razor thin disc, and this can explain accretion rates up to 10^8 g. The two white dwarfs that have previously displayed *K* band variability, WD J0959−0200 and WD 1226+110, have circumstellar gas emission in additional to dust emission. If the gas is produced in the most violent collisions then this could be mimicked in the *K* band, predicting that *K* band variability would only be found in those systems with detectable levels of circumstellar gas.

Theory maintains that once this material arrives in the atmosphere of the white dwarf, the material should sink to the core (where it is not observable) on incredibly short timescales, from days to weeks for Hydrogen dominated white dwarfs (Koester, 2009). Chapter 3 reports the optical spectroscopic monitoring campaigns that were conducted for five DAZ white dwarfs with HRS/SALT and MIKE/Magellan over a total baseline of $\sim$ 14 years. The equivalent widths of the metal absorption lines were calculated; for four of the five white dwarfs no statistically significant variation in the equivalent widths were observed. For one of the white dwarfs, WD 0106−328, these data were inconclusive. Therefore, no unambiguous change in the amount of material present in the white dwarf photosphere and therefore accretion rate was observed. This implies that either the processes which maintain the accretion of the planetary material are surprisingly stable, or there are unknown mechanisms in the white dwarf photospheres that are acting to increase the sinking timescales and therefore result in no variability.

Combining the results from Chapter 2 on the near-infrared monitoring, and Chapter 3 on the metal line monitoring, inferences can be made about the accretion disc of metallic gas. Although theory predicts this accretion disc as a vessel for the accretion of material from

the circumstellar dust disc to the atmosphere, it has not been observed. Chapter 3 reports no change in the amount of material present in the atmosphere of the white dwarf implying the accretion rate onto the white dwarf is constant. If the hypothesis of the inner disc being stable is true, as inferred from the near infrared monitoring in Chapter 2, it predicts that the material leaves the dust disc and arrives in the atmosphere at a constant rate and the accretion disc just acts as a vessel for the accretion. However, if this hypothesis is incorrect and the entire dust disc is dynamic and variable (with variability hidden from *K* band studies), then the metallic accretion disc must be acting to dampen out dust variability via gas viscosity for it to arrive in the atmosphere at a constant rate.

Previous works have argued that gas drag may cause enhanced accretion rates above what may be expected from PR drag alone (e.g. Rafikov, 2011a). If this is the case, and the gaseous emission is higher at the same radial location as the dust, then white dwarfs with circumstellar gaseous discs should be accreting at higher levels in comparison to the population. Chapter 4 reports the accretion rates of the bodies accreting onto white dwarfs with circumstellar gas discs. The range of accretion rates of those systems with gaseous discs spans a similar range to those without, with both high accretors and low accretors. These results hint that the presence of gas does not affect the accretion rate, however, due to small number statistics, definitive conclusions are impossible.

As more polluted white dwarfs are discovered with *Gaia* and large spectroscopic surveys, it is crucial to ensure that the most promising systems are followed up with high resolution spectroscopy such that in depth studies of the pollutant composition and geological history can be studied. We are transitioning to an era of population statistics, and it is imperative to include these highly polluted white dwarfs in the statistics. Chapter 4 reports abundances for the exoplanetary material that were accreted by seven white dwarfs which all have circumstellar gaseous discs. Circumstellar dust and gas around white dwarfs tell us about the current, potentially violent accretion of planetary material. These systems are extreme examples of polluted white dwarfs, and as such they are perfect targets for studying high levels of pollution in their atmospheres. These white dwarfs with gas discs all reveal multiple detected elements from ground based optical spectroscopy. Solar system material appears commonplace in exoplanetary systems as all but one of the white dwarfs has an equivalent composition within the solar system. Gaia J0006+2858 and WD 1622+587 have refractory compositions close to that of bulk Earth. Gaia J0644−0352 and Gaia J2100+2122 have compositions consistent with accreting material similar to Earth's mantle and core respectively. Core-mantle differentiation with an iron rich core and iron poor mantle, and disruptive collisions appear commonplace in exoplanetary systems, agreeing with previous findings (e.g. Bonsor et al., 2020). Gaia J0510+2315 is accreting a rocky body enhanced

in volatiles similar to volatile-rich bodies in the Kuiper-belt. Gaia J0347+1624 is refractory rich with a [Ca/Mg] of 0.09, few white dwarfs have such extreme [Ca/Mg] ratios (Jura & Xu, 2012), in the solar system CAI's have even more extreme [Ca/Mg] ratios, these formed in the inner regions of the solar system during formation under high temperatures. The high [Ca/Mg] may also explain the high blackbody temperature of its dust emission as these refractory grains can survive closer in to the white dwarf. Gaia J0611−6931 appears to be both core-rich and water-rich with abundances that don't fit with bulk abundances of a single body in the solar system.

Gaia J0510+2315 and Gaia J0611−6931 have swallowed a body with exceptionally high oxygen in comparison to bulk Earth, these bodies were likely rich in water. This adds to the handful of other white dwarfs which also show evidence for the accretion of volatile-rich exoplanetary material. The discovery of water-rich planetesimals in other planetary systems is crucial as it informs us that volatile rich bodies can survive formation, and subsequent evolution, and can deliver volatiles to planetary systems as late as in the white dwarf phase. For the Earth, volatiles are crucial for life, but it is hypothesised that the Earth formed dry and accreted volatiles later. Additional discoveries of water rich planetary bodies across the Milky Way, can be linked to questions regarding terrestrial and extra-terrestrial life.

When analysing the abundances of the body that was accreted by the white dwarf, it is assumed to be a single body accreting from one reservoir of planetesimals. However, Chapter 4 highlights two examples where this may not be the case. The material accreted by Gaia J0611−6931 appears to be both water-rich, and core-rich. Gaia J0644−0352 shows evidence for currently accreting a dry, rocky, body but in the past having accreted at least one water-rich body. These findings indicate that it is likely that the assumption of a single body being accreted by the white dwarf is incorrect for some systems, providing evidence for the predicted accretion of many smaller bodies with high probabilities of observing multiple bodies in the white dwarf at any one time (e.g. Turner & Wyatt, 2020). Also, as both white dwarfs may be accreting bodies from different radial locations, this can give an insight into the architecture of these exoplanetary systems. In depth modelling which can perturb bodies from both the inner and outer system towards the white dwarf are required to explain these observations.

5.2 Future Work

Dust emission

The discovery of ubiquitous mid-IR variability with *Spitzer* (Swan et al., 2020) was shortly followed by operations ending in January 2020. No telescope will have the resolution and

capabilities to perform a large mid-infrared monitoring campaign of white dwarfs with circumstellar dust on short cadences. *neoWISE* will continue to survey the sky in the mid-infrared with a cadence of 6 months, due to the large pixel sizes further high resolution imaging is needed to rule out contaminants in the field of view. Nonetheless, for those systems that are already known to be free from contaminants, *neoWISE* will be a useful resource to continue variability searches. As the near-infrared is accessible with ground based high resolution imaging instruments, large monitoring campaigns using the near-infrared are more technically feasible. The two white dwarfs which have previously shown *K* band variability (WD J0959−0200 and WD 1226+110) had observations separated by 7–8 years (although it should be noted no intermittent observations were conducted). Therefore, following up the targets with the most significant *K* band excesses on decade long timescales will provide useful insight into whether *K* band variability is the norm or the exception. Also, targeting systems with known gaseous emission discs may reveal whether *K* band variability only occurs when the most violent collisions occur. In order to understand the link between the near and mid infrared, and what this means about the distribution, temperature, and grain size of the dust, it is crucial to obtain mid-infrared spectroscopy and perform in depth modelling of the dust. The *JWST* MIRI instrument spans a wavelength range of 5–28.5μm covering a large number of dust mineralogy features, allowing in depth studies of the circumstellar dust. It will be particularly useful to obtain dust mineralogy for those systems with both circumstellar dust and gas discs as the planetary material can be compared between the dust, gas and the pollution. Gaia J0611−6931 is a particularly good target for this as it has the most elements detected in emission in a gaseous disc, and it is heavily polluted. Recent COS/Hubble UV spectra (PI: Rogers) of Gaia J0611−6931 have revealed a myriad of pollution lines allowing further in depth analysis into the composition of the pollutant.

Monitoring metal lines

No unambiguous variability was found in the amount of material present in the photospheres of five DAZ white dwarfs over timescales of > 10 years. In order to conclusively determine whether the equivalent width of the Mg II doublet varied in WD 0106−328, follow-up MIKE/Magellan data is required. Theoretical efforts must be dedicated to resolving the accretion and diffusion processes to explain the lack of variability considering diffusion timescales of days. For example, further investigations into mixing processes in the photosphere of white dwarfs. Recent X-ray observations of G29-38 revealed the X-ray luminosity and therefore instantaneous accretion rate of material onto the white dwarf, independent of stellar atmosphere models (Cunningham et al., 2022). The X-ray observations were taken between 22 and 27 September 2020, optical ground based spectra from HRS/SALT of G29-38 were obtained

two weeks before, and one month after (as reported in Chapter 3). The sinking timescales for G29-38 are of the order of 2–3 months, therefore, no changes should be expected between the photosphere as measured by HRS/SALT and at the time of the X-ray observations. Therefore, these spectra can be used to investigate the link between instantaneous accretion rates and the accretion rates inferred from the photosphere. Follow-up X-ray observations of G29-38 may be more fruitful to investigate whether there is variability in the instantaneous accretion rate, as this is independent of atmospheric models.

Increase the number of well studied polluted white dwarfs.

With $>$ 350,000 white dwarfs discovered with *Gaia* eDR3 (Gentile Fusillo et al., 2021) and large spectroscopic follow-up surveys (e.g. 4MOST, WEAVE, DESI, SDSS-V), thousands of new polluted white dwarfs will be discovered. It is crucial that once identified, the most promising polluted white dwarfs are followed up with high resolution ground-based spectrographs, and space-based UV spectrographs to ensure the new polluted white dwarfs are well studied and characterised. With increased numbers of polluted white dwarfs, unbiased samples can be created such that the bulk composition of exoplanets, and their distribution across the galaxy, can be well studied. Currently, there are only 19 systems with detections or stringent upper limits of C and O, 42 systems are required in order to distinguish the distribution of these volatiles across exoplanets. Future Hubble observations in the upcoming cycle (PI: Rogers) will reach this number. Also, as mentioned previously, there are insufficient numbers of white dwarfs with detectable gas discs, and especially those with derived abundances for multiple elements. To conclusively discover whether white dwarfs with circumstellar gas have enhanced accretion rates due to gas drag, the number of gas systems discovered and characterised needs to be at least doubled. With upcoming large spectroscopic surveys, this number will drastically increase.

References

Adams F. C., Laughlin G., 1997, Reviews of Modern Physics, 69, 337

Alexander C. M., McKeegan K. D., Altwegg K., 2018, Space science reviews, 214, 1

Armstrong B., 1967, Journal of Quantitative Spectroscopy and Radiative Transfer, 7, 61

Ballhaus C., et al., 2013, EPSL, 362, 237

Barber S. D., Kilic M., Brown W. R., Gianninas A., 2014, ApJ, 786, 77

Barnes S., et al., 2008, in Ground-based and Airborne Instrumentation for Astronomy II. pp 247–258

Barstow M. A., Barstow J., Casewell S., Holberg J., Hubeny I., 2014, MNRAS, 440, 1607

Batalha N. M., 2014, Proceedings of the National Academy of Sciences, 111, 12647

Bauer E. B., Bildsten L., 2018, ApJL, 859, L19

Bauer E. B., Bildsten L., 2019, ApJ, 872, 96

Becklin E., Farihi J., Jura M., Song I., Weinberger A., Zuckerman B., 2005, ApJL, 632, L119

Belardi C., Kilic M., Munn J. A., Gianninas A., Barber S. D., Dey A., Stetson P. B., 2016, MNRAS, 462, 2506

Bergeron P., Saffer R. A., Liebert J., 1992, ApJ, 394, 228

Bergeron P., Wesemael F., Dufour P., Beauchamp A., Hunter C., et al., 2011, ApJ, 737, 28

Bergeron P., Dufour P., Fontaine G., Coutu S., Blouin S., Genest-Beaulieu C., Bédard A., Rolland B., 2019, ApJ, 876, 67

Bergfors C., Farihi J., Dufour P., Rocchetto M., 2014, MNRAS, 444, 2147

Bernstein R., Shectman S. A., Gunnels S. M., Mochnacki S., Athey A. E., 2003, in Instrument Design and Performance for Optical/Infrared Ground-based Telescopes. pp 1694–1704

Bizzarro M., Connelly J. N., Krot A. N., 2017, in , Formation, evolution, and dynamics of young solar systems. Springer, pp 161–195

Blackman J., et al., 2021, Nature, 598, 272

Bonsor A., Wyatt M., 2010, MNRAS, 409, 1631

Bonsor A., Mustill A., Wyatt M. C., 2011, MNRAS, 414, 930

Bonsor A., Farihi J., Wyatt M. C., van Lieshout R., 2017, MNRAS, 468, 154

Bonsor A., Carter P. J., Hollands M., Gänsicke B. T., Leinhardt Z., Harrison J. H., 2020, MNRAS, 492, 2683

Borucki W. J., et al., 2010, Science, 327, 977

Brahic A., 1977, A&A, 54, 895

Brewer J. M., Fischer D. A., 2016, ApJ, 831, 20

Brinkworth C., Gänsicke B. T., Marsh T., Hoard D. W., Tappert C., 2009, ApJ, 696, 1402

Brinkworth C., Gänsicke B., Girven J., Hoard D., Marsh T., Parsons S., Koester D., 2012, ApJ, 750, 86

Brouwers M. G., Bonsor A., Malamud U., 2022, MNRAS, 509, 2404

Brown J. C., Veras D., Gänsicke B. T., 2017, MNRAS, 468, 1575

Brown A., Vallenari A., Prusti T., De Bruijne J., Babusiaux C., Bailer-Jones C., Biermann M., et al., 2018, A & A, 616, A1

Buchan A. M., Bonsor A., Shorttle O., Wade J., Harrison J., Noack L., Koester D., 2022, MNRAS, 510, 3512

Budde G., Burkhardt C., Brennecka G. A., Fischer-Gödde M., Kruijer T. S., Kleine T., 2016, EPSL, 454, 293

Burns J. A., Lamy P. L., Soter S., 1979, Icarus, 40, 1

Carpenter J. M., 2001, AJ, 121, 2851

Carroll B. W., Ostlie D. A., 2017, An introduction to modern astrophysics. Cambridge University Press

Cassan A., et al., 2012, Nature, 481, 167

Charbonneau D., Brown T. M., Latham D. W., Mayor M., 1999, ApJ, 529, L45

Chayer P., Fontaine G., Wesemael F., 1995a, ApJS, 99, 189

Chayer P., Vennes S., Pradhan A., Thejll P., Beauchamp A., Fontaine G., Wesemael F., 1995b, ApJ, 454, 429

Chu Y.-H., et al., 2011, AJ, 142, 75

Collaboration G., et al., 2016, arXiv preprint arXiv:1609.04153

Collaboration G., et al., 2022, A & A

Connelly J. N., Bizzarro M., Krot A. N., Nordlund Å., Wielandt D., Ivanova M. A., 2012, Science, 338, 651

Coutu S., Dufour P., Bergeron P., Blouin S., Loranger E., Allard N., Dunlap B., 2019, ApJ, 885, 74

Crossfield I. J., 2015, PASP, 127, 941

Cunningham T., Tremblay P.-E., Freytag B., Ludwig H.-G., Koester D., 2019, MNRAS, 488, 2503

Cunningham T., et al., 2021, MNRAS, 503, 1646

Cunningham T., Wheatley P. J., Tremblay P.-E., Gänsicke B. T., King G. W., Toloza O., Veras D., 2022, Nature, 602, 219

Davidsson B. J., 1999, Icarus, 142, 525

Debes J. H., López-Morales M., 2008, ApJ, 677, L43

Debes J. H., Sigurdsson S., 2002, ApJ, 572, 556

Debes J. H., Hoard D., Wachter S., Leisawitz D. T., Cohen M., 2011, ApJS, 197, 38

Debes J. H., Walsh K. J., Stark C., 2012a, ApJ, 747, 148

Debes J., Kilic M., Faedi F., Shkolnik E., Lopez-Morales M., Weinberger A., Slesnick C., West R. G., 2012b, ApJ, 754, 59

Dennihy E., Debes J. H., Dunlap B., Dufour P., Teske J. K., Clemens J., 2016, ApJ, 831, 31

Dennihy E., Clemens J., Debes J. H., Dunlap B., Kilkenny D., O'Brien P., Fuchs J., 2017, ApJ, 849, 77

Dennihy E., Clemens J., Dunlap B., Fanale S., Fuchs J., Hermes J., 2018, ApJ, 854, 40

Dennihy E., et al., 2020, arXiv preprint arXiv:2010.03693

Dones L., 1991, Icarus, 92, 194

Dorn C., Khan A., Heng K., Connolly J. A., Alibert Y., Benz W., Tackley P., 2015, Astronomy & Astrophysics, 577, A83

Doyle A. E., Young E. D., Klein B., Zuckerman B., Schlichting H. E., 2019, Science, 366, 356

Dufour P., Kilic M., Fontaine G., Bergeron P., Melis C., Bochanski J., 2012, ApJ, 749, 6

Dufour P., et al., 2015, in Astron. Soc. Pac. Conf. Ser. p. 37

Dufour P., Blouin S., Coutu S., Fortin-Archambault M., Thibeault C., Bergeron P., Fontaine G., 2017, ASPC, 509, 3

Dupuis J., Fontaine G., Wesemael F., 1993, ApJS, 87, 345

Dye S., Warren S., Hambly N., Cross N., Hodgkin S., Irwin M., Lawrence A., et al., 2006, MNRAS, 372, 1227

Eisenstein D. J., et al., 2006, ApJS, 167, 40

Elkins-Tanton L. T., 2012, Annual Review of EPS, 40, 2012

Elkins-Tanton L. T., Weiss B. P., Zuber M. T., 2011, EPSL, 305, 1

Farihi J., Zuckerman B., Becklin E., 2008, ApJ, 674, 431

Farihi J., Jura M., Zuckerman B., 2009, ApJ, 694, 805

Farihi J., Barstow M., Redfield S., Dufour P., Hambly N., 2010a, MNRAS, 404, 2123

Farihi J., Jura M., Lee J.-E., Zuckerman B., 2010b, ApJ, 714, 1386

Farihi J., Brinkworth C., Gänsicke B., Marsh T., Girven J., Hoard D., Klein B., Koester D., 2011, ApJL, 728, L8

Farihi J., Gänsicke B., Steele P., Girven J., Burleigh M., Breedt E., Koester D., 2012a, MNRAS, 421, 1635

Farihi J., Gänsicke B., Wyatt M., Girven J., Pringle J., King A., 2012b, MNRAS, 424, 464

Farihi J., Gänsicke B., Koester D., 2013, Science, 342, 218

Farihi J., Wyatt M., Greaves J., Bonsor A., Sibthorpe B., Panić O., 2014, MNRAS, 444, 1821

Farihi J., Parsons S., Gänsicke B., 2017, Nature Astronomy, 1, 0032

Farihi J., van Lieshout R., Cauley P., Dennihy E., Su K., Kenyon S., et al., 2018, MNRAS, 481, 2601

Ferrario L., de Martino D., Gänsicke B. T., 2015, Space Science Reviews, 191, 111

Fischer D. A., Howard A. W., Laughlin G. P., Macintosh B., Mahadevan S., Sahlmann J., Yee J. C., 2015, arXiv preprint arXiv:1505.06869

Fontaine G., Michaud G., 1979, ApJ, 231, 826

Fontaine G., Brassard P., Bergeron P., 2001, PASP, 113, 409

Freudling W., Romaniello M., Bramich D. M., Ballester P., Forchi V., García-Dabló C. E., Moehler S., Neeser M. J., 2013, , 559, A96

Gänsicke B. T., Marsh T., Southworth J., Rebassa-Mansergas A., 2006, Science, 314, 1908

Gänsicke B., Marsh T., Southworth J., 2007, MNRAS:L, 380, L35

Gänsicke B., Koester D., Marsh T., Rebassa-Mansergas A., Southworth J., 2008, MNRAS:L, 391, L103

Gänsicke B., Koester D., Farihi J., Girven J., Parsons S., Breedt E., 2012, MNRAS, 424, 333

Gänsicke B. T., Schreiber M. R., Toloza O., Fusillo N. P. G., Koester D., Manser C. J., 2019, Nature, 576, 61

Gary B., Rappaport S., Kaye T., Alonso R., Hambschs F.-J., 2017, MNRAS, 465, 3267

Gaudi B. S., 2012, Annual Review of Astronomy and Astrophysics, 50, 2012

Gelman A., Rubin D. B., et al., 1992, Statistical science, 7, 457

Genest-Beaulieu C., Bergeron P., 2019, ApJ, 871, 169

Gentile Fusillo N., et al., 2015, MNRAS, 452, 765

Gentile Fusillo N. P., Gänsicke B. T., Farihi J., Koester D., Schreiber M. R., Pala A. F., 2017, MNRAS, 468, 971

Gentile Fusillo N. P., Tremblay P.-E., Gänsicke B. T., Manser C. J., Cunningham T., Cukanovaite E., et al., 2018, MNRAS, 482, 4570

Gentile Fusillo N., et al., 2020, arXiv e-prints, pp arXiv–2010

Gentile Fusillo N., et al., 2021, MNRAS, 508, 3877

Gianninas A., Bergeron P., Ruiz M. T., 2011, ApJ, 743, 138

Girven J., Brinkworth C., Farihi J., Gänsicke B., Hoard D., Marsh T., Koester D., 2012, ApJ, 749, 154

Gounelle M., 2015, A & A, 582, A26

Graham J. R., Matthews K., Neugebauer G., Soifer B., 1990, ApJ, 357, 216

Grevesse N., Asplund M., Sauval A., 2007, Space Science Reviews, 130, 105

Guerrero N. M., et al., 2021, ApJSS, 254, 39

Hallis L., 2017, Philosophical Transactions of the Royal Society A: Mathematical, Physical and Engineering Sciences, 375, 20150390

Hamers A. S., Portegies Zwart S. F., 2016, MNRAS:L, 462, L84

Hansen B. M., Liebert J., 2003, Annual Review of A&A, 41, 465

Hardy F., Dufour P., Jordan S., 2017, in 20th European White Dwarf Workshop. p. 205

Harrison J. H., Bonsor A., Madhusudhan N., 2018, MNRAS, 479, 3814

Harrison J. H., Bonsor A., Kama M., Buchan A. M., Blouin S., Koester D., 2021, MNRAS, 504, 2853

Hayashi C., 1981, Progress of Theoretical Physics Supplement, 70, 35

Hevey P. J., Sanders I. S., 2006, Meteoritics & Planetary Science, 41, 95

Hewett P. C., Warren S. J., Leggett S. K., Hodgkin S. T., 2006, MNRAS, 367, 454

Hinkel N. R., Timmes F., Young P. A., Pagano M. D., Turnbull M. C., 2014, AJ, 148, 54

Hogg M. A., Cutter R., Wynn G., 2021, MNRAS, 500, 2986

Holberg J., Wesemael F., Wegner G., Bruhweiler F., 1985, ApJ, 293, 294

Hollands M., Gänsicke B., Koester D., 2015, MNRAS, 450, 681

Hollands M., Koester D., Alekseev V., Herbert E., Gänsicke B. T., 2017, MNRAS, 467, 4970

Hollands M., Gänsicke B., Koester D., 2018, MNRAS, 477, 93

Hoskin M. J., et al., 2020, MNRAS, 499, 171

Irwin M. J., et al., 2004, in Optimizing scientific return for astronomy through information technologies. pp 411–422

Irwin J., Irwin M., Aigrain S., Hodgkin S., Hebb L., Moraux E., 2007, MNRAS, 375, 1449

Izquierdo P., Toloza O., Gänsicke B. T., Rodríguez-Gil P., Farihi J., Koester D., Guo J., Redfield S., 2021, MNRAS, 501, 4276

Jura M., 2003, ApJL, 584, L91

Jura M., 2006, ApJ, 653, 613

Jura M., 2008, AJ, 135, 1785

Jura M., Xu S., 2012, AJ, 145, 30

Jura M., Young E., 2014, AREPS, 42, 45

Jura M., Farihi J., Zuckerman B., Becklin E., 2007a, AJ, 133, 1927

Jura M., Farihi J., Zuckerman B., 2007b, ApJ, 663, 1285

Jura M., Farihi J., Zuckerman B., 2009a, AJ, 137, 3191

Jura M., Muno M., Farihi J., Zuckerman B., 2009b, ApJ, 699, 1473

Jura M., Dufour P., Xu S., Zuckerman B., Klein B., Young E., Melis C., 2015, ApJ, 799, 109

Kawka A., Vennes S., 2014, MNRAS: Letters, 439, L90

Kawka A., Vennes S., Ferrario L., Paunzen E., 2019, MNRAS, 482, 5201

Kelson D. D., 2003, PASP, 115, 688

Kelson D. D., Illingworth G. D., van Dokkum P. G., Franx M., 2000, ApJ, 531, 159

Kemp J. C., Swedlund J. B., Landstreet J., Angel J., 1970, ApJ, 161, L77

Kenyon S. J., Bromley B. C., 2017a, ApJ, 844, 116

Kenyon S. J., Bromley B. C., 2017b, ApJ, 850, 50

Kepler S., Koester D., Pelisoli I., Romero A. D., Ourique G., 2021, MNRAS, 507, 4646

Kilic M., von Hippel T., Leggett S., Winget D., 2005, ApJ, 632, L115

Kilic M., von Hippel T., Leggett S., Winget D., 2006, ApJ, 646, 474

Klein B., Jura M., Koester D., Zuckerman B., Melis C., 2010, ApJ, 709, 950

Klein B., Jura M., Koester D., Zuckerman B., 2011, ApJ, 741, 64

Klein B. L., Doyle A. E., Zuckerman B., Dufour P., Blouin S., Melis C., Weinberger A. J., Young E. D., 2021, ApJ, 914, 61

Kleine T., Budde G., Burkhardt C., Kruijer T., Worsham E., Morbidelli A., Nimmo F., 2020, Space Science Reviews, 216, 1

Kleinman S. J., et al., 1998, ApJ, 495, 424

Kniazev A., Gvaramadze V., Berdnikov L., 2016, MNRAS, 459, 3068

Kniazev A. Y., Gvaramadze V. V., Berdnikov L. N., 2017, in Balega Y. Y., Kudryavtsev D. O., Romanyuk I. I., Yakunin I. A., eds, Astronomical Society of the Pacific Conference Series Vol. 510, Stars: From Collapse to Collapse. p. 480 (arXiv:1612.00292)

Koester D., 2009, A&A, 498, 517

Koester D., Chanmugam G., 1990, Rep. Prog. Phys., 53, 837

Koester D., Kepler S. O., 2015, A & A, 583, A86

Koester D., Napiwotzki R., Voss B., Homeier D., Reimers D., 2005, A & A, 439, 317

Koester D., Girven J., Gänsicke B., Dufour P., 2011, A & A, 530, A114

Koester D., Gaensicke B. T., Farihi J., 2014, A&A, 566, A34

Koester D., Kepler S., Irwin A., 2020, A & A, 635, A103

Lacombe P., Liebert J., Wesemael F., Fontaine G., 1983, ApJ, 272, 660

Lai S., et al., 2021, ApJ, 920, 156

Lichtenberg T., Golabek G. J., Burn R., Meyer M. R., Alibert Y., Gerya T. V., Mordasini C., 2019, Nature Astronomy, 3, 307

Lodders K., 2003, ApJ, 591, 1220

Lomb N. R., 1976, Astrophysics and space science, 39, 447

Longstaff E., Casewell S., Wynn G., Page K., Williams P., Braker I., Maxted P., 2019, MNRAS, 484, 2566

Madhusudhan N., 2019, arXiv preprint arXiv:1904.03190

Madhusudhan N., Nixon M. C., Welbanks L., Piette A. A., Booth R. A., 2020, ApJL, 891, L7

Manser C. J., Gänsicke B. T., Marsh T. R., Veras D., Koester D., Breedt E., et al., 2015, MNRAS, 455, 4467

Manser C. J., et al., 2016a, MNRAS, 455, 4467

Manser C. J., Gänsicke B. T., Koester D., Marsh T. R., Southworth J., 2016b, MNRAS, 462, 1461

Manser C. J., Gänsicke B. T., Eggl S., Hollands M., Izquierdo P., Koester D., et al., 2019, Science, 364, 66

Manser C. J., Gänsicke B. T., Gentile Fusillo N. P., Ashley R., Breedt E., Hollands M., Izquierdo P., Pelisoli I., 2020, MNRAS, 493, 2127

Marino S., 2022, arXiv preprint arXiv:2202.03053

Mayor M., Queloz D., 1995, Nature, 378, 355

McCook G. P., Sion E. M., 1999, ApJS, 121, 1

McDonald C. H., Veras D., 2021, MNRAS, 506, 4031

McDonough W., 2003a, Treatise on geochemistry, 2, 547

McDonough W., 2003b, Treatise on geochemistry, 2, 568

Melis C., Dufour P., 2016, ApJ, 834, 1

Melis C., Jura M., Albert L., Klein B., Zuckerman B., 2010, ApJ, 722, 1078

Melis C., Farihi J., Dufour P., Zuckerman B., Burgasser A. J., Bergeron P., Bochanski J., Simcoe R., 2011, ApJ, 732, 90

Melis C., Dufour P., Farihi J., Bochanski J., Burgasser A. J., Parsons S., Gänsicke B., et al., 2012, ApJL, 751, L4

Melis C., Klein B., Doyle A. E., Weinberger A., Zuckerman B., Dufour P., 2020, arXiv preprint arXiv:2010.03695

Mestel L., 1952, MNRAS, 112, 583

Metzger B. D., Rafikov R. R., Bochkarev K. V., 2012, MNRAS, 423, 505

Michel P., DeMeo F. E., Bottke W. F., 2015, Asteroids iv. University of Arizona Press

Mittlefehldt D. W., McCoy T. J., Goodrich C. A., Kracher A., 1998, Reviews in Mineralogy and Geochemistry

Morbidelli A., Chambers J., Lunine J., Petit J.-M., Robert F., Valsecchi G., Cyr K., 2000, Meteoritics & Planetary Science, 35, 1309

Morbidelli A., Lunine J. I., O'Brien D. P., Raymond S. N., Walsh K. J., 2012, Annual Review of EPS, 40, 251

Mustill A. J., Villaver E., 2012, ApJ, 761, 121

Mustill A. J., Villaver E., Veras D., Gänsicke B. T., Bonsor A., 2018, MNRAS, 476, 3939

Nava C., López-Morales M., Haywood R. D., Giles H. A., 2019, AJ, 159, 23

Patil A., Huard D., Fonnesbeck C. J., 2010, Journal of statistical software, 35, 1

Payne M. J., Veras D., Holman M. J., Gänsicke B. T., 2016, MNRAS, 457, 217

Pelletier C., Fontaine G., Wesemael F., Michaud G., Wegner G., 1986, ApJ, 307, 242

Petrovich C., Muñoz D. J., 2017, ApJ, 834, 116

Prusti T., De Bruijne J., Brown A. G., Vallenari A., Babusiaux C., Bailer-Jones C., et al., 2016, A & A, 595, A1

Quanz S. P., et al., 2021, arXiv preprint arXiv:2101.07500

Raddi R., Gänsicke B., Koester D., Farihi J., Hermes J., Scaringi S., Breedt E., Girven J., 2015, MNRAS, 450, 2083

Rafikov R. R., 2011a, MNRAS, 416, L55

Rafikov R. R., 2011b, ApJL, 732, L3

Rajpaul V., Aigrain S., Osborne M. A., Reece S., Roberts S., 2015, MNRAS, 452, 2269

Rappaport S., Gary B., Kaye T., Vanderburg A., Croll B., Benni P., Foote J., 2016, MNRAS, 458, 3904

Rappaport S., Gary B., Vanderburg A., Xu S., Pooley D., Mukai K., 2017, MNRAS, 474, 933

Raymond S. N., Izidoro A., 2017, Icarus, 297, 134

Raymond S. N., Morbidelli A., 2022, in , Demographics of Exoplanetary Systems. Springer, pp 3–82

Reach W. T., Kuchner M. J., von Hippel T., Burrows A., Mullally F., Kilic M., Winget D., 2005, ApJL, 635, L161

Reach W. T., Lisse C., von Hippel T., Mullally F., 2009, ApJ, 693, 697

Rebassa-Mansergas A., Solano E., Xu S., Rodrigo C., Jiménez-Esteban F., Torres S., 2019, MNRAS, 489, 3990

Robertson H., 1937, MNRAS, 97, 423

Rocchetto M., Farihi J., Gänsicke B., Bergfors C., 2015, MNRAS, 449, 574

Rogers L. K., Xu S., Bonsor A., Hodgkin S., Su K. Y., von Hippel T., Jura M., 2020, MNRAS, 494, 2861

Rubie D. C., et al., 2011, EPSL, 301, 31

Sanderson H., Bonsor A., Mustill A. J., 2022, arXiv preprint arXiv:2206.02505

Scargle J. D., 1982, ApJ, 263, 835

Schreiber M. R., Belloni D., Gänsicke B. T., Parsons S. G., 2021, MNRAS: Letters, 506, L29

Scott E. R., 2007, Annual Review of EPS, 35, 577

Seager S., Kuchner M., Hier-Majumder C., Militzer B., 2007, ApJ, 669, 1279

Smallwood J. L., Martin R. G., Livio M., Lubow S. H., 2018, MNRAS, 480, 57

Sohl F., Schubert G., 2007, Planets and Moons. Treatise on Geophysics, 10, 27

Stark J., 1913, Nature, 92, 401

Steckloff J. K., Debes J., Steele A., Johnson B., Adams E. R., Jacobson S. A., Springmann A., 2021, ApJ:L, 913, L31

Steele A., Debes J., Xu S., Yeh S., Dufour P., 2021, ApJ, 911, 25

Stephan A. P., Naoz S., Zuckerman B., 2017, ApJL, 844, L16

Su K. Y., et al., 2007, ApJL, 657, L41

Swan A., Farihi J., Wilson T. G., 2019a, MNRAS:L, 484, L109

Swan A., Farihi J., Koester D., Hollands M., Parsons S., Cauley P. W., Redfield S., Gänsicke B. T., 2019b, MNRAS, 490, 202

Swan A., Farihi J., Wilson T. G., Parsons S. G., 2020, arXiv preprint arXiv:2006.05999

Swan A., Kenyon S. J., Farihi J., Dennihy E., Gänsicke B. T., Hermes J., Melis C., von Hippel T., 2021, MNRAS, 506, 432

Tody D., 1986, in Instrumentation in astronomy VI. pp 733–748

Trierweiler I. L., Doyle A. E., Melis C., Walsh K. J., Young E. D., 2022, arXiv preprint arXiv:2205.07935

Turner S. G., Wyatt M. C., 2020, MNRAS, 491, 4672

Urey H. C., 1955, Proceedings of the National Academy of Sciences of the United States of America, 41, 127

Van Dishoeck E. F., Bergin E. A., Lis D. C., Lunine J. I., 2014, arXiv preprint arXiv:1401.8103

Van Horn H., 1971, in Symposium-International Astronomical Union. pp 97–115

Van Maanen A., 1917, PASP, 29, 258

VanderPlas J. T., 2018, ApJSS, 236, 16

Vanderbosch Z. P., et al., 2021, ApJ, 917, 41

Vanderburg A., Johnson J. A., Rappaport S., Bieryla A., Irwin J., et al., 2015, Nature, 526, 546

Vanderburg A., Plavchan P., Johnson J. A., Ciardi D. R., Swift J., Kane S. R., 2016, MNRAS, 459, 3565

Vanderburg A., et al., 2020, Nature, 585, 363

Vauclair G., Vauclair S., Greenstein J., 1979, A&A, 80, 79

Veras D., Wyatt M. C., Mustill A. J., Bonsor A., Eldridge J. J., 2011, MNRAS, 417, 2104

Veras D., Mustill A. J., Bonsor A., Wyatt M. C., 2013, MNRAS, 431, 1686

Veras D., Leinhardt Z. M., Bonsor A., Gänsicke B. T., 2014, MNRAS, 445, 2244

Veras D., Leinhardt Z. M., Eggl S., Gänsicke B. T., 2015, MNRAS, 451, 3453

Veras D., Georgakarakos N., Dobbs-Dixon I., Gänsicke B. T., 2016, MNRAS, 465, 2053

Vernet J., et al., 2011, A & A, 536, A105

Villaver E., Livio M., 2007, ApJ, 661, 1192

Vogt S. S., et al., 1994, in Instrumentation in Astronomy VIII. pp 362–375

Voss B., Koester D., Napiwotzki R., Christlieb N., Reimers D., 2007, A & A, 470, 1079

Wänke H., 1981, Philosophical Transactions of the Royal Society of London. Series A, Mathematical and Physical Sciences, 303, 287

Warren P. H., 2011, EPSL, 311, 93

Weisberg M. K., McCoy T. J., Krot A. N., et al., 2006, Meteorites and the early solar system II, 19, 19

Wilson D. J., Gänsicke B. T., Koester D., Raddi R., Breedt E., Southworth J., Parsons S. G., 2014, MNRAS, 445, 1878

Wilson D. J., Gänsicke B. T., Koester D., Toloza O., Pala A. F., Breedt E., Parsons S. G., 2015, MNRAS, 451, 3237

Wilson D. J., Gänsicke B. T., Farihi J., Koester D., 2016, MNRAS, 459, 3282

Wilson T. G., Farihi J., Gänsicke B. T., Swan A., 2019, MNRAS, 487, 133

Wolszczan A., Frail D. A., 1992, Nature, 355, 145

Wood B. J., Wade J., Kilburn M. R., 2008, Geochimica et Cosmochimica Acta, 72, 1415

Wyatt M. C., 2021, arXiv preprint arXiv:2110.04319

Wyatt M., Farihi J., Pringle J., Bonsor A., 2014, MNRAS, 439, 3371

Xu S., Bonsor A., 2021, arXiv preprint arXiv:2108.08384

Xu S., Jura M., 2012, ApJ, 745, 88

Xu S., Jura M., 2014, ApJL, 792, L39

Xu S., Jura M., Klein B., Koester D., Zuckerman B., 2013, ApJ, 766, 132

Xu S., Jura M., Koester D., Klein B., Zuckerman B., 2014, ApJ, 783, 79

Xu S., Ertel S., Wahhaj Z., Milli J., Scicluna P., Bertrang G.-M., 2015a, A&A, 579, L8

Xu S., Jura M., Pantoja B., Klein B., Zuckerman B., Su K., Meng H., 2015b, ApJL, 806, L5

Xu S., Jura M., Dufour P., Zuckerman B., 2016, ApJL, 816, L22

Xu S., Zuckerman B., Dufour P., Young E., Klein B., Jura M., 2017, ApJL, 836, L7

Xu S., Rappaport S., van Lieshout R., Vanderburg A., Gary B., Hallakoun N., Ivanov V., et al., 2018a, MNRAS, 474, 4795

Xu S., Su K., Rogers L., Bonsor A., et al., 2018b, ApJ, 866, 108

Xu S., Dufour P., Klein B., Melis C., Monson N. N., Zuckerman B., Young E. D., Jura M. A., 2019, AJ, 158, 242

Xu S., Lai S., Dennihy E., 2020, arXiv preprint arXiv:2009.00193

Yoshizaki T., McDonough W. F., 2021, Geochemistry, 81, 125746

Young E. D., 2016, ApJ, 826, 129

Zuckerman B., Becklin E., 1987, Nature, 330, 138

Zuckerman B., Koester D., Reid I. N., Hünsch M., 2003, ApJ, 596, 477

Zuckerman B., Koester D., Melis C., Hansen B. M., Jura M., 2007, ApJ, 671, 872

Zuckerman B., Melis C., Klein B., Koester D., Jura M., 2010, ApJ, 722, 725

Zuckerman B., Koester D., Dufour P., Melis C., Klein B., Jura M., 2011, ApJ, 739, 101

van Roestel J., et al., 2021, ApJL, 919, L26

von Hippel T., Thompson S. E., 2007, ApJ, 661, 477

Chapter 6

Appendix 1: Additional tables and figures from Chapter 2

6.1 Observation Information

Table 6.1 shows the dates of the observations for each white dwarf in the sample. Table 6.2 shows the frame numbers for each white dwarf in the sample.

Table 6.1 All the polluted white dwarfs with an infrared excess observed with the UKIRT and the dates they were observed.

WD Name	2014B	2015A	2015B	2016A	2016A	2016B	2016B	2017A	2017A
WD 0010+280	03/10/14	N	N	N	N	06/07/16	N	N	N
WD 0106−328	03/10/14	N	N	N	N	11/10/16	N	N	N
WD 0146+187	03/10/14	N	N	N	N	12/07/16	N	N	N
WD 0300−013	03/10/14	N	N	N	N	22/07/16	31/01/17	N	N
WD 0307+077	03/10/14	N	N	N	N	10/10/16	N	N	
WD 0408−041	03/10/14	N	N	N	N	10/10/16	31/01/17	N	N
WD 0435+410	03/10/14	N	31/01/16	N	N	10/10/16	N	N	N
WD J0738+1835	N	03/05/15	N	29/02/16	N	10/10/16	28/01/17	N	N
WD J0959−0200	09/11/14	02/02/15	N	05/03/16	07/05/16	N	N	23/05/17	N
WD 1015+161	30/10/14	N	N	09/05/16	N	N	N	N	N
WD 1018+410	30/10/14	N	N	09/05/16	N	N	N	N	N
WD 1041+092	N	02/05/15	N	04/03/16	09/05/16	N	N	N	N
WD 1116+026	N	02/05/15	N	05/03/16	10/05/16	N	N	30/05/17	N
WD 1145+017	N	02/05/15	N	N	N	N	N	09/05/17	24/05/17*
WD 1145+288	N	02/05/15	N	23/02/16	09/05/16	N	N	30/05/17	N
WD 1150−153	N	03/05/15	N	05/03/16	10/05/16	N	N	01/06/17	N
WD J1221+1245	N	02/05/15	N	01/03/16	10/05/16	N	N	25/05/17	N
WD 1225−079	N	03/05/15	N	04/03/16	10/05/16	N	N	25/05/17	N
WD 1226+110	N	02/05/15	N	29/02/16	10/05/16	N	N	09/05/17	N
WD J1234+5606	N	03/05/15	N	04/03/16	05/06/16	N	N	07/06/17	N
WD 1349−230	N	03/05/15	N	04/03/16	06/06/16	N	N	30/05/17	N
WD 1456+298	N	02/05/15	N	17/02/16	10/05/16	N	N	14/05/17	N
WD 1504+329	N	01/05/15	N	29/02/16	08/05/16	N	N	12/05/17	N
WD 1536+520	N	02/05/15	N	05/03/16	29/05/16	N	N	28/05/17	N
WD 1551+175	N	01/05/15	N	03/03/16	31/05/16	N	N	14/05/17	N
WD 1554+094	N	01/05/15	N	29/02/16	08/05/16	N	N	20/05/17	18/07/17
WD J1617+1620	N	01/05/15	N	17/02/16	10/05/16	N	N	10/05/17	17/07/17
WD 1729+371	N	02/05/15	02/08/15	28/02/16	10/05/16	N	N	12/05/17	17/07/17
WD 1929+011	06/10/14	N	02/08/15	N	N	10/07/16	10/05/17	15/07/17	N
WD 2132+096	N	03/05/15	09/08/15	21/04/16	N	10/07/16	N	11/05/17	15/07/17
WD 2207+121	13/10/14	N	08/08/15	N	N	29/06/16	N	15/07/17	N
WD 2221−165	30/10/14	N	09/08/15	N	N	13/07/16	N	N	N
WD 2326+049	03/10/14	N	09/08/15	N	N	06/07/16	N	N	N
WD 2328+107	N	N	08/08/15	01/06/16	N	06/07/16	N	02/06/17	15/07/17

(*) For WD 1145+017, there are three more dates for 2017A: 06/06/2017, 21/06/2017 and 22/06/2017.

6.2 SEDs

SEDs of the targets in the survey. White dwarf models kindly provided by P. Dufour.

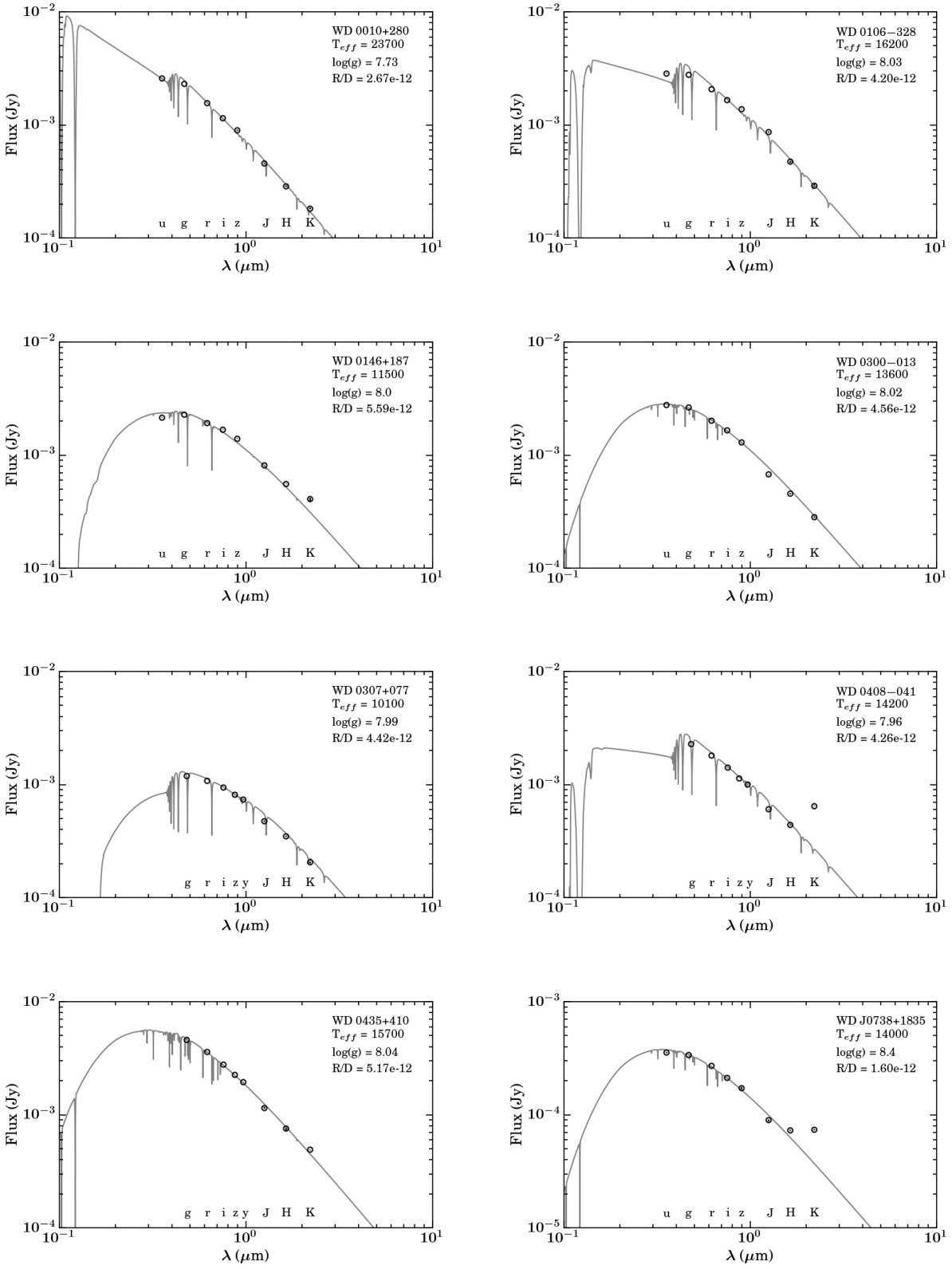
WD 0010+280
T$_{eff}$ = 23700
log(g) = 7.73
R/D = 2.67e-12
u g r i z J H K
WD 0106−328
T$_{eff}$ = 16200
log(g) = 8.03
R/D = 4.20e-12
u g r i z J H K
WD 0146+187
T$_{eff}$ = 11500
log(g) = 8.0
R/D = 5.59e-12
u g r i z J H K
WD 0300−013
T$_{eff}$ = 13600
log(g) = 8.02
R/D = 4.56e-12
u g r i z J H K
WD 0307+077
T$_{eff}$ = 10100
log(g) = 7.99
R/D = 4.42e-12
g r izy J H K
WD 0408−041
T$_{eff}$ = 14200
log(g) = 7.96
R/D = 4.26e-12
g r izy J H K
WD 0435+410
T$_{eff}$ = 15700
log(g) = 8.04
R/D = 5.17e-12
g r izy J H K
WD J0738+1835
T$_{eff}$ = 14000
log(g) = 8.4
R/D = 1.60e-12
u g r i z J H K
Flux (Jy)
λ (μm)

Figure B1.

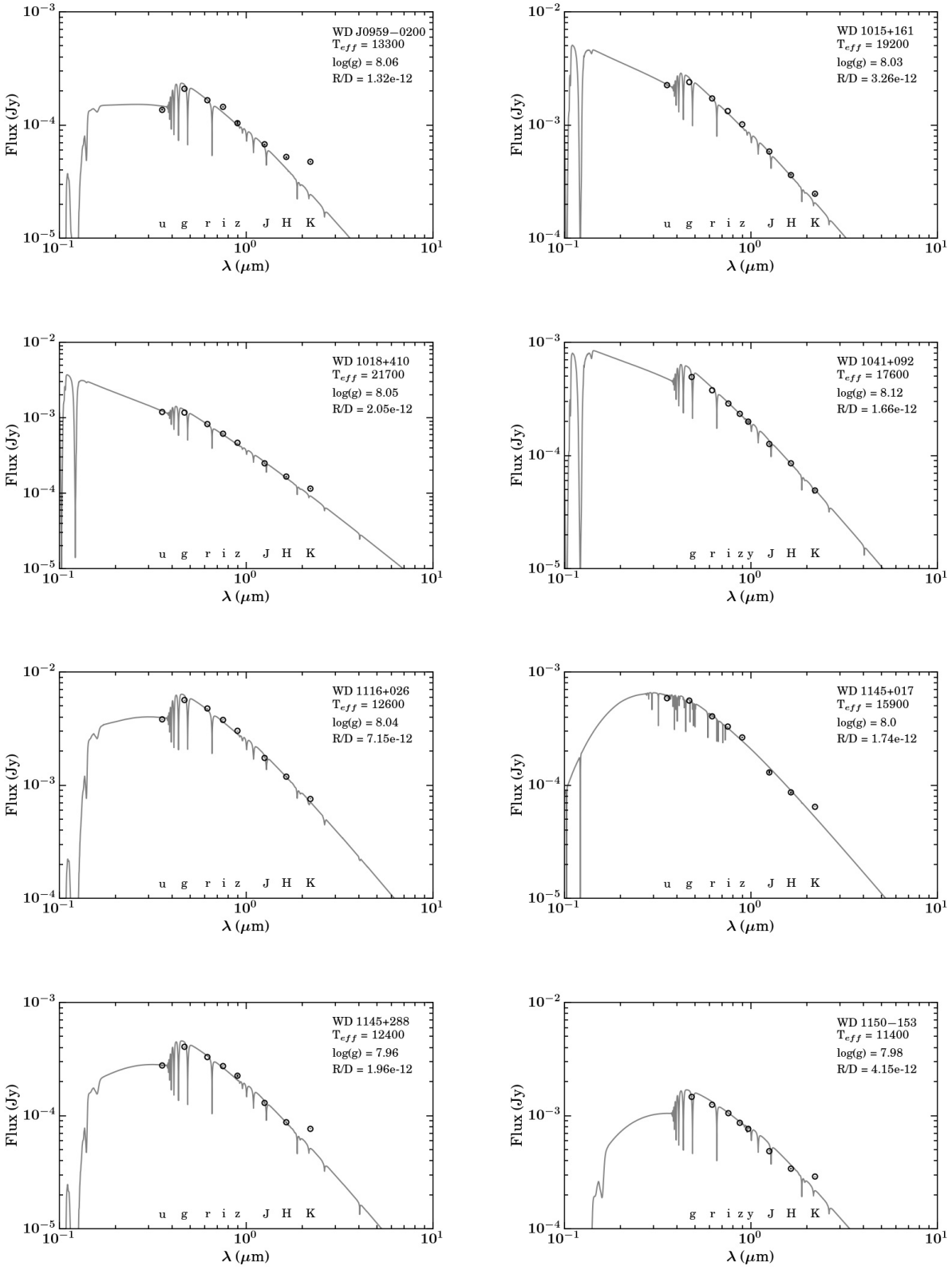
WD J0959−0200
T$_{eff}$ = 13300
log(g) = 8.06
R/D = 1.32e-12
u g r i z J H K
WD 1015+161
T$_{eff}$ = 19200
log(g) = 8.03
R/D = 3.26e-12
u g r i z J H K
WD 1018+410
T$_{eff}$ = 21700
log(g) = 8.05
R/D = 2.05e-12
u g r i z J H K
WD 1041+092
T$_{eff}$ = 17600
log(g) = 8.12
R/D = 1.66e-12
g r i z y J H K
WD 1116+026
T$_{eff}$ = 12600
log(g) = 8.04
R/D = 7.15e-12
u g r i z J H K
WD 1145+017
T$_{eff}$ = 15900
log(g) = 8.0
R/D = 1.74e-12
u g r i z J H K
WD 1145+288
T$_{eff}$ = 12400
log(g) = 7.96
R/D = 1.96e-12
u g r i z J H K
WD 1150−153
T$_{eff}$ = 11400
log(g) = 7.98
R/D = 4.15e-12
g r i z y J H K
Flux (Jy)
λ (μm)

Figure B1.

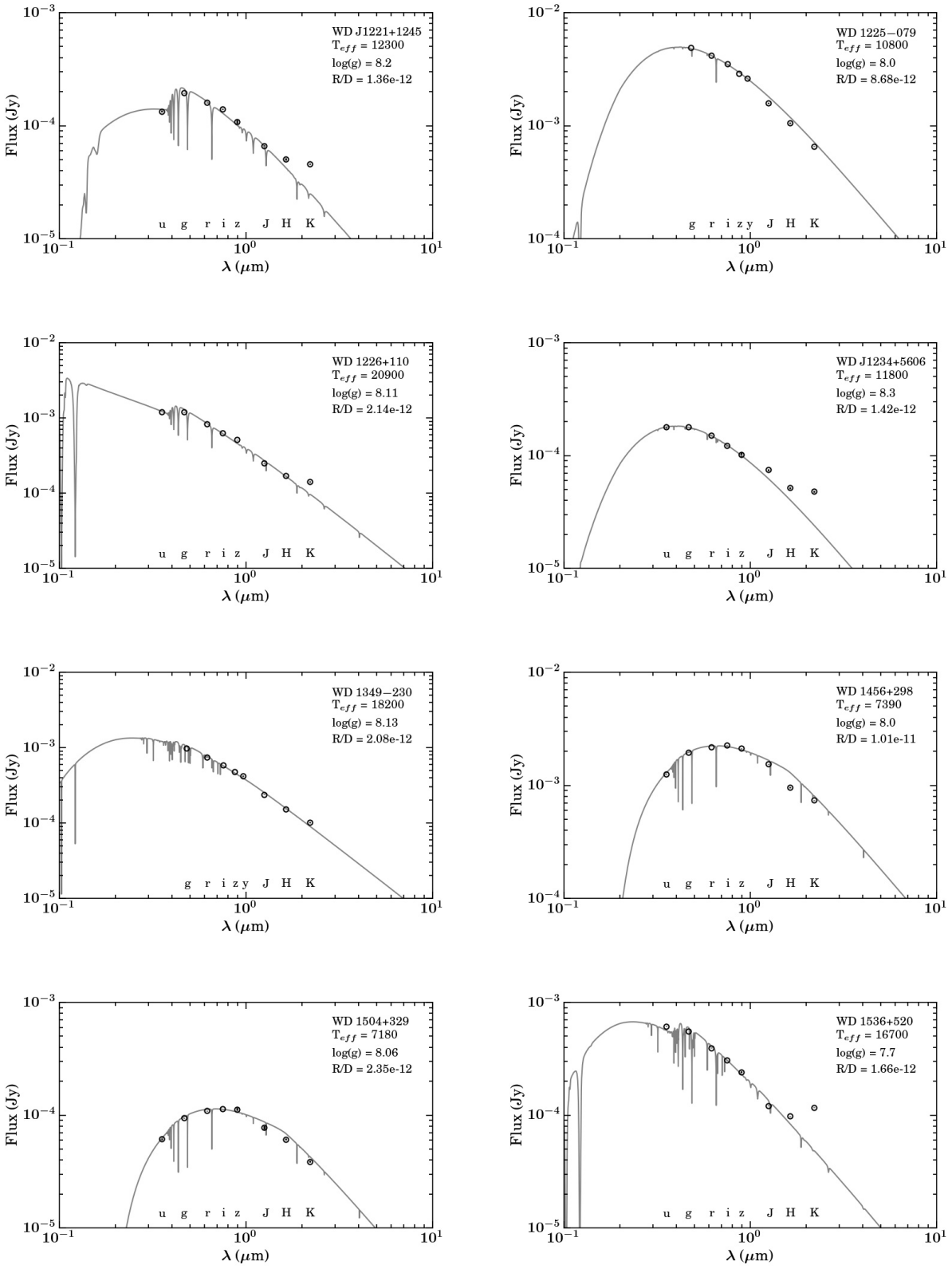
WD J1221+1245
T$_{eff}$ = 12300
log(g) = 8.2
R/D = 1.36e-12
u g r i z J H K
WD 1225−079
T$_{eff}$ = 10800
log(g) = 8.0
R/D = 8.68e-12
g r i z y J H K
WD 1226+110
T$_{eff}$ = 20900
log(g) = 8.11
R/D = 2.14e-12
u g r i z J H K
WD J1234+5606
T$_{eff}$ = 11800
log(g) = 8.3
R/D = 1.42e-12
u g r i z J H K
WD 1349−230
T$_{eff}$ = 18200
log(g) = 8.13
R/D = 2.08e-12
g r i z y J H K
WD 1456+298
T$_{eff}$ = 7390
log(g) = 8.0
R/D = 1.01e-11
u g r i z J H K
WD 1504+329
T$_{eff}$ = 7180
log(g) = 8.06
R/D = 2.35e-12
u g r i z J H K
WD 1536+520
T$_{eff}$ = 16700
log(g) = 7.7
R/D = 1.66e-12
u g r i z J H K
Flux (Jy)
λ (μm)

Figure B1.

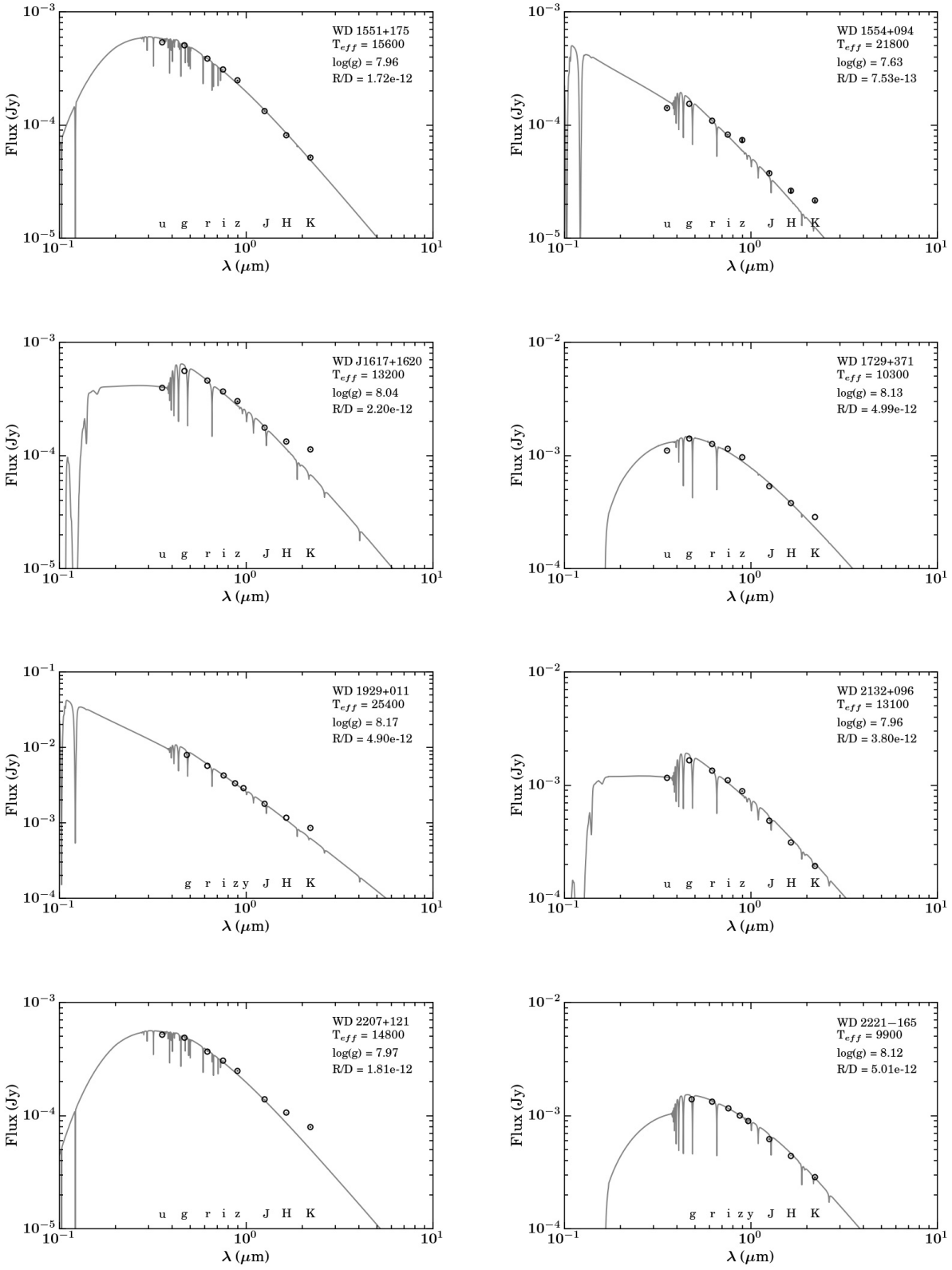
WD 1551+175
T$_{eff}$ = 15600
log(g) = 7.96
R/D = 1.72e-12
u g r i z J H K
WD 1554+094
T$_{eff}$ = 21800
log(g) = 7.63
R/D = 7.53e-13
u g r i z J H K
WD J1617+1620
T$_{eff}$ = 13200
log(g) = 8.04
R/D = 2.20e-12
u g r i z J H K
WD 1729+371
T$_{eff}$ = 10300
log(g) = 8.13
R/D = 4.99e-12
u g r i z J H K
WD 1929+011
T$_{eff}$ = 25400
log(g) = 8.17
R/D = 4.90e-12
g r izy J H K
WD 2132+096
T$_{eff}$ = 13100
log(g) = 7.96
R/D = 3.80e-12
u g r i z J H K
WD 2207+121
T$_{eff}$ = 14800
log(g) = 7.97
R/D = 1.81e-12
u g r i z J H K
WD 2221−165
T$_{eff}$ = 9900
log(g) = 8.12
R/D = 5.01e-12
g r izy J H K
Flux (Jy)
λ (μm)

Figure B1.

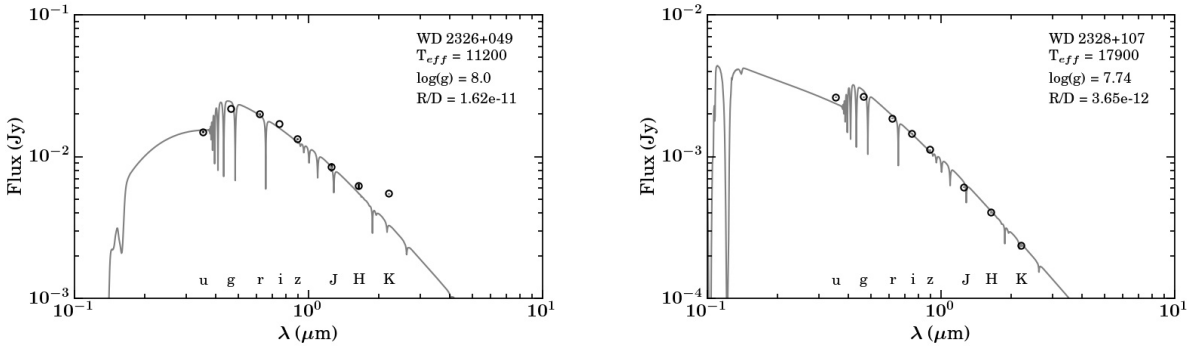

Figure B1. The spectral energy distributions for the 34 white dwarfs in this sample. The temperature and log(g) used within the models are shown. R/D is the scaling factor used for the radii/distance needed in order for the models to fit the SDSS or Pan-STARRS optical data. The 11 white dwarfs without a significant K band excess are: WD 0106−328, WD 0300−013, WD 0307+077, WD 1041+092, WD 1225−079, WD 1456+298, WD 2132+096, WD 2221−165, WD 2328+107, WD 1504+329, and WD 1551+175.

Table 6.2 All the polluted white dwarfs with an infrared excess observed with the UKIRT survey and the total number of frames. Each frame consists of a dithered stack of 5 exposures, each with the corresponding frame time of 5 or 10 seconds. FT = frame time for each individual exposure in the dithered stack, FN = total number of dithered stacks over all observations.

WD Name	FT J (secs)	FN J	FT H (secs)	FN H	FT K (secs)	FN K
WD 0010+280	5	6	10	6	10	10
WD 0106−328	5	6	5	6	5	6
WD 0146+187	5	6	5	6	5	6
WD 0300−013	5	6	5	6	5	9
WD 0307+077	5	6	10	6	10	10
WD 0408−041	5	9	5	9	5	9
WD 0435+410	5	3	5	3	5	9
WD J0738+1835	10	9	10	27	10	75
WD J0959−0200	10	9	10	27	10	75
WD 1015+161	5	6	5	6	10	6
WD 1018+410	5	6	10	6	10	10
WD 1041+092	10	9	10	21	10	51
WD 1116+026	5	4	5	4	5	12
WD 1145+017	10	18	10	42	10	102
WD 1145+288	10	12	10	28	10	68
WD 1150−153	5	12	5	11	10	12
WD J1221+1245	10	12	10	36	10	100
WD 1225−079	5	4	5	4	5	12
WD 1226+110	5	12	10	12	10	20
WD J1234+5606	10	9	10	27	10	75
WD 1349−230	5	12	10	12	10	20
WD 1456+298	5	3	5	3	5	6
WD 1504+329	10	9	10	27	10	75
WD 1536+520	10	12	10	28	10	68
WD 1551+175	10	12	10	28	10	68
WD 1554+094	10	15	10	45	10	125
WD J1617+1620	5	19	10	23	10	45
WD 1729+371	5	19	5	19	10	23
WD 1929+011	5	6	5	10	5	20
WD 2132+096	5	20	5	22	10	26
WD 2207+121	10	18	10	36	10	76
WD 2221−165	5	6	5	6	5	6
WD 2326+049	5	3	5	3	5	9
WD 2328+107	5	19	5	19	5	23

Chapter 7

Appendix 2: Additional tables and figures from Chapter 4

7.1 Spectral Energy Distributions

Spectral energy distributions for the seven white dwarfs are shown in Figure 7.1 showing the best fitting white dwarf models derived both spectroscopically and photometrically.

7.2 Spectral Lines and abundances

For each of the white dwarfs, the stellar parameters were determined spectroscopically and photometrically. For each set of parameters the abundances were obtained. Tables 7.1 – 7.7 show the spectral lines that were identified in the X-shooter, HIRES and MIKE data for the seven white dwarfs, their associated equivalent width, radial velocity, and the abundance derived.

7.3 Equivalent Width Upper Limits

Using the method discussed in Section 4.2.3 the equivalent width upper limits were derived, as listed in Table 7.8. The strongest optical line was used to derive the equivalent width upper limit.

The HIRES data were used to obtain the equivalent width upper limits as the higher resolution allowed more stringent constraints to be used. For Gaia J0611−6931 the X-shooter data was used to derive the upper limits. At the resolution of X-shooter it is difficult to

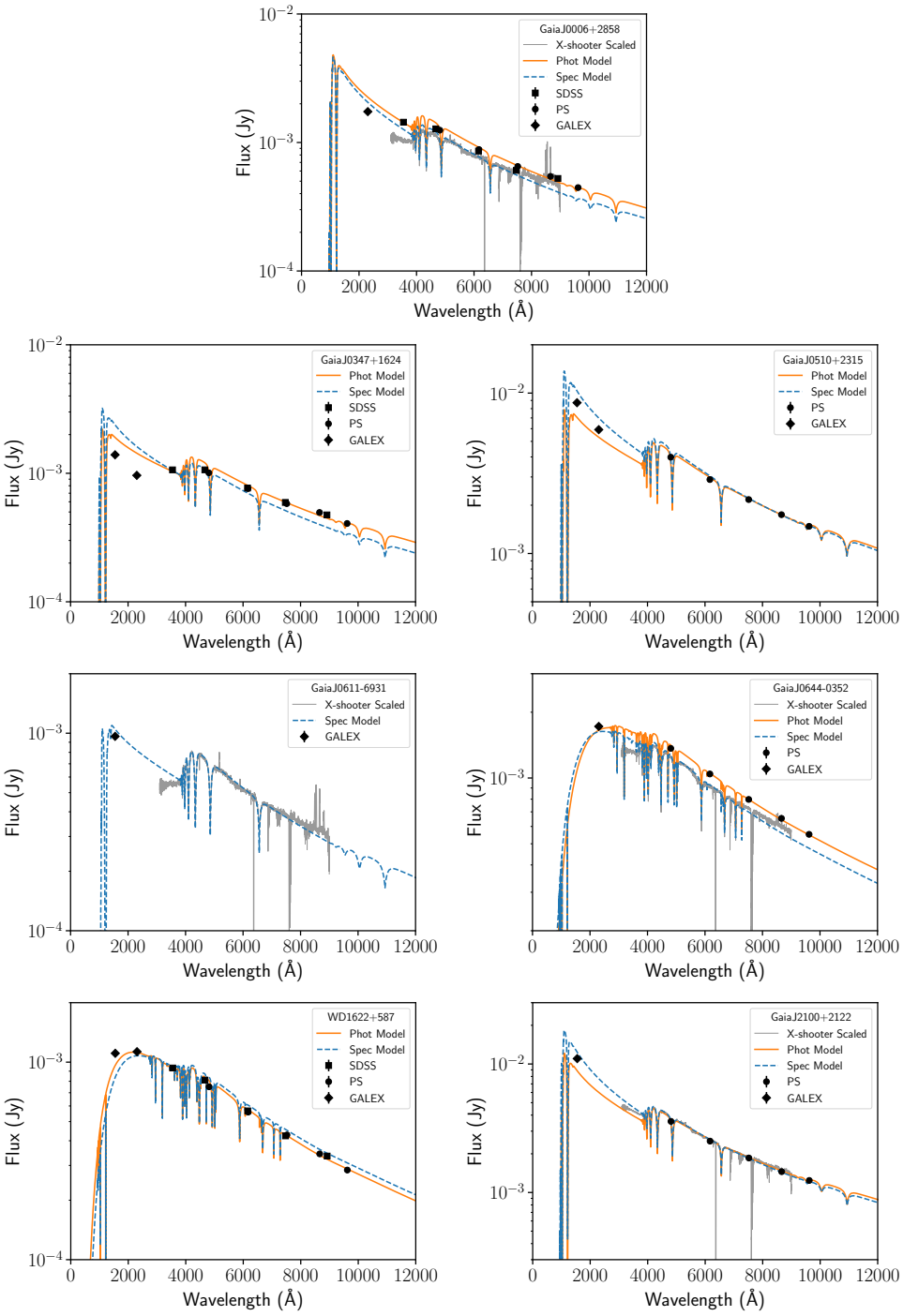

Fig. 7.1 Spectral energy distributions for the seven white dwarfs. The X-shooter spectra for the four white dwarfs observed are shown in grey, this is scaled to fit the spectroscopic models as the spectra suffer from flux loss due to non-ideal weather conditions and slit losses. There is a gap in the data between 6360 Å– 6375 Å and telluric absorption features are present in the reddest parts of the spectra. The photometric data points are given in black, errors are plotted but are smaller than the data points. The photometric and spectroscopic model fits are shown in orange (solid line) and blue (dashed line) where available. Missing *GALEX* FUV or NUV fluxes implies either a non-detection in that band, or the flux was flagged as it contained an artefact.

Table 7.1 The absorption lines in Gaia J0006+2858. If two lines lie within ~ 10 Å, equivalent widths and abundances were fitted simultaneously.

Line	λ_{air} (Å)	λ_{obs} (Å)	EW (Å)	RV (km/s)	Spec Abundance		Phot Abundance	
					HIRES	X-sh	HIRES	X-sh
Ca II	3179.3315	3179.66	0.013 (0.003)	31.3	−6.21		−6.33	
Ca II†	3933.6631	3934.02*	0.041 (0.006)	27.3	−6.13		−6.32	
Ca Average:					−6.17	-	−6.33	-
Mg II	4481.1250	4481.59	0.208 (0.007)	31.2	−5.00	−4.90	−5.10	−4.97
Si II	3856.0184	3856.37	0.029 (0.003)	27.5	−4.79		−4.89	
Si II	3862.5947	3862.94	0.015 (0.002)	26.8	−4.78		−4.90	
Si II	4128.0542	4128.40	0.024 (0.003)	24.8	−4.99		−5.10	
Si II	4130.8934	4131.26	0.024 (0.003)	26.3	−4.99		−5.10	
Si II	5041.0230	5041.59	0.036 (0.006)	33.8	−5.10	−4.97	−5.20	−5.05
Si II	5055.9830	5056.53	0.055 (0.006)	32.3	−5.14	−4.97	−5.24	−5.05
Si II	6347.1062	6347.68	0.083 (0.008)	27.0	−4.95	−4.86	−5.04	−4.94
Si II	6371.3676	6371.99	0.046 (0.008)	29.2	−4.93		−5.03	
Si Average:					−4.95	−4.92	−5.06	−4.99

† Gaseous emission at this wavelength, additional 12 percent error added in quadrature.
* Ca II 3933 has extra absorption at rest wavelength of line, this was fitted simultaneously and subtracted to derive the equivalent width. This could be the core of the double peaked circumstellar emission feature.

Table 7.2 The absorption lines measured in the HIRES spectrum of Gaia J0347+1624. There are also Na D lines at both 5890 Angstrom and 5896 Angstrom. However, in checking the ISM model, this line of sight intercepts LIC (RV of 22.36 km/s) and Hyades (RV of 14.16 km/s). This is close to the measured RV of 15 km/s so it is deduced that these lines are not photospheric.

Line	λ_{air} (Å)	λ_{obs} (Å)	EW (Å)	RV (km/s)	Spec Abundance	Phot Abundance
Ca II	3933.6631	3933.90	0.062 (0.006)	18.1	−5.79	−6.29
Ca II	3968.4690	3968.71	0.022 (0.004)	18.2	−5.60	−5.72
Ca Average:					−5.69	−6.01
Mg II	4481.1250*	4481.36	0.040 (0.012)	16.0	−5.78	−6.05

* This is a merged Mg II doublet with 4481.3249. RV is calculated with respect to the line listed.

Table 7.3 The absorption lines in the HIRES spectra of Gaia J0510+2315. If two lines lie within ~ 10 Å, equivalent widths and abundances were fitted simultaneously.

Line	λ_{air} (Å)	λ_{obs} (Å)	EW (Å)	RV (km/s)	Spec Abundance	Phot Abundance
Ca II	3933.6631	3934.03	0.032 (0.004)	27.6	−6.31	−7.10
Mg II*	4481.1250	4481.53	0.114 (0.011)	26.9	−5.23	−5.45
Mg II*	4481.3249	4481.74	0.037 (0.007)	27.8	−5.23	−5.45
Mg Average:					−5.23	−5.45
O I†	7771.9377	7772.63	0.023 (0.005)	26.6	−4.23	−4.42
O I†	7774.1561	7774.88	0.020 (0.004)	27.8	−4.23	−4.42
O I†	7775.3858	7776.04	0.005 (0.002)	25.3	−4.23	−4.42
O Average:					−4.23	−4.42
Si II	3856.0184	3856.35	0.019 (0.003)	26.0	−5.00	−4.99
Si II	4128.0542	4128.44	0.015 (0.005)	28.0	−4.90	−4.82
Si II	4130.8934	4131.25	0.030 (0.006)	25.8	−4.90	−4.82
Si II	5055.9830	5056.48	0.039 (0.003)	29.2	−5.36	−5.34
Si II	5041.0230	5041.52	0.014 (0.002)	29.8	−5.33	−5.31
Si II	6347.1062	6347.65	0.058 (0.004)	25.7	−5.19	−5.19
Si II	6371.3676	6371.92	0.031 (0.004)	26.1	−5.15	−5.14
Si Average:					−5.15	−5.13

† Gaseous emission at this wavelength, additional 12 percent error added in quadrature.

* Both Mg II features resolved and fitted simultaneously for EW and RV.

An additional spectrum was obtained with HIRES and stacked for increased SNR to resolve the O lines.

O line at 7775.3858 Å is marginal.

Table 7.4 The absorption lines in Gaia J0611−6931. If two lines lie within $\sim$ 10 Å, equivalent widths and abundances were fitted simultaneously.

Line	$\lambda_{\rm air}$ (Å)	$\lambda_{\rm obs}$ (Å)	EW (Å)	RV (km/s)	Spec Abundance	
					X-sh	MIKE
Ca II†	3933.6631	3934.51	0.118 (0.025)	64.5	−6.19	−5.92
Mg II	4481.1250	4482.14	0.546 (0.014)	67.6	−4.66	−4.53
Mg II	7896.0371	7898.08	0.080 (0.025)	77.6	−4.68	−4.50
Mg Average:					−4.67	−4.52
O I†	7771.9377	7773.48	0.049 (0.014)	59.4		−3.67
O I†	7774.1561	7775.72	0.038 (0.014)	60.3		−3.67
O I†	7775.3858	7776.96	0.033 (0.017)	60.6		−3.67
O Average:					-	−3.67
Si II	5041.0230	5042.05*	0.007 (0.002)	61.3	−4.73	
Si II	5055.9830	5057.13*	0.010 (0.003)	68.1	−4.73	−4.68
Si II	6347.1062	6348.40	0.117 (0.017)	60.9	−4.71	−4.79
Si II	6371.3676	6372.68	0.090 (0.0065)	61.8		−4.53
Si Average:					−4.73	−4.67
Fe II†	5169.0318	5170.12	0.055 (0.023)	63.2		−4.24

† Gaseous emission at this wavelength, additional 12 percent error added in quadrature.
* Si II 5041 and 5055 measured line position and equivalent widths from X-shooter.

Table 7.5 The absorption lines in Gaia J0644−0352. If two lines lie within ~ 10 Å, equivalent widths and abundances were fitted simultaneously.

Line	λ_{air} (Å)	λ_{obs} (Å)	EW (Å)	RV (km/s)	Spec Abundance		Phot Abundance	
					HIRES	X-sh	HIRES	X-sh
Al II	3586.5564	3587.63	0.030 (0.005)	89.9	−6.76		−7.05	
Al II	3587.0723	3588.18	0.021 (0.006)	92.8	−6.76		−7.05	
Al II	3587.4452	3588.53	0.011 (0.004)	90.5	−6.76		−7.05	
Al Average:					−6.76	–	−7.05	–
Ca II	3158.8697	3159.86	0.092 (0.004)	93.5	−6.97	−6.91	−7.60	−7.52
Ca II	3179.3315	3180.34	0.094 (0.009)	95.1	−6.97	−6.72	−7.58	−7.32
Ca II	3181.2750	3182.27	0.025 (0.004)	93.4	−6.97	−6.72	−7.58	−7.32
Ca II	3706.0235	3707.19	0.020 (0.006)	94.2	−6.94	−6.57	−7.66	−7.44
Ca II	3736.9025	3738.07	0.061 (0.003)	93.5	−6.89	−6.86	−7.54	−7.50
Ca II	3933.6631	3934.87	0.333 (0.004)	91.7	−6.67	−6.70	−7.50	−7.52
Ca II	3968.4690	3969.69	0.181 (0.013)	92.4	−6.84	−6.84	−7.69	−7.68
Ca II†	8498.0177	8500.62	0.041 (0.015)	91.8	−6.60	−6.76	−7.21	−7.40
Ca II†	8542.0858	8544.76	0.157 (0.028)	93.8	−6.42	−6.56	−7.14	−7.26
Ca II†	8662.1352	8664.87	0.102 (0.022)	94.7	−6.63	−6.45	−7.30	−7.14
Ca Average:					−6.77	−6.71	−7.47	−7.42
Cr II	3120.3584	3121.30	0.022 (0.006)	90.4	−7.65		−8.41	
Cr II	3124.9732	3125.95	0.011 (0.004)	93.6	−7.93		−8.70	
Cr II	3128.6923	3129.61	0.009 (0.003)	87.5	−7.77		−8.58	
Cr II	3132.0534	3133.04	0.023 (0.005)	94.4	−7.77		−8.58	
Cr II	3368.0416	3369.06	0.009 (0.002)	90.8	−7.90		−8.61	
Cr Average:					−7.81	–	−8.58	–
Fe II	3154.1928	3155.19	0.011 (0.003)	94.5	−6.69		−7.32	
Fe II *	3193.7988	3194.80	0.003 (0.001)	94.1	−6.49		−7.09	
Fe II *	3193.8588	3194.88	0.002 (0.001)	95.9	−6.49		−7.09	
Fe II	3213.3089	3214.31	0.014 (0.003)	93.0	−6.49		−7.14	
Fe II	3227.7423	3228.74	0.013 (0.002)	92.3	−6.44		−7.18	
Fe II	4583.8367	4585.27	0.005 (0.002)	93.9	−6.20		−6.78	
Fe II	5169.0318	5170.64	0.018 (0.005)	93.1	−6.45		−7.02	
Fe Average:					−6.46	–	−7.09	–
Mg I	3832.3036	3833.45	0.015 (0.004)	89.4	−5.71		−6.46	
Mg I	3838.2921	3839.43	0.021 (0.003)	88.8	−5.71		−6.46	
Mg II	4481.1250	4482.59	0.229 (0.013)	97.9	−5.52	−5.58	−6.35	−6.31
Mg II	7877.0502	7879.88	0.147 (0.045)	107.7	−5.85	−5.89	−6.30	−6.31
Mg II * (blended)	7896.04	7898.94	0.179 (0.027)	110.2	−5.87	−5.85	−6.32	−6.27
Mg Average:					−5.74	−5.77	−6.36	−6.29
OI -	7771.9377	7774.41	0.102 (0.011)	95.2	−5.08	−5.10	−5.50	−5.55
OI -	7774.1561	7776.65	0.096 (0.016)	96.0	−5.08	−5.10	−5.50	−5.55
OI -	7775.3858	7777.89	0.050 (0.017)	96.6	−5.08	−5.10	−5.50	−5.55
OI	8446.3548	8448.87	0.050 (0.027)	89.1	−5.38	−5.20	−5.79	−5.62
O Average:					−5.23	−5.15	−5.64	−5.58
Si II	3853.6650	3854.86	0.014 (0.003)	93.2	−5.80	−5.93	−6.31	−6.40
Si II	3856.0184	3857.21	0.099 (0.004)	92.3	−5.80	−5.93	−6.31	−6.40
Si II	3862.5947	3863.77	0.064 (0.003)	91.0	−5.80	−5.93	−6.31	−6.40
Si II *	4128.0542	4129.34	0.050 (0.005)	93.2	−6.01	−6.02	−6.51	−6.41
Si II *	4130.8934	4132.16	0.092 (0.005)	91.7	−6.01	−6.02	−6.51	−6.41
Si II	5055.9830	5057.73	0.092 (0.013)	103.7	−6.09		−6.47	
Si II	6347.1062	6349.07	0.242 (0.011)	92.6	−6.00	−5.98	−6.06	−6.01
Si II	6371.3676	6373.34	0.145 (0.011)	92.6	−5.98		−6.24	
Si Average:					−5.98	−5.97	−6.32	−6.27
Ti II	3234.5145	3235.52	0.013 (0.002)	93.6	−8.25		−9.05	
Ti II	3236.5720	3237.54	0.013 (0.003)	89.8	−8.25		−9.05	
Ti II	3239.0364	3239.99	0.008 (0.002)	88.7	−8.25		−9.05	
Ti II	3341.8742	3342.89	0.007 (0.002)	90.7	−8.37		−9.15	
Ti II **	3349.0334	3350.07	0.015 (0.003)	92.9	−8.22		−9.04	
Ti II **	3349.4023	3350.42	0.011 (0.002)	91.2	−8.22		−9.04	
Ti II ***	3361.2123	3362.24	0.007 (0.002)	91.4	−8.49		−9.28	
Ti II	3372.7923	3373.79	0.010 (0.002)	89.0	−8.34		−9.13	
Ti II	3383.7585	3384.79	0.008 (0.002)	91.3	−8.37		−9.10	
Ti II	3685.19/0.20	3686.31	0.004 (0.001)	90.1	−8.58		−9.29	
Ti II	3759.2916	3760.45	0.007 (0.002)	92.5	−8.31		−9.04	
Ti Average:					−8.37	–	−9.14	–

Table 7.6 The absorption lines measured in the WD 1622+587 HIRES spectra. If two lines lie within ~ 10 Å, equivalent widths and abundances were fitted simultaneously.

Line	λ_{air} (Å)	λ_{obs} (Å)	EW (Å)	RV (km/s)	Spec Abundance	Phot Abundance
Ca II	3179.3315	3179.11	0.031 (0.012)	-21.2	−7.42	−6.94
Ca II	3933.6631	3933.40	0.111 (0.010)	-20.3	−7.95	−7.48
Ca Average:					−7.68	−7.21
Mg II (doublet)	4481.1250	4480.95	0.060 (0.009)	-11.6	−6.60	−6.18
Mg II	7877.0502	7876.43	0.048 (0.016)	-23.5	−5.97	−5.63
Mg II	7896.3620	7895.86	0.079 (0.018)	-19.0	−6.17	−5.82
Mg Average:					−6.25	−5.88
Si II	3856.0184	3855.79	0.062 (0.009)	-17.9	−6.64	−6.29
Si II	3862.5947	3862.31	0.052 (0.010)	-22.1	−6.38	−6.04
Si II*	4128.0542	4127.79	0.036 (0.008)	-19.4	−6.44	−6.14
Si II*	4130.8934	4130.52	0.067 (0.009)	-26.9	−6.44	−6.14
Si II	5055.9830	5055.77	0.087 (0.011)	-12.8	−6.39	−6.11
Si II	6347.1062	6346.69	0.207 (0.017)	-19.7	−6.15	−5.87
Si II	6371.3676	6370.90	0.152 (0.018)	-22.4	−6.12	−5.85
Si Average:					−6.35	−6.05

* Fitted together

Table 7.7 The absorption lines measured in Gaia J2100+2122. If two lines lie within ~ 10 Å, equivalent widths and abundances were fitted simultaneously.

Line	λ_{air} (Å)	λ_{obs} (Å)	EW (Å)	RV (km/s)	Spec Abundance		Phot Abundance	
					HIRES	X-sh	HIRES	X-sh
Ca II	3179.3315	3179.35	0.009 (0.002)	2.1	−6.32		−6.66	
Ca II*	3933.6631	3933.72	0.022 (0.001)	4.1	−6.13	−5.79	−6.65	−6.25
Ca Average:					−6.23	−5.79	−6.65	−6.25
Fe II	3227.7423	3227.80	0.004 (0.001)	5.4	−4.96		−5.50	
Mg II	4481.1250	4481.25	0.140 (0.005)	8.4	−5.12	−5.04	−5.40	−5.30
Si II	3856.0184	3856.07	0.015 (0.002)	3.9	−5.04		−5.32	
Si II	3862.5947	3862.65	0.005 (0.001)	4.1	−5.10		−5.38	
Si II *	4128.0542	4128.10	0.017 (0.002)	3.0	−4.96		−5.16	
Si II *	4130.8934	4130.94	0.025 (0.002)	3.4	−5.12		−5.33	
Si II	5055.9830	5056.15	0.027 (0.004)	9.7	−5.31	−5.32	−5.54	−5.53
Si II	6347.1062	6347.20	0.051 (0.003)	4.2	−5.14	−5.01	−5.41	−5.26
Si II	6371.3676	6371.44	0.019 (0.002)	3.6	−5.19		−5.46	
Si Average:					−5.12	−5.16	−5.4	−5.39

* Ca II has extra absorption bluewards. This is not resolved in X-shooter and is resolved in HIRES. Therefore the abundance is higher in X-shooter and the average abundance only includes the HIRES data.

Table 7.8 The upper limit equivalent widths in mÅ of the material polluting the seven white dwarfs in this study. * denotes when gaseous emission is present at this wavelength. When calculating abundance upper limit, add 12 percent onto the equivalent width quoted to be conservative.

Element	Line (Å)	J0006	J0347	J0510	J0611	J0644	WD1622	J2100
O I	7771.9377	20.78*	-	-	-	-	31.4*	11.42*
Na II	5889.9483	12.6	-	8.5	n/a*	25.1	16.5	8.7
Al II	3586.5564	7.0	16.6	14.3	92.1	-	13.0	3.4
Ti II	3349.0334	7.3	19.7	18.9	103.0	-	14.7	3.8
Cr II	3368.0416	7.2	19.1	18.4	121.8	-	14.8	3.8
Fe II	5169.0318	7.2*	20.3*	15.2*	-	-	8.0*	-
Ni II	3513.9871	7.0	16.9	14.5	91.2	7.3	12.7	3.4

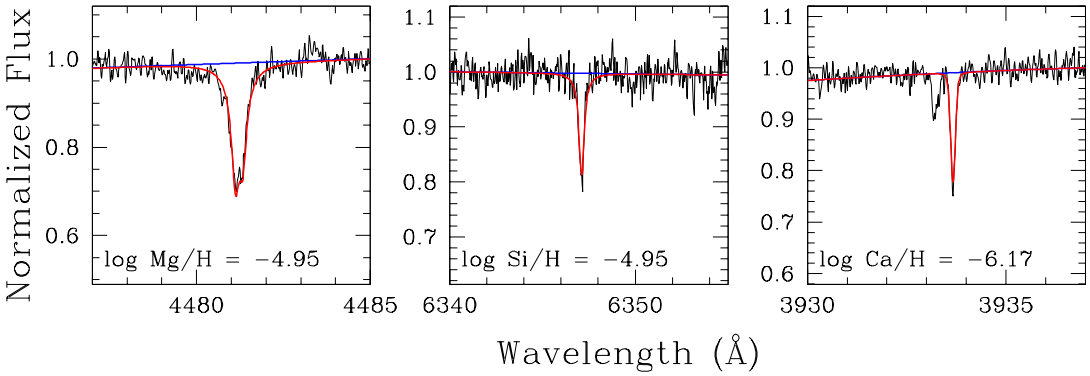

Fig. 7.2 Model fits (red lines) to the HIRES data using the average abundances for Gaia J0006+2858. There is additional non-photospheric absorption bluewards of the Ca II K line.

accurately normalise out the narrow gaseous emission features. Therefore, as there are no sodium optical lines without gaseous emission, no upper limit is reported for this element.

7.4 Model fits to spectral lines

Figures 7.2 – 7.7 show the average model abundances fit to the strongest spectral line for each element in six of the white dwarfs. The average abundance is plotted which is derived from multiple spectral lines, so sometimes the fit to individual lines can be discrepant. Note that for WD 1622+587 the abundance fits are shown in Fig. 4.3.

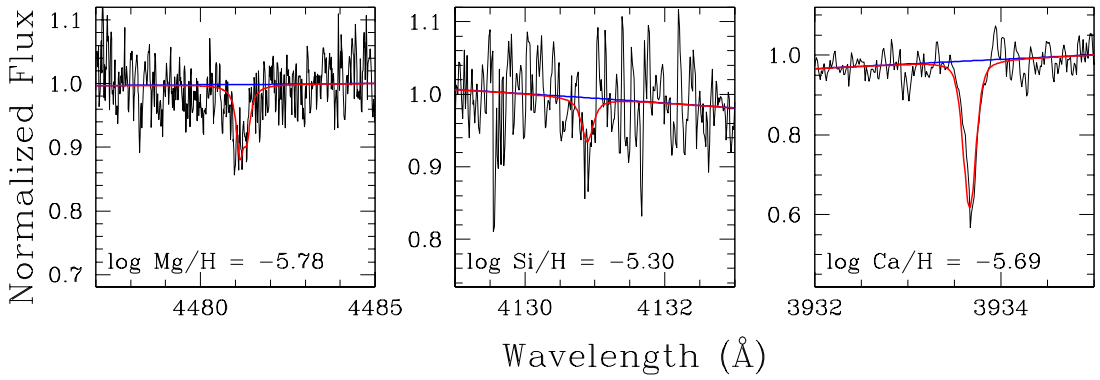

Fig. 7.3 Model fits (red lines) to the HIRES data using the average abundances for Gaia J0347+1624. Silicon is shown for reference, the absorption is not significant to 3 σ and is therefore taken as an upper limit.

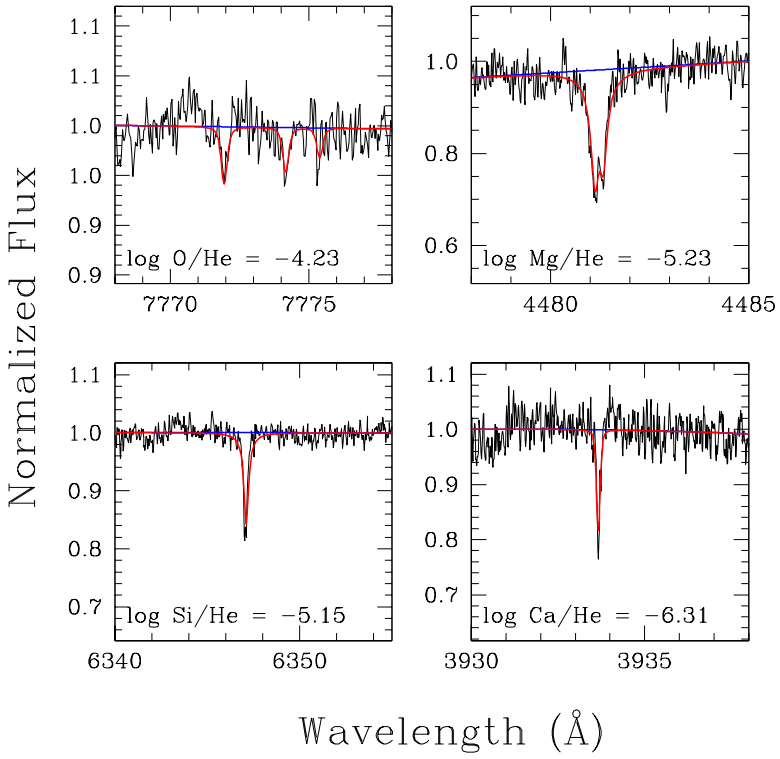

Fig. 7.4 Model fits (red lines) to the HIRES data using the average abundances for Gaia J0510+2315.

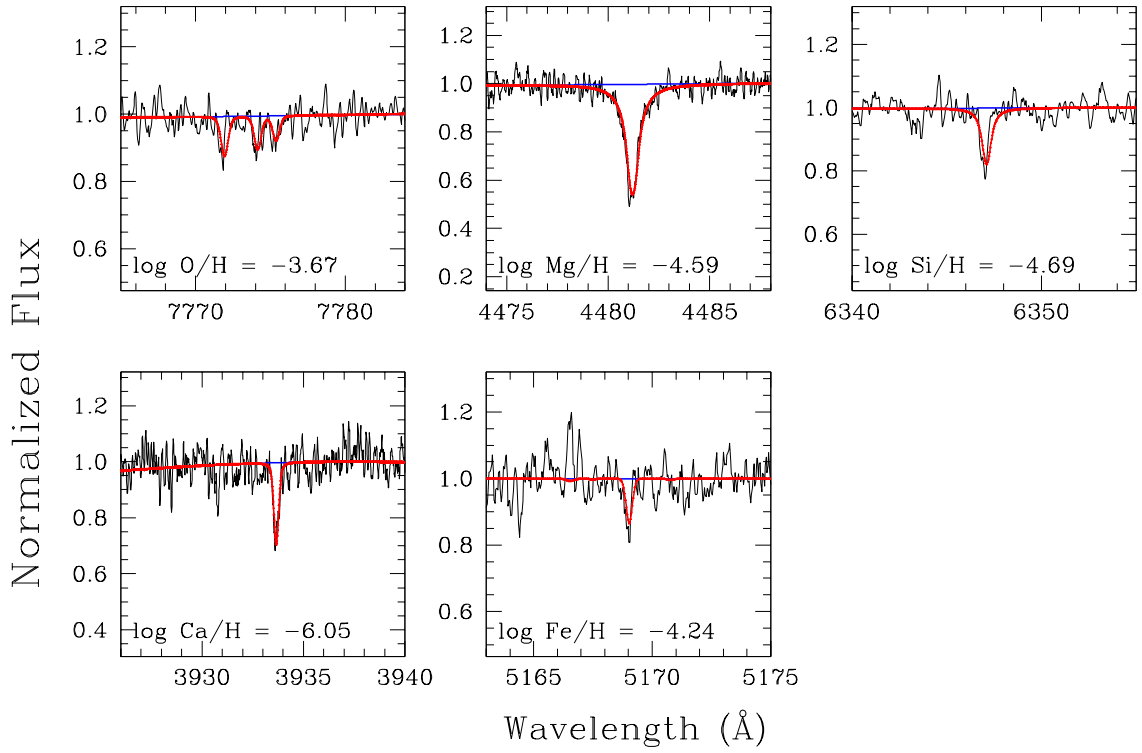

Fig. 7.5 Model fits (red lines) to the MIKE data using the average abundances for Gaia J0611−6931.

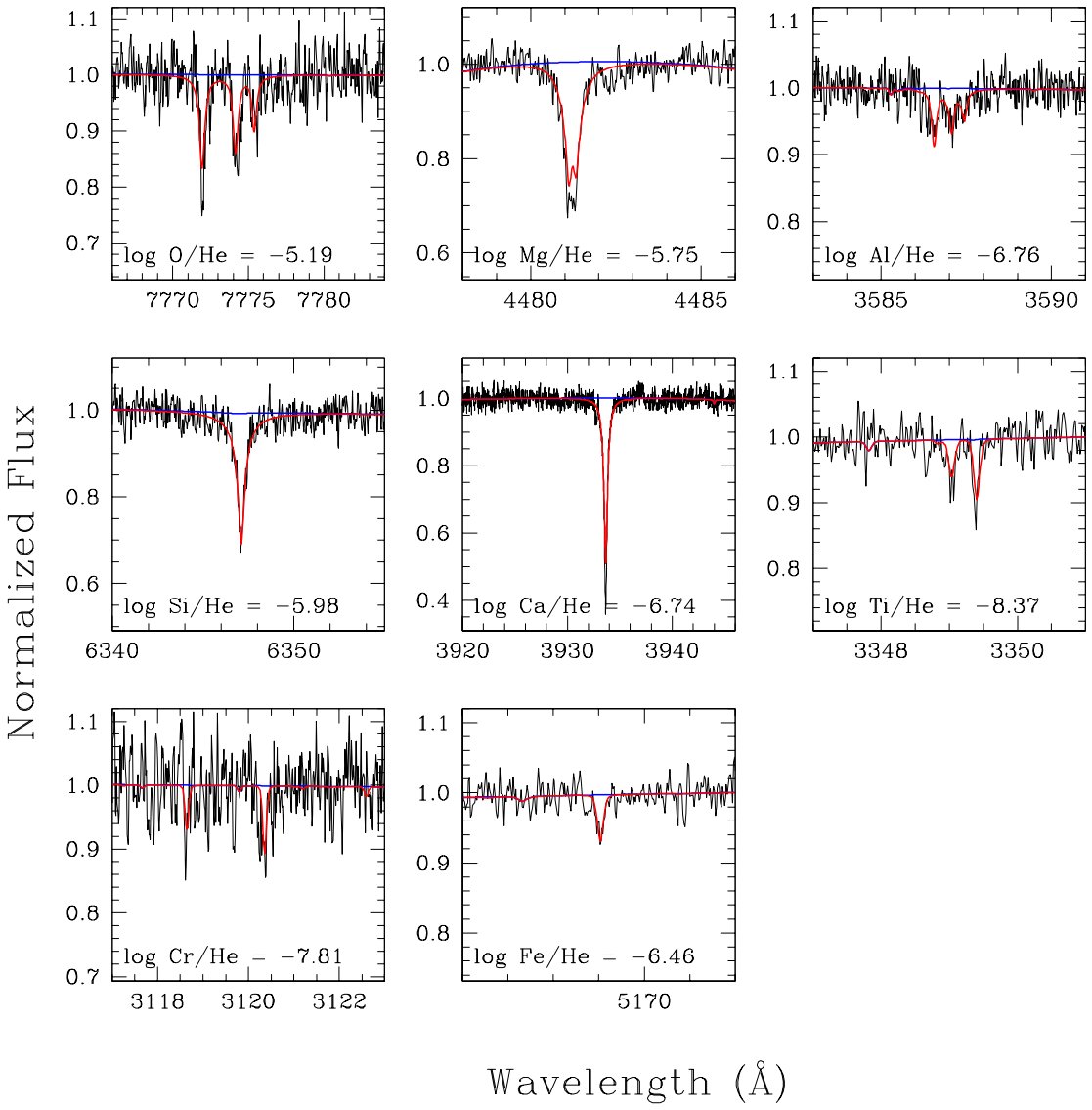

Fig. 7.6 Model fits (red lines) to the HIRES data using the average abundances for Gaia J0644−0352.

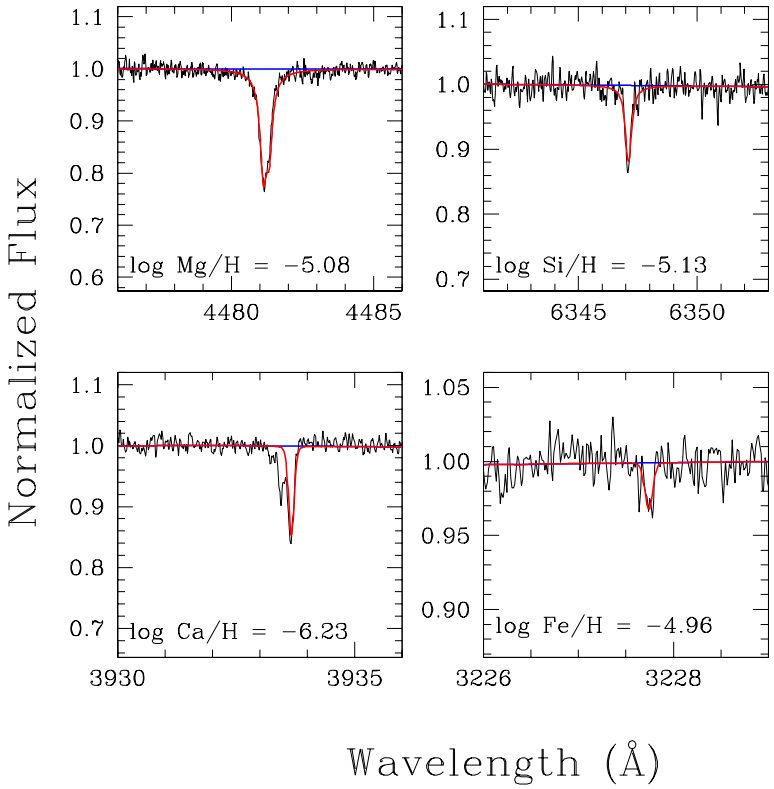

Fig. 7.7 Model fits (red lines) to the HIRES data using the average abundances for Gaia J2100−2122. There is an additional non-photospheric absorption bluewards of the Ca II K line.

7.5 Bayesian output

The resulting median parameters from the Bayesian models for the seven white dwarfs are given in Table 7.9.

Table 7.9 The resulting median parameters from the Bayesian models, errors are given as 16th and 84th percentiles. A description of the parameters is presented in Section 4.2.4. The basic model uses a best-fitting initial stellar composition, 'Stellar metallicity'; this is omitted from this table as most white dwarfs are equally likely to have accreted material that started with a wide range of initial compositions. The pollution fraction and the most likely accretion phase: build up (BU), steady state (SS) or declining phase (DP) are output for the basic primitive model. Italics represent optional complex parameters that are only invoked when the Bayes factor is > 1. The fragment core fraction (fcf) is quoted based on number fraction, and in brackets mass fraction, which is calculated assuming the output core and mantle composition of the median Bayesian model.

Parameter	Gaia J0006	Gaia J0347	Gaia J0510	Gaia J0611	Gaia J0644	WD 1622	Gaia J2100
log(Pollution Fraction)	$-4.57^{+0.05}_{-0.05}$	$-5.49^{+0.06}_{-0.07}$	$-4.12^{+0.05}_{-0.05}$	$-3.53^{+0.05}_{-0.05}$	$-5.00^{+0.05}_{-0.06}$	$-6.09^{+0.10}_{-0.13}$	$-4.61^{+0.04}_{-0.04}$
Accretion phase	SS	SS	SS	SS	SS	SS	SS
Temperature (K)	-	1550^{+20}_{-20}	-	129^{+3}_{-3}	1381^{+182}_{-80}	609^{+929}_{-385}	329^{+132}_{-272}
Feeding Zone Size (au)	-	-	-	-	$0.12^{+0.03}_{-0.04}$	$0.09^{+0.04}_{-0.06}$	-
fcf number {mass}	-	-	-	$0.26^{+0.06}_{-0.05}$ {0.52}	-	-	$0.30^{+0.11}_{-0.08}$ {0.52}
Differentiation Pressure (Gpa)	-	-	-	$25.3^{+2.6}_{-2.4}$	-	-	$25.6^{+19.7}_{-15.2}$
Oxygen Fugacity	-	-	-	$-2.4^{+0.4}_{-0.4}$	-	-	$-2.0^{+0.6}_{-0.6}$
Bayes Factor	n/a	2.1×10^{13}	n/a	4.3×10^{4}	5.6×10^{4}	17	4.6×10^{2}
N σ	n/a	8.1	n/a	5.0	5.1	2.9	3.9